UNIVERSITY OF SOUTHAMPTON

FACULTY OF NATURAL AND ENVIRONMENTAL SCIENCES

School of Chemistry

INVESTIGATION INTO THE INTERNAL STRUCTURE OFMESOPOROUS METALS

by

Thomas Frédéric Esterle

Thesis for the degree of Doctor of Philosophy

May 2012

UNIVERSITY OF SOUTHAMPTON

ABSTRACT

FACULTY OF NATURAL AND ENVIRONMENTAL SCIENCES

School of Chemistry

Doctor of Philosophy

INVESTIGATION INTO THE INTERNAL STRUCTURE OF MESOPOROUS METALS

By Thomas Frédéric Esterle

Nanostructured metal films were electrodeposited through the hexagonal lyotropic liquid crystalline phase (H_1). The mesoporous structure consists of porous channels (a few nm in diameter) arranged in an hexagonal array. These mesoporous metal films exhibit high surface areas supplied by the concave surface within the pores. The properties of these mesoporous materials have been investigated to gain an insight on the mesoporous structure.

Cyclic voltammetry in acid of H_1 mesoporous Pt is similar to polycrystalline Pt made up of low index Pt facets. However CO stripping voltammetry shows differences between the H_1 mesoporous Pt and polished Pt electrodes. The CO stripping voltammogram for the H_1 mesoporous Pt electrode exhibits a CO oxidation pre-wave and CO oxidation at lower overpotentials. These differences result from the presence of trough sites corresponding to the intersection of two pore walls within the mesoporous structure.

The adsorption of foreign atoms Bi and Ge on H_1 mesoporousPt was investigated to identify the different crystalline Pt facets. The features of the voltammetric profiles recorded in acid revealed the absence of large (111) domains and the presence of (100) terraces sites. CO stripping voltammetry for H_1 mesoporous Pt modified with Bi suggests the presence of a CO-Bi mixed adlayer. However, the absence of the aforementioned pre-wave was attributed to the adsorption of Bi on the trough sites thus causing inefficiency in oxygen transfer for CO oxidation. In contrast, the significant pre-wave observed for H_1 mesoporous Pt-Ge leads to an enhancement for CO oxidation.

H_1 mesoporous metal films grown on microelectrodes show good stability of the measurement of hydrogen peroxide. H_1 mesoporous Rh with a variety of film thicknesses was extensively studied over a wide range of hydrogen peroxide concentrations. A kinetic model is proposed to describe the diffusion of hydrogen peroxide and the surface reaction in the pore.

The accessibility of the ionic liquid BMIM-PF_6 in the pores was investigated to assess the performance of mesoporous electrodes in supercapacitors. H_1 mesoporous Pt of diverse pore size and polished Pt electrodes were characterised in 1 M sulphuric acid and then tested in BMIM-PF_6. The double layer capacitances were higher for the H_1 mesoporous Pt films thanks to their internal surface area leading to the confirmation that the ionic liquid penetrates into the pores. The analysis of electrochemical impedance spectroscopy shows that the results fit a transmission line model and provides useful parameters for the characterisation of the nanostructured Pt film in BMIM-PF_6.

Table of Contents

DECLARATION OF AUTHORSHIP

I, THOMAS FREDERIC ESTERLE,

declare that the thesis entitled

INVESTIGATION INTO THE INTERNAL STRUCTURE OF MESOPOROUS METALS

and the work presented in the thesis are both my own, and have been generated by me as the result of my own original research. I confirm that:

- this work was done wholly or mainly while in candidature for a research degree at this University;
- where any part of this thesis has previously been submitted for a degree or any other qualification at this University or any other institution, this has been clearly stated;
- where I have consulted the published work of others, this is always clearly attributed;
- where I have quoted from the work of others, the source is always given. With the exception of such quotations, this thesis is entirely my own work;
- I have acknowledged all main sources of help;
- where the thesis is based on work done by myself jointly with others, I have made clear exactly what was done by others and what I have contributed myself;
- parts of this work have been published as:

T. F. Esterle, A. E. Russell, P. N. Bartlett"Study of Carbon Monoxide Oxidation on Mesoporous Platinum"*ChemPhysChem*. **2010**, 11, 2896-2905. **DOI: 10.1002/cphc.201000212**

T. F. Esterle, A. E. Russell, P. N. Bartlett "The effect of Bi adsorption on CO oxidation inside 1.8 nm Pt pores"*Phys. Chem. Chem. Phys.***2011**, 13, 17964-17968.**DOI: 10.1039/c1cp21741k**

Signed:

Date: 27th March 2012

Acknowledgements

I would first like to thank Prof. Phil Bartlett for his guidance and encouragement over the last three and half years and his ability to make electrochemistry an understandable world.

I would also like to thank all the members of the electrochemistry group but in particular: Dr. David A. Cook whose help was invaluable, Dr. Maciek Sosna who helped me during my PhD (and his encouragement to go to the pub on Fridays) and Dr. Liz Tull (for useful discussions at the beginning of my PhD). I would also like to thank them for the numerous cups of coffee taken at 9.30 and 14.30 every day. I would like to thank Dr. Matthew Roberts for his help in electrochemical impedance spectroscopy and useful observations (when things did not go as planned).

EPSRC for financial support.

I would like to thank my friends for their support.

I must thank my parents for their encouragements through these years who always helped somehow.

Lastly and by no means I would like to thank Peristeraki for her love, her support, her patience and her help and who brought light from a dark room.

Chapter 1: Introduction

The recent technological scientific trend focuses on the manufacturing of small devices with the maximum capacity. Novel structures with new essential intrinsic properties are demanded for a variety of technological fields such as batteries, selective sensors, capacitors and photovoltaic applications. Different materials and structures in a nanoscale range present fascinating properties owing to the high surface area compared to the bulk.

Materials researchers turned towards nanostructures of high surface areas compared to conventional materials. Nanostructured materials of high surface area have aroused a growing interest to have or enhance materials properties in a multitude of academic and industrial activities. High surface areas can be obtained by fabricating small particles where the surface-to-volume ratio is high (convex surface) or by creating materials presenting a high surface area from the voids compared to the bulk material (concave surface). In the first category of convex surface, one can find nanoparticles and the latter category of concave surface, one can find porous materials such as zeolites.

Since the discovery of zeolites, new materials with defined structure have been developed with porous channels of tunable dimensions at a nanometer scale. Different properties appear related to the control over the shape and the size of the pore. The possibility to synthesise materials with a particular pore size can create novel opportunities of research in catalytic or sorption technologies. The domain of mesoporous materials thus offers future challenges and prospects in different fields of science. New strategies emerge continually to fabricate mesostructured materials using templating methods.

Materials science exploits the use of surfactants to form supramolecules arrangements to create self-assembled nanostructures; an example is the synthesis of templated mesoporous silica[1]. One of the approach reported by Attard *et al.* was to use lyotropic liquid crystalline phases as templates to synthesise a nanostructured porous material[2]; this method will be used in the work of this thesis. The design of mesoporous ordered

materials with different pore sizes can be achieved by tuning the template molecules. These materials have high surface area thanks to their internal surface area within the pores but an inherent problem is to describe the structure formed with a sufficient accuracy to predict the behaviour of the material at an atomic scale. Surfactant templated materials can have a real potential in science and technology but a better understanding of their characterisation and their synthesis is required.

In this thesis, the aim is to describe the structure of mesoporous materials formed from the hexagonal lyotropic liquid crystalline phase acting as a template. In the next section, lyotropic liquid crystalline phases will be presented from which mesoporous materials can be obtained.

1.1 Liquid Crystals (LC)

Liquid crystals are a state of matter that possesses the properties of both liquid and crystalline solid. The crystalline solid is a structure whose molecules occupy specific sites in a lattice extending in three specific orientations. In contrast, the liquid is a state in that the molecules do not have a positional or orientational order and diffuse randomly. In liquid crystals, the molecules are free to diffuse as in a liquid but some of the orientational order remains. In fact, the order is not as ideal as in a crystalline solid; the molecules in a liquid crystal spend more time pointing in one direction than along the others. Liquid crystals are like liquids but with a degree of order which constitutes another state of matter between solid and liquid[3]. The common characteristic of all the liquid crystals is their anisotropy.

One of the main categories of the liquid crystals is lyotropic phases.

1.1.1 Lyotropic Liquid Crystals

The term ‘lyotropic’ is employed to call a material if liquid crystalline phases are formed because of the addition of a solvent. Lyotropic liquid crystals are formed by dissolution of anisotropic molecules in a solvent (typically water). The lyotropic liquid crystal phases are dependent of the temperature and the concentration of one component in another[4]. The lyotropic liquid crystal molecules are amphiphilic having end groups with different properties. One end of the molecule is polar with a hydrophilic headgroup and the other end is nonpolar with a long hydrophobic hydrocarbon chain as shown in

Figure 1-1a. The amphiphilic molecules dissolved in both polar and nonpolar solvents will generate lyotropic liquid crystals. The amphiphilic molecules are also known as surfactants. Figure 1-1b shows the structure of a surfactant, octaethylene glycol monohexadecyl ether ($C_{16}EO_8$), with a hydrophobic alkyl tail and a hydrophilic polyethylene oxide headgroup.

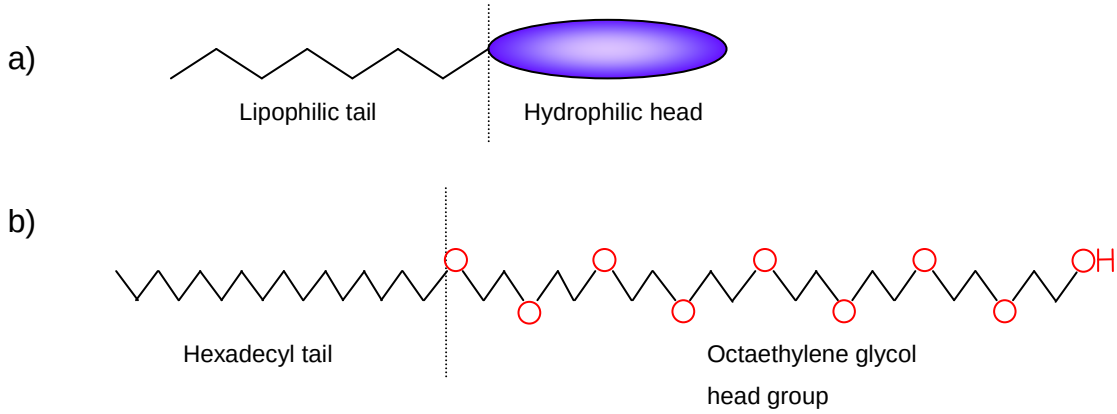

Figure 1-1. a) Archetype of an amphiphilic molecule. b) Octaethylene glycol monohexadecyl ether ($C_{16}EO_8$).

Different structures are formed depending on the proportion of surfactant mixed with a solvent, e.g. water. At very low concentrations, the amphiphilic molecules are dissolved and dispersed in the solution without any order. As the concentration of surfactant increases above a certain concentration, called the critical micelle concentration (CMC), the amphiphilic molecules arrange themselves into supramolecular structures. Two different structures are possible: micelles (in the case of soap) and vesicles (in the case of phospholipids). For the micellar structure shown in Figure 1-2B, the polar head groups of the molecules form the outside of the structure with the hydrophobic chains toward the centre, shielded from the solvent. The micelles may also pack into a cubic arrangement. For the vesicle structure shown in Figure 1-2D, the amphiphilic molecules create a double layer which forms a shell with the water inside and outside of the structure.

With increasing the concentration of surfactant (usually around 50 % wt), the micelles or vesicles combine to form cylindrical rods packing into an hexagonal array. The hydrophobic chains are turned toward the rod axis and the hydrophilic head groups form the outside of the structure. Such a structure is called the hexagonal phase as shown in Figure 1-2A.

At even higher concentrations, another phase is formed called the lamellar phase. The amphiphilic molecules form bilayers with the hydrophobic chains pointing to the inside and the head groups outside as shown in Figure 1-2C. The bilayers are separated from each other by water in between. At very high concentrations, inverse phases are formed where the hydrophilic head groups are inside the structure locking water inside such as the inverse micellar phase shown in Figure 1-2E.

The inverted structures can also be formed if the amphiphilic molecules are added to a non-polar solvent (e.g. oil) where it is favourable for the hydrophobic chains to be in contact with this type of solvent.

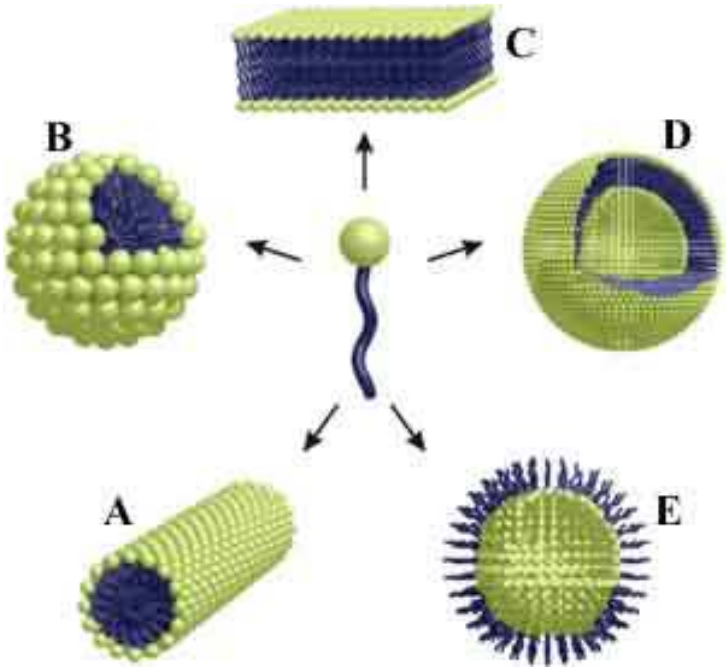

Figure 1-2. Schematic representing the different types of aggregation of amphiphilic molecules forming supramolecular structures when solvated in a polar solvent. Liquid crystal phases: a) hexagonal, b) micellar, c) lamellar, d) vesicle, e) inverse micellar. This image can be found from the link in the reference [5].

1.1.2 Liquid Crystal Templating (LCT)

The surfactant $C_{16}EO_8$ possesses a hydrophobic alkyl chain and a hydrophilic ether headgroup which forms lyotropic liquid crystalline phases when in water. Figure 1-3 shows the phase diagram of $C_{16}EO_8$ in water.

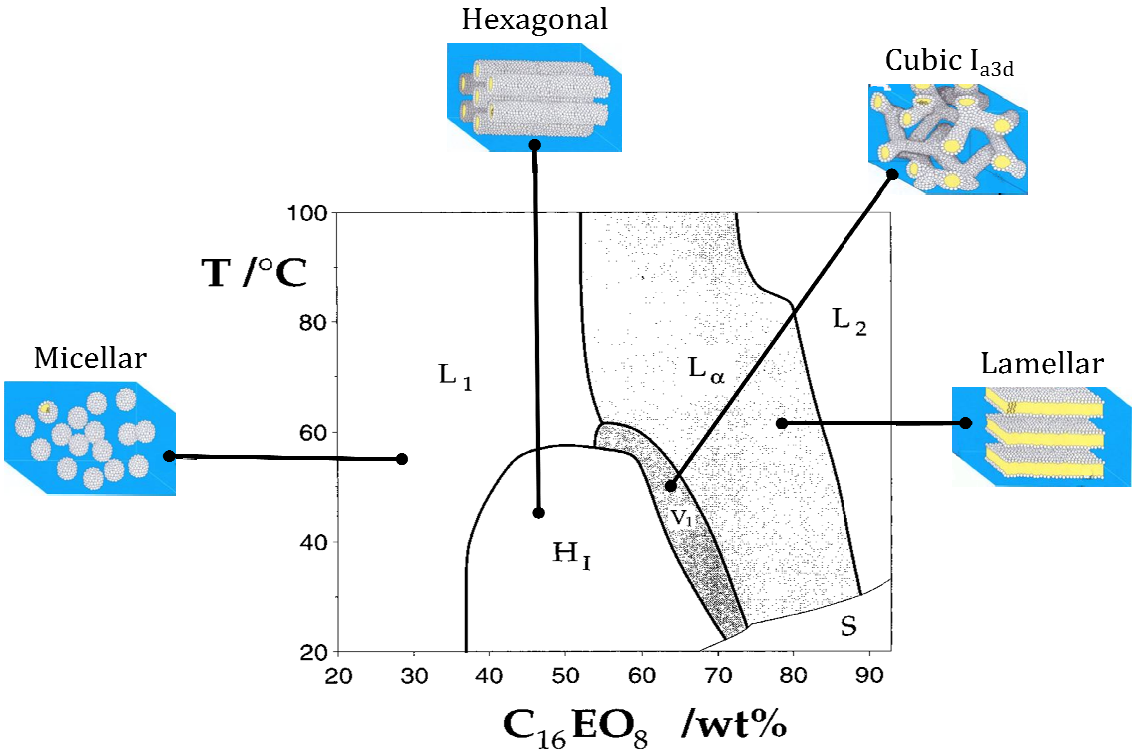

Figure 1-3. Phase diagram for octaethylene glycol monohexadecyl ether ($C_{16}EO_8$) in water taken from Attard *et al.*[6] L_1 is the micellar phase, H_1 is the hexagonal phase, V_1 is the cubic phase, L_α is the lamellar phase, L_2 is the inverse micellar phase and S is a solid phase.

If a surfactant, such as $C_{16}EO_8$, is mixed with water, different phases are formed under appropriate conditions of concentration and temperature. The amphiphilic molecules aggregate and arrange themselves into different structures as shown in Figure 1-2. The formation of these structures creates a cast in the case of the deposition of a metal salt. If a metal salt is dissolved in the aqueous solution, the chemical reduction of the metal salt occurs between the surfactant aggregates forming a solid. On removing the surfactant, the architecture of the resulting material is a cast of the mould formed by the surfactant.

When a metal salt is dissolved in water, the boundaries of the phase diagram change. For example, the phase diagram for $C_{16}EO_8$ with 1.92 M hexachloroplatinic acid is represented in Figure 1-4. The hexagonal phase is quite broad in terms of a wide range of concentrations and temperatures which make this phase appealing as a template for the metal deposition.

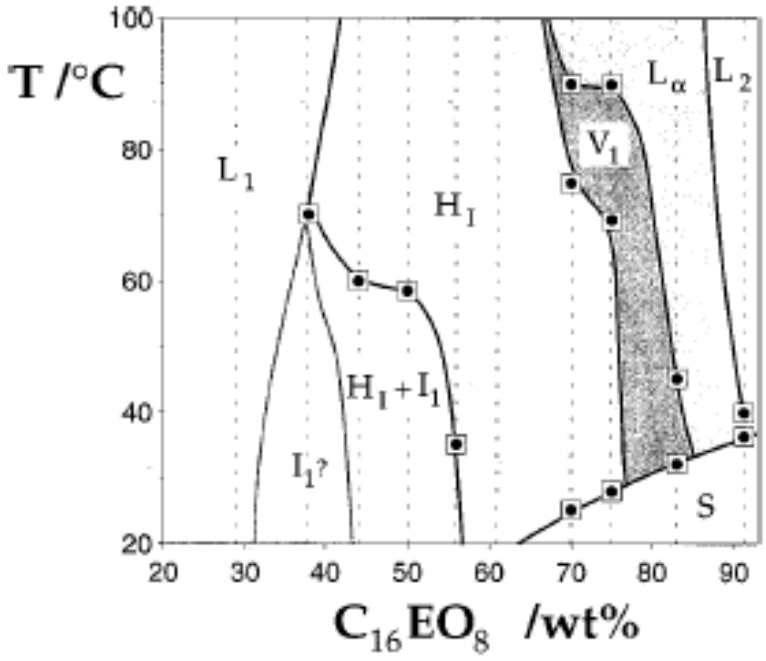

Figure 1-4. Phase diagram for $C_{16}EO_8$ in the solution of 1.92 M HCPA taken from Attard *et al.*[6] L_1 is the micellar phase, I_1 is a cubic phase, H_1 is the hexagonal phase, V_1 is also a cubic phase, L_α is the lamellar phase, L_2 is the inverse micellar phase and S is a solid phase.

1.2 Porous Materials

Porous materials have been of great interest due to their potential applications as molecular sieves and high surface area catalysts. Zeolites in particular have received a lot of attention because of their importance in many industrials applications in selective catalysis and are commonly found in household products such as washing powders and water softeners[7]. Zeolites are microporous solids with a porous structure consisting of tunnels or a network of interconnected cavities. Zeolite structures are found in naturally occurring minerals and the first synthetic examples were synthesised in the 1950s.

Zeolites have a narrow range of pore sizes smaller than 1 nm, i.e. microporous (microporous materials have pores smaller than 2 nm). Zeolites can be used for catalysis and size selective separation involving only small molecules. Synthetic materials have been produced with larger pore size but are amorphous or paracrystalline (materials having short or medium ordering in their lattice) such as silicas[8] or transitional aluminas[9]. The synthetic materials with the largest pore that have been manufactured were the aluminophosphates $AlPO_4$-8[10], VPI-5[11] and cloverite[12] which have pore sizes in the range of 0.8 – 1.3 nm.

1.2.1 The Mobil Method

A new family of silicate/aluminosilicate mesoporous molecular sieves designated as M41S was discovered in 1992[1, 13]. These materials were synthesised by the calcination of the silicate gel containing organic surfactants. One of the members of this family of mesoporous sieves, MCM-41 (Mobil Composition of Matter-41), presented an hexagonal array of pores with diameters from 15 to 100 Å depending on the experimental conditions used for the synthesis. Other members of this family were also synthesisedfrom a cubic phase. The structure and the pore diameters of these materials were always related with the nature of the surfactant. A liquid crystal templating (LCT) mechanism was proposed for the synthesis of these materials[1].

The concentration of surfactant used for the synthesis of these materials is below the concentration needed to form liquid crystal phases (as low as 1 %). A study of this synthesis by Monnier *et al.* led to the conclusion that the mesophase formation and associated silica polymerisation were attributed with strong interactions between the cationic surfactant and oligomeric silicate polyanions[14]. This results in a high concentration of silicate species at the silicate-surfactant interface favouring the silicate polymerisation and ordering the silicate-encased surfactant micelles into structures. A proof of this mechanism was provided by Cheng *et al.* who demonstrated that MCM-41 can be formed if the surfactant concentration was above the CMC[15].

These materials are of interest because they extend the molecular sieve materials into a larger pore range; previously, the largest pore dimensions were found up to 1.3 nm for some metallophosphates[11, 12]. The larger pore structures of MCM-41 have surface areas over 700 $m^2\ g^{-1}$ and hydrocarbon sorption capacities of 0.7 $cm^3\ g^{-1}$ and greater. These materials have aroused a growing interest producing many papers[14, 16] and the same approach has been extended to mesoporous metal oxides[17].

1.2.2 True Liquid Crystal Templating (TLCT)

In 1995 Attard *et al.* reported that templated silica mesostructures were obtained from liquid crystalline mesophases using octaethylene glycol monododecyl ether ($C_{12}EO_8$) and octaethylene glycol mono hexadecyl ether ($C_{16}EO_8$) in water with tetramethyl orthosilicate (TMOS) as the silica precursor[18]. The formation of the mesostructured

silica was performed under acidic conditions and at room temperature; the methanol formed by the hydrolysis of TMOS was removed under partial vacuum because the presence of methanol in the mixture modifies the mesophase.

This method uses higher concentration of surfactant (about 50 % wt) than in the Mobil method and true liquid crystalline phases are generated by the preparation of the mixture. Unlike the Mobil method, the formation of mesostructured silica is independent on the interaction between the surfactant and the silica precursor. Different mesoporous silica architectures were successfully cast using the hexagonal, cubic and lamellar liquid crystalline phases. The silica obtained from the sol-gel synthesis in a lyotropic phase yields a monolithic film as opposed to sub-micron powders produced by precipitation in the Mobil method.

The lyotropic liquid crystalline phases were confirmed by observation of the mixture under a polarising light microscope and transmission electron microscopy was used to investigate the silica mesostructures. The TEM study showed the hexagonal, cubic and lamellar structures of silica with pore diameters of 2-3 nm and wall thicknesses of 1.2 nm[19].

1.2.3 Advantages of TLCT

The reasons to perform the synthesis of ordered mesoporous silica through a true liquid cyrstal template are manifold. Unlike the Mobil method, the TLCT method avoids the interaction between the silica precursor and the surfactant. Therefore, the TLCT is dependent of the structure and the charge of the surfactant. Another advantage is the possibility to use the pre-formed liquid crystalline phase as a template to predict the structure of the product. The presence of inorganic precursors has a little effect on the phase behaviour of a liquid crystal. Hence, the phase diagrams of surfactant-water systems reported in the literature can serve as guidelines to predict the mesostructure of the product. The final advantage is that the synthesis through the TLCT results in a monolithic product unlike the formation of the fine particles prepared by the Mobil method.

1.2.4 Mesoporous platinum from TLCT

This approach was later developed by Attard *et al.* who produced powders of mesoporous platinum by dissolving the platinum salt into the aqueous regions of a hexagonal lyotropic liquid crystalline template and then chemically reducing this to platinum metal[2]. This type of structured platinum exhibits very high specific surface area, up to ~ 60 m^2 g^{-1}. The synthesised product consisted of particles with diameters in the range of 90 and 500 nm and showed the inverse architecture of the LC phase. The TEM observation showed a hexagonal array of 3 nm diameter pores separated by 3 nm thick walls.

Thereafter it was reported that the electrodeposition of mesoporous platinum films was possible from mixtures in the hexagonal lyotropic liquid crystalline phase[2]. Scanning tunnelling microscopy (STM) observation indicated that the film was uniform and flat with a surface roughness of 20 ± 5 nm over a 1 mm^2 area. TEM imaging revealed a mesoporous structure consisting of an hexagonal array of cylindrical pores. The pore diameter of mesoporous Pt electrodeposited from the hexagonal LC phase could be controlled by variation of the length of the alkyl chains of surfactant in combination with a hydrophobic additive. For example, the use of $C_{12}EO_8$ in the mixture gives a pore size of ~ 1.7 nm whereas the use of $C_{16}EO_8$ yields a pore size of ~ 2.5 nm; the addition of n-heptane with $C_{16}EO_8$ in the latter mixture gives a pore size of ~ 3.5 nm.

A later work by Elliott *et al.* investigated the electrodeposition of mesoporous platinum onto gold or platinum microelectrodes[20]. The analysis of the cyclic voltammetry in acid revealed roughness factors of ~ 210 (corresponding to a surface area of 6.45 m^2 g^{-1})[20]. Cyclic voltammetry in potassium ferricyanide demonstrated that nanostructured platinum microelectrodes with high surface area retain the efficient mass transport characteristics. A greater double layer capacitance was also obtained due to the high surface area of the material. This combination of properties is unique and can be useful for amperometric detection of organic species with poor electrode kinetics. If the surface area of the electrode is too small, the reaction of some species could be kinetically limited. A solution to avoid this issue is to increase the electroactive surface area of the electrode while the microelectrode maintains its diffusional properties.

1.2.5 Advances and Applications of TLCT

The electrodeposition of mesoporous metal or alloy films is possible from lyotropic liquid crystalline mixtures with various metal salts dissolved in the aqueous domains. The material primarily electrochemically deposited was platinum[2]; then, this approach was carried on not only pure metals such as Cd[21], Co[22], Ni[23, 24], Pd[25], Rh[26], Se[27], Sn[28], Te[29], but also their alloys like Pt-Ru[30], Pt-Ni[31], Pt-Pd[32], Ni-Co[33].The compound Cd-Te was also electrodeposited by this method[34]. These mesoporous films have pore sizes over a range of 1.7 – 10 nm. The characteristics of the mesoporous films such as the film thickness or the pore dimensions can be controlled by the different conditions of deposition (i.e. temperature, surfactant, deposition charge and source of metal ions)[35].

Mesoporous nanostructured materials were used in a wide variety of applications such as gas sensors[36], fuel cells[37], supercapacitors and batteries[38] over these last years. It was reported that mesoporous platinum increases the kinetics of oxygen reduction when compared to bulk polycrystalline platinum[39]. Similar microelectrodes were also used in the detection of glutamate[40] and for hydrogen peroxide detection[41] (discussed in Chapter 5).
The technique was extended to mesoporous nickel for supercapacitors and batteries[38]. Since the presence of interparticle resistances was eliminated, the electron conductivity was enhanced and hence, power losses decrease. Moreover, the porous nanostructure enables a rapid and unimpeded movement of electrolyte species. The design of the nanostructure has therefore improved supercapacitor and batteries performance. The application of liquid-crystal-templated mesoporous cobalt was realised for mesoporous magnetic materials. Cobalt films electrodeposited from the hexagonal phase showed better results in terms of coercivity than bulk polycrystalline cobalt and the method could encourage the development in advanced storage media[2]. Mesoporous palladium catalyses methane and was investigated for gas sensors[42].

H_1 mesoporous Pt have received interest as electrocatalysts towards the electrooxidation of small organic molecules such as CO or CH_3OH. The design of the porous structure is attractive since high surface areas can be exhibited thanks to the concave nature of the structure. However, the catalytic surface plays a key role in a broad range of

electrocatalytic reactions. These reactions are mostly structure sensitive and hence it is necessary to know the atomic structure of the electrode surface. In electrochemistry, carbon monoxide is a probe molecule to investigate the electrode surface and provide insight into the nanoscale structure of H_1 mesoporous materials.

1.3 Carbon monoxide electrochemistry

In electrocatalysis, carbon monoxide electrochemical oxidation is one of the most studied reactions for fuel cell applications and it is also a probe molecule to investigate the properties of the electrode surface. Carbon monoxide is a by-product of the oxidation of many organic molecules such as methanol[43] or formic acid[44] acting a poison on the electrode surface. Platinum is a common noble metal used as a catalyst for electrochemical reactions. Unfortunately, when the oxidation of the organic molecules occurs, carbon monoxide is formed and adsorbs on platinum reducing the surface area and, in consequence, the performance of the electrode. The possible pathway for the oxidation of carbon monoxide involves the formation of oxygenated species on the electrode surface. A possible mechanism for the oxidation of carbon monoxide on platinum could be[45]:

$$Pt + H_2O - e^- \rightarrow Pt - OH + H^+ \quad (1)$$

$$Pt - OH + Pt - CO \rightarrow CO_2 + 2Pt + H^+ + e^- \quad (2)$$

where the OH species and CO are adsorbed on neighbouring sites.

1.3.1 Adsorption of CO

The adsorption process of carbon monoxide molecules on a metal surface results in chemical adsorption without charge transfer as represented in Figure 1-5a[46].

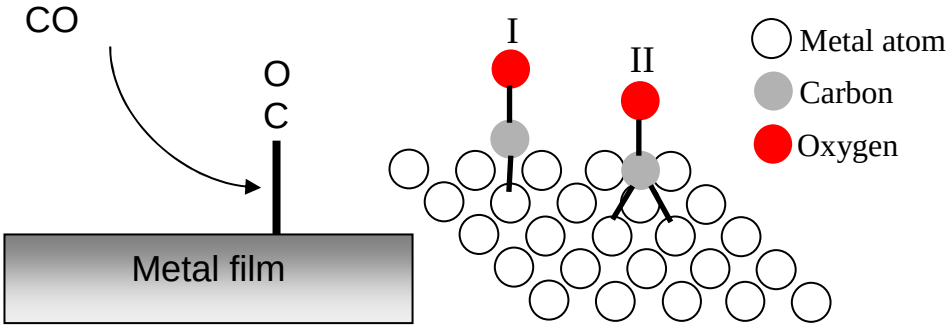

Figure 1-5. (a) Scheme for the carbon monoxide adsorption, (b) Representation of CO bonded linearly (I) and bridge bond (II).

The adsorption of the CO molecule at the metal surface is realised by the metal-carbon atom bond. Two forms of bond for the CO adsorption exist, either the CO molecule is bonded linearly or the carbon atom forms a bridge between two adsorption sites which are adjacent (Figure 1-5b)[46]. The adsorption states of CO on the metal substrate are highly structure dependent. The information on bonding and adsorbate structure can be obtained by infrared (IR) spectroscopy. This technique was employed to probe the electrochemical interface of CO species at controlled potential for different types of Pt electrode surfaces[47, 48]. These results can be combined with the voltammetric behaviour which is also structure dependent. The CO stripping voltammetry can monitor the changes in the electrochemical interface of the CO adlayer on platinum. The features of the CO voltammogram are sensitive to the type of Pt surface such as single-crystals[49-51] or stepped surfaces[52]. This will be discussed in Chapter 3.

1.3.2 Pt-based catalysts for CO oxidation

From the study of CO oxidation on platinum, two options can be considered on the design of Pt-based to improve CO oxidation. The first option lies in the modification of the platinum electrode surface at a nanoscale generating a weakly adsorbed state of CO on Pt, leading to ease CO oxidation and possibly higher reactivity[51]. The second option aims to modify the platinum surface with a foreign atom which preferably does not adsorb CO and insure the formation of reactive hydroxyls at low potentials. In the latter option, the modification of the platinum surface can occur through two different processes, either by adsorption on the surface of a foreign adatom or by creating an alloy.

Alloy catalysts based on platinum can be envisaged to facilitate CO electrooxidation where the two metals have different roles in the reaction. In general, the catalytic enhancement arises from a bifunctional effect in which the second metal provides the reactive intermediate species. The catalytic improvement can also be ascribed from other contributions such as the ligand effects and the morphological effects[51]. The ligand effects involve the promoter that alters the electronic properties of the catalytically active metal. The morphological effects lead to the dilution of the active component with the catalytically inert metal changes the distribution of active sites, thereby opening different reaction pathways[51].

For instance, a common Pt-based alloy used as catalyst for CO oxidation is platinum-ruthenium alloy. Ruthenium is more easily oxidised than platinum so PtRu alloy is employed as a catalyst since the adsorption of oxygenated species on the surface becomes easier[53]. Other combinations of Pt based alloy were found to improve the catalysis of CO oxidation such as PtMo[54, 55], PtSn[56].

Another concept to enhance the catalysis is the addition of the second metal on platinum to nucleate oxygenated species at lower potentials than a pure Pt electrode, resulting in the early oxidation of adsorbed CO.

1.4 Foreign atoms adsorption

The modification of the electrode surface by foreign adatoms can improve significantly the electrocatalytic properties towards CO oxidation.

1.4.1 Catalytic activity improvement

As mentioned in the previous Section, platinum is susceptible to poisoning by species such as CO during the electrooxidation of organic molecules reducing its catalytic performance. The adsorption of foreign atoms on platinum can improve the catalytic activity in order to minimise the poisoning effect. The coverage of the surface by a second metal promotes the catalytic reaction of many organic substances like methanol[57] or formic acid[58, 59]. The ad-atoms for such reactions are various and include Bi[44, 60], Ge[57], Sn[57, 61], As[44, 62], Pb[63], Ru[64]. This was accomplished by various methods including the adsorption of foreign atoms on the platinum surface via underpotential deposition or spontaneous adsorption by immersion.

1.4.2 Surface Probe

The modification of the platinum surface does not only improve the performance of the electrode but also identifies the crystalline facets of the surface. Most of the electrochemical reactions are structure-sensitive therefore it is useful to have knowledge of the surface structure of the electrode. The types of sites (terrace, kinks, steps...) present will determine the reactivity of the electrode. It is necessary to develop methods to identify the different sites on the electrode surface. The electrochemical *in situ* technique commonly used is cyclic voltammetry to characterise the electrode surface.

This topic has been the interest for electrochemists generating a large number of papers on metal single-crystals[51, 65-73]. The study of single-crystals is fundamental to establish the properties of the electrochemical reaction on the different surface sites. The results can then be extrapolated to the electrocatalytic response for polycrystalline surfaces.
In the case of platinum, the characterisation of the different surface sites can be performed by cyclic voltammetry in acid. The adsorption of hydrogen and anions are used as probes to determine the surface sites. However, it is difficult to quantify the different surface sites since hydrogen and anions adsorb in a similar potential range[74]. Another problem concerns the shape and number of peaks for the different surface sites on the voltammogram to separate the different contributions and make the best deconvolution[75, 76]. An alternative method to probe the surface sites is to use the adsorption of foreign atoms. The information of the different domains of the surface can be obtained by the irreversible adsorption of the foreign atoms which occurs on specific surface sites of platinum. If the adatom undergoes a surface reaction in a potential range in which the contributions from other surface symmetries are negligible, it is possible to monitor the presence of a specific crystal symmetry. For instance, these surface reactions can be relevant to probe the symmetry of different domains of platinum such as the (111) symmetry with adsorbed tellurium or bismuth atoms or (100) terraces of platinum with adsorbed germanium atoms[77].

The adsorption of foreign adatoms Cu, Pb and Ag on H_1 mesoporous Pt electrode has already been investigated but in that study, the aim was to quantify the concentration of the ions in solution[78] and the internal surface of the pores was not investigated using this method.

Knowing the structure of H_1 mesoporous materials is of importance to understand the mechanism of the reaction at the electrode surface. The peculiar architecture of H_1 mesoporous materials is likely to affect the kinetics of the reaction.

1.5 Kinetic study

1.5.1 Mechanism for an Electron Transfer Reaction

Redox reactions involve the transfer of electrons between a chemical species and an electrode. If the applied potential is sufficient enough at the working electrode, an

exchange of electrons occurs with the species at the surface which can imply either oxidation or reduction. The current is generated by a transfer of electrons between the electrode and the species in solution. A general expression for the current under mass transport control is:

$$i = nFAk_m c \quad (1)$$

where i is the current generated by the reaction (A), n is the number of electrons transferred, F is the Faraday constant (96485 C mol^{-1}), A is the electrode area (m^{-2}), k_m is either the mass transfer coefficient of the species involved (m s^{-1}) or the rate constant and c is the bulk concentration of the species (mol m^{-3}).

1.5.2 Microelectrodes

Microelectrodes are defined as electrodes with at least one dimension in the scale of tens of micrometers or less, down to submicrometer range[79]. Microelectrodes were originally constructed for biologist to carry out *in situ* measurement in living organisms with limited tissue damage[80]. Their application in electrochemistry was developed later when low current measurements became possible. The unusual properties of microelectrodes on mass transport have been then explored leading to the analysis of fast heterogeneous or homogeneous electrode processes, which is not possible with conventional electrodes.

Different geometries of microelectrodes exist such as disc, hemisphere, ring or band electrodes; nevertheless, disc microelectrodes are the easiest to build just by sealing wires into glass. Therefore, only disc microelectrodes will be considered. The range for the radii of the microwires is between 0.1 and 100 µm and the range of 5 – 25 µm is most commonly used in laboratory.

The properties of microelectrodes are different from larger electrodes:

- **Mass transport regime.**

Since the steady state is rapidly established, microelectrodes yield true diffusion-control currents[81]. This is true if all the dimensions of the microelectrodes are < 50 µm.

- **Charging current**.

The double layer capacitance of an electrode is proportional to its surface area. In the case of the microelectrode, the surface area is small so the capacitance is small. This means that the Faradaic process will be attained after short times, which facilitates the investigation of fast electron transfer reactions and very short lived species.

- **Decrease of the ohmic drop**.

As the electrode area is small, the current passing through the microelectrode is low, in the order of a few nA, this reduces the distortion from *IR* drop. One advantage of this is to study electrochemical reactions at the microelectrode surface in solution without supporting electrolyte or in resistive media[82-84].

The different properties of microelectrodes are advantageous for practical reasons. Their size enables them to be used in experiments in a small volume without modifying the concentration of the species. The time scale of the experiment is short as the steady state is reached rapidly. In the case of the disc microelectrode, the expression for the current at steady state is[85]:

$$i_L = 4nFDca \qquad (2)$$

where i_L is the limiting current (A), D is the diffusion coefficient ($m^2\ s^{-1}$) and a is the radius of the microdisc (μm).

1.5.3 Rotating Disc Electrode (RDE)

The rotating disc electrode is a type of experiment where the mass transport is induced by convection. For kinetic studies, it is necessary to understand the hydrodynamics of the system. A RDE consists of a polished disc of the electrode material, with a diameter typically between 0.2 and 2 cm, surrounded by an insulating sheath of larger diameter. The RDE is rotated with a perpendicular axis to the surface of the disc. By rotating, the RDE acts as a pump and the solution is pulled vertically upwards to the disc perpendicular to the surface. While rotating, the solution near the electrode surface becomes more viscous and is thrown outwards radially creating an under pressure in the electrode centre vicinity, hence the pumping motion of the solution. This phenomenon account for fresh reactant from the bulk solution brought to the electrode surface. Figure

1-6 shows the flow pattern of the solution close the electrode surface when a circular object is in rotation[45].

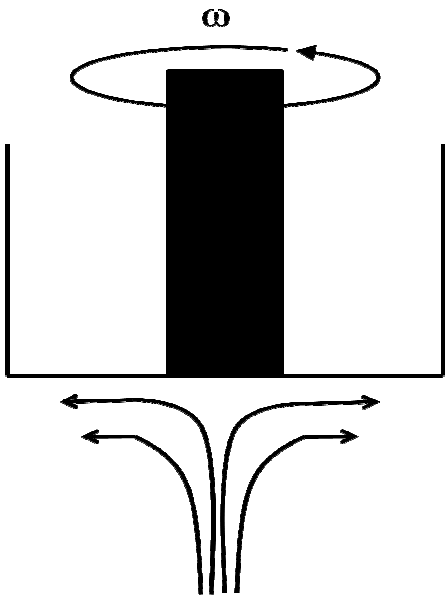

Figure 1-6. Solution flow close to the rotating disc electrode surface in an electrolyte.

The RDE gives a steady state mass transport regime and the mass transfer coefficient is proportional to the square root of the rotation rate of the disc:

$$k_m = \frac{1.554 D^{2/3} W^{1/2}}{\nu^{1/6}} \qquad (3)$$

where W is the rotation rate (Hz) and ν is the kinematic viscosity ($m^2\ s^{-1}$)

The limiting current for a mass transport controlled reaction is given by the well known Levich equation:

$$i_L = 1.554 \frac{nFAD^{2/3}c}{\nu^{1/6}} W^{1/2} \qquad (4)$$

where A is the geometric surface area of the electrode (m^2).

So far, H_1 mesoporous electrodes have been investigated using aqueous solutions. The electrolyte chemistry based on solvent-free ionic liquids is of interest, especially in the development of double-layer supercapacitors. The structure of H_1 mesoporous electrodes is made up of cylindrical pores in the range of a few nanometers arranged into a hexagonal array. The accessibility of the ionic liquids into such a structure would be of relevance for considering H_1 mesoporous films as supercapacitor electrodes.

1.6 Ionic liquids

1.6.1 Archetype of the ionic liquid

Ionic liquids, or room temperature molten salts, are non-aqueous solvents composed only of ions. Ionic liquids by definition are salts whose melting point is below the boiling point of water[86]. These salts exhibit weak coulombic interactions thanks to the combination of large cations and charge-delocalised anions. As a result, the ionic liquid is prevented from forming a regular crystal lattice because of the flexibility of the anion and the assymetry of the cation. Ionic liquids are composed of organic ions which may undergo a wide range of structural variations thanks to the preparation of a multitude of their components. Various kinds of salts can be used to design an ionic liquid that has the desired properties for a given application; ionic liquids have been investigated for various applications such as solar cells, fuel cells and batteries[86-91]. Ionic liquids can be divided into different groups according to the types of cation and anion. The most common cations include imidazolium, quaternary ammonium[88], piperidinium[91] and pyrrolidinium[90]. However, recent studies have focused on the use of ionic liquids with the particular anion bis(trifluoromethanosulfonyl) imide ($TFSI^-$) though others are commonly used such as bis(fluorosulphonyl)imide and hexafluorophosphate as anions. Figure 1-7 shows a cation and anion used to form an ionic liquid.

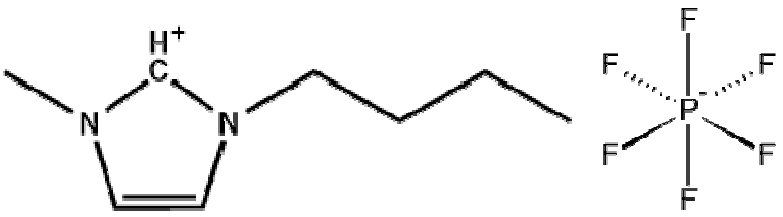

Figure 1-7. Representations of the cation 1-N-butyl-3-methylimidazolium $[BMIM]^+$ and the anion hexafluorophosphate $[PF6]^-$.

Ionic liquids have also been considered as electrolytes in supercapacitors. Most commonly, supercapacitors employ aqueous or organic electrolytes limiting the operating voltage of the electrochemical double layer capacitors (EDLCs) systems to 1.23 and 2.7 V respectively[92]. Thanks to their high potential window stability, ionic liquids allow operating voltages > 3.5 V increasing the energy capability of the devices.

The crucial factor behind the high capacitance is the thickness of the electrochemical double layer so as to have an effective material.

The structure of the electrical double-layer in dilute aqueous solutions has been profoundly studied and descriptions of the double layer have been developed to understand its behaviour quite accurately. However, the structure of the double layer of ionic liquids is of debate and the behaviour of the electrical double layer of the ionic liquids needs yet to be developed. It is thus necessary to describe the current understanding of the electrical double-layer at a perfectly polarisable electrode in aqueous media.

1.6.2 Electrical double layer in dilute aqueous solutions

1.6.2.1 Helmholtz model

The first model was suggested by Helmholtz who compared the electrical double-layer to the two parallel plates of a capacitor as illustrated in Figure 1-8. The charge on the electrode is balanced by a layer of ions of opposite charge directly contiguous to the surface.

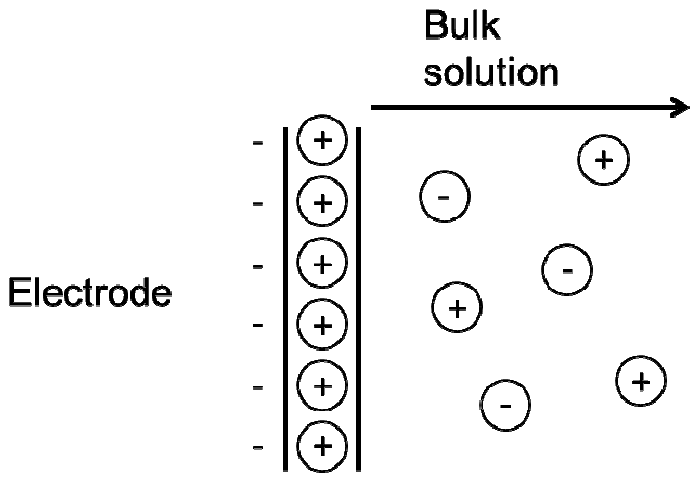

Figure 1-8. Schematic representation of the Helmholtz model for the electrical double layer[45].

Outside the layer, the solution is neutral having an equal concentration of cations and anions and has the same composition as the bulk.

1.6.2.2 Gouy-Chapman model

Later, the ability of ions to move freely through the electrolyte was considered. Figure 1-9 illustrates the Gouy-Chapman model.

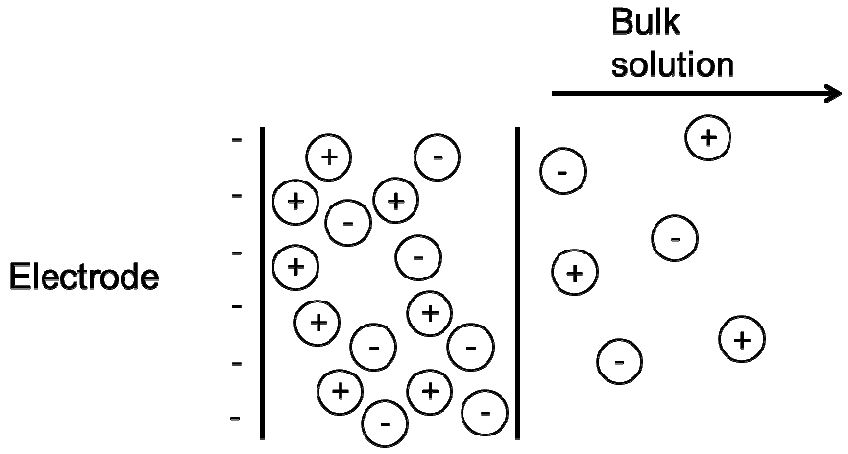

Figure 1-9. Schematic representation of the Gouy-Chapman model for the electrical double layer[45].

The charge on the electrode is balanced by ions in solution of opposite charge which are free to scramble under thermal quanta instead of being bound to the surface. There is an excess of cations over anions nearby the surface, which decreases gradually until the composition of the bulk concentration is reached.

1.6.2.3 Gouy-Chapman-Stern

The Gouy-Chapman-Stern model is a combination of the two previous models as illustrated in Figure 1-10.

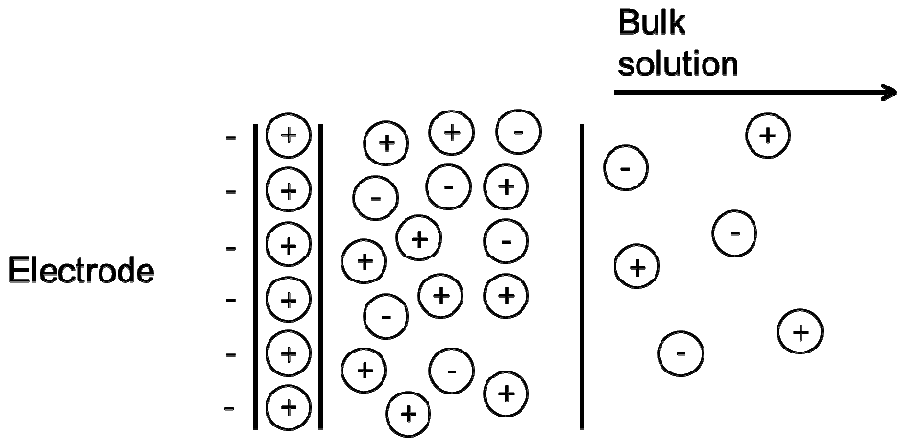

Figure 1-10. Schematic representation of the Gouy-Chapman-Stern model for the electrical double layer[45].

The electrical double-layer of the Gouy-Chapman-Stern model is composed of an inner compact layer (Helmholtz layer) and an outer layer (diffuse layer) where cations outnumber anions with a progressive change to the bulk solution composition with distance from the surface.

The Gouy-Chapman-Stern model is accepted for dilute aqueous solutions but fails to describe the behaviour of concentrated solutions and ionic liquids. One of the complication to the prediction of the Gouy-Chapman-Stern model is the ions outside the compact layer are considered as point charges which occupy no volume whereas the ions of the ionic liquids are large, flexible, highly polarisable[93]. Besides, the low melting point of the ionic liquids induces interionic forces in addition to Coulombic forces which may affect the electrical double-layer[93]. New models have been proposed to predict the behaviour of the electrical double-layer of ionic liquids but it is interesting to notice that these models also comprise an inner layer and an outer layer as the Gouy-Chapman-Stern model describes for dilute aqueous solutions[94]. Since a potential importance exists in ionic liquids for supercapacitors and other fields in electrochemistry, a real effort is engaged towards the understanding of the electrical double-layer in ionic liquids near an electrode interface.

1.7 Thesis overview

This work deals with the characterisation of the H_1 mesoporous metal electrodes, notably to give an insight to the internal atomic structure of the pores. Another objective is to study the kinetics of surface reaction within the mesoporous film and the performance of these materials towards electrolytes such as ionic liquids.

In Chapter 3, cyclic voltammetry in sulphuric acid and CO stripping voltammetry of H_1 mesoporous Pt electrode are compared to those of polished Pt electrodes. The effects of the scan rate and the adsorption potential of CO were also investigated. The features of the voltammograms for each electrode are analysed and a model for a single pore of the H_1 mesoporous architecture was proposed.

Chapter 4 is concerned with the adsorption of foreign atoms on H_1 mesoporous Pt electrodes in order to identify the different crystalline Pt facets. Two foreign atoms were chosen namely bismuth and germanium. Surface reactions on bismuth and germanium

monitored by cyclic voltammetry in sulphuric acid can reveal the presence of different Pt symmetries. CO stripping voltammetry on H_1 mesoporous Pt modified with each foreign atom was also performed to identify any changes on the CO stripping voltammetric profile compared to that obtained with the unmodified H_1 mesoporous Pt electrode. Conclusions were drawn about the mechanism of CO oxidation on H_1 mesoporous Pt and each foreign adatom. The catalytic performance for CO oxidation with each combination Pt-Bi or Pt-Ge was discussed.

Chapter 5 is concerned with polished Pt, H_1 mesoporous Pt and H_1 mesoporous Rh microelectrodes for hydrogen peroxide detection. It has been shown that H_1 mesoporous Pt microelectrode improves greatly the electrochemical response for hydrogen peroxide oxidation[41]. Several films of different thicknesses of H_1 mesoporous Rh are electrodeposited on the microelectrodes. The experimental data of the electrochemical response of hydrogen peroxide oxidation are gathered in order to fit to a theoretical kinetic model. Complementary experiments are then performed using a Pt RDE modified with a H_1 mesoporous Rh film to obtain a new set of data for the model and draw a conclusion on the presence of a product inhibitor remaining within the pores.

In Chapter 6, polished Pt and H_1 mesoporous Pt with different pore sizes were used to assess the behaviour of an ionic liquid in a mesoporous electrode. The access of the ionic liquid in the mesoporous structure is investigated with cyclic voltammetry by measuring the double layer capacitances. A study in aqueous electrolyte in identical H_1 mesoporous Pt electrodes has shown Electrochemical Impedance Spectroscopy (EIS) as a method to quantify the accessibility and the electrochemical behaviour of these mesoporous Pt films[95]. The same method is used to determine the behaviour of the ionic liquid in a mesoporous film and thus to know if a mesoporous electrode with such small pores could be employed as supercapacitor.

1.8 References

[1] J. S. Beck, J. C. Vartuli, W. J. Roth, M. E. Leonowicz, C. T. Kresge, K. D. Schmitt, C. T. W. Chu, D. H. Olson, E. W. Sheppard, S. B. McCullen, J. B. Higgins, J. L. Schlenker *J. Am. Chem. Soc.* **1992**, 114, 10834-10843.

[2] G. S. Attard, C. G. Goltner, J. M. Corker, S. Henke, R. H. Templer *Angew. Chem.-Int. Edit. Engl.* **1997**, 36, 1315-1317.

[3] P. J. Collings, Liquid Crystals: Natures Delicate Phase of Matter, Princeton University Press, Princeton, **1990**.

[4] P. J. Collings, Introduction to Liquid Crystals, Taylor and Francis, London, **1997**.

[5] L. Pierson, **2011**. Amphiphiles [Online] (Updated: 17 October 2011) Available at: http://www.vcbio.science.ru.nl/en/fesem/applets/amphiphiles/. [Accessed *2 March 2012*]

[6] G. S. Attard, P. N. Bartlett, N. R. B. Coleman, J. M. Elliott, J. R. Owen *Langmuir*. **1998**, 14, 7340-7342.

[7] M. E. Raimondi, J. M. Seddon *Liq. Cryst.* **1999**, 26, 305-339.

[8] R. K. Iler *J. Colloid Interface Sci.***1973**, 43, 399-408.

[9] M. H. Healy, L. F. Wieserman, E. M. Arnett, K. Wefers *Langmuir*. **1989**, 5, 114-123.

[10] R. M. Dessau, J. L. Schlenker, J. B. Higgins *Zeolites*. **1990**, 10, 522-524.

[11] M. E. Davis, C. Saldarriaga, C. Montes, J. Garces, C. Crowder *Nature*. **1988**, 331, 698-699.

[12] M. Estermann, L. B. McCusker, C. Baerlocher, A. Merrouche, H. Kessler *Nature*. **1991**, 352, 320-323.

[13] C. T. Kresge, M. E. Leonowicz, W. J. Roth, J. C. Vartuli, J. S. Beck *Nature*. **1992**, 359, 710-712.

[14] A. Monnier, F. Schuth, Q. Huo, D. Kumar, D. Margolese, R. S. Maxwell, G. D. Stucky, M. Krishnamurty, P. Petroff, A. Firouzi, M. Janicke, B. F. Chmelka *Science*. **1993**, 261, 1299-1303.

[15] C. F. Cheng, Z. H. Luan, J. Klinowski *Langmuir*. **1995**, 11, 2815-2819.

[16] P. Behrens, G. D. Stucky *Angew. Chem.-Int. Edit. Engl.* **1993**, 32, 696-699.

[17] Q. S. Huo, D. I. Margolese, U. Ciesla, P. Y. Feng, T. E. Gier, P. Sieger, R. Leon, P. M. Petroff, F. Schuth, G. D. Stucky *Nature*. **1994**, 368, 317-321.

[18] G. S. Attard, J. C. Glyde, C. G. Goltner *Nature*. **1995**, 378, 366-368.

[19] G. S. Attard, M. Edgar, C. G. Goltner *Acta Mater*. **1998**, 46, 751-758.

[20] J. M. Elliott, P. R. Birkin, P. N. Bartlett, G. S. Attard *Langmuir*. **1999**, 15, 7411-7415.

[21] F. Bender, R. K. Mankelow, D. B. Hibbert, J. J. Gooding *Electroanalysis*. **2006**, 18, 1558-1563.

[22] P. N. Bartlett, P. N. Birkin, M. A. Ghanem, P. de Groot, M. Sawicki *J. Electrochem. Soc.* **2001**, 148, C119-C123.

[23] P. A. Nelson, J. M. Elliott, G. S. Attard, J. R. Owen *Chem. Mat.* **2002**, 14, 524-529.

[24] P. A. Nelson, J. M. Elliott, G. S. Attard, J. R. Owen *J. New Mat.Electrochem. Syst.* **2002**, 5, 63-65.

[25] P. N. Bartlett, B. Gollas, S. Guerin, J. Marwan *Phys. Chem. Chem. Phys.* **2002**, 4, 3835-3842.

[26] P. N. Bartlett, J. Marwan *Microporous Mesoporous Mat.* **2003**, 62, 73-79.

[27] I. Nandhakumar, J. M. Elliott, G. S. Attard *Chem. Mat.* **2001**, 13, 3840-+.
[28] A. H. Whitehead, J. M. Elliott, J. R. Owen, G. S. Attard *Chem. Commun.* **1999**, 331-332.
[29] T. Gabriel, I. S. Nandhakumar, G. S. Attard *Electrochem. Commun.* **2002**, 4, 610-612.
[30] G. S. Attard, S. A. A. Leclerc, S. Maniguet, A. E. Russell, I. Nandhakumar, P. N. Bartlett *Chem. Mat.* **2001**, 13, 1444-+.
[31] Y. Yamauchi, S. S. Nair, T. Momma, T. Ohsuna, T. Osaka, K. Kuroda *J. Mater. Chem.* **2006**, 16, 2229-2234.
[32] S. Guerin, G. S. Attard *Electrochem. Commun.* **2001**, 3, 544-548.
[33] Y. Yamauchi, T. Yokoshima, T. Momma, T. Osaka, K. Kuroda *J. Mater. Chem.* **2004**, 14, 2935-2940.
[34] J. Solla-Gullon, F. J. Vidal-Iglesias, E. Herrero, J. M. Feliu, A. Aldaz *Electrochem. Commun.* **2006**, 8, 189-194.
[35] J. M. Elliott, G. S. Attard, P. N. Bartlett, N. R. B. Coleman, D. A. S. Merckel, J. R. Owen *Chem. Mat.* **1999**, 11, 3602-3609.
[36] P. N. Bartlett, J. Marwan *Chem. Mat.* **2003**, 15, 2962-2968.
[37] R. Campbell, M. G. Bakker *J. Porous Mat.* **2004**, 11, 63-69.
[38] P. A. Nelson, J. R. Owen *J. Electrochem. Soc.* **2003**, 150, A1313-A1317.
[39] P. R. Birkin, J. M. Elliott, Y. E. Watson *Chem. Commun.* **2000**, 1693-1694.
[40] J. H. Han, H. Boo, S. Park, T. D. Chung *Electrochim. Acta*. **2006**, 52, 1788-1791.
[41] S. A. G. Evans, J. M. Elliott, L. M. Andrews, P. N. Bartlett, P. J. Doyle, G. Denuault *Anal. Chem.* **2002**, 74, 1322-1326.
[42] S. M. Lee, D. C. Dyer, J. W. Gardner *Microelectron. J.* **2003**, 34, 115-126.
[43] A. S. Aricò, S. Srinivasan, V. Antonucci *Fuel Cells*. **2001**, 1, 133-161.
[44] E. Herrero, A. Fernandezvega, J. M. Feliu, A. Aldaz *J. Electroanal. Chem.***1993**, 350, 73-88.
[45] D. Pletcher, A First Course in Electrode Processes, 2nd Edition, The Royal Society of Chemistry, Cambridge, **2009**.
[46] H. Siwek, W. Tokarz, P. Piela, A. Czerwinski *J. Power Sources*. **2008**, 181, 24-30.
[47] H. Kita, H. Naohara, T. Nakato, S. Taguchi, A. Aramata *J. Electroanal. Chem.* **1995**, 386, 197-206.
[48] A. Cuesta, A. Couto, A. Rincon, M. C. Perez, A. Lopez-Cudero, C. Gutierrez *J. Electroanal. Chem.* **2006**, 586, 184-195.
[49] P. Inkaew, W. Zhou, C. Korzeniewski *J. Electroanal. Chem.* **2008**, 614, 93-100.
[50] N. M. Markovic, B. N. Grgur, C. A. Lucas, P. N. Ross *Surf. Sci.* **1997**, 384, L805-L814.
[51] N. M. Markovic, P. N. Ross *Surf. Sci. Rep.* **2002**, 45, 121-229.
[52] N. P. Lebedeva, M. T. M. Koper, E. Herrero, J. M. Feliu, R. A. van Santen *J. Electroanal. Chem.* **2000**, 487, 37-44.
[53] K. A. Friedrich, K. P. Geyzers, U. Linke, U. Stimming, J. Stumper *J. Electroanal. Chem.* **1996**, 402, 123-128.
[54] B. N. Grgur, N. M. Markovic, P. N. Ross *J. Phys. Chem. B.* **1998**, 102, 2494-2501.
[55] B. N. Grgur, N. M. Markovic, P. N. Ross *J. Electrochem. Soc.* **1999**, 146, 1613-1619.
[56] H. A. Gasteiger, N. M. Markovic, P. N. Ross *J. Phys. Chem.* **1995**, 99, 8945-8949.

[57] S. Motoo, M. Watanabe *J. Electroanal. Chem.* **1976**, 69, 429-431.
[58] S. P. E. Smith, K. F. Ben-Dor, H. D. Abruna *Langmuir*. **2000**, 16, 787-794.
[59] M. D. Maciá, E. Herrero, J. M. Feliu *Electrochim. Acta*. **2002**, 47, 3653-3661.
[60] M. Shibata, N. Furuya, M. Watanabe, S. Motoo *J. Electroanal. Chem.* **1989**, 263, 97-108.
[61] M. Watanabe, Y. Furuuchi, S. Motoo *J. Electroanal. Chem.* **1985**, 191, 367-375.
[62] S. Motoo, M. Watanabe *J. Electroanal. Chem.* **1980**, 111, 261-268.
[63] M. Shibata, S. Motoo *J. Electroanal. Chem.* **1985**, 188, 111-120.
[64] M. Watanabe, S. Motoo *J. Electroanal. Chem.* **1975**, 60, 267-273.
[65] P. N. Ross *J. Electrochem. Soc.* **1979**, 126, 78-82.
[66] P. N. Ross *J. Electrochem. Soc.* **1979**, 126, 67-77.
[67] S. Motoo, N. Furuya *J. Electroanal. Chem.* **1984**, 172, 339-358.
[68] N. M. Markovic, N. S. Marinkovic, R. R. Adzic *J. Electroanal. Chem.* **1988**, 241, 309-328.
[69] N. Markovic, M. Hanson, G. McDougall, E. Yeager *J. Electroanal. Chem.* **1986**, 214, 555-566.
[70] A. Fernandezvega, J. M. Feliu, A. Aldaz, J. Clavilier *J. Electroanal. Chem.* **1989**, 258, 101-113.
[71] J. Clavilier, K. Elachi, M. Petit, A. Rodes, M. A. Zamakhchari *J. Electroanal. Chem.* **1990**, 295, 333-356.
[72] J. Clavilier *J. Electroanal. Chem.* **1980**, 107, 211-216.
[73] J. C. Canullo, W. E. Triaca, A. J. Arvia *J. Electroanal. Chem.* **1986**, 200, 397-400.
[74] A. Rodes, K. Elachi, M. A. Zamakhchari, J. Clavilier *J. Electroanal. Chem.* **1990**, 284, 245-253.
[75] D. Armand, J. Clavilier *J. Electroanal. Chem.* **1987**, 233, 251-265.
[76] D. Armand, J. Clavilier *J. Electroanal. Chem.* **1987**, 225, 205-214.
[77] J. Solla-Gullon, P. Rodriguez, E. Herrero, A. Aldaz, J. M. Feliu *Phys. Chem. Chem. Phys.***2008**, 10, 1359-1373.
[78] P. L. Sanchez, J. M. Elliott *Analyst*. **2005**, 130, 715-720.
[79] K. Stulik, C. Amatore, K. Holub, V. Marecek, W. Kutner *Pure Appl. Chem.***2000**, 72, 1483-1492.
[80] A. G. Ewing, M. A. Dayton, R. M. Wightman *Anal. Chem.* **1981**, 53, 1842-1847.
[81] M. A. Dayton, J. C. Brown, K. J. Stutts, R. M. Wightman *Anal. Chem.* **1980**, 52, 946-950.
[82] A. M. Bond, M. Fleischmann, J. Robinson *J. Electroanal. Chem.* **1984**, 168, 299-312.
[83] A. M. Bond, P. A. Lay *J. Electroanal. Chem.* **1986**, 199, 285-295.
[84] J. Cassidy, S. B. Khoo, S. Pons, M. Fleischmann *J. Phys. Chem.* **1985**, 89, 3933-3935.
[85] Y. Saito *Rev. Polarog. (Japan)*. **1968**, 15, 177-187.
[86] S. V. Dzyuba, R. A. Bartsch *Chem. Commun.* **2001**, 1466-1467.
[87] X. L. Peng, C. H. Xiang, Q. J. Xie, Q. Kang, S. Z. Yao *J. Electroanal. Chem.* **2006**, 591, 74-84.
[88] M. C. Buzzeo, O. V. Klymenko, J. D. Wadhawan, C. Hardacre, K. R. Seddon, R. G. Compton *J. Phys. Chem. A*. **2003**, 107, 8872-8878.
[89] A. B. McEwen, H. L. Ngo, K. LeCompte, J. L. Goldman *J. Electrochem. Soc.* **1999**, 146, 1687-1695.

[90] S. Randstrom, M. Montanino, G. B. Appetecchi, C. Lagergren, A. Moreno, S. Passerini *Electrochim. Acta*. **2008**, 53, 6397-6401.
[91] H. Sakaebe, H. Matsumoto *Electrochem. Commun.* **2003**, 5, 594-598.
[92] F. B. Sillars, S. I. Fletcher, M. Mirzaeian, P. J. Hall *Energy Environ. Sci.* **2011**, 4, 695-706.
[93] V. Lockett, M. Horne, R. Sedev, T. Rodopoulos, J. Ralston *Phys. Chem. Chem. Phys.* **2010**, 12, 12499-12512.
[94] A. A. Kornyshev *J. Phys. Chem. B.* **2007**, 111, 5545-5557.
[95] J. M. Elliott, J. R. Owen *Phys. Chem. Chem. Phys.* **2000**, 2, 5653-5659.

Chapter 2: Experimental Methods

2.1 Solutions and reagents

2.1.1 Chemicals

All solutions were prepared with deionised water from a Whatman Still and RO 50 water purification system. Hexachloroplatinic acid hydrate (HCPA, 99.9% purity). $RhCl_3$ (99.9% purity), $Ru(NH_3)_6Cl_3$ (99.9% purity) and n-heptane (99% purity) were purchased from Aldrich. The surfactants, octaethylene glycol monododecyl ether ($C_{12}EO_8$) (98% purity) and octaethylene glycol monohexadecyl ether ($C_{16}EO_8$) (98% purity) were purchased from Fluka. Quick-set epoxy resin and silver paint were purchased from RS. Alumina powders were purchased from Buehler. Buffer solutions were prepared from 0.2 M $NaH_2PO_4.H_2O$ and 0.2 M $Na_2HPO_4.12H_2O$ (99% purity, BDH). Hydrogen peroxide (30%, unstabilised, upgrade reagent) was purchased from Fisher Scientific. 1 M sulphuric acid solutions were diluted from concentrated sp. gr. 1.84 acid (95% purity) purchased from Aristar. The argon, nitrogen and carbon monoxide gases used were of high-purity grade (Boc gases, 99.9 % purity). All compounds were used as received.

2.1.2 Ionic liquid

The1-n-butyl-3-methylimidazolium hexaflurophosphate (BMIM-PF_6) ionic liquid (IoLiTec, 99% purity) was dried under vacuum at 120 ºC for two days to remove any water from the sample, before being transferred to the glove box.

2.2 Electrodes

2.2.1 Working electrodes

2.2.1.1 Pt disc electrodes

Working electrodes were made of platinum wires (with the appropriate diameter) sealed into a glass tube. The tip of the electrode was polished until the exposure of the Pt disc. The electrical contact was made to a standard copper wire with indium.

2.2.1.2 Pt rotating disc electrode

Concerning the platinum rotating disc electrode (RDE), the electrode consists of a 5 mm diameter Pt disc surrounded by a PTFE insulating sheath purchased from Pine.

2.2.1.3 Gold slides

Gold slides were used for XRD and TEM characterisation. The slides used were composed of a layer of glass, a 18 nm thick layer of chromium and a 250 nm thick layer of gold. The gold coated slide was cut to an adequate size to fit into a glass three electrode electrochemical cell, the working area was defined by covering the surface with nail polish acting as a mask (generally the area of gold used for the electrodeposition was 0.5 cm^2). The electrical contact was realised with a crocodile clip welded on to a standard copper wire. The crocodile clip was coated with silver paint to ensure the electrical contact and was protected by enrobing with a quick-set epoxy resin.

2.2.2 Preparation of the platinum disc electrodes

The electrodes were polished using silica carbide paper (CC 1200, English abrasive) and then with alumina slurries of 1 µm and 0.3 µm particle size on a Buehler microcloth to obtain a mirror appearance. Platinum discs were then characterised by cyclic voltammetry in 1 M sulphuric acid. Around 30-40 scans were necessary to remove impurities at the surface of the electrode and obtain a stable cyclic voltammogram in sulphuric acid between - 0.65 and 0.85 V vs. SMSE.

2.2.3 Reference electrodes

Most of the electrochemical experiments were carried out in a thermostated glass cell using a three electrode system. Platinum gauze was used as a counter electrode. Both home-built saturated mercury/mercurous sulphate (SMSE) and saturated calomel (SCE) electrodes were used as reference electrodes. The details of the experiments are given through all the chapters.

2.3 Mesoporous metal deposition

The constituents were heated in a sealed vial to 40° C for 30 min, then stirred in order to produce a homogeneous mixture texture. The vial was again sealed (to prevent

evaporation of water and/or heptane) and placed in the oven at 40 °C for a further 30 min.

The template mixtures contained: 42 wt% $C_{12}EO_8$, 29 wt% H_2PtCl_6 and 29 wt% deionised water. The second ternary mixture contained 42 wt% $C_{16}EO_8$, 29 wt% H_2PtCl_6 and 29 wt% deionised water. The quaternary mixture contained 38.8 wt% $C_{16}EO_8$, 29 wt% H_2PtCl_6, 29 wt% deionised water and 3.2 wt% heptane. The plating mixture for rhodium contained $RhCl_3$ (12% w/w), n-heptane (2% w/w), water (39% w/w) and $C_{12}EO_8$ (47% w/w).

The formation of the H_1hexagonal lyotropic liquid crystalline phase was confirmed by using an Olympus BH-2 polarized light microscope equipped with a Linkam TMS90 heating/cooling stage and a control unit. The experiment consisted of the preparation of a thin film of mixture between a glass slide and a coverslip. The phase was attributed to the features according to the optical texture.

Once the plating mixture was prepared, it was then spread out onto a platinum gauze and the working electrode was inserted into the plating mixture as well as the reference electrode. It is noteworthy that a tiny amount of plating mixture was also spread onto the tip of the working and reference electrodes before insertion to ensure a good coating of the mixture onto the electrode surface.

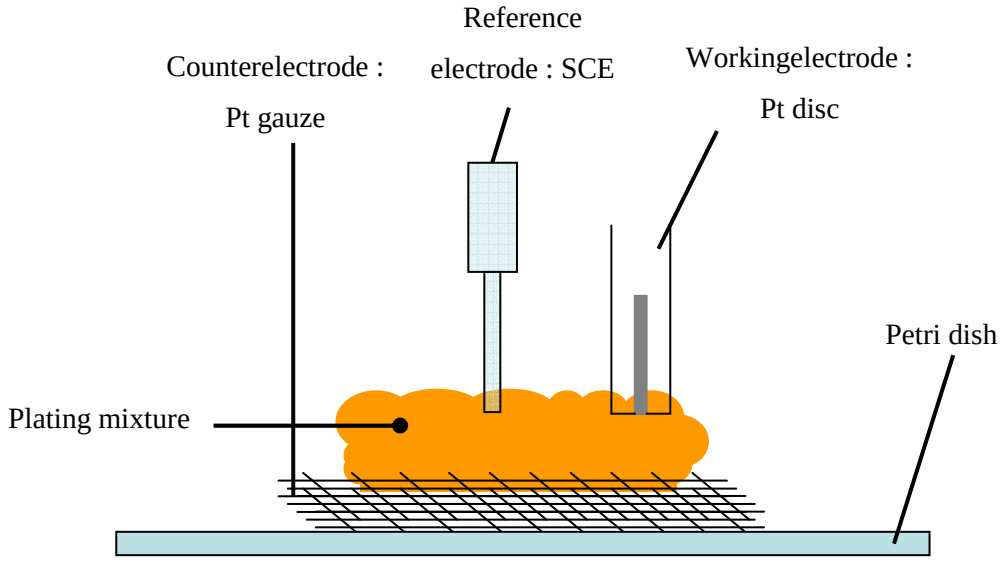

Figure 2-1. Schematic representation for the electrodeposition of mesoporous metal film onto a Pt disc

The electrodepositions of the metal were carried out by holding the potential (- 0.2 V for rhodium and - 0.1 V vs. SCE for platinum) until the charge required was passed. The resulting films were first cleaned by isopropanol and then soaked in water for several hours to remove the surfactant.

Cyclic voltammetry in 1 M sulphuric was performed before and after deposition to ascertain the increase of the surface area after deposition.

2.4 Carbon monoxide

The electrode was held at a fixed potential (in the range of - 0.65 and - 0.15 V vs. SMSE) in a 1 M sulphuric acid solution while carbon monoxide gas was bubbled for 30 min (enough time to cover the surface with a CO monolayer). Then nitrogen gas was flowed through the solution in order to remove any traces of CO for 15 min maintaining the electrode potential at the same value. Two voltammograms were recorded; the first one referred to the CO stripping and the second voltammogram was to verify the complete removal of CO from the surface.

2.5 Adsorption of foreign atoms

2.5.1 Adsorption of Bi atoms

Bismuth oxide was calcined for 45 min at 500 °C before use. Bi adsorption on platinum electrodes can be performed by different methods. In this work, two of them were carried out. The first method consisted in cycling at 200 mV s^{-1} between – 0.65 and 0.85 V vs. SMSE the electrode in 1 M H_2SO_4 + 1 mM Bi_2O_3 until a stable cycling voltammogram was obtained. The second method, used for carbon monoxide experiments, consisted in immersing the electrode in 0.6 M $HClO_4$ + 0.01 M Bi_2O_3 for a period of time. In this case, perchloric acid solution was used to match the method employed by Clavilier *et al.* to cover the platinum surface with bismuth atoms.[1] The period of time was about 10 min, it was noticed that leaving the electrode immersed for longer times did increase adsorption. After immersion, the electrode was rinsed with deionised water and plunged into a solution of 1 M H_2SO_4 where the carbon monoxide experiment was performed.

2.5.2 Adsorption of Ge atoms

Ge adsorption on platinum electrodes was performed by putting a droplet of 1 M NaOH + 0.5 M GeO_2 on the tip of the electrode and immersing the electrode in 1 M H_2SO_4 while the potential was maintained at - 0.65 V vs. SMSE. This method was adapted from Gomez *et al.* to adsorb Ge atoms on Pt single-crystals[2].

2.6 Hydrogen peroxide

2.6.1 Preparation of hydrogen peroxide solution

The solution was standardised by iodometric titration according to the method of Vogel[3]. The solutions were made by dilution of hydrogen peroxide in a home made 0.1 M sodium phosphate buffer (pH = 7) or in water.

2.6.2 Calibration curve

The experiment was carried out in a water jacketed cell with a platinum gauze counter electrode. The potential at the working electrode (5, 10, 25 and 50 μm in diameter for microelectrodes and 0.5 cm for the RDE) was held at 0 V vs. SMSE (potential for hydrogen peroxide oxidation) in 0.1 M sodium phosphate buffer (pH = 7) thermostated at 25 °C. The background current was recorded 20 min before adding 20 aliquots of H_2O_2. The solution was stirred during addition using a magnetic stirrer. After addition of H_2O_2 and stirring for 1 min, the stirring was stopped and measurement was made for 2-3 min (when the current became stable) before the next addition of H_2O_2.

2.6.3 RDE study

The experiment was carried out in a water jacketed cell with a platinum gauze counter electrode. The electrode potential was held at -0.85 V vs. SMSE in ruthenium hexamine solution at various rotation rates. Experiments were performed in order 240, 960, 2160, 1500, 540 and 60 RPM. For hydrogen peroxide oxidation, the experiment consists in holding the potential at 0 V vs. SMSE and measuring the current at different concentrations of hydrogen peroxide and for various rotation rates performed in the same order as before.

2.7 Electron microscopy

2.7.1 SEM

The diameters of the electrodes were checked with a XL30 ESEM from Philips. The thickness of the mesoporous metal films was checked by tilting the translating stage by 70 ° to have a lateral view of the film.

2.7.2 TEM

The pores of the films were investigated using a JOEL 3010 TEM. The preparation of the sample consisted of scraping the surface of the electrodeposited mesoporous film on the gold coated slide with a scalpel to collect some particles onto a carbon TEM grid 300 mesh (Agar).

2.8 X-ray diffraction (XRD)

XRD was performed using a Bruker D5000 using a Cu-Kα radiation with a wavelength of 1.54 Å. The preparation of the sample consisted in cutting the electrodeposited mesoporous film on the gold coated slide in half. The scan was from 0.5 to 6° at a scanspeed of 12° min^{-1}.

2.9 Instrumentation and software

The cyclic voltammetry and electrochemical depositions in Chapters 3, 5 and 6 were done using an EG&G model 263A potentiostat/galvanostat. The experiments for carbon monoxide electrooxidation in the Chapter 3 were performed on an Autolab PGSTAT30.

Cyclic voltammetry and the experiments for carbon monoxide electrooxidation in Chapter 4 were carried out on an Uniscan Instruments PG580.

Electrochemical impedance spectroscopy was carried out on a VMP Bio-Logic instrument.

The data from the EG&G model 263A potentiostat/galvanostat, from the Autolab PGSTAT30 and PG580 were recorded using the PowerSuite, GPES and UiEchem softwares repectively.

The graphs, fits and simulations were done using Sigmaplot version 11. In the Chapter 4, Origin 8.1 was also used to determine the curved baselines.

The fits for the Bode plots were simulated using ZView 2.

The pore model was drawn using CrystalMaker version 3.2 and the mesoporous film was drawn using POV-Ray for Windows v3.62.

2.10 Electrochemical Impedance spectroscopy

The system consisted of three electrodes: the counter electrode was a Pt gauze, the reference electrode was a SCE and the working electrode was either the polished platinum electrode or the mesoporous platinum film. The investigated frequency range was from 200 kHz to 1 mHz.

2.11 References

[1] J. Clavilier, J. M. Feliu, A. Aldaz *J. Electroanal. Chem.* **1988**, 243, 419-433.
[2] R. Gomez, M. J. Llorca, J. M. Feliu, A. Aldaz *J. Electroanal. Chem.* **1992**, 340, 349-355.
[3] A. I. Vogel, J. Bassett, Vogel's textbook of Quantitative inorganic analysis : including elementary instrumental analysis, English Language Book Society, [Great Britain], **1986**.

Chapter 3: Carbon monoxide oxidation

The work presented in this chapter has been published[1] and was presented at the ISE meeting in Nice 2010.

3.1. Overview

H_1 mesoporous platinum was synthesised by electrodeposition from the hexagonal lyotropic liquid crystalline phase, as shown in Figure 3-1, exhibiting high specific surface area (up to 60 m^2 g^{-1})[2]. The hexagonal mesoporous structure consists of a hexagonal array of cylindrical pores. Previous work demonstrated that surfactants with shorter or longer alkyl chains could control the size of the pore diameter[3]. For example, the use of $C_{12}EO_8$ in the mixture gives a pore size of ~ 1.7 nm whereas the use of $C_{16}EO_8$ entails the pore size of ~ 2.5 nm from transmission electron microscopy observations[3]. Thanks to their highly porous surface distribution, the mesoporous materials have as high surface areas as other types of materials such as nanoparticles. Whereas the surface of nanoparticles more commonly encountered in the literature is convex, the surface of H_1 mesoporous materials is concave (Figure 3-1). The surface structure is a key point for reactions which are structure sensitive.

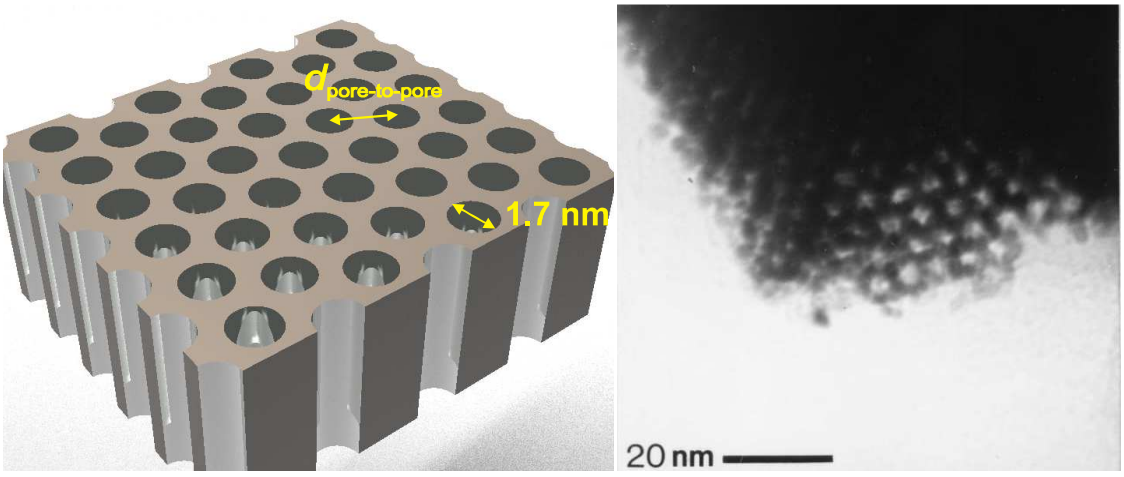

Figure 3-1. (left) Drawing of an H_1 mesoporous platinum film. (right) TEM picture showing the nanostructure of an H_1 mesoporous Pt electrodeposited onto a gold substrate[3].

The high surface area of these nanostructured materials make them of great interest for fuel cells. Nanostructured materials are known to affect the oxidation of small organic molecules such as CO-species[4]. The atomic arrangement of the platinum surface results in differences in the electronic structure[5, 6] which affect the electrocatalytic reaction[7]. The literature refers mainly to convex surfaces such as stepped surfaces[8], polished surfaces[9] or nanoparticles[10]. The peculiar characteristic of the H_1 mesoporous architecture is the concave surface formed by the cylindrical pores.

Based on studies by cyclic voltammetry in acid, the hydrogen desorption/adsorption peaks reflect the crystallinity of each specific surface of platinum and can identify defects such as stepped surfaces and kinks[11-14]. This approach has been extended to Pt nanoparticles[11, 15, 16] and carbon supported Pt nanoparticle electrodes[16].

Fuel molecules adsorb onto catalytic surfaces leading to the formation of intermediate species. Platinum is a common metal used as an electrocatalyst for fuel cells because it has an intermediate bond strength for the hydrogen charge transfer reaction. Carbon monoxide is an intermediate species in the electrochemical oxidation of many organic molecules[7, 17]. Carbon monoxide is also known to adsorb at the platinum surface and acts as a poison. The reaction of CO oxidation has been investigated due to its technological importance in the area of fuel cells and is considered to be the most understood catalytic reaction[18]. The structure-sensitivity of CO oxidation on platinum has been established in the literature[19]. Therefore CO oxidation is used as a model system to probe the reaction on the concave surface within the H_1 mesoporous structure.

Carbon monoxide oxidation was studied extensively on different types of platinum surfaces. The use of single-crystals provided information to explain the effects of the surface atom structure on electrocatalytic mechanisms. The voltammetric profile for stripping an electrosorbed CO adlayer depends on the characteristics of the platinum surface, e.g. single-crystals Pt(111)[20-24] and Pt(100)[25, 26] and also stepped surfaces[8, 19, 27-31]. These studies show the relationship between the CO adlayer and the Pt surface structure[8, 19, 27-31]. These surfaces are important for the study of structure-sensitive reactions where much of our understanding comes from. The studies on single-crystals can serve as catalyst models for a better comprehension for CO oxidation on the platinum nanoparticle surfaces[10, 32-36]. Indeed, the design of the platinum nanoparticle

presents edges and corners which can be highly active. CO oxidation is closely dependent on the platinum atomic surface. Some works were done by infrared spectroscopy to probe the surface bonding and the electrochemical environment of CO on platinum since the vibrational frequency for CO is dependent on the morphology of the surface[37-39]. Clavilier *et al.* attempted to elucidate voltammetric features from the structure of the platinum surface[40].

The present work comes closer to Jiang and Kucernak's study which focused on the electrocatalytic properties of the mesoporous platinum to the electrooxidation of carbon monoxide[41]. They mentioned that their CO stripping voltammogram was similar to the CO stripping voltammogram of platinum polycrystalline electrodes. However, the CO stripping potentials vary depending on the structure of the platinum electrode surface. However, they did not deepen their study to look in detail at the voltammetry. In this chapter, the study concentrated on the differences between a polished platinum electrode and an H_1 mesoporous Pt electrode and on the effect of two factors, namely, the scan rate and the adsorption potential. According to the literature on CO oxidation on stepped Pt surfaces, the results are consistent with the presence of a trough at the step in the concave structure of the platinum surface within the pores of the H_1 mesoporous architecture[31].

3.2. Preparation and characterisation of the electrodes

3.2.1. Electrodeposition of the mesoporous platinum film

The platinum disc was made by sealing a 500 µm diameter wire into glass and was polished with slurry of 0.3 µm alumina to have a fine mirror finish on a Buehler microcloth. The electrode was then cleaned by cycling in sulphuric acid.

The polished platinum disc electrodes were ready to be modified by the electrodeposition of a mesoporous platinum film. A plating mixture was prepared from an aqueous solution containing a platinum salt and a non-ionic surfactant. The proportions were chosen so that the amphiphilic molecules aggregate into rods which are arranged in a hexagonal lattice. Thus the electrodeposition of the metal is driven through the hexagonal phase template. Changing the proportions of the different components entails changing the lyotropic liquid crystalline phases since the phases

depend on the concentration of the components and the temperature of the mixture[42]. The exact phase was identified by polarised optical microscopy using a cooling/heating stage.

The potential was held at - 0.1 V vs. SMSE until the charge of 6.27 mC had passed. Then the electrode was soaked in iso-propanol and then in water overnight to remove the plating mixture from the electrode surface. The resulting metal film is then the inverse of the hexagonal template.

Cyclic voltammetry was then performed to remove the plating mixture within the pores until a stable cyclic voltammogram was obtained on cycling between - 0.65 and 0.85 V vs. SMSE at 200 mV s^{-1} in 1 M sulphuric acid.

3.2.2. Characterisation of the mesoporous platinum film by cyclic voltammetry in acid

Figure 3-2 shows cyclic voltammograms for a $C_{12}EO_8$ mesoporous platinum film and a polished platinum electrode with the same geometric surface area in 1 M sulphuric acid. The current for the polished platinum electrode has been multiplied by 35 to match the current for the mesoporous electrode at the double layer region around - 0.2 V.

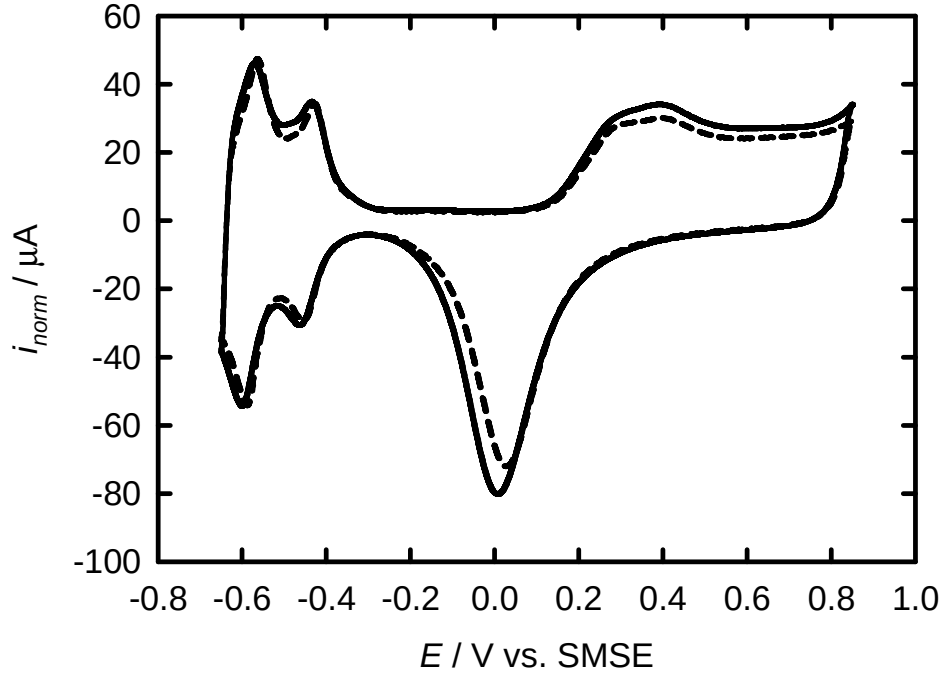

Figure 3-2. Cyclic voltammograms of a $C_{12}EO_8$ mesoporous platinum film electrodeposited onto a platinum disc electrode (solid line) and a polished polycrystalline platinum disc electrode (dashed line×35) (both 500 µm diameter) in 1 M sulphuric acid recorded at 200 mV s^{-1}. The solution was deaereated by purging with argon for at least 20 min prior to the measurements. The currents for the polished polycrystalline platinum electrode have been multiplied by 35 to match the currents in the double layer region and aid comparison.

Both cyclic voltammograms show the same characteristics of a polycrystalline platinum electrode in 1 M sulphuric acid electrolyte solution. The surface oxide formation commences at 0.1 V and develops two peaks at 0.27 and 0.4 V followed by a broad region until we reach oxygen evolution positive of 0.8 V. Positive of - 0.3 V, water oxidation occurs to form a monolayer of OH species adsorbed on the platinum surface as described in equation (1)[43]

$$Pt + H_2O \longleftrightarrow Pt - OH_{ads} + H^+ + e^- \qquad (1)$$

Other arrangements of the Pt/OH structure are probably formed such as Pt_4OH or Pt_2OH in the potential range 0.1 – 0.4 V[43]. However none of the peaks were assigned to the different Pt/OH arrangements[43]. By increasing the potential towards more positive potentials over the broad region, the further oxidation process occurs

$$Pt - OH_{ads} \longleftrightarrow PtO + H^{+} + e^{-} \quad (2)$$

Once the oxygenated species are adsorbed on the platinum surface, a mechanism of place exchange occurs at the interface where oxygenated species interchange with platinum atoms. From the literature, this exchange mechanism seems to occur over a wide range of potentials; in consequence it is believed that both OH and O species rearrange within the platinum lattice[44-47].

Nevertheless only a single stripping peak is observed on the voltammogram. The peak involves the reduction of the different oxide species formed. It is important to notice that the oxide stripping peak is not symmetric to the oxidation peaks. As soon as the potential shifts backwards from the oxide region, the exchange mechanism proceeds to the reverse process. A more negative potential must be then supplied to strip the oxides off the surface hence the appearance of the oxide stripping peak at more negative potentials[45].

The oxide stripping peak for the mesoporous platinum film is at more cathodic potential than that of the polished platinum electrode. The variation of the peak potential might stem from local pH change at the platinum surface within the pores of the mesoporous structure.

Over the potential range of - 0.3 and - 0.65 V, two peaks are clearly observed on the anodic sweep though a third peak is present, overlapping between the two. The peaks refer to the hydrogen desorption peaks from the low index Pt facets[11, 13, 14]. These peaks are mirrored on the cathodic sweep by the hydrogen adsorption. From the peaks in the hydrogen region, both polished and the mesoporous platinum electrodes are polycrystalline made up of low index Pt facets[13, 14, 47]. The active surface areas were calculated from the hydrogen desorption region. The surface areas of the polished platinum electrode and the mesoporous platinum film were 0.0049 cm^2 and 0.181 cm^2 respectively using the conversion factor 210 $\mu C\ cm^{-2}$[48]. The roughness factor for the polished electrode is 2.5 and that of the mesoporous platinum electrode is 92.

3.3. CO electrooxidation on platinum electrodes

3.3.1. CO stripping voltammetry on a polished platinum electrode

Figure 3-3 shows a CO stripping voltammogram for a polished polycrystalline platinum disc electrode in 1 M H_2SO_4. In this experiment, CO was adsorbed at - 0.65 V vs. SMSE for 30 minutes and the solution was purged with N_2 for 15 minutes in order to remove all traces of dissolved CO before stripping. A second cyclic voltammogram was performed right after CO stripping to confirm the complete removal of CO.

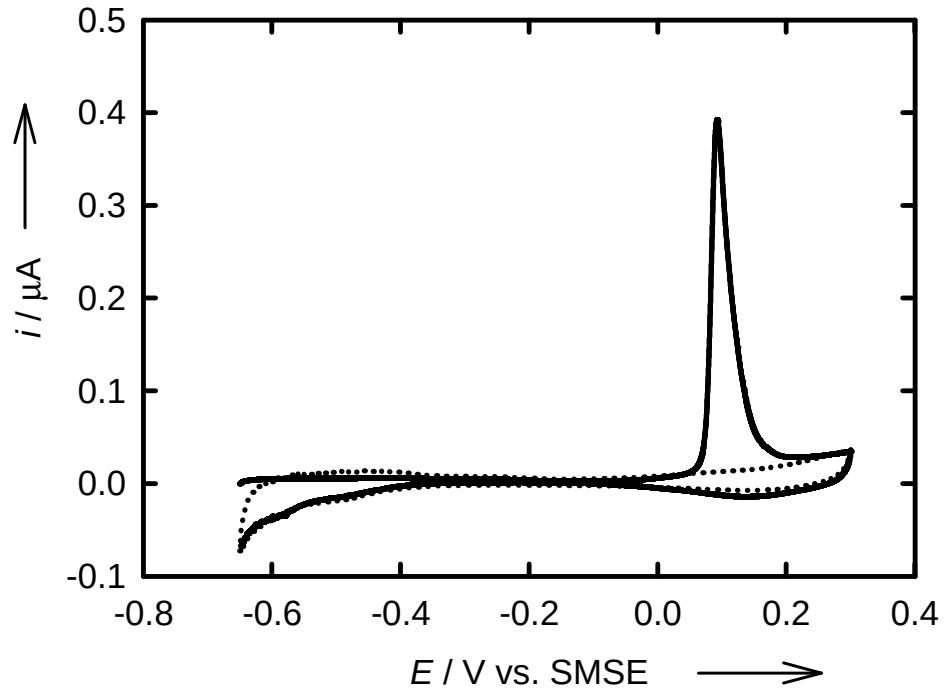

Figure 3-3. CO stripping voltammogram (solid line) for a polished polycrystalline Pt electrode (500 µm diameter) recorded 1 M sulphuric acid, scan rate 10 mV s^{-1}. CO was adsorbed at -0.65 V with CO bubbling for 30 min and then the solution was sparged with N_2 for 15 min before recording the stripping. Second cycle (dotted line).

The CO stripping voltammogram shows one sharp peak at 0.09 V vs. SMSE with an onset at - 0.04 V vs. SMSE and no pre-wave; no hydrogen desorption peaks were observed on the CO stripping voltammogram. It is similar to that reported in the literature for a polished polycrystalline platinum RDE[9]. The recovery of the hydrogen adsorption and desorption peaks and the absence of the CO oxidation peak on the second cyclic voltammogram confirms that all the CO was oxidised during the first sweep (a comment on the recovery of the hydrogen peaks is in Section 3.3.2.).

3.3.2. CO stripping voltammetry on a mesoporous platinum electrode

Figure 3-4 shows the corresponding CO stripping voltammogram for the $C_{12}EO_8$ mesoporous platinum electrode in 1 M H_2SO_4 realised under the same conditions.

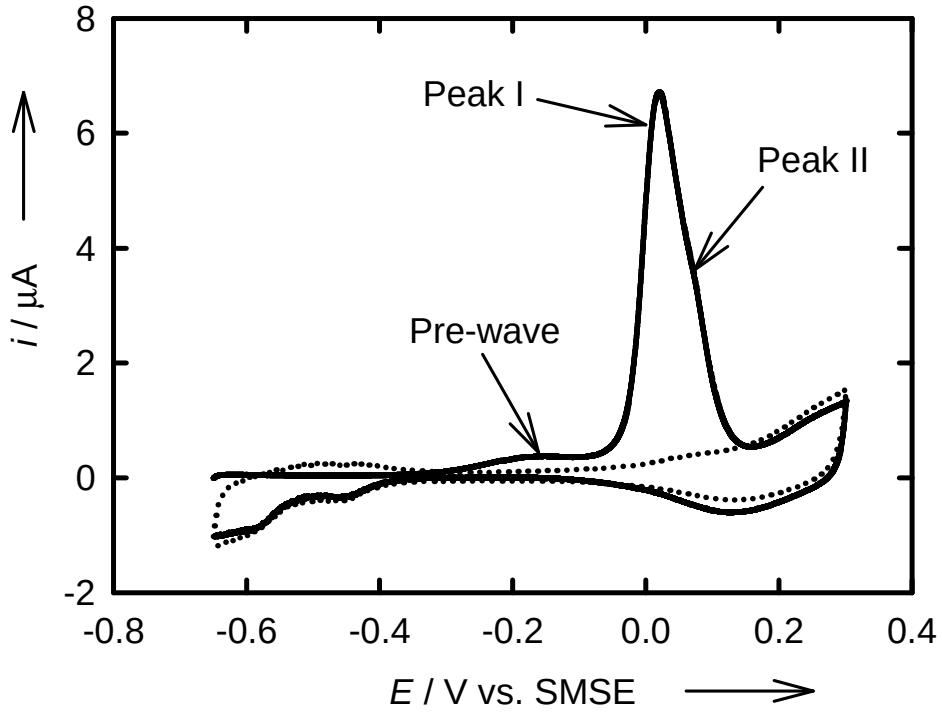

Figure 3-4. CO stripping voltammogram (solid line) for a $C_{12}EO_8$ mesoporous Pt electrode (500 µm diameter, 6.27 mC for the deposition charge) obtained using the same conditions as in Figure 3-3. Second cycle (dotted line).

The CO stripping voltammogram exhibits the pre-wave (as denoted on the Figure 3-4) followed by the main peak (peak I) and a shoulder which will be attributed to a second peak (peak II). Peak I is about 70 mV more negative and appeared broader than the corresponding peak for the polished platinum electrode. Besides, the onset potential for CO oxidation commences at about - 0.34 V vs. SMSE which is much lower than for the polished platinum electrode (- 0.04 V vs. SMSE) but is similar to the values reported for different types of platinum electrodes[10, 25, 49]. The desorption peaks cannot be very well distinguished on the graph, though they are present, because of a low scan rate. A low scan rate was used for this experiment to give rise to the prewave; if the scan rate is too fast, the prewave tends to fuse with the main CO stripping peak.

3.3.3. Contribution of the CO peaks

The relationship of the three peaks observed on the CO stripping voltammogram for the mesoporous platinum film was investigated by recording three successive cyclic voltammograms by increasing the upper potential limit (Figure 3-5). The potential was held at - 0.65 V vs. SMSE for 30 minutes while a monolayer of CO was formed and then the solution was purged with nitrogen for 15 minutes to remove any traces of CO. The first voltammogram was recorded between - 0.65 V and - 0.05 V (potential at the onset of the peak I). The second voltammogram was obtained from - 0.65 to 0.04 V (a potential chosen arbitrarily between peaks I and II). The third voltammogram was recorded from - 0.65 to 0.3 V where only peak II is present. A fourth voltammogram was recorded to prove the complete removal of the CO monolayer. The voltammograms demonstrate the independence of each peak. Once the species is oxidised, the peak produced in the forward cycle does not appear on the following cycle. This phenomenon was also observed by Markovic *et al.* who found that the pre-wave was not recovered until the potential goes down below 0.05 V vs. RHE (equivalent to - 0.6 V vs. SMSE) in the CO saturated solution[25]. Hence the remaining CO on the platinum surface does not move to the Pt sites that are oxidised at lower potentials on the time scale of the measurements. According to Markovic *et al.*, the origin of this effect was ascribed to a relaxation of the compact/saturated CO monolayer after suppression of the pre-wave CO[25] whereas the presence of the pre-wave was attributed to non-CO species on the platinum surface by other authors[10, 24, 26, 31, 50, 51]. The origin of the pre-wave is a subject of debate and will be discussed later in Section 3.7. The interpretation of the results for the second and third cyclic voltammograms also demonstrates that CO is not highly mobile on the mesoporous platinum electrode surface. When the second cyclic voltammogram is recorded, the pre wave feature does not appear and when the third cycle is recorded, the peak appearing on the second cycle is absent. If CO were mobile on the platinum surface, the remaining CO would adsorbed on the free sites more easily oxidable.

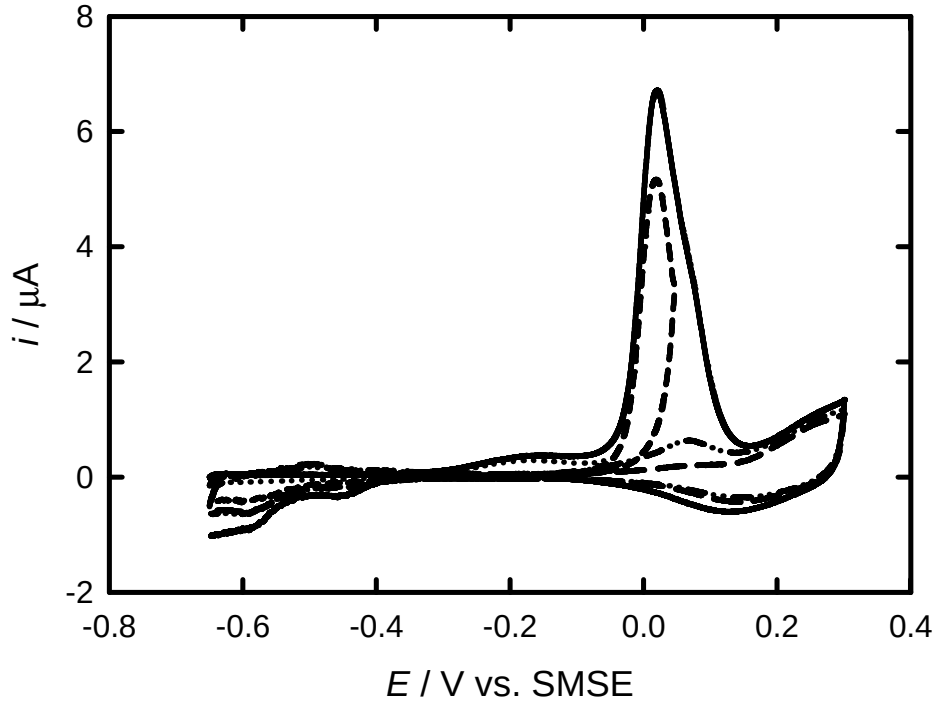

Figure 3-5. Three successive CO stripping voltammograms for a mesoporous platinum electrode recorded in 1 M H_2SO_4 with different potential windows (- 0.65 to – 0.05 V (dotted line); - 0.65 to 0.04 (dashed line); - 0.65 to 0.3 V (dot-dot-dashed line)). The potential was held at - 0.65 V vs. SMSE while the solution was bubbled with CO for 30 minutes and then purged with nitrogen for 15 minutes. The solid line is a reproduction of the CO stripping voltammogram from the Figure 3-3. The scan rate was 10 mV s^{-1}.

3.4. Effect of the scan rate

3.4.1. Polished platinum electrode

Figure 3-6 shows CO stripping voltammograms at different scan rates for a polished polycrystalline platinum disc electrode in 1 M H_2SO_4. CO was adsorbed at - 0.65 V vs. SMSE for 30 minutes and the solution was purged with N_2 for 15 minutes in order to remove any traces of CO in the solution.

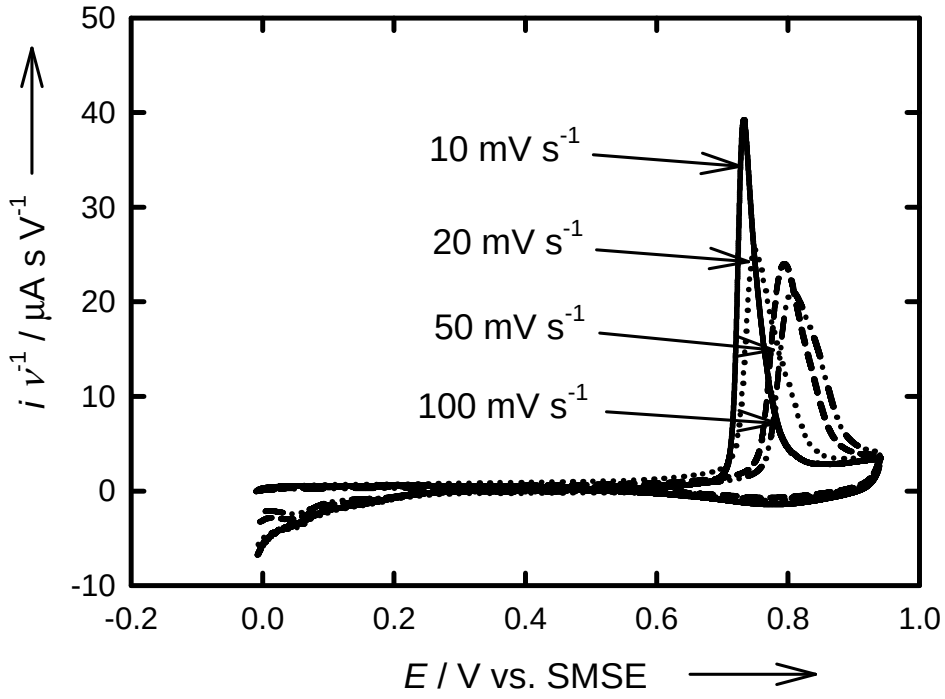

Figure 3-6. CO stripping voltammograms recorded at different scan rates for a polished polycrystalline Pt electrode (500 µm diameter) in 1 M sulphuric acid. CO was adsorbed at - 0.65 V with CO bubbling for 30 min and then the solution was sparged with N_2 for 15 min before recording the stripping. The currents have been normalised by the scan rate for ease of comparison.

The CO stripping peak shifts towards more positive potentials with the increase of the scan rate. The scan rate normalised peak current decreases with increasing scan rate; however, the total charge for CO stripping peak remains constant.

3.4.2. Mesoporous platinum electrode

Figure 3-7 corresponds to the CO stripping voltammograms at different scan rates of a mesoporous platinum electrode in 1 M H_2SO_4 where the conditions of the CO adsorption were identical to the previous experiment.

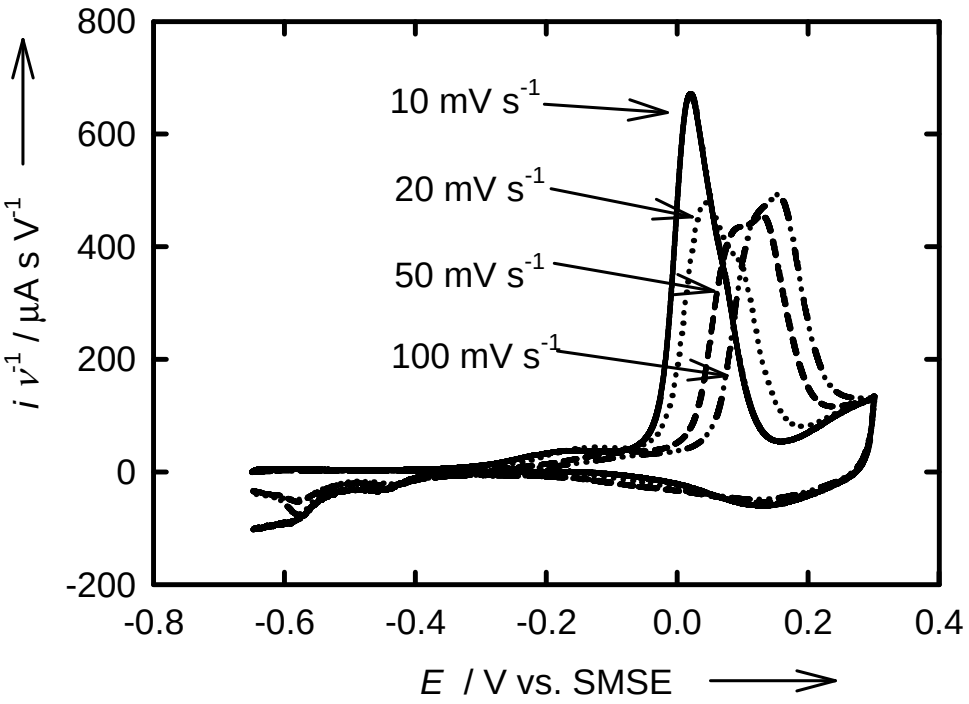

Figure 3-7. CO stripping voltammograms recorded at different scan rates for a mesoporous Pt electrode (500 µm diameter, 6.27 mC for the deposition charge) in 1 M sulphuric acid. CO was adsorbed at -0.65 V with CO bubbling for 30 min and then the solution was sparged with N_2 for 15 min before recording the stripping. The currents have been normalised with the scan rate for ease of comparison.

The onset potential of the peak and all the peaks shift towards more positive potentials with the scan rate. This is in agreement with results of single-crystal studies; however, the shift in the positions of the peaks for the mesoporous Pt electrode is larger. The total charge for CO stripping remains constant independent of the scan rate although the scan rate normalised peak current for peak II becomes larger at higher scan rates. In addition, the pre-wave becomes unclear and fuses in with peak I at high scan rates, consequently it becomes difficult to assign a peak potential to the pre-wave.

The determination of $dE_{peak}/d(\log \nu)$ for the three peaks gives 101 mV decade^{-1} for the pre-wave, 114 mV decade^{-1} for peak I and 93 mV decade^{-1} for peak II. These values are all higher than those proposed by Brimaud *et al.* for different surface facets on platinum nanoparticles as well as by Palaikis *et al.* on single-crystals, i.e. 80 ± 5 mV decade^{-1} for the Pt(111) surface and 60 ± 3 mV decade^{-1} for the Pt(100) surface[10, 52]. This indicates that the shift of the onset of the main CO stripping peak and all the CO stripping peaks

is larger for the mesoporous Pt electrode, which is probably due to the atomic surface structure within the pores.

3.4.3. Deconvolution of peaks

Figure 3-8 shows a CO stripping voltammogram deconvoluted into three peaks following the fit of a Gaussian equation (the three Gaussian peaks involved in the fitting corresponded to the pre-wave, peak I and peak II).

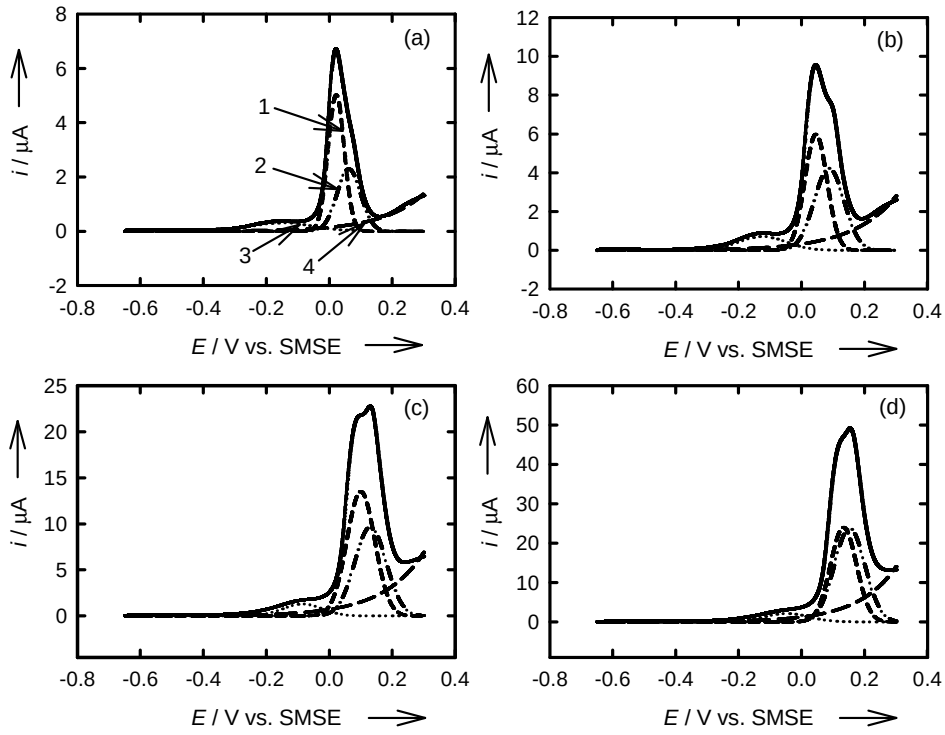

Figure 3-8. Anodic CO stripping scans recorded at a mesoporous Pt electrode (500 µm diameter, 6.27 mC for the deposition charge) in 1 M sulphuric acid at different scan rates; (a) 10 mV s^{-1}, (b) 20 mV s^{-1}, (c) 50 mV s^{-1} and (d) 100 mV s^{-1}. CO was adsorbed at -0.65 V with CO bubbling for 30 min and then the solution was sparged with N_2 for 15 min before recording the stripping. The curves are deconvoluted into three Gaussian functions, $a_n\exp[-0.5((E-E_{peak,n})/b_n)^2]$ and an exponential background, $\exp\{k(E-E_{bg})$ as shown in panel (a) (1) Peak I, (2) Peak II, (3) pre-wave, (4) background current.

The CO stripping voltammograms can be deconvoluted into three overlapping Gaussian peaks, $a_n\exp[-0.5((E-E_{peak,n})/b_n)^2]$, sitting on an exponentially rising background. The values of the peak potential $E_{peak,n}$ were fixed by inspection of the CO stripping voltammograms and the contribution of the three peaks and the background optimised by a non-linear regression using Sigmaplot version 11.

The results are in agreement with the experimental data and the deconvolution suggests that the charge associated with peak I decreases with increasing scan rate whereas the charge associated with peak II increases. Although this effect can be inferred, the charges associated to peak I and peak II as function of the scan rate appear to be scattered. Hence, it was not possible to analyse the results further since the sensitivity of the deconvolution relies essentially on the precise choice of the peak potential. However, the CO stripping peak for the polished platinum electrode did not fit a Gaussian peak.

3.5. Effect of the adsorption potential

3.5.1. Polished platinum electrode

Figure 3-9(a-f) represents CO stripping voltammograms of a polished polycrystalline Pt disc electrode in 1 M H_2SO_4 where CO was adsorbed at different potentials for 30 minutes and the solution was purged with N_2 for 15 minutes in order to remove any traces of CO.

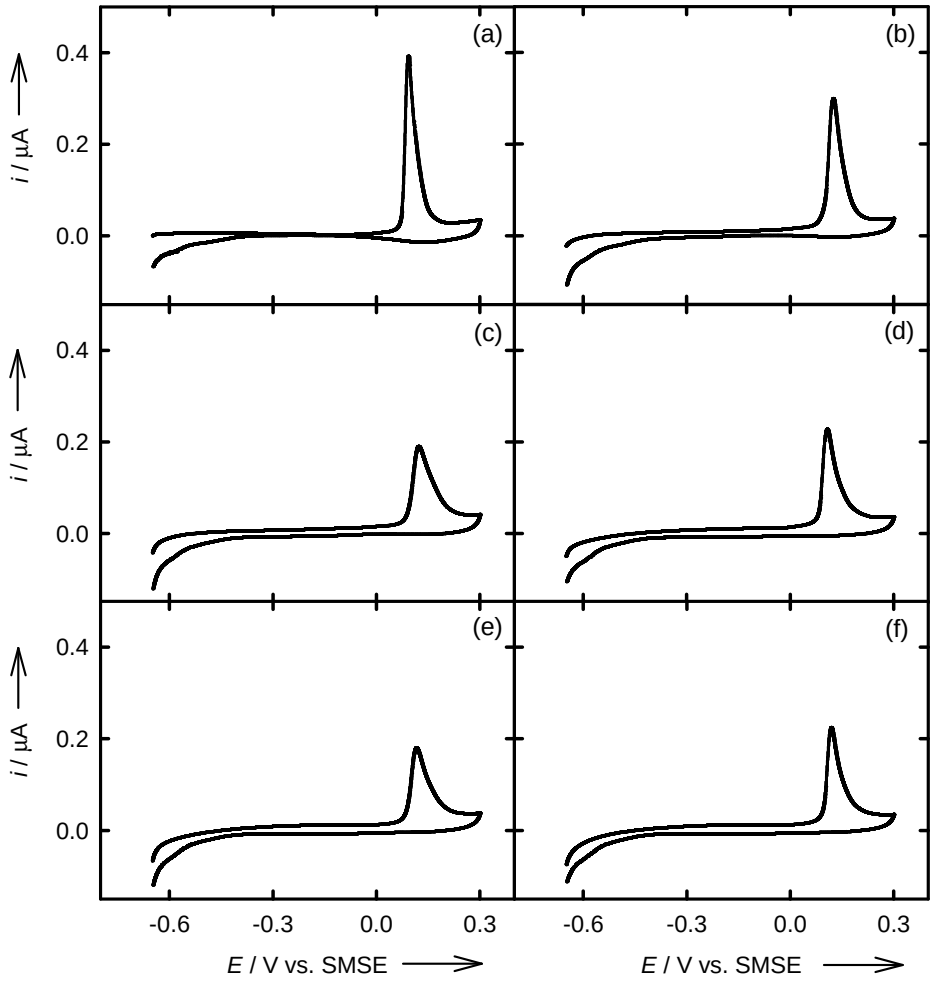

Figure 3-9. CO stripping voltammograms for a polished polycrystalline Pt electrode (500 µm diameter) in 1 M sulphuric acid, scan rate 10 mV s^{-1}. CO was adsorbed at different potentials with CO bubbling for 30 min and then the solution was sparged with N_2 for 15 min before recording the stripping. The adsorption potentials, E_{ads}, were: (a) -0.65 V; (b) -0.55 V; (c) -0.45 V; (d) -0.35 V; (e) -0.25; and (f) -0.15 V. After CO adsorption and N_2 sparging the potential was stepped to - 0.65 V and the scan started immediately.

In each case the CO stripping scan starts at - 0.65 V. No difference was seen when starting the CO stripping scan at the adsorption potential or when starting at - 0.65 V. In every case in Figure 3-9 a single CO stripping peak is seen which occurs at around the same potential (0.094 – 0.124 V vs. SMSE).

As the adsorption potential, E_{ads}, shifts more anodic the stripping peak current and the CO stripping charge decrease. The stripping charge is plotted against the deposition potential in Figure 3-10. Here the CO stripping charges have been calculated by

subtracting the blank background voltammogram from the CO stripping voltammogram. It can be observed that the CO stripping charge changes approximately linearly with the adsorption potential[52], decreasing by 30% between - 0.65 and - 0.25 V. These results are similar to those reported by Markovic *et al.* for single-crystal Pt(100)[25] and Pt(111)[25] and for polished polycrystalline Pt electrodes[51].

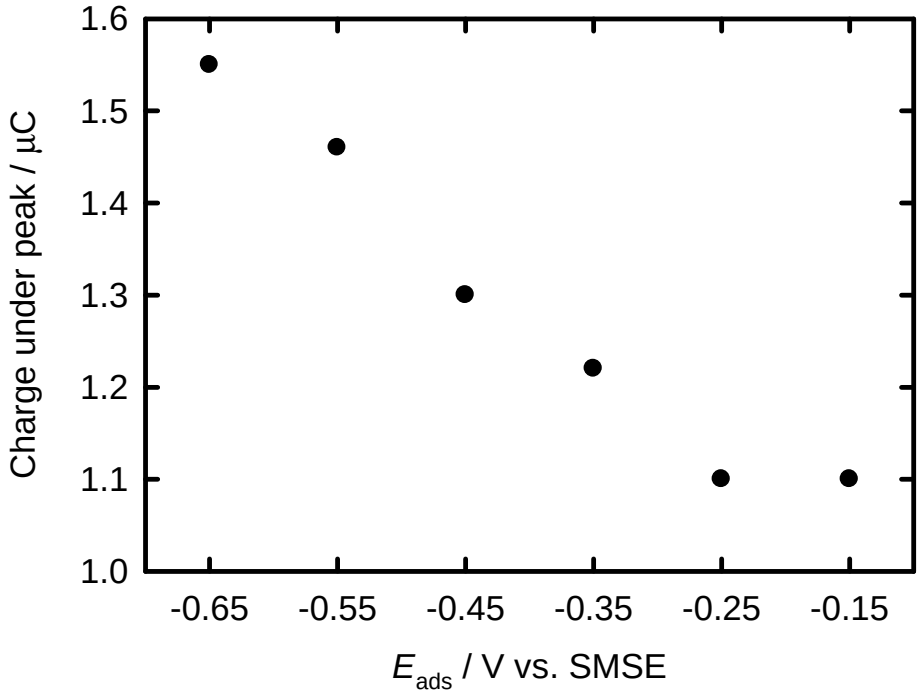

Figure 3-10. Variation of the charge under the CO stripping peak for a polished polycrystalline Pt electrode (500 µm diameter) with the CO adsorption potential, E_{ads}.

3.5.2. Mesoporous platinum electrode

Figure 3-11(a-f) represents CO stripping voltammograms for a mesoporous platinum electrode in 1 M H_2SO_4 where CO was adsorbed at different potentials for 30 minutes and the solution was purged with N_2 for 15 minutes in order to remove any traces of CO.

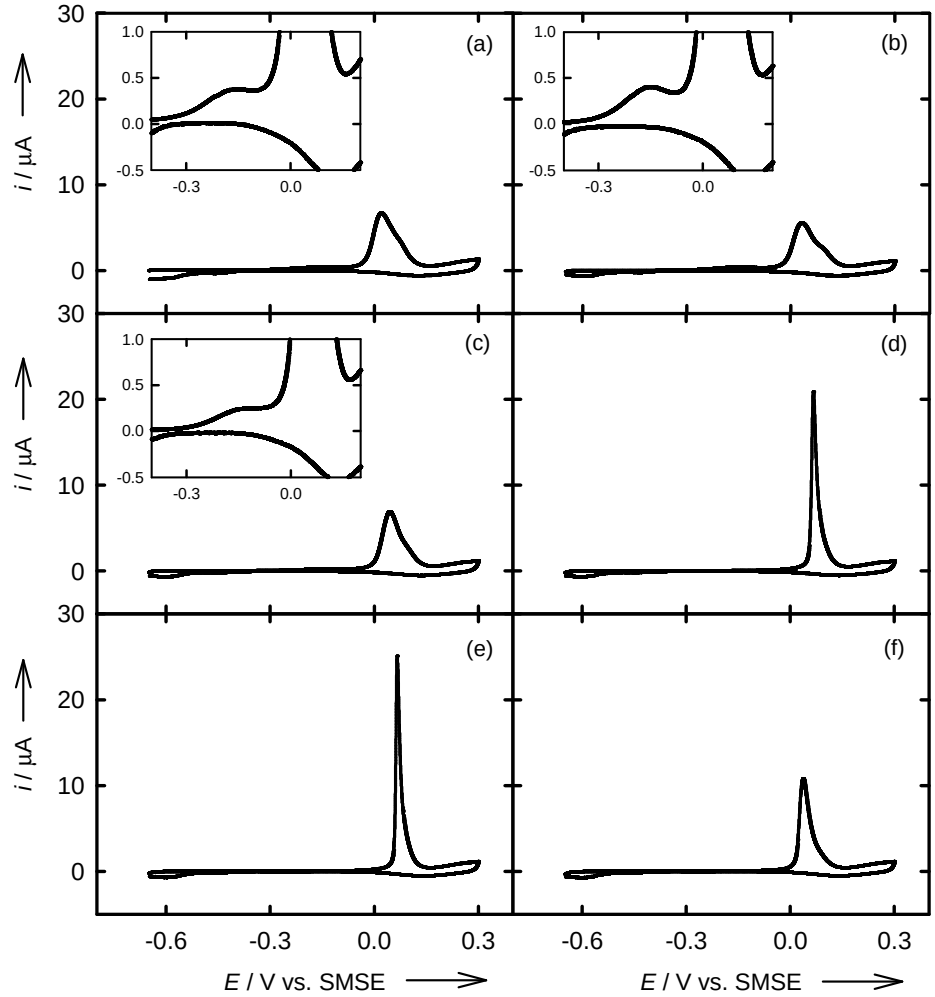

Figure 3-11. CO stripping voltammograms for a mesoporous Pt electrode (500 µm diameter, 6.27 mC for the deposition charge) in 1 M sulphuric acid, scan rate 10 mV s^{-1}. CO was adsorbed at different potentials with CO bubbling for 30 min and then the solution was sparged with N_2 for 15 min before recording the stripping. The adsorption potentials, E_{ads}, were: (a) -0.65 V; (b) -0.55 V; (c) -0.45 V; (d) -0.35 V; (e) -0.25; and (f) -0.15 V. After CO adsorption and N_2 sparging the potential was stepped to -0.65 V and the scan started immediately. The insets show the pre-wave.

When the adsorption potential is situated in the hydrogen region (E < - 0.35 V vs. SMSE) of the cyclic voltammogram of platinum in 1 M sulphuric acid, the three peaks are present: the pre-wave, peak I and peak II. For the adsorption potentials of - 0.35 and - 0.25 V, one single and sharp peak appears at the potential corresponding to peak II. For the adsorption potential at - 0.15 V, one broader peak is obtained at the potential corresponding to peak I. This effect was already reported previously on a single-crystal Pt(100)[25]. This suggests that CO adsorbed at potentials in the double layer region is more difficult to oxidize than CO adsorbed in the hydrogen region.

Figure 3-12 shows the total charge under the CO stripping peaks plotted as a function of the adsorption potential for the mesoporous Pt. Again the total CO stripping charge decreases approximately linearly as the adsorption potential becomes more anodic. Compared to the results for the polished polycrystalline Pt electrode (Figure 3-10), the CO stripping charge is less dependent on the adsorption potential for the mesoporous Pt (~20 % decrease in the charge on going from - 0.65 V to - 0.15 V).

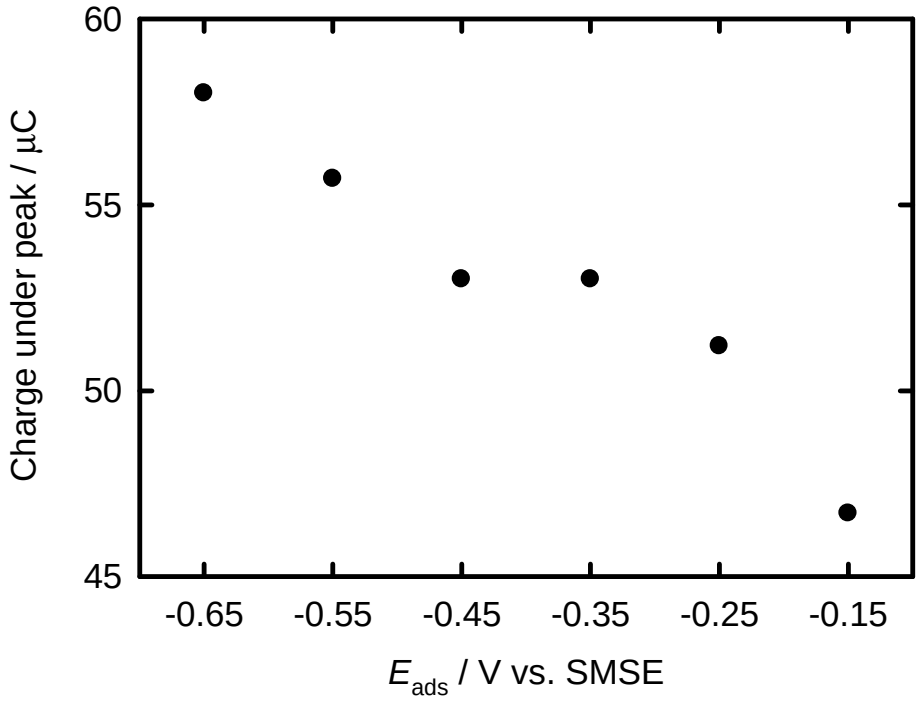

Figure 3-12. Variation of the charge under the CO stripping peak for a mesoporous Pt electrode (500 µm diameter, 6.27 mC for the deposition charge) with the CO adsorption potential, E_{ads}.

3.6. Effect of the pore size

Changing the pore size might have an influence on the CO electrooxidation. The pore size can be varied by using a different surfactant like $C_{16}EO_8$ in the mixture. It has been reported that the use of the surfactant $C_{16}EO_8$ yields a pore size of 2.5 nm[3].

3.6.1. Characterisation of the mesoporous platinum films by voltammetry in acid

Figure 3-13 shows a cyclic voltammogram for a mesoporous Pt film electrodeposited onto a polished Pt electrode from a mixture containing $C_{16}EO_8$ of the same geometric area in 1 M sulphuric. The use of a different surfactant could reveal another atomic surface structure of platinum, which can be identified by cyclic voltammetry in sulphuric acid in the hydrogen adsorption/desorption region. This could result in differences observed on the CO stripping voltammogram recorded later. The features of the cyclic voltammogram are identical to those presented for the polished Pt and the $C_{12}EO_8$ mesoporous Pt electrodes and are also similar to polycrystalline Pt dominated by low index Pt facets. The surface area was 0.294 cm^2 calculated from the hydrogen desorption peaks and hence the roughness factor of 150.

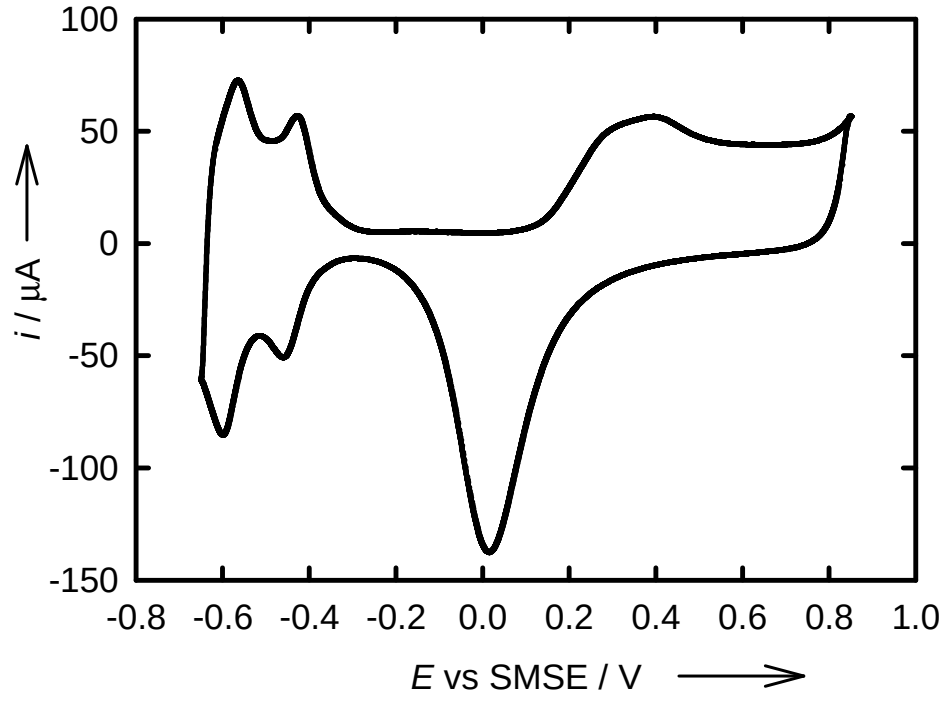

Figure 3-13. Cyclic voltammogram of a $C_{16}EO_8$ mesoporous platinum film electrodeposited onto a platinum disc electrode (500 µm in diameter) in 1 M sulphuric acid recorded at 200 mV s^{-1}. The solution was deareated by purging with argon for at least 20 min prior to the measurements.

3.6.2. CO stripping voltammetry on mesoporous platinum films

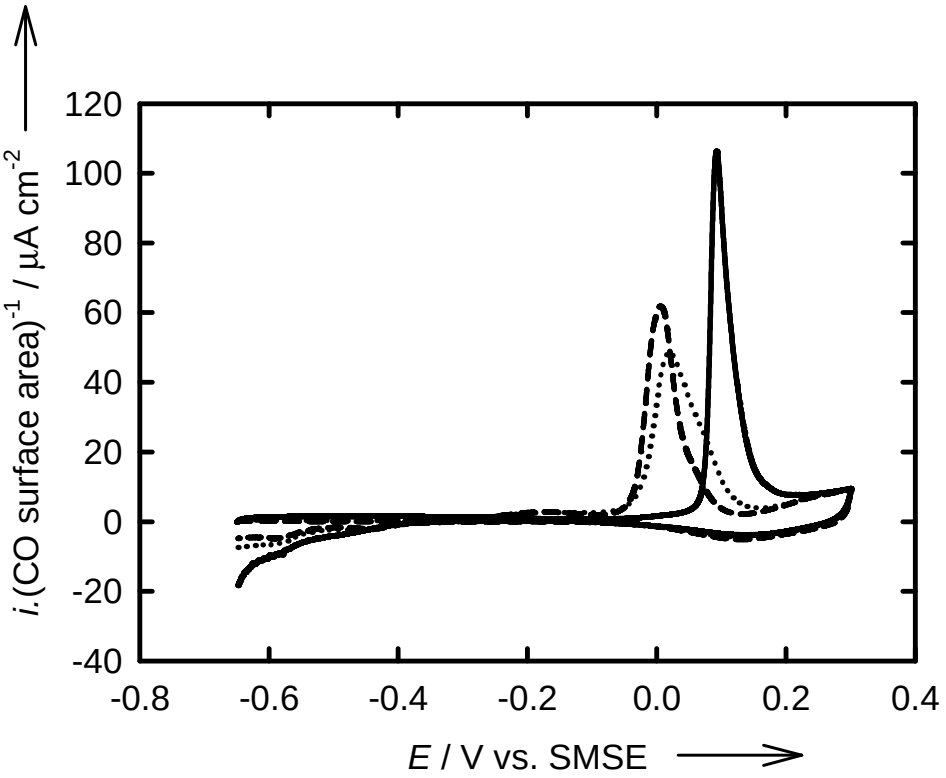

Figure 3-14. CO stripping voltammogram (solid line) for a polished polycrystalline Pt electrode (500 µm diameter). CO stripping voltammograms for mesoporous platinum films electrodeposited from a mixture containing $C_{12}EO_8$ (dotted line) and from a mixture containing $C_{16}EO_8$ (dashed line) (500 µm in diameter, 6.27 mC for the deposition charge). The CO stripping voltammograms were recorded in 1 M sulphuric acid at a scan rate of 10 mV s^{-1}. CO was adsorbed at - 0.65 V vs. SMSE bubbling for 30 min and the solution was sparged with N_2 for 15 min before recording the stripping.

Figure 3-14 shows the CO stripping voltammograms for a polished polycrystalline electrode and for the H_1 mesoporous Pt electrodeposited from the mixture containing either $C_{12}EO_8$ or $C_{16}EO_8$. The currents were normalised by the surface area calculated from the CO stripping peak of each electrode for a better comparison. The CO surface areas were obtained from the charge of the CO stripping peak using the conversion factor 420 µC cm^{-2}[32]. The CO stripping peak for both mesoporous electrodes is shifted towards more negative potentials compared to the polished polycrystalline electrode; the CO oxidation onset for both H_1 mesoporous Pt electrodes occurs at similar potentials. The details for the CO peak position and for the CO stripping charges associated with the peaks are different for the two mesoporous electrodes. However, similarities are observed for the main characteristics, e.g. the pre-wave, peak I and peak II.

3.7. Discussion

Bimolecular reactions involving surfaces can be classified into different categories depending on whether on or two molecules are adsorbed on the surface. The Langmuir-Hinshelwood mechanism suggests that two molecules are adsorbed on the surface and undergo a bimolecular reaction. The electrooxidation of CO on platinum in acid occurs through a Langmuir-Hinshelwood mechanism in which adsorbed CO molecules react with oxygen species coming from water decomposition[31, 53, 54].

$$H_2O + * \leftrightarrow OH_{ads} + H^+ + e^- \quad (3)$$

$$CO_{ads} + OH_{ads} \rightarrow COOH_{ads} \quad (4)$$

$$COOH_{ads} \rightarrow CO_2 + H^+ + e + 2* \quad (5)$$

Where * denotes a free surface site. Previous studies have shown that this reaction on Pt single-crystals is very structure sensitive[8, 10, 25, 31, 55-57].

The cyclic voltammogram in acid for the H_1 mesoporous Pt film displays the same features as polycrystalline platinum seen in this work and from previous studies[3, 17, 41, 58] and shows that the H_1 mesoporous Pt film is made of low-index facets Pt(111), Pt (100) and Pt(110) according to the peaks in the hydrogen region. However the CO stripping voltammograms exhibited differences between the polycrystalline Pt electrode and the H_1 mesoporous Pt film. The CO stripping voltammogram for the H_1 mesoporous Pt film shows a pre-wave followed by two overlapping peaks whereas the CO stripping voltammogram for the polycrystalline Pt electrode shows one single sharp peak at more positive potentials under the same experimental conditions. The pre-wave feature was also reported by Jiang and Kucernak for H_1 mesoporous Pt[41]. Identical features have been noticed in the literature for different types of platinum electrodes such as electrodispersed Pt[9], Pt single-crystals[25, 56] and Pt nanoparticles[10, 34, 36]. Nevertheless, the true origin of the pre-wave still remains controversial[24-26, 50, 51, 55].

According to Markovic *et al.*[25], a highly compact CO adlayer formed on the platinum surface (0.75 CO/Pt on Pt(111)) entails a strong repulsive interaction between the molecules. The pre-wave was probably due to the oxidation of a part of this highly

compact layer, represented as weakly adsorbed $CO_{ad,w}$ and the main stripping peaks were ascribed to more strongly adsorbed $CO_{ad,s}$ at lower coverage (0.6 CO/Pt on Pt(111)) in a relaxed state without long range order[25]. The pre-wave and the main stripping peaks are not related to specific adsorption sites on the platinum surface but stem from the strong repulsive interactions between CO molecules at high coverage. According to Lopez-Cudero *et al.*[24, 26, 51], the pre-waves on Pt(111) and Pt(100) are associated to the oxidation of CO adsorbed at the vicinity of steps and defects on the platinum surface reacting with oxygenated species which nucleate at these steps and defects. Based on these studies, Lebedeva *et al.*[31] have shown that CO stripping voltammograms are correlated with CO oxidation on the various locations of stepped surfaces where Pt(100) or Pt(110) are at the inner corner. The inner corner of either Pt(100) or Pt(110) step is believed to be the active site for CO oxidation and the most reactive combination in the Langmuir-Hinshelwood mechanism involving the reaction of CO from a near-step terrace site with the oxygen species in the step trough[31]. According to Anderson[50], the pre-wave might arise from the oxidation of CO with OH molecules formed on the platinum surface at low potentials.

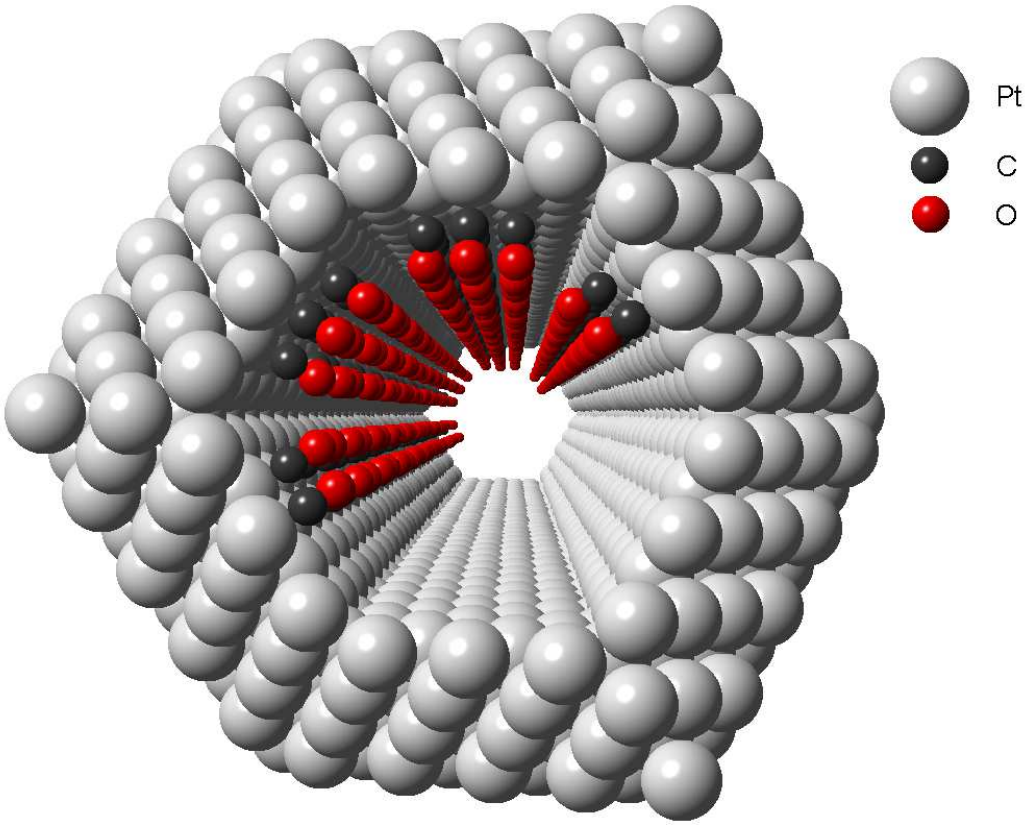

Figure 3-15. Drawing of an idealised structure looking down a single Pt pore, diameter 1.8 nm. The pore walls are shown as (111) surfaces and 0.67 ML CO is shown on atop sites on the top half of the pore.

The H_1 mesoporous Pt consists of a regular hexagonal porous structure, the morphology of the platinum surface is very different from the majority of Pt surfaces studied before. In the vast majority of cases the Pt surfaces were either flat (such as single crystal surfaces) or convex (such as Pt nanoparticles). In contrast the H_1 mesoporous Pt surfaces are dominated by the insides of the cylindrical pores (a few nanometers in diameter) and predominantly concave. Figure 3-15 represents an idealised structure of an individual pore within the H_1 mesoporous Pt film pore. The results presented above for the voltammetry in sulphuric acid (Figure 3-2) for the H_1 mesoporous Pt show that the surface is made up of low index and for simplicity a pore made up of Pt(111) faces was drawn with a diameter of 1.8 nm corresponding to the pore diameter when $C_{12}EO_8$ is used in the plating mixture. On the top left corner, adsorbed CO molecules are represented on atop-Pt-sites with a coverage of 0.67 ML. According to the model presented in the Figure 3-15, the inside of the pores exhibit a high proportion of trough sites due to the narrow pore diameter and the concave shape; the trough sites are located at the junction where two short terraces (corresponding to the pore walls) inside the pore meet and, for this pore size, the terraces cannot be more than three or four Pt atoms wide. It is evident from this model that CO is sterically hindered from adsorbing on the trough sites if CO occupies the terrace Pt in the vicinity of the trough sites. It is clear from the model that the H_1 mesoporous Pt film is substantially different because of the concave characteristic of the structure from the Pt nanoparticles even though their specific surface areas are similar (up to 60 $m^2\ g^{-1}$).

As the prewave corresponds to oxidation at lower overpotentials, it may be related to the reaction at lower energy sites. The presence of the trough generates steric hindrance so the molecules adsorbed on these sites oxidise first. In this work, the results for CO stripping are consistent with a model where the pre-wave is due to the reaction of adsorbed CO near the trough sites with oxygenated species, like OH_{ads}, formed at low potentials on the trough sites as suggested by Anderson[50]. The charge related with the pre-wave corresponds to 15 % of the total CO stripping charge; it is consistent with the model in Figure 3-15 which has one trough site for three terraces sites. The oxidation of the bulk of adsorbed CO occurring at lower overpotentials for the H_1 mesoporous Pt than for the polished polycrystalline electrode can be explained by the highly active sites in the trough inside the pores and by their high proportion compared to the terrace sites. This justification is consistent with a similar model presented by Lebedeva *et*

al.[31] in which the sites at the inner corner of the stepped surfaces, similar to the trough sites of the present study, are the active sites for CO oxidation (see Figure 11 in their paper)[31].

The idealised representation of Figure 3-15 was drawn without consideration of the history of the electrode. However, cycling of the H_1 mesoporous Pt electrode in sulphuric acid to potentials positive of oxide formation can lead to surface reconstruction creating ad-islands or kinks on the terraces inside the pores. The high activity of the ad-islands was demonstrated by Strmcnik *et al.*[59] for bulk CO oxidation on platinum. Strmcnik *et al.*[59] have suggested that the presence of ad-islands on the surface accounts for the pre-wave on the voltammogram. Crystalline defects have also shown an enhanced activity for CO oxidation on platinum as presented by Lebedeva *et al.*[31]. The history of the platinum electrode might bring about changes on the atomic arrangement at the surface, which might engender different types of crystalline defects, and this can reflect the different features of the CO stripping voltammetry.

3.8. Conclusion

The H_1 mesoporous Pt consists of porous channels (approximately 2 nm in diameter) organised in a hexagonal arrangement. Cyclic voltammetry of the H_1 mesoporous Pt in sulphuric acid has shown that the inside of the pores exhibits low-index Pt faces in agreement with polycrystalline Pt. However, the CO stripping voltammetry for the H_1 mesoporous Pt is significantly different from the polished polycrystalline Pt electrode under the same conditions. The pre-wave feature is present on the CO stripping voltammogram for the H_1 mesoporous Pt and corresponds to 15 % of the total CO stripping charge. This result was attributed to the presence of trough sites which are at the intersection of the low index faces of the Pt surface within the pores. At these trough sites, CO is sterically hindered from adsorbing due to the occupation of CO on the Pt terrace sites. Our results are consistent with the adsorption of oxygenated species on the trough sites accounting for the pre-wave and which ease the CO stripping reaction. The H_1 mesoporous Pt and Pt nanoparticles have comparable specific surface areas (up to 60 $m^2\ g^{-1}$) but differ fundamentally in the concave nature of the H_1 mesoporous Pt surface as opposed to the convex nanopaticle surfaces. This difference in the nature of the surface affects directly CO stripping.

3.9. References

[1] T. F. Esterle, A. E. Russell, P. N. Bartlett *ChemPhysChem*. **2010**, 11, 2896-2905.

[2] G. S. Attard, C. G. Goltner, J. M. Corker, S. Henke, R. H. Templer *Angew. Chem.-Int. Edit. Engl.* **1997**, 36, 1315-1317.

[3] G. S. Attard, P. N. Bartlett, N. R. B. Coleman, J. M. Elliott, J. R. Owen, J. H. Wang *Science*. **1997**, 278, 838-840.

[4] A. S. Aricò, S. Srinivasan, V. Antonucci *Fuel Cells*. **2001**, 1, 133-161.

[5] B. Hammer, J. K. Norskov *Adv. Catal.* **2000**, 45, 71-129.

[6] B. N. Grgur, G. Zhuang, N. M. Markovic, P. N. Ross *J. Phys. Chem. B.* **1997**, 101, 3910-3913.

[7] Z. M. Peng, H. Yang *Nano Today*. **2009**, 4, 143-164.

[8] N. P. Lebedeva, M. T. M. Koper, E. Herrero, J. M. Feliu, R. A. van Santen *J. Electroanal. Chem.* **2000**, 487, 37-44.

[9] A. M. Debecdelievre, J. Debecdelievre, J. Clavilier *J. Electroanal. Chem.* **1990**, 294, 97-110.

[10] S. Brimaud, S. Pronier, C. Coutanceau, J. M. Leger *Electrochem. Commun.* **2008**, 10, 1703-1707.

[11] W. F. Lin, M. S. Zei, M. Eiswirth, G. Ertl, T. Iwasita, W. Vielstich *J. Phys. Chem. B.* **1999**, 103, 6968-6977.

[12] V. Stamenkovic, M. Arenz, B. B. Blizanac, K. J. J. Mayrhofer, P. N. Ross, N. M. Markovic *Surf. Sci.* **2005**, 576, 145-157.

[13] B. N. Grgur, N. M. Markovic, P. N. Ross *J. Phys. Chem. B.* **1998**, 102, 2494-2501.

[14] S. Mukerjee, S. J. Lee, E. A. Ticianelli, J. McBreen, B. N. Grgur, N. M. Markovic, P. N. Ross, J. R. Giallombardo, E. S. De Castro *Electrochem. Solid State Lett.* **1999**, 2, 12-15.

[15] Z. Y. Zhou, Z. Z. Huang, D. J. Chen, Q. Wang, N. Tian, S. G. Sun *Angew. Chem.-Int. Edit.* **2010**, 49, 411-414.

[16] J. Solla-Gullon, F. J. Vidal-Iglesias, A. Lopez-Cudero, E. Garnier, J. M. Feliu, A. Aldaza *Phys. Chem. Chem. Phys.* **2008**, 10, 3689-3698.

[17] J. Jiang, A. Kucernak *J. Electroanal. Chem.* **2002**, 520, 64-70.

[18] J. N. Armor *Appl. Catal. A-Gen.* **1999**, 176, 159-176.

[19] N. P. Lebedeva, M. T. M. Koper, J. M. Feliu, R. A. van Santen *J. Phys. Chem. B.* **2002**, 106, 12938-12947.

[20] N. M. Markovic, B. N. Grgur, C. A. Lucas, P. N. Ross *J. Phys. Chem. B.* **1999**, 103, 487-495.

[21] C. A. Lucas, N. M. Markovic, P. N. Ross *Surf. Sci.* **1999**, 425, L381-L386.

[22] J. S. Spendelow, G. Q. Lu, P. J. A. Kenis, A. Wieckowski *J. Electroanal. Chem.* **2004**, 568, 215-224.

[23] N. P. Lebedeva, M. T. M. Koper, J. M. Feliu, R. A. van Santen *Electrochem. Commun.* **2000**, 2, 487-490.

[24] A. Lopez-Cudero, A. Cuesta, C. Gutierrez *J. Electroanal. Chem.* **2005**, 579, 1-12.

[25] N. M. Markovic, C. A. Lucas, B. N. Grgur, P. N. Ross *J. Phys. Chem. B.* **1999**, 103, 9616-9623.

[26] A. Lopez-Cudero, A. Cuesta, C. Gutierrez *J. Electroanal. Chem.* **2006**, 586, 204-216.

[27] G. Garcia, M. T. M. Koper *Phys. Chem. Chem. Phys.* **2008**, 10, 3802-3811.
[28] B. Hammer, O. H. Nielsen, J. K. Norskov *Catal. Lett.* **1997**, 46, 31-35.
[29] P. Inkaew, W. Zhou, C. Korzeniewski *J. Electroanal. Chem.* **2008**, 614, 93-100.
[30] N. P. Lebedeva, M. T. M. Koper, J. M. Feliu, R. A. van Santen *J. Electroanal. Chem.* **2002**, 524, 242-251.
[31] N. P. Lebedeva, A. Rodes, J. M. Feliu, M. T. M. Koper, R. A. van Santen *J. Phys. Chem. B.* **2002**, 106, 9863-9872.
[32] O. V. Cherstiouk, P. A. Simonov, V. I. Zaikovskii, E. R. Savinova *J. Electroanal. Chem.* **2003**, 554, 241-251.
[33] F. Maillard, E. R. Savinova, U. Stimming *J. Electroanal. Chem.* **2007**, 599, 221-232.
[34] J. Solla-Gullon, F. J. Vidal-Iglesias, E. Herrero, J. M. Feliu, A. Aldaz *Electrochem. Commun.* **2006**, 8, 189-194.
[35] K. J. J. Mayrhofer, M. Arenz, B. B. Blizanac, V. Stamenkovic, P. N. Ross, N. M. Markovic *Electrochim. Acta*. **2005**, 50, 5144-5154.
[36] K. A. Friedrich, F. Henglein, U. Stimming, W. Unkauf *Electrochim. Acta*. **2000**, 45, 3283-3293.
[37] C. S. Kim, W. J. Tornquist, C. Korzeniewski *J. Phys. Chem.* **1993**, 97, 6484-6491.
[38] C. S. Kim, C. Korzeniewski, W. J. Tornquist *J. Chem. Phys.* **1994**, 100, 628-630.
[39] C. S. Kim, W. J. Tornquist, C. Korzeniewski *J. Chem. Phys.* **1994**, 101, 9113-9121.
[40] J. Clavilier, J. M. Orts, R. Gomez, J. M. Feliu, A. Aldaz *J. Electroanal. Chem.***1996**, 404, 281-289.
[41] J. H. Jiang, A. Kucernak *J. Electroanal. Chem.***2002**, 533, 153-165.
[42] G. S. Attard, P. N. Bartlett, N. R. B. Coleman, J. M. Elliott, J. R. Owen *Langmuir*. **1998**, 14, 7340-7342.
[43] Angerste.H, B. E. Conway, W. B. A. Sharp *J. Electroanal. Chem.***1973**, 43, 9-36.
[44] G. Jerkiewicz, G. Vatankhah, J. Lessard, M. P. Soriaga, Y. S. Park *Electrochim. Acta*. **2004**, 49, 1451-1459.
[45] B. E. Conway, B. Barnett, H. Angersteinkozlowska, B. V. Tilak *J. Chem. Phys.***1990**, 93, 8361-8373.
[46] K. J. Vetter, J. W. Schultze. **1972**, 34, 131-139.
[47] J. Vetter, J. W. Schultze *J. Electroanal. Chem.* **1972**, 34, 131-&.
[48] T. Biegler, D. A. J. Rand, R. Woods *J. Electroanal. Chem.* **1971**, 29, 269-&.
[49] A. M. C. Luna, M. C. Giordano, A. J. Arvia *J. Electroanal. Chem.* **1989**, 259, 173-187.
[50] A. B. Anderson *Electrochim. Acta*. **2002**, 47, 3759-3763.
[51] A. Cuesta, A. Couto, A. Rincon, M. C. Perez, A. Lopez-Cudero, C. Gutierrez *J. Electroanal. Chem.* **2006**, 586, 184-195.
[52] L. Palaikis, D. Zurawski, M. Hourani, A. Wieckowski *Surf. Sci.* **1988**, 199, 183-198.
[53] M. T. M. Koper, A. P. J. Jansen, R. A. van Santen, J. J. Lukkien, P. A. J. Hilbers *J. Chem. Phys.* **1998**, 109, 6051-6062.
[54] S. Gilman *J. Phys. Chem.* **1964**, 68, 70-80.
[55] H. Kita, H. Naohara, T. Nakato, S. Taguchi, A. Aramata *J. Electroanal. Chem.* **1995**, 386, 197-206.

[56] N. M. Markovic, B. N. Grgur, C. A. Lucas, P. N. Ross *Surf. Sci.* **1997**, 384, L805-L814.
[57] F. J. Vidal-Iglesias, J. Solla-Gullon, J. M. Campina, E. Herrero, A. Aldaz, J. M. Feliu *Electrochim. Acta*. **2009**, 54, 4459-4466.
[58] J. M. Elliott, G. S. Attard, P. N. Bartlett, N. R. B. Coleman, D. A. S. Merckel, J. R. Owen *Chem. Mat.* **1999**, 11, 3602-3609.
[59] D. S. Strmcnik, D. V. Tripkovic, D. van der Vliet, K. C. Chang, V. Komanicky, H. You, G. Karapetrov, J. Greeley, V. R. Stamenkovic, N. M. Markovic *J. Am. Chem. Soc.* **2008**, 130, 15332-15339.

Chapter 4: Adsorption of bismuth and germanium on mesoporous platinum and effect on CO oxidation

In the last chapter, differences in CO stripping voltammetry were observed for H_1 mesoporous Pt due its concave structure. The pre-wave feature was associated with the presence of trough sites where the pore walls of the concave surface meet. In this Chapter, the adsorption of foreign atoms on the H_1 mesoporous Pt surface is investigated as a method to identify the crystalline Pt facets inside the pores.

4.1 Overview

The adsorption/desorption of species in solution can provide a fingerprint for the electrode surface structure that can be monitored by cyclic voltammetry. For example, the adsorption energy of hydrogen on platinum sites is different for sites of different symmetry and consequently the voltammetry is different for different Pt surfaces. Platinum surfaces have been investigated in acidic media by cyclic voltammetry in the hydrogen adsorption/desorption region to determine the low index Pt faces of polycrystalline Pt electrodes [1, 2].

An alternative way to characterise the surface is to deposit foreign adatoms on the metal substrate. Irreversible adsorption of foreign adatoms on the metal surface takes place when the adatoms remain on the metal surface over a wide range of potentials even though the electrolyte does not contain ions of the adatoms that could be in equilibrium with the adsorbed species[3]. A surface reaction can occur on the adatom adsorbed on specific surface sites at a potential range dictated by the underlying crystal symmetry of the platinum. It is then possible to identify the presence of the sites of this particular crystal symmetry on the surface of polycrystalline samples.

The adsorption of foreign atoms on platinum electrodes occurs preferentially on specific low index Pt facets as seen on Pt single-crystals. Numerous studies on adsorbed Bi and Ge on platinum surfaces have demonstrated the influence of these foreign atoms on the

peaks in the hydrogen region of the voltammogram in acid[4-8]; hence it was possible to quantify the coverage of the foreign atoms on the Pt surface. Thanks to the adsorption of the foreign atoms on specific platinum sites, it was possible to quantify the low index Pt sites on nanoparticles by cyclic voltammetry[4]. In the present study, these findings are exploited to extrapolate the results to the H_1 mesoporous platinum.

It has been shown that the adsorption of foreign atoms improved the electrocatalytic activity of Pt towards the oxidation of small organic molecules[7]. The adsorption of bismuth atoms on H_1 mesoporous platinum has already been investigated for formic acid oxidation[7] and for glucose oxidation[9]. The main objective of these studies was to increase the activity of the reaction thanks to the high electroactive area provided by the concave structure and the contribution from the Bi adatoms. In the present study, in contrast, the adsorption of Bi atoms on H_1 mesoporous Pt is used to give an insight of the atomic structure inside the pores. Bismuth is one of the adsorbed species on the platinum surface which has incited a lot of attention[4, 6, 7, 9, 10]. Many studies of the adsorption of Bi atoms on platinum electrodes were driven by the desire to improve the catalytic activity for formic acid oxidation[7, 11-17]. One path of the reaction leads to the formation of an intermediate species, namely CO, poisoning the platinum substrate[14-17]. The outcome of earlier work on formic acid oxidation can lead to conclusions on the effect of the surface structure for CO oxidation on H_1 mesoporous Pt modified with Bi. Previous studies on stepped Pt surfaces modified with Bi have shown that Bi atoms adsorb preferentially on the step sites[13, 14, 18]. This effect can be relevant for the present work with the H_1 mesoporous Pt.

The other adsorbed species on H_1 mesoporous platinum examined here is germanium; there is no published article on the adsorption of germanium on mesoporous platinum to date. Previous studies have demonstrated that the adsorption of germanium atoms on the platinum surface increases the electro-catalytic activity towards CO oxidation[19, 20]. The results of the present study were interpreted in regards to the literature on the CO oxidation on the platinum modified by adsorbed Bi and Ge atoms.

4.2 Adsorption of Bi and Ge atoms on platinum

4.2.1 Adsorption of Bi atoms

Three different procedures were used to adsorb bismuth atoms on the platinum surface. From the literature, different acid solutions were employed such as H_2SO_4[4, 9] or $HClO_4$[2] and different bismuth species were also used like Bi_2O_3[2, 4] or $Bi(NO)_3$[9]. The first method is the spontaneous adsorption which consists of immersing the electrode for a period of time at open circuit in the acidic solution containing the dissolved bismuth salt[2]. In the second method, bismuth adsorption can occur by cycling the potential between - 0.65 and 0.85 V vs. SMSE in the same type of solutions as aforementioned[7]. This potential window includes the hydrogen adsorption/desorption region and bismuth under potential deposition (UPD), hence the coverage of bismuth θ_{Bi} can be estimated. The last method consists of applying a constant potential in the double layer region from the same solutions as in the first method[7].

For all these techniques, the electrode is rinsed with deionised water and then immersed in the solution containing only sulphuric acid to record the cyclic voltammogram. The bismuth coverage can be controlled by the Bi concentration in the acid solution or by the deposition time. In the present work, these parameters were not investigated because the objective was to deposit a full monolayer of Bi[2].

In this work, all three techniques have been tried but, when comparing the bismuth coverage, the values were close to each other. Therefore, the simple spontaneous adsorption method was used into the bulk of the study. In the present work, the bismuth salt was dissolved in 0.6 M perchloric acid as reported by Clavilier *et al.*[2]. The effect of Cl^- on the electrode was neglected by considering the minute amount of $HClO_4$ dissolved in 1 M H_2SO_4 (a droplet of $HClO_4$ compared with 25 mL H_2SO_4).

4.2.2 Adsorption of Ge atoms

Ge adsorption on platinum electrodes was performed by putting a droplet of 1 M NaOH + 0.5 M GeO_2 on the tip of the electrode and immersing the electrode in 1 M H_2SO_4 while the potential was maintained at - 0.65 V vs. SMSE. This method was adopted from the literature[21]. The adsorption of the germanium atoms is thus performed by

underpotential deposition (UPD) to be able to maintain constant coverages on the platinum surface.

4.3 Bismuth adsorption

4.3.1 Characterisation of the mesoporous platinum film by voltammetry in acid

Figure 4-1 shows a cyclic voltammogram of a polished platinum electrode and a $C_{12}EO_8$mesoporous platinum film in 1 M H_2SO_4.

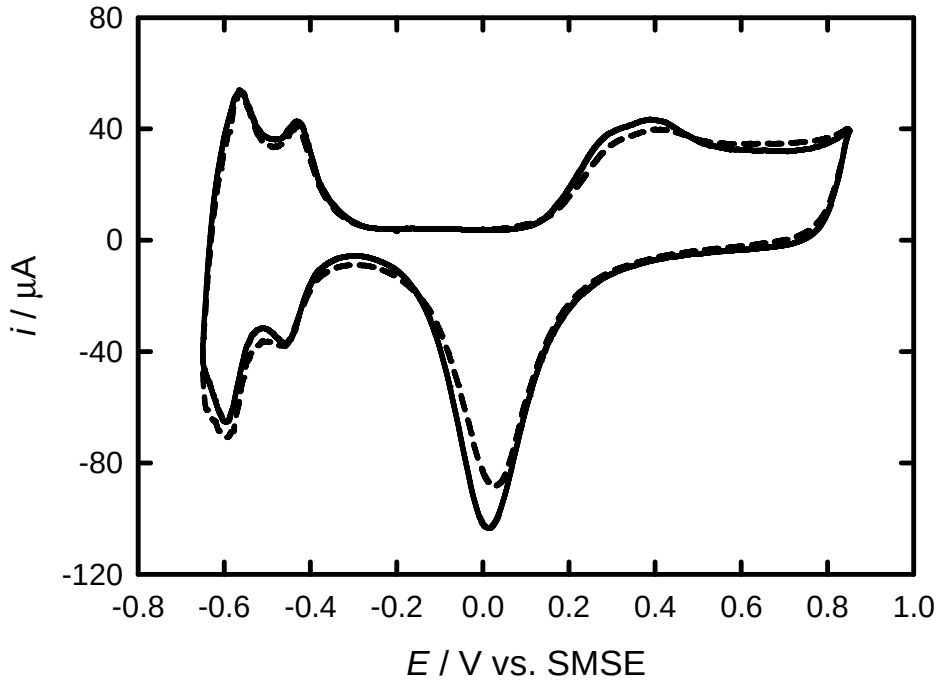

Figure 4-1. Cyclic voltammograms in deaerated 1 M H_2SO_4 of a polished platinum electrode (500 µm in diameter) (dashed line) and a $C_{12}EO_8$ mesoporous platinum film electrodeposited (charge 6.27 mC) on a polished platinum electrode (500 µm in diameter) (solid line). The scan rate was 200 mV s^{-1}.

From the analysis of the cyclic voltammograms, the surface area of the mesoporous platinum electrode (0.220 cm^2) was higher than the polished platinum electrode (0.0048 cm^2) due to the internal surface within the pores. The surface area of the electrodes was calculated from the hydrogen desorption region of the cyclic voltammogram. By examining the features of the cyclic voltammograms from the literature, it was deduced that both polished and mesoporous platinum are polycrystalline[1, 22, 23]. The different

characteristics of the cyclic voltammogram were discussed in the previous Chapter in Section 3.2.2.

4.3.2 Bismuth adsorption by voltammetry

This cyclic voltammogram of the mesoporous Pt electrode was then compared to a cyclic voltammogram of the same electrode recorded in deaerated 1 M H_2SO_4 + 1 mM Bi_2O_3as shown in Figure 4-2.

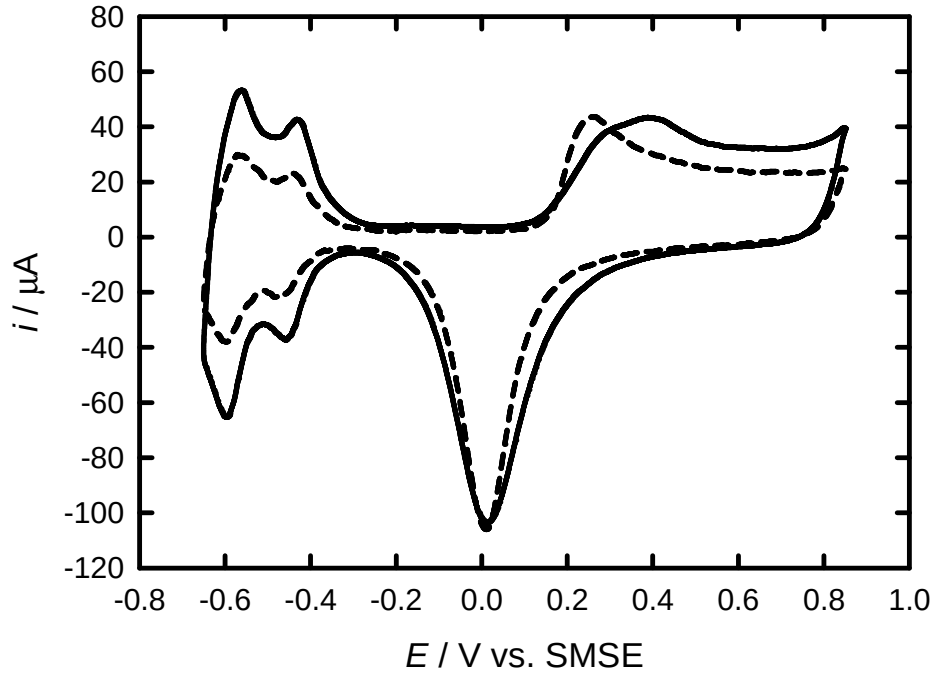

Figure 4-2. Cyclic voltammograms of a $C_{12}EO_8$mesoporous platinum film electrodeposited (charge 6.27 mC) on a polished platinum electrode (500 µm in diameter) in deaerated 1 M H_2SO_4 (solid line) and in deaerated 1 M H_2SO_4 + 1mM Bi_2O_3 (dashed line). The scan rate was 200 mV s^{-1}.

The peak at 0.25 V vs. SMSE on the anodic scan corresponds to the oxidation of bismuth, though a contribution of Pt oxidation can be added at this potential[7].The bismuth on platinum involved during the oxidation process can form different oxidised species such as BiOH, BiO and $Bi(OH)_2$[2]. The peak at 0 V vs. SMSE on the cathodic scan corresponds not only to oxide stripping but also to the reduction of Bi[7]. However, the hydrogen adsorption and desorption region was partially suppressed although the peaks can still be observed. A similar behaviour was reported for smooth polycrystalline Pt electrodes when the sulphuric acid solution contains Bi(III) ions[2, 7, 11, 24-26].

The suppression observed in the hydrogen region arises from the inability of hydrogen to adsorb on bismuth[2]. Therefore, the uncovered Pt sites are free for hydrogen adsorption. Consequently, the apparent coverage of Bi on the platinum surface can thus be evaluated by assuming that each bismuth adatom blocks three platinum sites for hydrogen adsorption[27] and calculating the charge in the hydrogen region before and after the adsorption of Bi on the electrode surface, using the expression[7, 26] :

$$\theta_{Bi} = (Q_H^b - Q_H^a)/3 \times Q_H^b$$

where θ_{Bi} is the coverage of Bi on the platinum surface, Q_H^b the charge before Bi adsorption in hydrogen desorption and Q_H^a the charge after Bi adsorption in the hydrogen desorption. From the analysis of the cyclic voltammograms, the coverage θ_{Bi} represents 0.15 of the Pt sites.

According to Clavilier *et al.*[2], a reversible peak for Bi adsorbate on the terrace is present at 0.61 V vs. RHE (- 0.03 V vs. SMSE) for stepped surfaces with Pt(111) bidimensional ordered domains (terraces 6 atomic rows wide). Thus the bismuth adsorbate seems to be a good probe for the detection of (111) surface domains at the surface of a platinum sample. However, no peak appears at this potential in the voltammogram in Figure 4-2 which suggests that surfaces of Pt(111) domains of terraces with at least 6 atom wide do not exist inside the pores of these H_1 mesoporous Pt electrodes. This is consistent with the model in Figure 3-15 in Chapter 3 where the pore wall is constituted of 3-4 atoms in width.

For the preparation of the H_1 mesoporous Pt modified with Bi adatoms for CO stripping voltammetry, the electrode was immersed in an acidic solution containing the Bi(III) salt for a period of time and then was transferred into 1 M H_2SO_4. Bismuth adatoms covered the H_1 mesoporous Pt surface by spontaneous adsorption. Cyclic voltammetry in 1 M H_2SO_4 was carried out to determine the coverage, θ_{Bi}, on the electrode. The cyclic voltammogram resembles to that in Figure 4-2 and the coverage θ_{Bi} was similar to that found by cycling in 1 M H_2SO_4 + 1 mM Bi_2O_3.

4.3.3 CO stripping voltammetry of the mesoporous platinum film in acid

Figure 4-3 shows a CO stripping voltammogram of a mesoporous platinum film in 1 M H_2SO_4 where CO was adsorbed at - 0.65 V vs. SMSE and the solution was purged with N_2 gas. The subsequent cycle was used to verify that all the carbon monoxide was stripped off the surface.

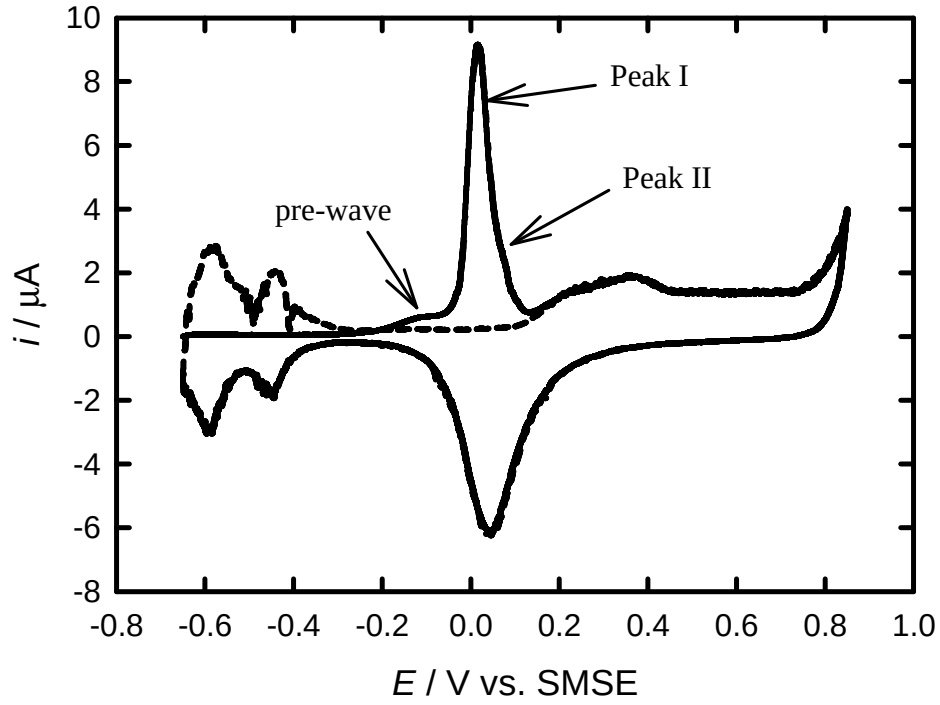

Figure 4-3. CO stripping voltammogram (solid line) and successive voltammogram (dashed line) of a mesoporous platinum film electrodeposited (charge 6.27 mC) on a polished platinum electrode in 1 M H_2SO_4. CO was adsorbed at -0.65 V with CO bubbling for 30 min and then the solution was sparged with N_2 for 15 min before recording the stripping. The scan rate was 10 mV s^{-1}.

The CO stripping voltammogram shows a pre-wave, a main peak (denoted as the peak I) and a shoulder (denoted as the peak II) as depicted on the Figure 4-3. The analysis of these peaks has been described in our paper concerning CO oxidation on mesoporous platinum[28] and in the previous Chapter. The pre-wave was attributed to the reaction of CO near the trough sites with oxide species such as OH molecules adsorbed on the trough sites. The trough sites are the platinum sites situated at the inner corner of the pore where the pore walls intersect.

The same experiment was carried out on a mesoporous Pt electrode modified with irreversibly adsorbed Bi. Figure 4-4 shows a CO stripping voltammogram of a mesoporous platinum film covered with adsorbed Bi atoms and the subsequent cycle to demonstrate that all the CO was oxidized. The experimental conditions were identical to the previous experiment.

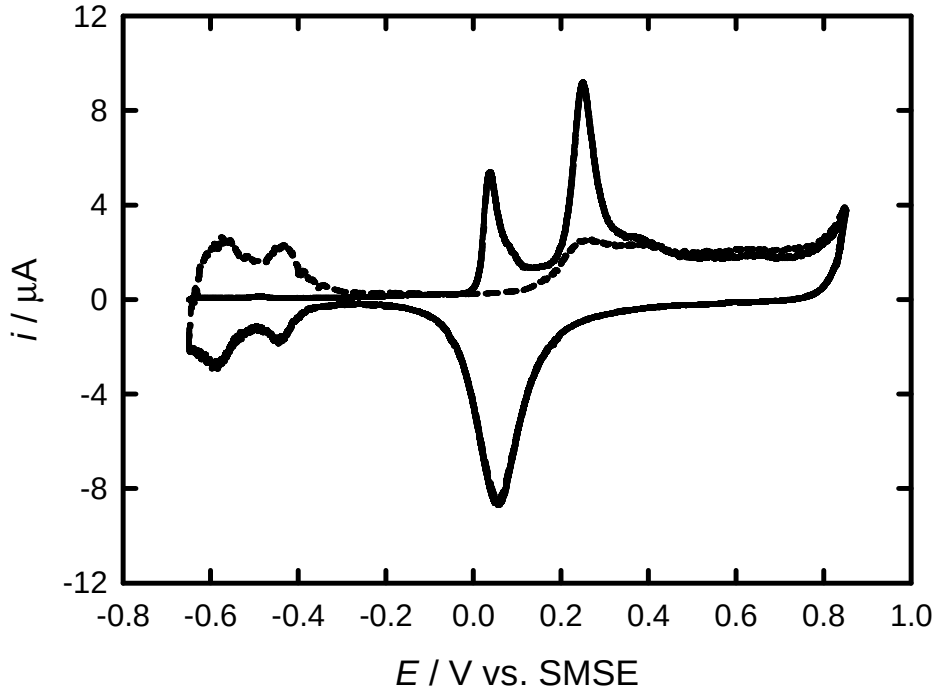

Figure 4-4. CO stripping voltammogram (solid line) and successive voltammogram (dashed line) of a mesoporous platinum film electrodeposited (charge 6.27 mC) on a polished platinum electrode in 1 M H_2SO_4 after soaking the electrode in 0.6 M $HClO_4$ + 0.01 M Bi_2O_3 for 10 minutes. CO was adsorbed at -0.65 V with CO bubbling for 30 min and then the solution was sparged with N_2 for 15 min before recording the stripping. The scan rate was 10 mV s^{-1}.

After CO adsorption, all the platinum sites have been blocked and only the double layer charging can be observed in the potential range - 0.65 and - 0.1 V leading to a flat profile of the voltammogram in this potential range. Two distinguishable peaks can be observed at 0.02 V and 0.25 V vs. SMSE. The first peak corresponds to the main CO oxidation and is followed by a shoulder. Those were already observed on the unmodified H_1 mesoporous Pt film on Figure 4-3. The main CO oxidation peak is similar to that found for a carbon supported platinum electrode although the CO stripping voltammogram does not show the second peak[8]. The second peak is related to the oxidation of bismuth which occurs concomitantly with the oxide formation of

platinum by comparison of the Figure 4-2 (see details below). However, the current density of the second peak is higher than in Figure 4-2, which might be resulted from the lift of Pt oxides from CO oxidation. Two peaks were also observed on the CO stripping voltammogram on Pt(100) modified with Bi adatoms by Chang and Weaver[29]. However, in their study, $HClO_4$ was used as supporting electrolyte[29]. Both CO and Bi oxidation processes occur at separated potentials which could be the evidence for a mixed adlayer Bi/CO. According to previous results[8, 29-33], coadsorbed CO and Bi on platinum present an intermixed adlayer. It is worth noting that the pre-wave is absent on the CO stripping voltammogram in Figure 4-4.

The coverage of CO on the H_1 mesoporous Pt electrode with a Bi adalayer was estimated from the CO stripping voltammogram. The peak potential for CO oxidation for the H_1 mesoporous Pt electrode modified with Bi adatoms is similar to that on the unmodified surface. The charge under the CO peak represents 43 % of the total charge of the two peaks. Therefore the coverage of Bi θ_{Bi} on the H_1 mesoporous Pt electrode is 0.19. This result appears to be higher than the percentage calculated from the charge under the peaks of the hydrogen region.

On the subsequent cycle, the peak at 0.25 V attributed to bismuth oxidation is still present which means that a part of the Bi atoms (about 22 % of the bismuth coverage) is still adsorbed on the surface. The capacitance for the oxide formation is larger than on the CO stripping voltammogram but no peaks for CO oxidation were observed and the hydrogen desorption peaks were retrieved.

4.4 Germanium adsorption

4.4.1 Characterisation of the mesoporous platinum film modified with Ge atoms by voltammetry in acid

The experiment with the adsorption of Ge atoms on the mesoporous Pt electrode was performed on a freshly deposited $C_{12}EO_8$ mesoporous Pt film. The cyclic voltammograms of a mesoporous platinum electrode before and after adsorption of adsorbed Ge atoms recorded in 1 M H_2SO_4 are shown in Figure 4-5. The drop containing 0.5 M GeO_2 + 1 M NaOH is about a few µl compared to the amount of solution of 1 M sulphuric acid used in these experiments (in this work, 25 ml).

Therefore, the amount of NaOH is considered as negligible compared to sulphuric acid. Although sulphuric acid is contaminated by NaOH, it is believed that the presence of NaOH does not affect greatly the results.

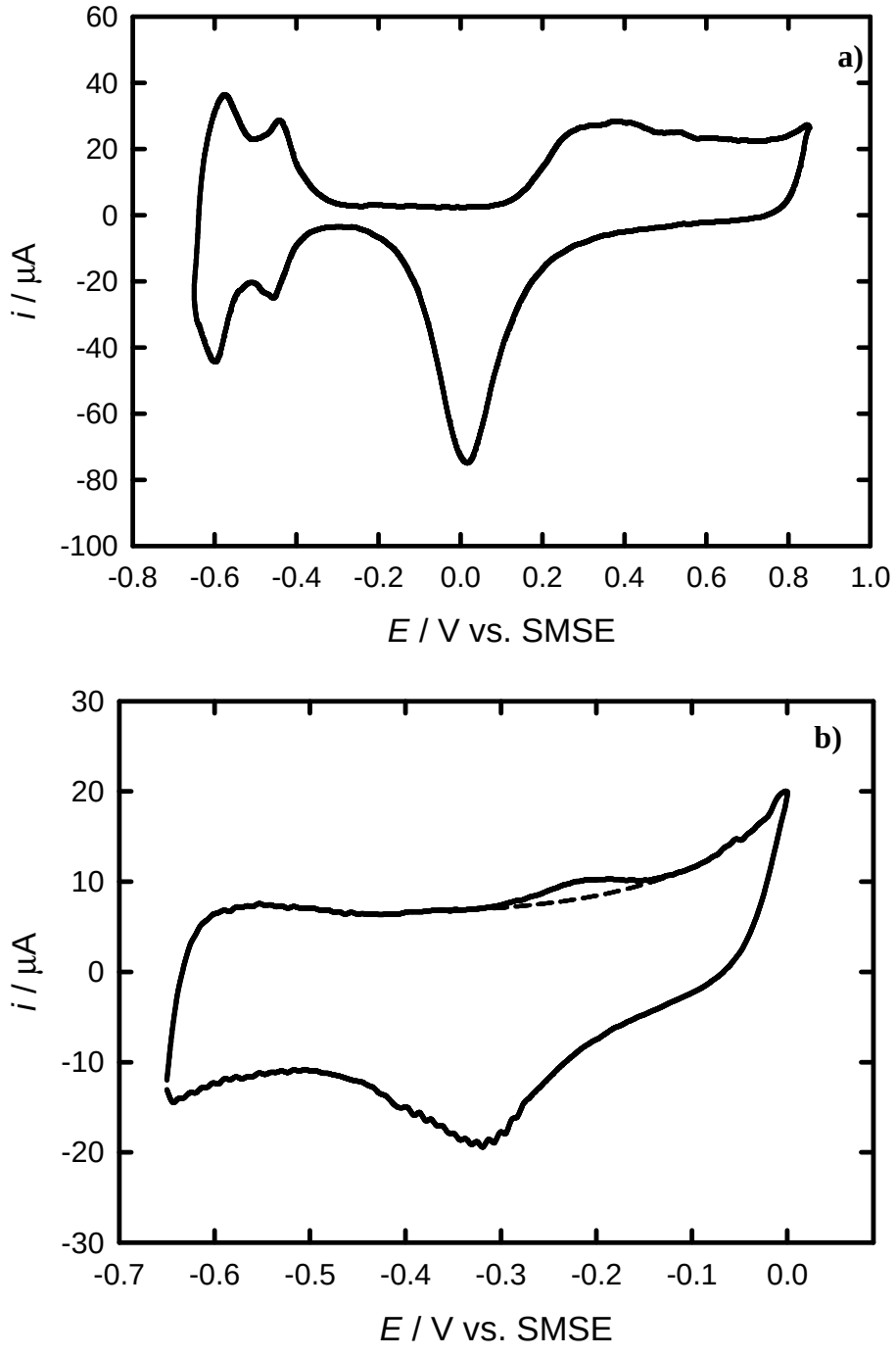

Figure 4-5. (a) Cyclic voltammogram of a $C_{12}EO_8$ mesoporous Pt film electrodeposited (charge 6.27 mC) on a polished platinum electrode (500 µm in diameter) in deaerated 1 M H_2SO_4. (b) Cyclic voltammogram of a mesoporous Pt film modified with Ge atoms in deaerated 1 M H_2SO_4 (third cycle recorded in a series of 3). A drop of 0.5 M GeO_2 + 1 M NaOH was put on the electrode. The electrode was then inserted in the solution while the potential was held at - 0.65 V vs. SMSE. The dashed line corresponds to the arbitrarily drawn baseline. The scan rate was 200 mV s^{-1}.

As described in Section 4.3.1, the cyclic voltammogram of the mesoporous Pt electrode in Figure 4-5a has the characteristics of a polycrystalline Pt of low index Pt facets. A cyclic voltammogram of a mesoporous Pt modified with Ge atoms was recorded in 1 M H_2SO_4 as shown in the Figure 4-5b. The voltammogram was obtained by cycling over this potential window three times.

The characteristics of the cyclic voltammogram for a polycrystalline platinum electrode modified with adsorbed germanium atoms have been already studied in the literature, i.e. no features in the hydrogen region and a redox process related to the presence of germanium on the Pt surface[3, 4]. The voltammogram shown in Figure 4-5b is in good agreement with previous studies on a polycrystalline Pt electrodes modified with Ge adatoms. The absence of adsorption/desorption peaks in the hydrogen region corresponds to a full coverage of germanium on the platinum surface. Within the range of potentials between - 0.4 and - 0.1 V, a redox process can be also identified by the presence of germanium on the platinum surface. It has been proposed that each Ge adatom exchanges four electrons and blocks two Pt sites leading to a maximum coverage of 0.25 Ge per Pt and the redox process undergone by the Ge adatom is a two electron transfer reaction as presented in equation (1)[21, 34],

$$Pt_4Ge_{ads} + H_2O \longrightarrow Pt_4GeO_{ads} + 2H^+ + 2e^- \qquad (1)$$

Based on a study on stepped Pt surfaces modified with Ge adatoms, it was found that the oxidation peaks below 0.6 vs. RHE (- 0.06 V vs. SMSE) correspond to the oxidation of germanium on the Pt(100) symmetry[3]. Rodriguez *et al.* attributed the oxidation peak below 0.6 V vs. RHE (- 0.06 V vs. SMSE) to the presence of Pt(100) terrace sites on polycrystalline platinum sample[3]. Consequently, in Figure 4-5b, the peak at - 0.23 V vs. SMSE is attributed to the oxidation of germanium on the Pt(100) terrace sites on H_1 mesoporous Pt. According to the literature[3], the number of Pt(100) sites can be estimated using the relation $q^{Ge} = 0.56 \times q^{Pt(100)}$ with q^{Ge} representing the charge density for the adsorbed germanium on the Pt surface and $q^{Pt(100)}$ representing the charge density for a process taking place on Pt(100) surface sites. An arbitrarily baseline was drawn as a continuity of the curve using Origin8.1. The charge under the peak was then calculated using Sigmaplot. The result indicates that the mesoporous Pt film consists

of6 % of Pt(100) sites on the surface. This percentage is in respect to the present sample and is not a fixed value for a mesoporous Pt film. The percentage of Pt(100) sites to the mesoporous Pt film may vary with the different exposed Pt faces of the surface.

4.4.2 Germanium oxidation

For a better understanding of the different contributions of Ge adatoms to CO oxidation, the electrode was cycled over a wider potential window. Figure 4-6 shows a series of cyclic voltammograms of a mesoporous platinum electrode modified with germanium atoms within the range of potentials - 0.65 and 0.3 V vs. SMSE. For the first cycle, the starting potential was - 0.65 V, the same as the potential at which the electrode was immersed in the solution.

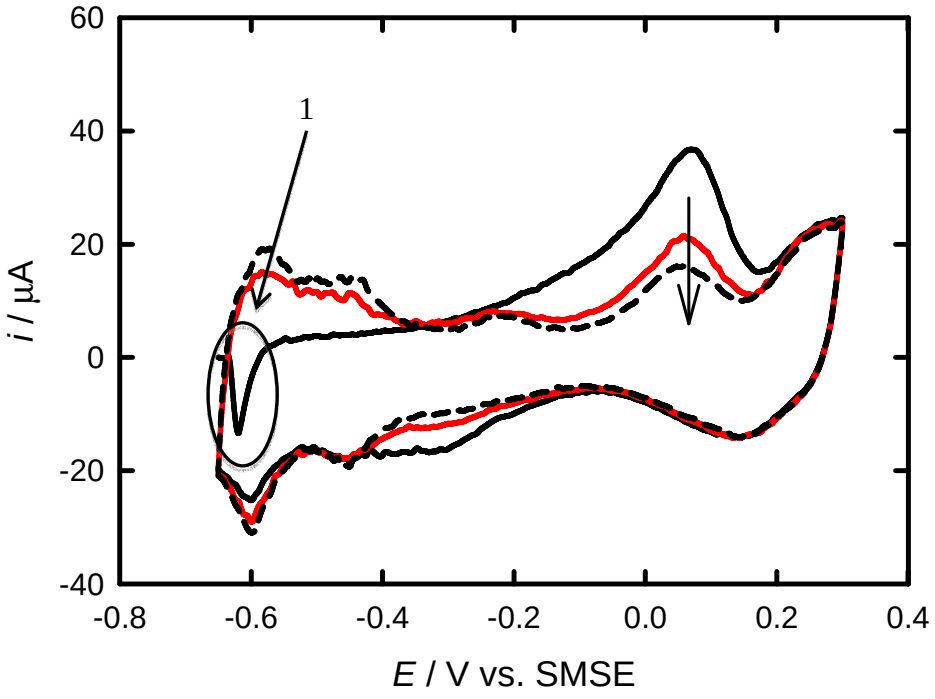

Figure 4-6. A series of cyclic voltammograms of a mesoporous Pt electrode (charge 6.27 mC,500 µm in diameter) modified with adsorbed Ge atoms in deaerated 1 M H_2SO_4. The scan rate was 200 mV s^{-1}. The solid black, the solid red and the dashed black lines are respectively the 1st and 2nd and 3rd cyclic voltammograms: A drop of 0.5 M GeO_2 + 1 M NaOH was on the electrode. The electrode was then inserted in the solution while the potential was held at - 0.65 V vs. SMSE. 1: this peak is an artefact due to the instrument while recording.

On the anodic branch of the first cycle between - 0.4 and - 0.1 V, the slowly rising current before the main peak is attributed to the presence of Pt(100) sites[3]. The main peak on the anodic branch appears at 0.05 V vs. SMSE and is related to the oxidation of adsorbed germanium atoms on the different platinum surfaces such as Pt(111) or Pt(110)[21]. The current for the peak decreases progressively with cycling. The cyclic voltammogram goes beyond the upper limit potential where germanium is dissolved in the solution, which could be attributed to the redox process described in equation (1).

Furthermore, it is worth considering the evolution of the hydrogen desorption region when cycling. No peaks in the hydrogen desorption region are observed on the first cycle since the Pt sites were blocked by the Ge atoms. Following the dissolution of germanium atoms in the solution when cycling at high potentials, the hydrogen adsorption peaks appear on the first cycle and their intensity increases for each forward cycle. The charge calculated under the hydrogen peaks on the third cycle is less than the charge calculated for the freshly made mesoporous Pt film, which indicates that some adsorbed Ge atoms remain on the surface. In addition, the presence of the peaks at - 0.23 and 0.05 V vs. SMSE on the anodic branch for the second and third cycles also confirm that Ge atoms are still adsorbed on the platinum surface.

4.4.3 Comparison of the different voltammograms

To give the reader a better appreciation, the cyclic voltammograms are now plotted altogether. Figure 4-7 shows a superposition of the previous cyclic voltammograms of the mesoporous Pt electrode before and after adsorption of Ge atoms and with different potential windows.

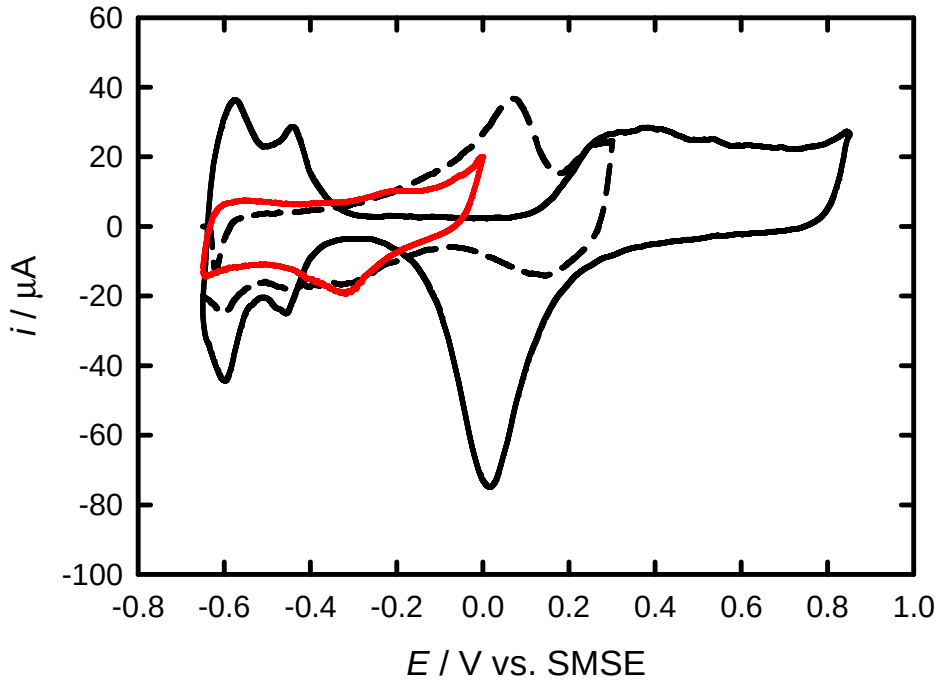

Figure 4-7. Cyclic voltammograms of a mesoporous Pt electrode (charge 6.27 mC, 500 µm in diameter) in dearated 1 M H_2SO_4 before and after Ge atom adsorption. The scan rate was 200 mV s^{-1}. (solid black line) Cyclic voltammogram of a mesoporous Pt film in 1M H_2SO_4. The solid red and dashed black lines are cyclic voltammograms of a mesoporous Pt electrode modified with adsorbed Ge atoms with different potential windows: a drop of 0.5 M GeO_2 + 1 M NaOH was put on the electrode. The electrode was then inserted in the solution while the potential was held at - 0.65 V vs. SMSE.

After the investigation of the mesoporous Pt electrode modified with adsorbed Ge atoms in 1 M H_2SO_4, the electrode was then tested for CO oxidation.

4.4.4 CO stripping voltammetry of the mesoporous platinum film modified with Ge adatoms

Figure 4-8 shows the CO stripping voltammogram of a mesoporous Pt film after Ge atom adsorption and the subsequent cycle to show that CO was removed from the platinum surface. A cyclic voltammogram of a mesoporous Pt electrode modified with adsorbed Ge atoms is also shown in the Figure 4-8 to interpret the different features in the CO stripping voltammogram.

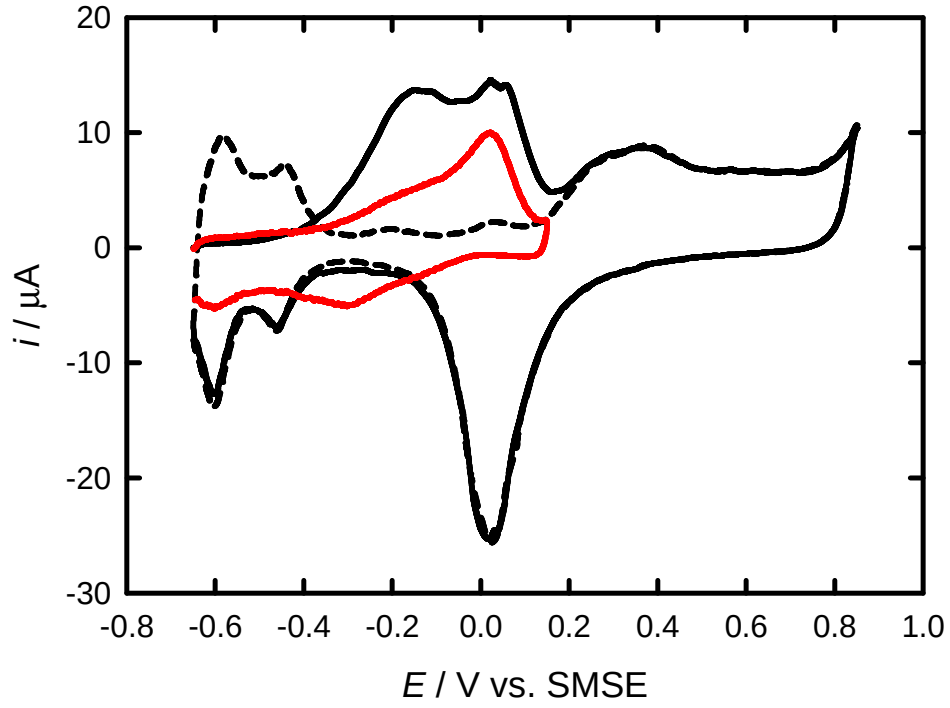

Figure 4-8. (solid black line) CO stripping voltammogram of a mesoporous Pt film (charge 6.27 mC, 500 µm in diameter) modified with Ge atoms in 1 M H_2SO_4 and (dashed black line) the successive cyclic voltammogram. The solid red line is a cyclic voltammogram of a mesoporous Pt film modified with Ge atoms recorded between - 0.65 and 0.15 V. A drop of 0.5 M GeO_2 + 1 M NaOH was put on the electrode. The electrode was then inserted in the solution while the potential was held at - 0.65 V vs. SMSE. CO was bubbled through the solution for 30 minutes then N_2 was sparged for 15 minutes. The scan rate was 50 mV s^{-1}.

Two peaks can be observed on the CO stripping cycle (solid black line), one at - 0.15 V defined as a pre-wave and the second one at 0.05 V defined as the main CO oxidation peak. The presence of the pre-wave with the mesoporous Pt electrode was previously attributed to the oxidation of CO adsorbed near the trough sites with OH_{ads}[28]. However, the current for the pre-wave herein is much higher than it was reported for the mesoporous Pt electrode as shown in Figure 4-9. The pre-wave is situated in the same range of potentials as for the oxidation of adsorbed Ge on Pt(100) wide terraces, which might contribute to the increase of the pre-wave current. Also, the oxidation of Ge adsorbed on the different Pt faces occurs at the same potential as CO oxidation on Pt. Nevertheless, the current peak for the CO oxidation is not increased but rather is decreased and the current for the two peaks are approximately equal which means that the adsorption of Ge causes the decrease of the charge under the CO peak.

The onset potential (~ - 0.5 V vs. SMSE) for CO oxidation at a mesoporous Pt electrode modified with Ge atoms occurs at lower potentials than the onset potential for the mesoporous Pt film. According to Watanabe *et al.*[19], the presence of Ge atoms on the platinum surface “reduced the overpotential for CO oxidation”.

The subsequent cycle shows two remaining peaks on the anodic scan at - 0.2 and 0.05 V vs. SMSE. As these peaks were not present when the experiment was performed with the unmodified mesoporous platinum film, they could be attributed to irreversibly adsorbed Ge adatoms on the platinum surface. The peak at - 0.2 V may represent irreversibly Ge atoms adsorbed on Pt(100) wide terraces. The second peak at 0.05 V might be due to the oxidation of adsorbed Ge atoms on the different low index Pt faces.In addition, the charges under the hydrogen desorption peaks for the cyclic voltammograms recorded before and after the CO stripping voltammogram were calculated. The results show a decrease of 25% in the charge under the peak after adsorption of germanium; these results concur with the presence of Ge adatoms on the Pt surface.

The CO stripping voltammograms of the mesoporous Pt unmodified and modified with Ge were plotted on the same graph to highlight the effect of Ge adsorption.

Figure 4-9 shows the CO stripping voltammogram of mesoporous Pt film modified with adsorbed Ge atoms. The dashed line corresponds to the CO stripping voltammogram of a mesoporous Pt film recorded right after the previous experiment. The dotted line is the CO stripping voltammogram of an unmodified mesoporous platinum electrode, it is the same as the voltammogram shown in Figure 4-3.

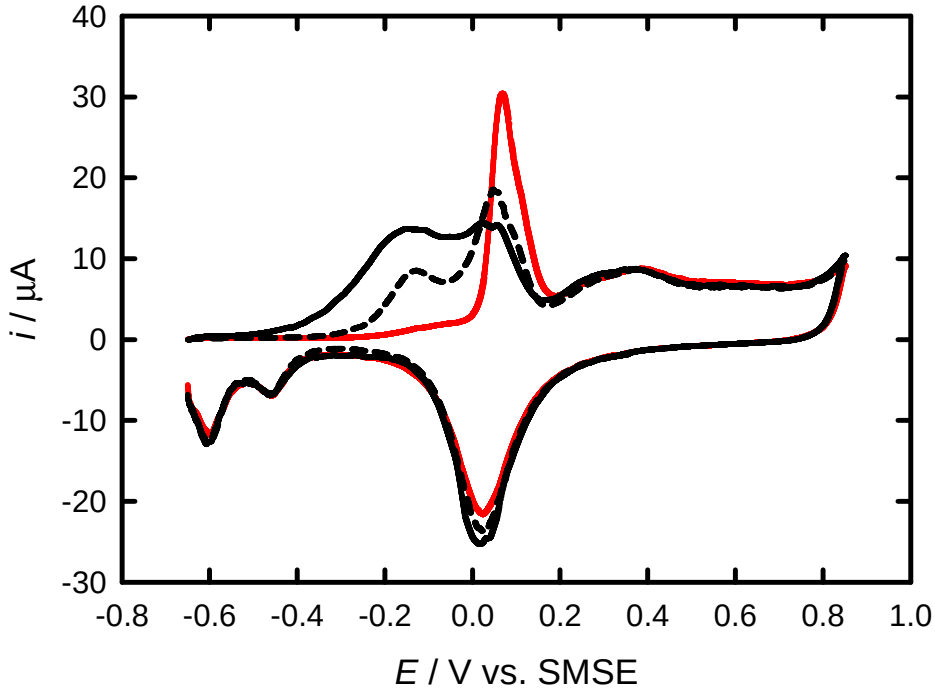

Figure 4-9. (solid black line) CO stripping voltammogram of a mesoporous Pt film (charge 6.27 mC, 500 µm in diameter) modified with Ge atoms in 1 M H_2SO_4. A drop of 0.5 M GeO_2 + 1 M NaOH was put on the electrode. The electrode was then inserted in the solution while the potential was held at - 0.65 V vs. SMSE. CO was bubbled through the solution for 30 minutes then N_2 was sparged for 15 minutes. (dashed black line) CO stripping voltammogram of a mesoporous Pt film which the surface was previously modified with Ge atoms but was not treated again for this experiment. (solid red line) CO stripping voltammogram of a mesoporous platinum film electrodeposited (charge 6.27 mC) on a polished platinum electrode in 1 M H_2SO_4. The scan rate was 50 mV s^{-1}.

The charges calculated for the CO stripping peaks are higher than expected; this is due to the contribution from simultaneous oxidation of adsorbed germanium.

After the record of the CO stripping voltammogram (solid black line) and the subsequent cycle (dashed black line) shown in Figure 4-8, the solution was bubbled with CO and purged with N_2 and another CO stripping voltammogram was recorded (dashed black line) shown in Figure 4-9. The same features appear on the second CO stripping voltammogram as on the first CO stripping cycle. The two peaks are still present however the current for the pre-wave decreases consistently and the current for the main CO peak increases; the onset potential for CO oxidation also increases. Nevertheless, the current for the pre-wave is still much higher than for the unmodified

mesoporous Pt film and the current for the main CO peak is still lower. This result suggests that a part of adsorbed Ge atoms was dissolved into the solution during the previous experiments. It also means that the platinum surface is still partly covered with Ge adatoms, which is confirmed by the subsequent cycle (dotted line) shown in Figure 4-8. The details of the subsequent cycle were described earlier in this Section and it was shown that Ge atoms occupy 25% of the Pt sites. Nevertheless, the current for the pre-wave is still large compared with the current recorded for the unmodified mesoporous platinum electrode. So it would signify that only a small amount of Ge could alter greatly the properties of CO adsorption on mesoporous platinum. The results in the present work are consistent with the results reported by Crabb and Ravikumar on carbon supported platinum modified with Ge adatoms[20].

4.5 Discussion

Adsorption of foreign atoms on the platinum surface is an excellent method to characterise the crystalline structure. Bismuth and germanium adsorb specifically on the platinum surface, and allow us to identify the different crystalline domains at the platinum surface. The H_1 mesoporous platinum is a polycrystalline electrode made up of low index platinum facets according to the stable cyclic voltammogram in sulphuric acid. The adsorption of bismuth has modified the surface of H_1 mesoporous platinum which is reflected on the cyclic voltammogram in sulphuric acid by a depression of the hydrogen peaks and the appearance of a new peak at 0.25 V vs. SMSE corresponding to the oxidation of Bi. In contrast, from the literature a peak at 0.61 V vs. RHE (- 0.03 V vs. SMSE) is observed in the voltammogram of single-crystal Pt(111) on which Bi adatoms are adsorbed[2, 30, 32]. This peak indicates the presence of large Pt(111) domains. This peak is absent in the voltammogram of the H_1 mesoporous Pt on Figure 4-2. This is consistent with the pore walls pictured as only a few atoms in width which could account for the absence of this peak.

CO stripping voltammetry shows differences because of the adsorption of Bi adatoms. The CO stripping on H_1 mesoporous Pt modified with Bi displays two separated peaks whereas under the same conditions the unmodified H_1 mesoporous Pt shows a pre-wave and two overlapping peaks. The two peaks on Figure 4-3 appeared at 0.01 and 0.25 V vs. SMSE corresponding to CO oxidation and Bi oxidation respectively. This

observation indicates the presence of a mixed CO/Bi adlayer on the H_1 mesoporous Pt surface within the pores. The potential of the main CO oxidation peak is slightly higher (0.01 V) than on the unmodified H_1 mesoporous platinum; a similar observation was reported previously by Hayden on Pt(110)-(1×2) surfaces and on carbon supported platinum catalysts[8]. Hayden assigned this effect to adsorbed Bi atoms on the platinum surface. In contrast, according to Herrero *et al.*, the CO onset potential for Pt(111) modified with Bi occurred at more negative (0.15 V) than for a clean Pt(111) electrode[30]; the presence of Bi on the platinum electrode shifted the CO onset potential towards more negative potential. Nevertheless, it appears that the presence of bismuth on the H_1 mesoporous Pt electrode does not ease oxygen transfer for CO oxidation, which can be explained by the fact that bismuth on H_1 mesoporous Pt oxidises at more positive potentials than CO.

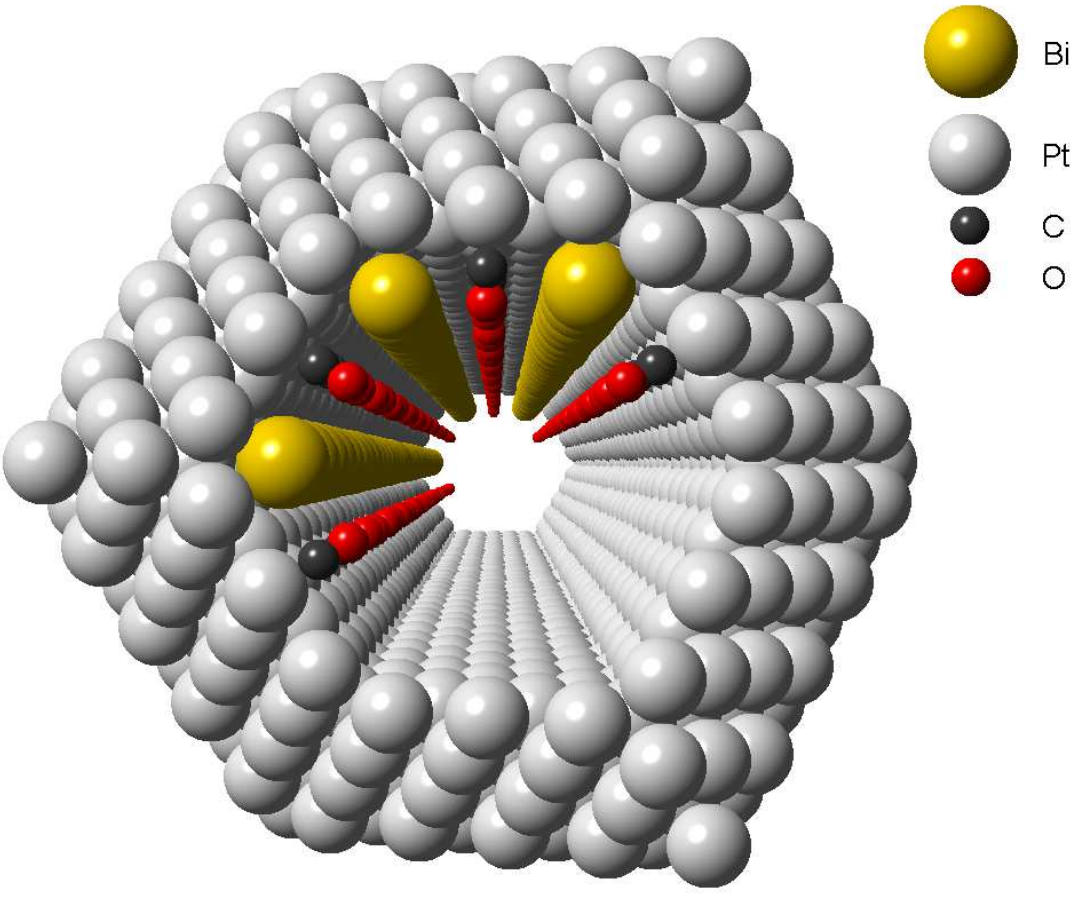

Figure 4-10. Drawing of an idealised structure looking down a single Pt pore, diameter 1.8 nm. The pore walls are shown as (111) surface. Bi adatoms are adsorbed on the trough sites and CO adsorbed on the middle of the pore wall is shown on atop sites on the top half of the pore.

Whereas a pre-wave for CO oxidation was present in the voltammogram of the H_1 mesoporous platinum electrode, the H_1 mesoporous platinum modified with Bi adatoms did not exhibit any pre-wave. From the model of a pore presented in Figure 3-15 in Chapter 3, the absence of the pre-wave can be accounted for if the Bi atoms are adsorbed on the trough sites or on the sites near the trough sites and hinder the adsorption of CO or oxygenated species on these sites. It is worth mentioning that, according to Lucas *et al.*, CO does not replace Bi on the surface[35]. Based on the same model as Figure 3-15 in Chapter 3, Figure 4-10 shows a schematic idealised representation of a single pore within the H_1 mesoporous Pt. The inner parts of the pore are represented by Pt(111) faces and the diameter of the pore is 1.8 nm corresponding to the $C_{12}EO_8$ templated film. On the top left half of the pore, CO molecules are adsorbed on the middle of the pore wall and Bi adatoms are adsorbed on the trough sites based on the side view of Pt(111) step sites blocked by Bi adatoms[36]. It was suggested that the ratio between bismuth atoms and CO adsorbed on the platinum surface is 1:1 to be consistent with the present model; the coverages of bismuth and CO are θ_{Bi} = 0.2 and θ_{CO} = 0.2 respectively for this model. It has been observed that Bi adsorbs preferentially on the step sites according to the studies on formic acid oxidation[14, 18, 37]. If this is the case, Bi adatoms adsorb primarily on the step trough sites and also block some neighbour terrace sites from adsorbing CO. According to the interpretation in Chapter 3, the pre-wave on the CO stripping finds its origin in the presence of step troughs inside the pores. If it is assumed that the step troughs are blocked by Bi adatoms, the pre-wave would not display on the voltammogram.

The adsorption of Ge atoms on H_1 mesoporous platinum surface can provide a good estimation of Pt(100) terrace sites[3, 4]. The voltammetry in 1 M H_2SO_4 shows a redox peak at - 0.2 V vs. SMSE which allows us to characterise the narrow Pt(100) terrace sites which is in good agreement with the model in Figure 3-15 in Chapter 3 representing a pore wall of 3-4 atom width.

The CO stripping voltammograms show interesting aspects such as the decrease of the current for the main CO peak and an increase for the pre-wave. The presence of Ge atoms has provoked an effect on the surface structure of the mesoporous Pt film where CO oxidation occurs at lower overpotentials. Such an effect on the activity of CO on platinum modified with Ge adatoms was reported previously in different studies[19, 20, 38].

According to Watanabe *et al.*, CO oxidation at low potentials comes about from the presence of oxygen on adatoms and the electrooxidation of CO occurs through this mechanism[19]

$$H_2O + M - Pt \longrightarrow O - M - Pt + 2H^+ + 2e^- \quad (2)$$

$$CO - Pt + O - M - Pt \longrightarrow CO_2 + M - Pt \quad (3)$$

where M corresponds to the metal adatom.

The onset potential of CO oxidation is related to reaction (2). The coverage of adatoms on platinum linked to the onset potential of CO oxidation also affects the surface reactions expressed in step (3), which is observed on Figure 4-9.

In the case of H_1 mesoporous Pt, the pore wall, made up of a few atoms, is considered as a terrace and the junction of two pore walls is considered as a trough step. Based on the study by Rodriguez *et al.*, the formation of an ordered Ge adlayer becomes difficult when the terraces are short[3]. Assuming that Ge atoms and CO molecules adsorb only on the pore wall, the trough sites are available for adsorbing oxygenated species such as OH_{ads} from water decomposition. In respect of equation (2), water oxidation provides oxygen to adsorb on the Ge atom. If it is believed that OH molecules are adsorbed on the trough sites, two contributions can be involved in the CO electrooxidation: on the one hand, from the reaction of adsorbed CO with the O adsorbed on Ge as in reaction (3) and on the other hand, from the oxidation of CO with OH as in a Langmuir-Hinshelwood mechanism[39, 40].

From the previous Chapter, the CO stripping for the unmodified H_1 mesoporous Pt shows a pre-wave which was assigned to the existence of the trough sites in the concave structure. Furthermore, the onset potential for the oxidation of Ge species occurs even before CO oxidation starts on H_1 mesoporous Pt. This early oxidation of Ge species can also result in an early oxidation of CO. These two processes can contribute to the current for the pre-wave in the CO stripping for a H_1 mesoporous Pt electrode modified with Ge adatoms as observed in Figure 4-8. The adsorption of Ge atoms on H_1 mesoporous Pt seems to facilitate oxygen transfer for CO oxidation, which can be accounted for by the early CO oxidation shown on the cyclic voltammogram.

4.6 Conclusion

Cyclic voltammetry in acid of the H_1 mesoporous Pt electrode demonstrates that the surface structure inside the pores is made up of low index Pt facets. However it is not possible to determine the true identity of the platinum sites by this method because the hydrogen adsorption/desorption occurs at the same potential range for the different surface sites. The adsorption of Bi and Ge atoms occurs on specific sites on the Pt surface and can be monitored by cyclic voltammetry in sulphuric acid. The adsorption of Ge and Bi adatoms on H_1 mesoporous Pt indicates respectively that the surface structure of platinum inside the pores is composed of 6 % of Pt(100) narrow terraces (i.e. the sites located on the pore walls) but does not contain Pt(111) large terraces. These results are consistent with the concave structure presenting a few atoms (3-4) wide terraces. In the case of the adatom Bi, the CO stripping voltammogram does not show any pre-wave which is attributed to the adsorption of Bi on the trough sites where two low coordinated faces meet and causes a reduction in CO tolerance. In contrast, the CO stripping voltammogram with the adsorption of Ge atoms has displayed a massive pre-wave which promotes greatly the electrooxidation of CO. This phenomenon is attributed to CO electrooxidation from two contributions: oxygen adsorbed on Ge and oxygen species, probably OH_{ads}, adsorbed on the trough sites. The particular adsorption of each of the atoms on H_1 mesoporous Pt can account for the features of the voltammetric response. The pre-wave feature in CO stripping voltammetry can be justified by the adsorption of oxygenated species in the trough sites; this explanation could be relevant to stepped platinum surfaces.

It can also be noted that the modification of the mesoporous Pt electrode with Ge adatoms have an effect on the electrocatalytic properties of the mesoporous Pt. In addition to the high surface area provided by the porous nanostructure, the enhancement of the electrocatalytic activity by the modification of the mesoporous Pt surface could be considerably advantageous in fuel cell applications.

4.7 References

[1] J. Clavilier, J. M. Orts, R. Gomez, J. M. Feliu, A. Aldaz *J. Electroanal. Chem.* **1996**, 404, 281-289.
[2] J. Clavilier, J. M. Feliu, A. Aldaz *J. Electroanal. Chem.* **1988**, 243, 419-433.
[3] P. Rodriguez, E. Herrero, J. Solla-Gullon, E. J. Vidal-Iglesias, A. Aldaz, J. M. Feliu *Electrochim. Acta*. **2005**, 50, 3111-3121.
[4] J. Solla-Gullon, P. Rodriguez, E. Herrero, A. Aldaz, J. M. Feliu *Phys. Chem. Chem. Phys.* **2008**, 10, 1359-1373.
[5] D. C. Godfrey, B. E. Hayden, A. J. Murray, R. Parsons, D. J. Pegg *Surf. Sci.* **1993**, 294, 33-42.
[6] R. Gomez, A. Fernandezvega, J. M. Feliu, A. Aldaz *J. Phys. Chem.* **1993**, 97, 4769-4776.
[7] S. Daniele, S. Bergamin *Electrochem. Commun.* **2007**, 9, 1388-1393.
[8] B. E. Hayden *Catal. Today*. **1997**, 38, 473-481.
[9] S. Daniele, D. Battistel, S. Bergamin, C. Bragato *Electroanalysis*. **2010**, 22, 1511-1518.
[10] M. Oana, R. Hoffmann, H. D. Abruna, F. J. DiSalvo *Surf. Sci.* **2005**, 574, 1-16.
[11] J. Y. Lee, P. Strasser, M. Eiswirth, G. Ertl *Electrochim. Acta*. **2001**, 47, 501-508.
[12] A. Lopez-Cudero, F. J. Vidal-Iglesias, J. Solla-Gullon, E. Herrero, A. Aldaz, J. M. Feliu *Phys. Chem. Chem. Phys.* **2009**, 11, 416-424.
[13] S. P. E. Smith, K. F. Ben-Dor, H. D. Abruna *Langmuir*. **2000**, 16, 787-794.
[14] M. D. Maciá, E. Herrero, J. M. Feliu, A. Aldaz *J. Electroanal. Chem.* **2001**, 500, 498-509.
[15] M. D. Maciá, E. Herrero, J. M. Feliu, A. Aldaz *Electrochem. Commun.* **1999**, 1, 87-89.
[16] M. D. Maciá, E. Herrero, J. M. Feliu *J. Electroanal. Chem.***2003**, 554-555, 25-34.
[17] M. D. Maciá, E. Herrero, J. M. Feliu *Electrochim. Acta*. **2002**, 47, 3653-3661.
[18] S. P. E. Smith, K. F. Ben-Dor, H. D. Abruña *Langmuir*. **1999**, 15, 7325-7332.
[19] M. Watanabe, M. Shibata, S. Motoo *J. Electroanal. Chem.***1985**, 187, 161-174.
[20] E. M. Crabb, M. K. Ravikumar *Electrochim. Acta*. **2001**, 46, 1033-1041.
[21] R. Gomez, M. J. Llorca, J. M. Feliu, A. Aldaz *J. Electroanal. Chem.* **1992**, 340, 349-355.
[22] J. Clavilier, K. Elachi, A. Rodes *Chem. Phys.* **1990**, 141, 1-14.
[23] J. Clavilier, D. Armand, S. G. Sun, M. Petit *J. Electroanal. Chem.* **1986**, 205, 267-277.
[24] S. Uhm, Y. Yun, Y. Tak, J. Lee *Electrochem. Commun.* **2005**, 7, 1375-1379.
[25] A. V. Tripkovic, K. D. Popovic, R. M. Stevanovic, R. Socha, A. Kowal *Electrochem. Commun.* **2006**, 8, 1492-1498.
[26] S. G. Sun, S. P. Chen, N. H. Li, G. Q. Lu, B. Z. Chen, F. C. Xu *Colloid Surf. A-Physicochem. Eng. Asp.* **1998**, 134, 207-220.
[27] R. Gomez, J. M. Feliu, A. Aldaz *Electrochim. Acta*. **1997**, 42, 1675-1683.
[28] T. F. Esterle, A. E. Russell, P. N. Bartlett *ChemPhysChem*. **2010**, 11, 2896-2905.
[29] S. C. Chang, M. J. Weaver *Surf. Sci.* **1991**, 241, 11-24.
[30] E. Herrero, J. M. Feliu, A. Aldaz *J. Catal.* **1995**, 152, 264-274.
[31] I. Villegas, X. P. Gao, M. J. Weaver *Electrochim. Acta*. **1995**, 40, 1267-1275.

[32] R. Carbo, R. Albalat, J. Claret, J. M. Feliu *J. Electroanal. Chem.* **1998**, 446, 79-89.
[33] E. Herrero, A. Rodes, J. M. Perez, J. M. Feliu, A. Aldaz *J. Electroanal. Chem.* **1995**, 393, 87-96.
[34] N. Furuya, S. Motoo *J. Electroanal. Chem.* **1979**, 99, 19-28.
[35] C. A. Lucas, N. M. Markovic, B. N. Grgur, P. N. Ross *Surf. Sci.* **2000**, 448, 65-76.
[36] P. Rodriguez, J. Solla-Gullon, F. J. Vidal-Iglesias, E. Herrero, A. Aldaz, J. M. Feliu *Anal. Chem.* **2005**, 77, 5317-5323.
[37] E. Herrero, V. Climent, J. M. Feliu *Electrochem. Commun.* **2000**, 2, 636-640.
[38] S. Motoo, M. Watanabe *J. Electroanal. Chem.* **1976**, 69, 429-431.
[39] S. Gilman *J. Phys. Chem*. **1964**, 68, 70-80.
[40] N. P. Lebedeva, M. T. M. Koper, J. M. Feliu, R. A. van Santen *J. Phys. Chem. B.* **2002**, 106, 12938-12947.

Chapter 5: Hydrogen peroxide

In the last Chapter, the adsorption of foreign atoms on H_1 mesoporous Pt was investigated to characterise the faceting inside the pores. This Chapter deals with the coupling between diffusion and surface reaction within the pores. Hydrogen peroxide oxidation is used as a model reaction to introduce a kinetic model accounting for the diffusion of hydrogen peroxide to the mesoporous film and then the binding to catalytic sites within the pores.

5.1 Overview

Mesoporous metal films electrodeposited from an hexagonal liquid crystalline phase have received much attention thanks to their potential applications. One of these applications concerns the detection of hydrogen peroxide over a wide range of concentrations[1]. Hydrogen peroxide is of interest in many fields, in industrial processes[2], for example in the food industry[3], as well as in waste water treatment[4]. In particular, many investigations have been undertaken for the detection of hydrogen peroxide with amperometric techniques in biosensing[5]. Therefore, it is important to monitor accurately the amounts of hydrogen peroxide, however the concentrations cover a wide range from micromolar *in vivo* conditions to millimolar for bleaching applications and even molar in the field of water treatment. The range of the concentration is limited to a given application.

However, measuring accurately the hydrogen peroxide concentration with amperometric techniques has been a difficult task since the reactions at the electrode are irreversible and the voltammograms are irreproducible for most electrode materials. Different electrode materials were used to monitor hydrogen peroxide concentration, for instance, carbon fibre[6], glassy carbon[7], platinum[8]. However, for a part of these electrodes, a lack of stability exists between the limiting current and the hydrogen peroxide concentration and the linearity of the measurement decays at high hydrogen peroxide concentrations. Although some electrodes have shown linear responses over a

range of concentrations between 1 and 20 mM, the amperometric responses remain unstable.

Solutions have been put forward to overcome the irreproducibility and instability of the responses such as the modification of the electrode surface with enzymes (horseradish peroxidise[9] and others[10, 11]) or Prussian Blue[12]. Enzyme based biosensors have shown a high sensitivity (1.5 A M^{-1} cm^{-2}) and detection at very low concentrations (10 nM)[13] nevertheless the upper limit of detection could not go beyond 12 mM[14]. The other disadvantage was the stability of the Prussian-Blue based sensor dropping down by repeated use[14].

The oxidation of hydrogen peroxide was studied on platinum and platinum/iridium electrodes and a decrease in the response for *i* vs. [H_2O_2] was observed above 1 mM which was attributed to the saturation of oxygen and hydrogen peroxide on the platinum sites[15]. The same conclusion was reached by Gorton who proposed a mechanism for hydrogen peroxide oxidation on high surface palladium electrodes[16]. Supporting a similar approach, Johnston *et al.* proposed a surface binding site model for the hydrogen peroxide oxidation on palladium assuming that the reaction process obeys a form of Michaelis-Menten kinetics[17]. An identical surface binding site model was then adapted by Hall *et al.* for hydrogen peroxide oxidation on Pt electrodes[18-22]. The mechanism of hydrogen peroxide reaction at platinum electrodes could offer an excellent justification for the lack of linearity observed in the current response. According to a series of papers from Hall *et al.*[18-22], the current response due to hydrogen peroxide oxidation is under mixed kinetic and diffusion control and the mechanism can be explained using a form of Michaelis-Menten kinetics. Nevertheless, two inhibiting side reactions can prevent hydrogen peroxide oxidation from proceeding. The first reaction is the adsorption of oxygen on the Pt surface sites and the second is the protonation of the surface Pt(II)/H_2O_2 complex[18]. The availability of Pt sites is a limiting factor in the reaction and thus causes a discrepancy in the current response at higher hydrogen peroxide concentrations.

Microdiscs are useful to measure the concentration of an analyte since the limiting current is proportional to the concentration. However, the use of microelectrodes did not succeed to amperometrically measure hydrogen peroxide concentrations. The reaction

appears to be kinetically limited by the small surface area. The solution to overcome this issue was to increase the electroactive surface area whilst maintaining the diffusion properties of the microelectrodes.

The deposition of a mesoporous platinum film from the hexagonal lyotropic liquid crystalline template onto a microelectrode has been reported by Elliott *et al.*[23]. The mesoporous film on the microelectrode provides a high surface area and forms a "mesoporous microelectrode". Hydrogen peroxide detection has already been investigated using H_1 mesoporous Pt films electrodeposited on platinum microelectrodes[1]. The steady-state response was found to be stable and linear over a wide range of concentrations.

In another paper on hydrogen peroxide detection using the same method, a H_1 mesoporous Pt film was also used to fabricate a glutamate microsensor[24]. This latter study also emphasises the improvement in the hydrogen peroxide detection thanks to the properties of the high surface area of the mesoporous platinum film[1]. A similar approach was adopted in this Chapter although mesoporous rhodium films were used. Rhodium was chosen over platinum since hydrogen peroxide can oxidise at lower overpotentials and this could be advantageous to avoid interferences from other species such as ascorbic acid. A surface binding model was adapted from Hall *et al.* for the oxidation of hydrogen peroxide on rhodium electrodes[18]. The mechanism for hydrogen peroxide reaction will be elaborated for mesoporous rhodium from Hall's mechanism. The mesoporous rhodium films produce reproducible current responses to hydrogen peroxide oxidation at pH 7. In this Chapter, a study of the oxidation of hydrogen peroxide on H_1 mesoporous Rh electrodes is presented and a detailed analysis of the kinetics for the reaction is described.

5.2 Preparation and characterisation of electrodes

5.2.1 Electrodeposition of mesoporous metal films

Platinum microdiscs were made by sealing platinum wires of the appropriate diameter into glass and were polished with a slurry of 0.3 alumina to obtain a fine mirror finish on a Buehler microcloth. The microelectrodes were then cleaned by cycling in sulphuric acid.

The polished platinum disc microelectrodes were modified by the electrodeposition of a mesoporous platinum or rhodium film. A plating mixture was prepared from an aqueous solution containing the appropriate metal salt and a non-ionic surfactant.

The preparation of the plating mixtures with platinum and rhodium were respectively:

- 42 wt.% $C_{12}EO_8$, 29 wt.% H_2PtCl_6 and 29 wt.% deionised water.
- 47 wt.% $C_{12}EO_8$, 12 wt.% $RhCl_3$, 39 wt.% deionised water and 2 wt.% n-heptane (heptane was added to the composition to obtain the hexagonal phase as reported by Bartlett and Marwan in their work using $C_{16}EO_8$ as the surfactant[25]).

The potential was held at - 0.1 and - 0.2 V vs. SMSE for the electrodeposition of platinum and rhodium films respectively until the required charge had been passed. The potentials for each metal were reported to be under ideal conditions for the deposition[25, 26]. Then the electrode was soaked in iso-propanol and then in water overnight to remove the plating mixture from the electrode surface. The resulting metal film is then the inverse of the hexagonal template.

Cyclic voltammetry was then performed to remove the residual plating mixture from the pores until a stable cyclic voltammogram was obtained on cycling between - 0.65 and 0.85 V vs. SMSE at 200 mV s^{-1} in 1 M sulphuric acid. The electrodes were then kept in deionised water at room temperature.

The cyclic voltammograms for the H_1 mesoporous Pt microelectrode and for the polished Pt microelectrode were similar to those recorded for the electrode in Chapter 3. The full description of the cyclic voltammogram was given in Chapter 3 in Section 3.2.2.

The active surface areas were calculated from the hydrogen desorption region using the method described in Chapter 3 in Section 3.2.2. The surface areas of the polished platinum electrode and the mesoporous platinum film were 0.0049 cm^2 and 0.181 cm^2 respectively using the conversion factor 210 µC cm^{-2}[27]. These values correspond to a

roughness factor of 86 for a H_1 mesoporous Pt microelectrode compared to 2.5 for a polished Pt microelectrode.

5.2.2 Characterisation of mesoporous rhodium films by voltammetry in acid

Figure 5-1 shows the cyclic voltammogram of a H_1 mesoporous Rh microelectrode in 1 M sulphuric acid.

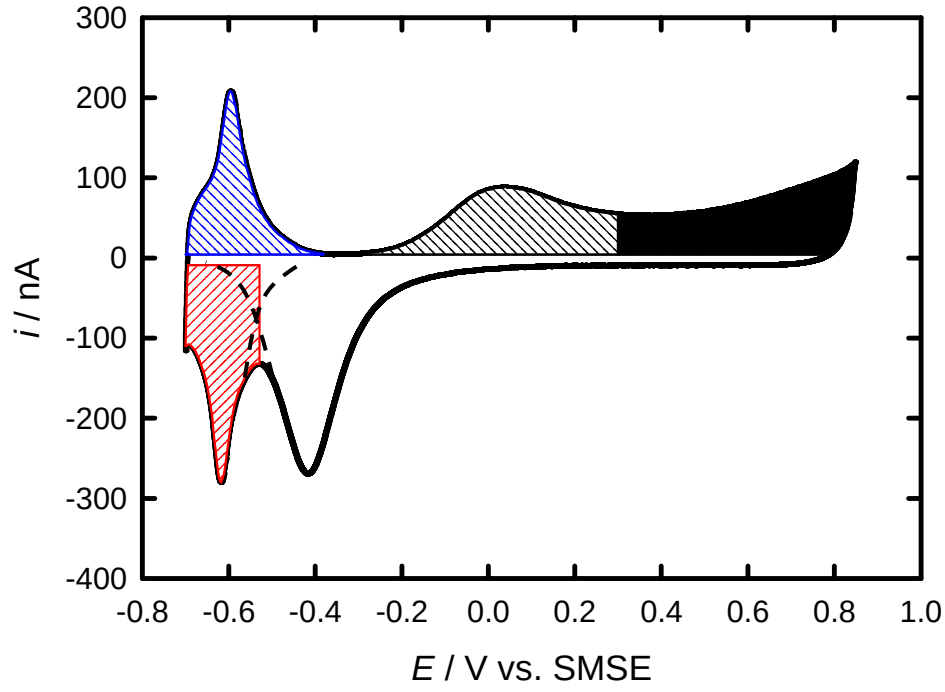

Figure 5-1. Cyclic voltammogram of a H_1 mesoporous Rh film electrodeposited onto a platinum disc microelectrode (25 µm in diameter, 8.68 µC for the deposition charge) in 1 M sulphuric acid recorded at 50 mV s^{-1}. The solution was deaerated by purging with argon for at least 20 min prior to the measurements. The crossed blue area corresponds to hydrogen desorption and the red area correspond to hydrogen adsorption and a part of the oxide stripping peak. The dashed lines correspond to the continuity of the peaks and give rise to the peak overlapping. The grey area corresponds to the formation of Rh(OH) and the black area corresponds to the formation of $Rh(OH)_3$. These assignments come from Jerkiewicz *et al.*[28, 29]

The characteristics of the cyclic voltammogram for H_1 mesoporous Rh in sulphuric acid are the same as those of polycrystalline rhodium[28]. According to Jerkiewicz *et al.*[28, 29], different oxide films on Rh grow with increasing potential on the anodic sweep. The first oxide formation on Rh starts at - 0.2 V vs. SMSE and involves the electrochemisorption of one monolayer of OH resulting in the formation of Rh(OH)

species. At about 0.3 V vs. SMSE, this leads to further oxidation and the formation of $Rh(OH)_3$ species. Based on a study by Peuckert, X-ray Photoelectron Spectroscopy (XPS) measurements coupled with cyclic voltammetry identified the existence of these oxide species on the Rh surface[30]. Simultaneously with the electrosorption of OH on the rhodium surface, a place exchange occurs between rhodium atoms and the adsorbed OH^- species leading to a reorganisation of the rhodium superficial layer[31]. A similar behaviour was observed for Pt and oxygen-containing anions[31].

If the potential increases further, another oxide, RhO(OH) could form. It has been considered that the species RhO(OH) has not been formed up to the chosen anodic potential limit. It is thought only $Rh(OH)_3$ oxide formation occurs because only one stripping oxide peak appeared in the cyclic voltammogram[28, 29].

Oxide formation of rhodium has been discussed involving other oxide species like Rh_2O_3[31], but only the case of $Rh(OH)_3$ formation has been retained in this work. Based on Jerkiewicz *et al.*[29], the oxide formation proceeds according to the following scheme in the range of potential used:

Formation

$$Rh + H_2O \longrightarrow Rh(OH) + H^+ + e^- : [-0.2 \text{ to } 0.3] \text{ V vs. SMSE} \quad (1)$$

$$Rh(OH) + 2H_2O \longrightarrow Rh(OH)_3 + 2H^+ + 2e^- : [0.3 \text{ to } 0.85] \quad (2)$$

$$2Rh(OH)_3 + Rh \longrightarrow 3RhO(OH) + 3H^+ + 3e^- : > 0.85 \quad (3)$$

Reduction

$$3RhO(OH) + 3H^+ + 3e^- \longrightarrow 2Rh(OH)_3 + Rh \quad (4)$$

$$Rh(OH)_3 + 3H^+ + 3e^- \longrightarrow Rh + 3H_2O : [0 \text{ to } -0.52] \quad (5)$$

It is assumed that the anodic scan limit (0.85 V vs. SMSE) is low enough to prevent the formation of the oxide RhO(OH). In the cyclic voltammogram from Figure 5-1, the oxide formation proceeds in two steps (1) and (2) whereas the oxide reduction occurs in one step (4). If the potential range had been increased towards more anodic potentials,

the oxide formation would have proceeded in three steps and the oxide reduction in two steps.

In the potential range - 0.4 and - 0.7 V, a single peak at - 0.6 V vs. SMSE is clearly observed on the anodic sweep corresponding to hydrogen desorption. This peak is mirrored on the cathodic sweep by the hydrogen adsorption. The hydrogen peaks for the H_1 mesoporous Rh film are similar to those reported for polycrystalline Rh electrodes. The surface area of rhodium electrodes can be calculated from the area of the oxide formation peaks by using a conversion factor of 660 $\mu C\ cm^{-2}$ or from the area under the hydrogen desorption peak using a conversion factor of 221 $\mu C\ cm^{-2}$[28]. The conversion factor of 660 $\mu C\ cm^{-2}$ corresponds to the experimental conditions in which the scan rate was 50 $mV\ s^{-1}$, the electrolyte was 0.5 M H_2SO_4 and the anodic potential limit was 1.3 V vs. NHE[28]. Calculating the surface area from the hydrogen adsorption peak or the oxide stripping peak can prove to be difficult since both peaks overlap. The charge under these peaks can be approximated by estimating the rest of the curve; nevertheless, details such as the shape of the curve at the base of the peak affect the estimation. For this reason, the surface area was calculated from the hydrogen desorption peak by subtracting off the double layer capacitance since no other contribution from other surface reaction is observed in this potential window for the anodic current. The roughness factor calculated from the hydrogen desorption peak is 380±50.

5.2.3 SEM image

Figure 5-2 shows an SEM image of a H_1 mesoporous rhodium film electrodeposited onto a platinum microelectrode.

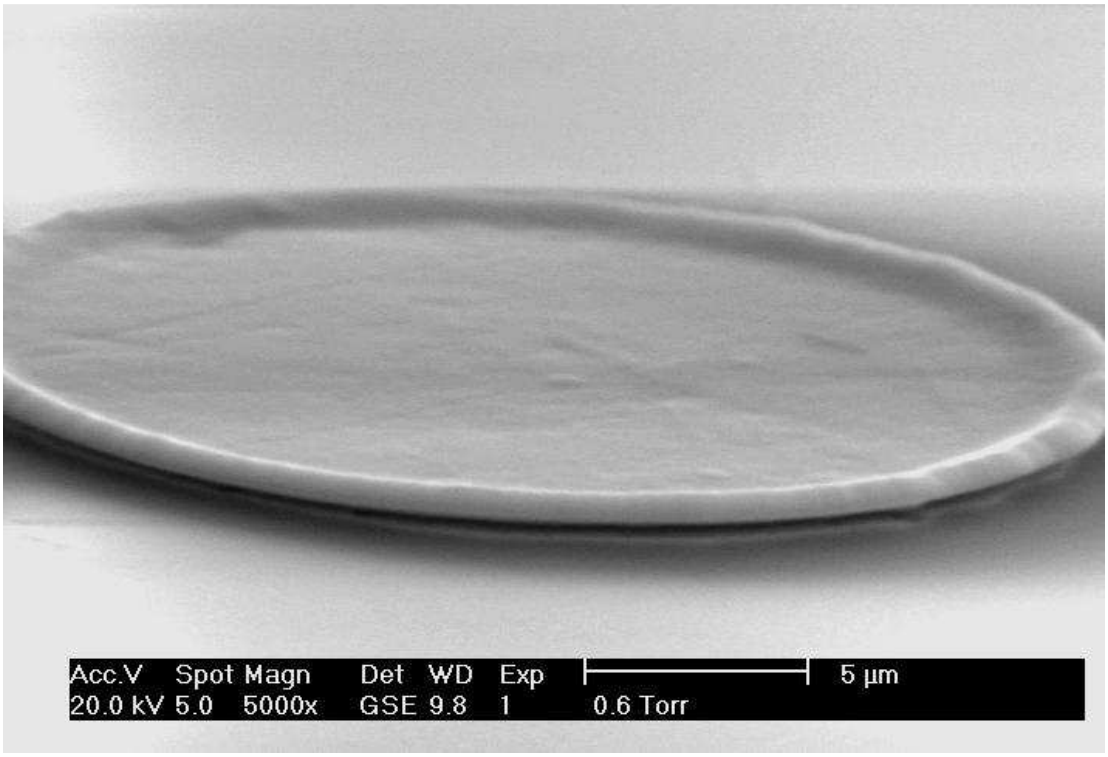

Figure 5-2. Scanning electron microscope image of a H_1 mesoporous Rh film electrodeposited on a platinum disc microelectrode (25 µm in diameter, 8.64 µC for the deposition charge) from a mixture of 12 wt% $RhCl_3$, 47 wt% $C_{12}EO_8$, 39 wt% water and 2 wt% heptane at - 0.2 V vs. SCE. The image was obtained at a tilt angle of 70°.

The film covers the whole surface of the platinum microelectrode. The film is smooth and uniform except that it looks lifted at the edge due to a higher rate of diffusion at the rim of the microdisc.

5.2.4 TEM image

Figure 5-3 shows a TEM image of a mesoporous rhodium particle taken from the mesoporous rhodium film by scraping off the surface of the film.

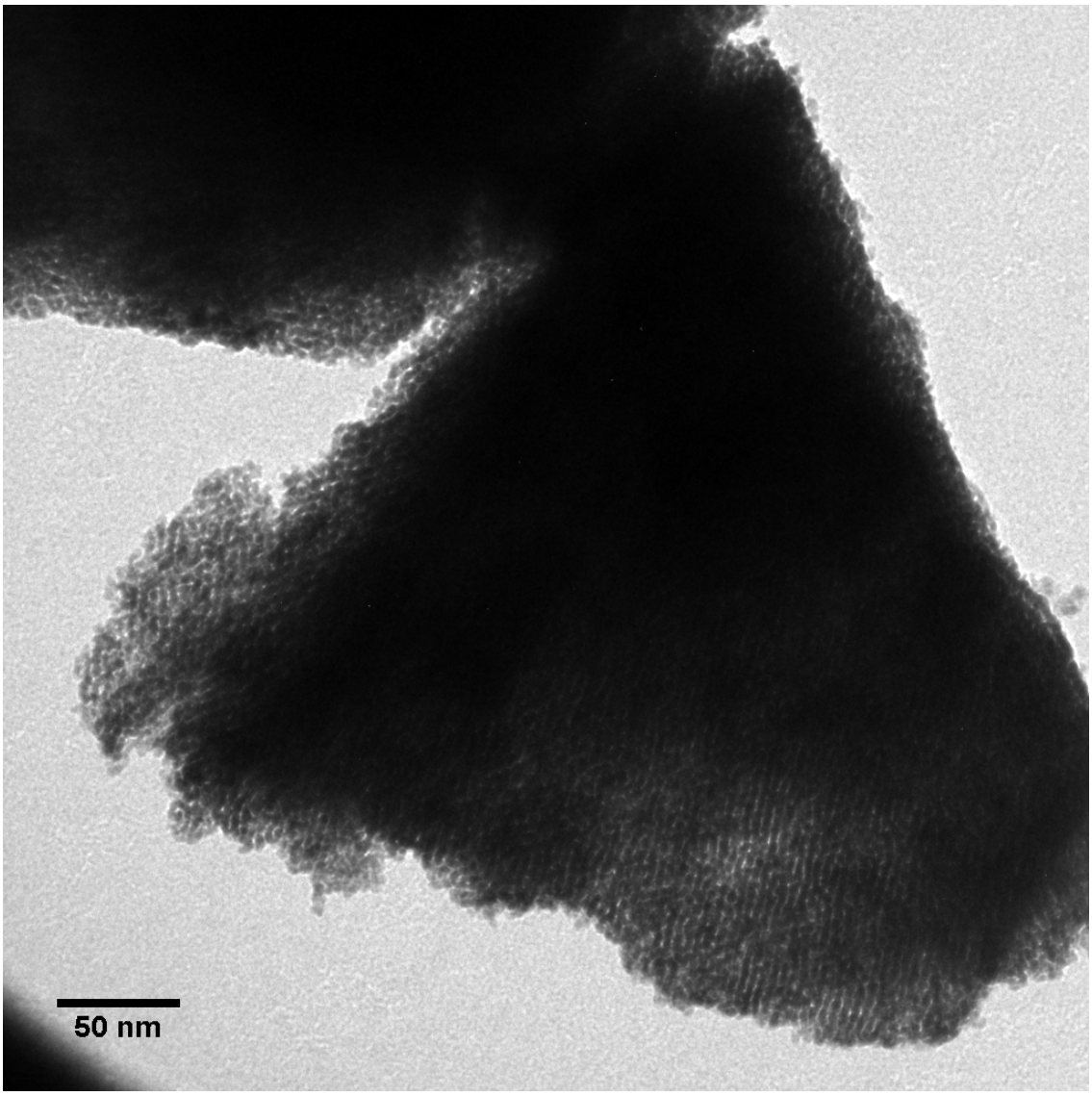

Figure 5-3. TEM image of a H_1 mesoporous Rh sample electrodeposited on a gold coated glass slide from a mixture of 12 wt% $RhCl_3$, 47 wt% $C_{12}EO_8$, 39 wt% water and 2 wt% heptane at - 0.2 V vs. SCE.

Pores can be observed on the edge of the particle since it is the thinnest part. Rows of pores are observed running through the metal and arranged into a hexagonal array. The film consists of a porous structure. Based on the observation of the TEM micrograph, the pore size was evaluated as 45 ± 2 Å with a wall thickness of 20 Å. These values are similar to those reported for earlier works on mesoporous Rh and also on other mesoporous metals electrodeposited from the hexagonal lyotropic liquid crystalline phase using $C_{12}EO_8$ and heptane.

5.2.5 Small-Angle XRD

Figure 5-4 shows a low angle XRD pattern of a H_1 mesoporous Rh film electrodeposited onto a gold substrate.

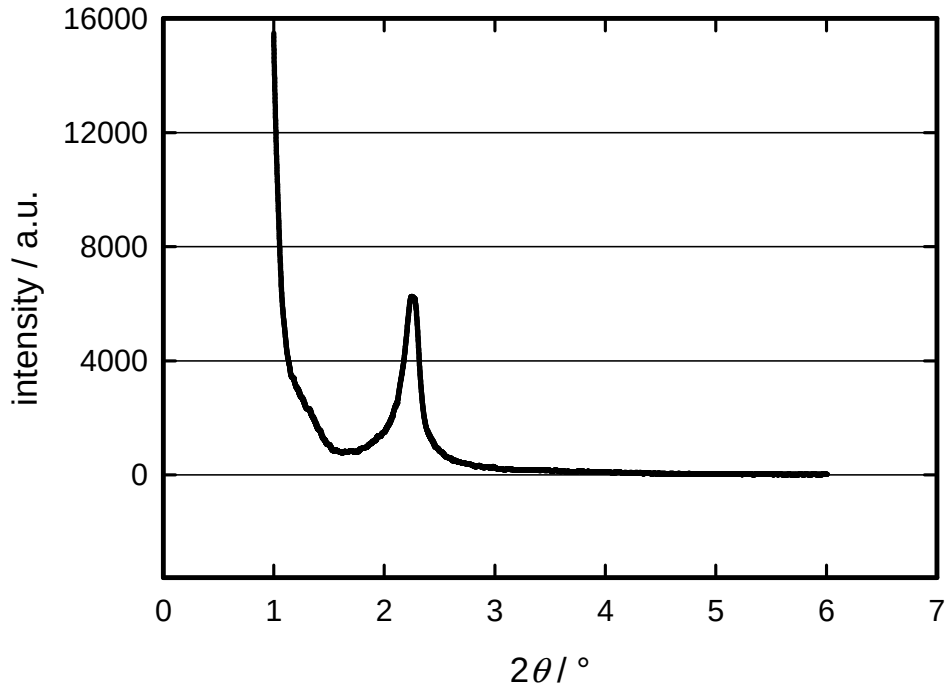

Figure 5-4. Small-angle X-ray diffraction pattern obtained using a Cu Kα radiation of a H_1 mesoporous Rh film electrodeposited on a gold coated glass slide from a mixture of 12 wt% $RhCl_3$, 47 wt% $C_{12}EO_8$, 39 wt% water and 2 wt% heptane at - 0.2 V vs. SCE.

A well resolved peak is observed on the X-ray diffraction pattern confirming the formation of a regular nanostructured film. The peak corresponds to the (100) lattice. The analysis of the peak demonstrates a pore size of 4 ± 1 nm. The periodicity of the lattice of the pore-to-pore distance was calculating by the d-spacing. This value is consistent with the value measured by TEM.

In Section 5.2, characterisation of the rhodium electrode was reviewed by cyclic voltammetry, TEM and small angle X-ray diffraction. Electrodeposition of mesoporous metals on microelectrodes through the hexagonal lyotropic liquid crystalline phase was successful. Evidence of a regular hexagonal array of pores running through the rhodium film was provided by TEM and small angle X-ray diffraction. The procedure to calculate the surface area is significant in this work to estimate the film thickness which

will be an important parameter for the kinetic study in Section 5.4. It was also necessary to identify the different rhodium oxide species involved in the cyclic voltammogram in acid to understand the surface chemistry of hydrogen peroxide on the rhodium electrode surface.

5.3 Hydrogen peroxide electrochemistry

5.3.1 Voltammetry in hydrogen peroxide

Figure 5-5 shows the cyclic voltammograms of a H_1 mesoporous Pt microelectrode and a polished Pt microdisc in 5 mM hydrogen peroxide in 0.1 M phosphate buffer (pH = 7) between - 0.7 and 0.4 V vs. SMSE at 2 mV s^{-1}.

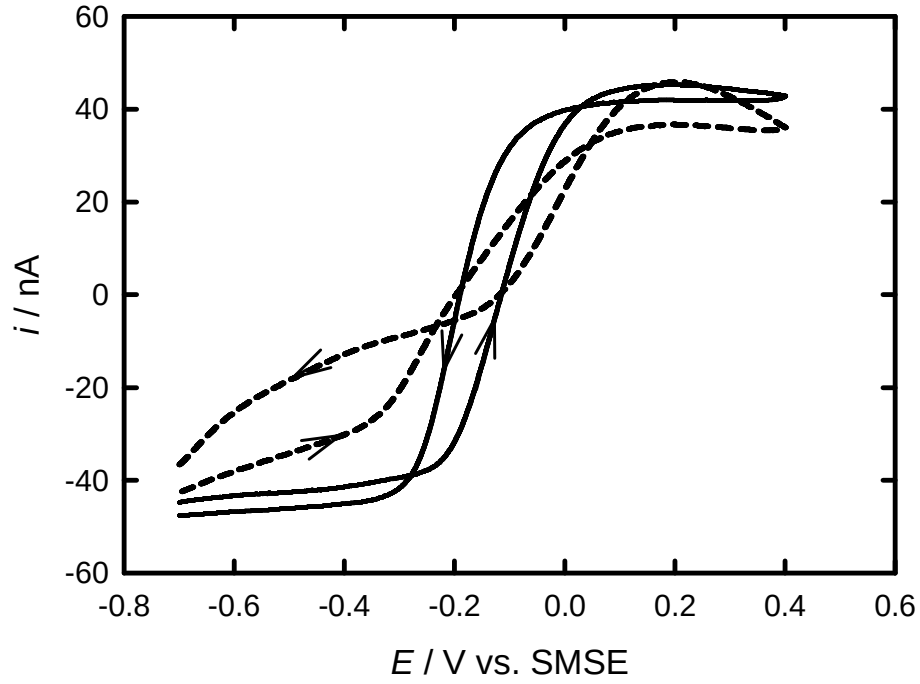

Figure 5-5. Cyclic voltammograms of a H_1 mesoporous Pt film electrodeposited onto a platinum disc microelectrode (15.7 µC for the deposition charge) (solid line) and a polished polycrystalline Pt microelectrode (dashed line) (both 25 µm in diameter) in 5mM H_2O_2 in 0.1 M phosphate buffer (pH =7) recorded at 2 mV s^{-1}. The solution was deaerated by purging with argon for at least 20 min prior to the measurements.

The decomposition of hydrogen peroxide at platinum electrodes at zero current is a chemical process. When the current is not null, it stems from the oxidation or the reduction of the metal surface and possibly of their combination. Indeed, two electrochemical reactions are involved:

$$H_2O_2 \longrightarrow 2e^- + O_2 + 2H^+ \quad (6)$$

$$H_2O_2 + 2H^+ + 2e^- \longrightarrow 2H_2O \quad (7)$$

When the current is zero (E = - 0.2 V vs. SMSE) the two processes proceed at equal and opposite rates. When the potential is scanned to more positive potentials than - 0.2 V, reaction (6) is preponderant and when the potential is scanned to more negative potentials reaction (7) becomes preponderant (the value of the potential, - 0.2 V, depends on the pH of the solution).

The cyclic voltammogram for the unmodified platinum microelectrode does not show well defined plateaux. The poor shape and low currents exhibited on the cyclic voltammogram lead to the conclusion that the oxidation and reduction of platinum involving a place exchange process between the platinum atoms and the oxide species diminishes the catalytic activity of the electrode surface towards hydrogen peroxide decomposition. The cyclic voltammogram for the H_1 mesoporous Pt microelectrode exhibited well defined plateaux indicating that high surface area of the mesoporous electrode increases the catalytic activity for hydrogen peroxide decomposition and hence, steady state responses can be obtained for both processes, oxidation and reduction of hydrogen peroxide. The number of binding sites of the mesoporous electrode has increased and therefore the current response changes from mixed kinetic/diffusion control to a diffusion limited response. In steady-state conditions, the mass transport limiting current for a microdisc electrode is given by the expression in equation (8):

$$i_L = 4nFDca \quad (8)$$

With n, the number of electrons involved in the reaction,
F, the constant of Faraday,
c, the concentration of the species,
D, the diffusion coefficient
and a, the radius of the microdisc.

The concentration of hydrogen peroxide is thus related to the measured current in the plateau region for the H_1 mesoporous Pt microelectrode, which is useful for analytical applications.

5.3.2 Oxidation of Hydrogen Peroxide

It is important to note that the cathodic and anodic sweeps cross over at the potentials 0.02 and - 0.29 V vs. SMSE. The reason of this can be accounted for by the mechanism for hydrogen peroxide reaction at platinum presented by Hall *et al.* in their series of papers[18-22]. They introduced a mechanism for the electrochemical oxidation of hydrogen peroxide on platinum, which was similar to that on palladium[16]:

$$H_2O_{2(bulk)} \longrightarrow H_2O_{2(surface)} \quad (9)$$

$$H_2O_2 + Pt(OH)_2 \rightleftharpoons Pt(OH)_2.H_2O_2 \quad (10)$$

$$Pt(OH)_2.H_2O_2 \longrightarrow Pt + 2H_2O + O_2 \quad (11)$$

$$Pt + 2H_2O \longrightarrow Pt(OH)_2 + 2H^+ + 2e^- \quad (12)$$

The reaction of hydrogen peroxide is dependent on the oxidation state of platinum. On the one hand, if the platinum surface is oxidized ($Pt(OH)_2$), the surface is more conducive to hydrogen peroxide oxidation; on the other hand, if the platinum surface is unoxidized (Pt(0)), the surface is more conducive to hydrogen peroxide reduction. For potentials positive of - 0.3 V vs. SMSE (see Figure 5-6), the oxidized platinum surface, $Pt(OH)_2$, is formed and the "place exchange" occurs[32]. Thus the exchange of atoms at the electrode surface could account for the delay of the oxide stripping on the cathodic scan. This could result in continued hydrogen peroxide oxidation at a lower overpotential on the cathodic sweep and that is why the anodic and cathodic sweeps cross over each other.

5.3.3 Characterisation in phosphate buffer

The H_1 mesoporous Pt microelectrode was then examined in phosphate buffer over the same potential window as in hydrogen peroxide to observe the potential of oxidation and reduction of platinum. Figure 5-6 shows the cyclic voltammogram of a H_1 mesoporous Pt microelectrode in 0.1 M sodium phosphate buffer.

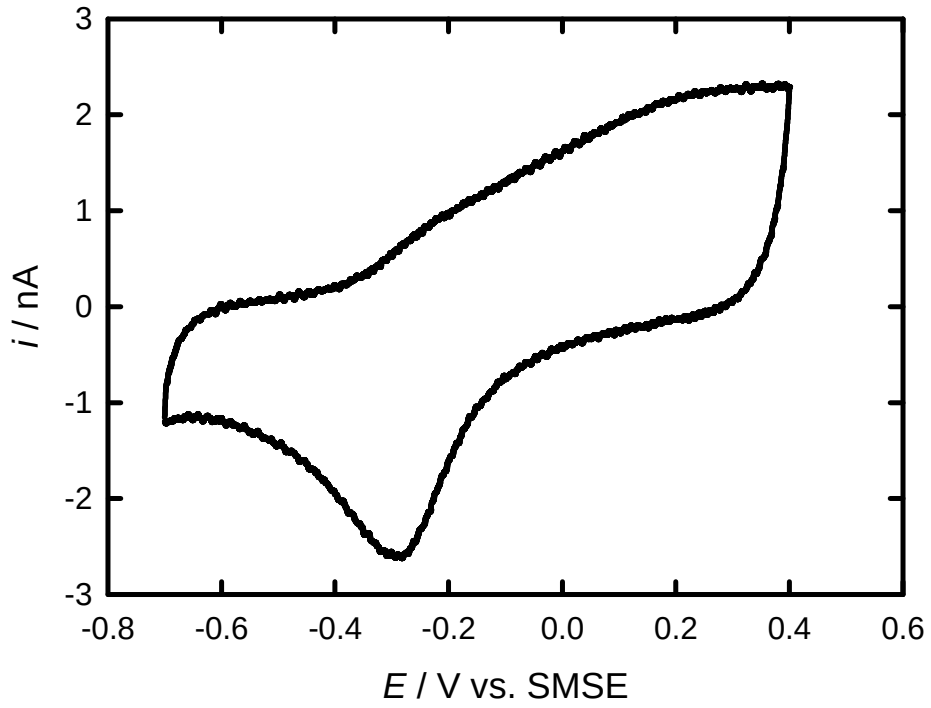

Figure 5-6. Cyclic voltammogram of a H_1 mesoporous Pt film electrodeposited onto a platinum disc microelectrode (25 µm in diameter, 15.7 µC for the deposition charge) in 0.1 M phosphate buffer (pH =7) recorded at 2 mV s^{-1}. The solution was deaerated by purging with argon for at least 20 min prior to the measurements.

It can be seen that the oxide formation and the oxide stripping occur in the same potential window as the oxidation and the reduction of hydrogen peroxide respectively. The delay of the oxide stripping in phosphate buffer results in a delay for the reduction of hydrogen peroxide, which accounts for the cross over on the voltammogram in phosphate buffer containing hydrogen peroxide.

These conclusions arise from previous studies by Hall *et al.*[18-22] and Evans *et al.*[1]. The high surface area of the H_1 mesoporous Pt film electrodeposited onto the Pt microelectrode improved the quality of the voltammogram in hydrogen peroxide. A mechanism described by Hall *et al*. accounts for the oxidation of hydrogen peroxide at platinum electrodes. In this work, these observations will be useful for a similar demonstration on rhodium electrodes. The rhodium electrode was used for the study of hydrogen peroxide oxidation since the oxide stripping occurs at less negative potentials than the platinum electrode avoiding any interference with other species.

5.3.4 Cyclic voltammetry of mesoporous rhodium in phosphate buffer

For a better understanding in the discussion, we discuss the cyclic voltammetry of rhodium in phosphate buffer before going on to the analysis of the hydrogen peroxide reaction. Figure 5-7 shows a cyclic voltammogram for a H_1 mesoporous Rh microelectrode in phosphate buffer scanned between - 1 and 0.4 V vs. SMSE.

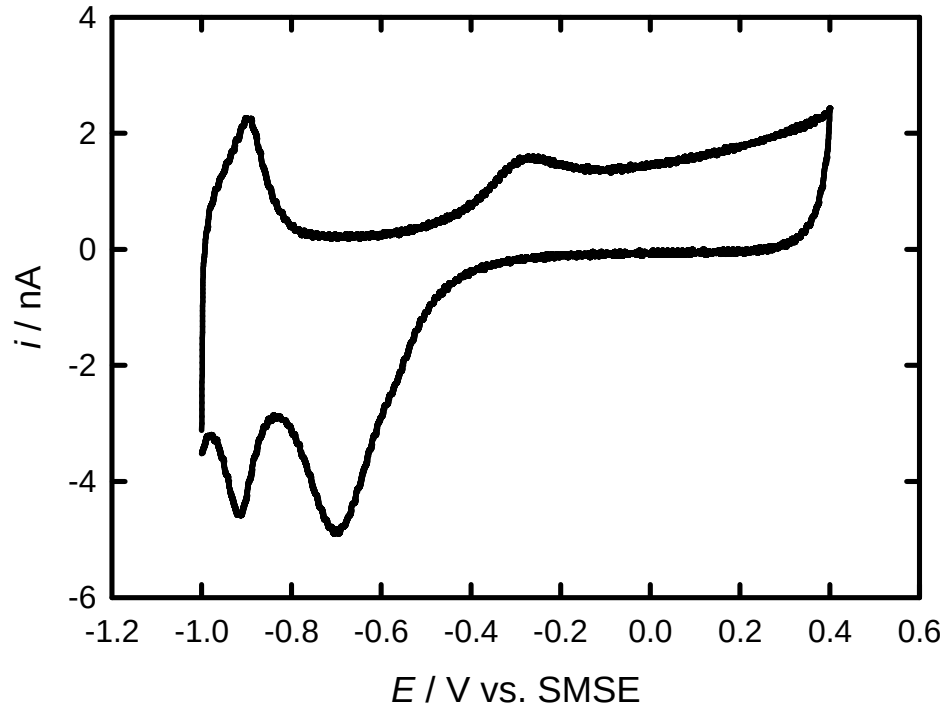

Figure 5-7. Cyclic voltammogram of a H_1 mesoporous Rh film electrodeposited onto a platinum disc microelectrode (25 µm in diameter, 8.68 µC for the deposition charge) in 0.1 M phosphate buffer (pH =7) recorded at 2 mV s^{-1}. The solution was deaerated by purging with argon for at least 20 min prior to the measurements.

The features on the cyclic voltammogram are similar to those recorded in sulphuric acid and this cyclic voltammogram can be compared with that recorded in sulphuric acid. The data of the cyclic voltammogram in phosphate buffer were multiplied by 50 to match the currents in the double layer and shifted by 0.3 V in order to overlay both voltammograms in sulphuric acid and phosphate buffer on the same graph as shown in Figure 5-8. It can be noticed that the current is low in 0.1 M phosphate buffer at pH 7 though a larger current could be expected due to the large surface area.

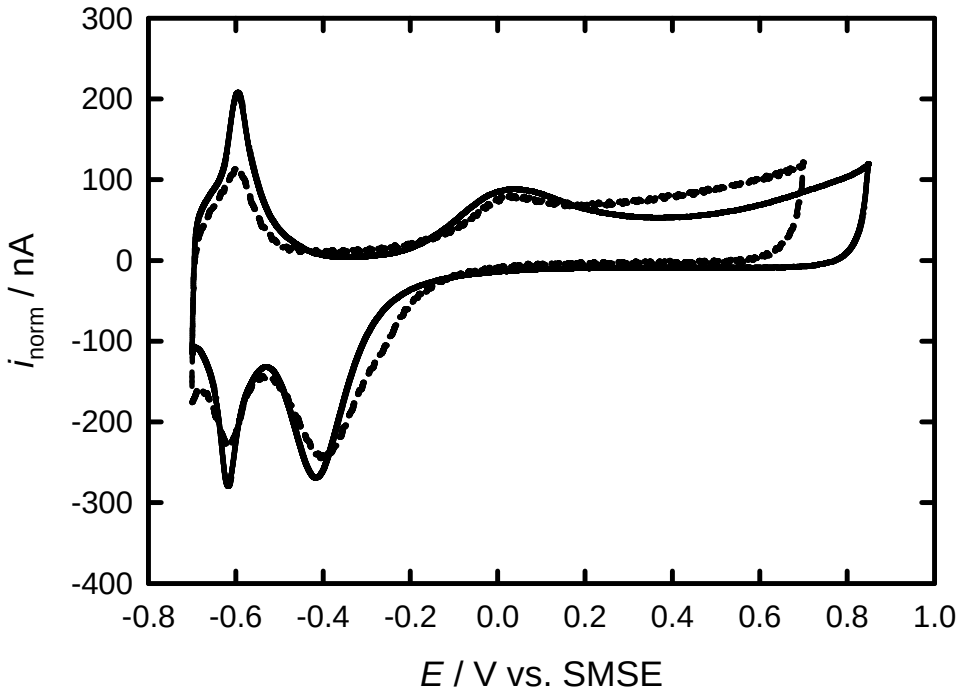

Figure 5-8. Cyclic voltammograms of a H_1 mesoporous Rh film electrodeposited onto a platinum disc microelectrode (25 µm in diameter, 8.68 µC for the deposition charge) (solid line) in 1 M sulphuric acid at 200 mV s^{-1} and (dashed line) in 0.1 M phosphate buffer (pH =7) at 2 mV s^{-1}. The data for the cyclic voltammogram in phosphate buffer were multiplied by 50 to match the values of the double layer charging (potential window: -0.5 to -0.3 V) and shifted by 0.3 V. The solution was deaerated by purging with argon for at least 20 min prior to the measurements.

The shift of potential with pH depends on the numbers of H^+ and e^- involved in the reaction. Thermodynamically, a shift of 59 mV per pH unit is expected for a n H^+/n e^- reaction whatever the value of n. For a 1 M sulphuric acid solution, the pH is about 0 and the pH for the sodium phosphate buffer is 7. Therefore, a potential shift of ~ 420 mV should be expected implying that the activity of protons a_{H+} is equivalent to $[H^+]$; however, 1 M sulphuric acid might not be an ideal activity. Instead, only a shift of 300 mV is observed to fit both voltammograms. Besides, this can be also explained by a local pH change within the pores, which is consistent with broader peaks even though the scan rate is much slower.

According to a similar shape (both peak positions and peak heights) of the cyclic voltammograms on Figure 5-8, it is assumed that the oxides formed in the phosphate buffer solution at the rhodium surface are identical to those involved in sulphuric acid. If an analogyin the oxide rhodium formation exists in sulphuric acid and in phosphate

buffer, the same evolution of oxide rhodium species ($Rh(OH) \longrightarrow Rh(OH)_3$) should occur.

5.3.5 Voltammetry of Mesoporous Rhodium Film in Hydrogen Peroxide

Figure 5-9 shows the cyclic voltammogram in 5 mM peroxide hydrogen with 0.1 M sodium phosphate buffer for a H_1 mesoporous Rh microelectrode. The cyclic voltammogram was scanned between - 1 and 0.4 V vs. SMSE.

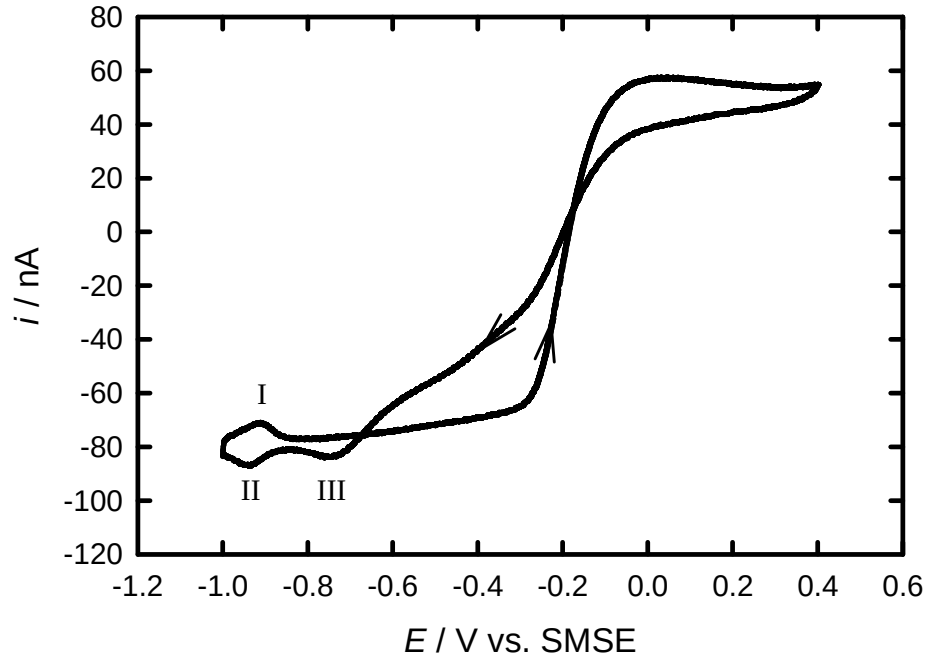

Figure 5-9. Cyclic voltammogram of a H_1 mesoporous Rh film electrodeposited onto a platinum disc microelectrode (25 µm in diameter, 8.68 µC for the deposition charge) in 5 mM H_2O_2 in 0.1 M phosphate buffer (pH =7) recorded at 2 mV s^{-1}. The solution was deaerated by purging with argon for at least 20 min prior to the measurements. The arrows indicate the direction of the cycle.

The voltammetry of the H_1 mesoporous Rh and H_1 mesoporous Pt microelectrodes in hydrogen peroxide is similar. It is noticeable that hydrogen peroxide oxidation takes place in the same potential window as the oxidation of the Rh surface in phosphate buffer.

Oxidation and reduction of hydrogen peroxide depend on the rhodium surface state. As for platinum, if the rhodium surface is in an oxidised state ($Rh(OH)_3$), the surface is more conducive to hydrogen peroxide oxidation; on the other hand, if the rhodium surface is in an unoxidised state (Rh(0)), the surface is more conducive to hydrogen

peroxide reduction. As for platinum, a place exchange occurs when oxide rhodium species start to form. There is a turnover process between Rh and OH. The delay of oxide stripping arises from Rh atoms moving back to their original places. This could explain the continued hydrogen peroxide oxidation at lower overpotential on the cathodic sweep; hence the anodic and cathodic sweeps cross over.

On the anodic sweep, the plateaux are well-defined whereas a slope is observed on the cathodic sweep. For potentials negative of - 0.6 V, three peaks are observed when H_2O_2 reduction occurs: one on the anodic sweep (I) and two on the cathodic sweep (II and III). These peaks can be identified thanks to the cyclic voltammogram in sodium phosphate buffer as shown in Figure 5-8. On the cathodic sweep, the peak (III) at ~ - 0.7 V corresponds to the oxide stripping peak in phosphate buffer. The two peaks (I) and (II) at ~ - 0.9 V match with those associated to hydrogen desorption/adsorption in phosphate buffer.

5.3.6 Analogy with the Hall Mechanism

A similar mechanism to platinum presented by Hall can be proposed with rhodium as shown below and considering that the Rh(OH) or $Rh(OH)_3$ species are involved. The mechanism mixes elementary steps (eq. 13-15, 18-19) and complexes. In eq. 15, the complex $Rh(OH)_3.H_2O_2$ was suggested but other ones could be involved.

$$H_2O_{2(bulk)} \longrightarrow H_2O_{2(surface)} \quad (13)$$

$$H_2O_2 + Rh(OH) \rightleftharpoons Rh(OH).H_2O_2 \quad (14)$$

or $$H_2O_2 + Rh(OH)_3 \rightleftharpoons Rh(OH)_3.H_2O_2 \quad (15)$$

$$Rh(OH).H_2O_2 \longrightarrow Rh + \frac{3}{2}H_2O + \frac{3}{4}O_2 \quad (16)$$

or $$Rh(OH)_3.H_2O_2 \longrightarrow Rh + \frac{5}{2}H_2O + \frac{5}{4}O_2 \quad (17)$$

$$Rh + H_2O \longrightarrow Rh(OH) + H^+ + e^- \quad (18)$$

or $$Rh + 3H_2O \longrightarrow Rh(OH)_3 + 3H^+ + 3e^- \quad (19)$$

5.3.7 Determination of the diffusion coefficient of hydrogen peroxide $D_{H_2O_2}$

Thanks to microelectrode properties, the diffusion coefficient can be determined by the simple expression (equation (8)) of the steady state current i_L for a microdisc:

$$i_L = 4nFDca \quad (8)$$

If the radius of the electrode, the concentration of the solution and the steady state current are known, it is possible to calculate the diffusion coefficient. The diffusion coefficient was determined by using Pt microelectrodes of different diameters 5, 10, 25 and 50 µm on which an H_1 mesoporous Rh film was electrodeposited. For each size of microelectrode, a cyclic voltammogram was recorded in 5 mM H_2O_2 in 0.1 M phosphate buffer (pH = 7) at 2 mV s^{-1} between - 1 and 0.4 V vs. SMSE. Only the oxidation of hydrogen peroxide is considered for this study; therefore, the limiting current for hydrogen peroxide oxidation was assessed in order to determine the diffusion coefficient. Figure 5-10 shows a magnification of Figure 5-9 in the potential range - 0.2 and 0.4 V corresponding to the hydrogen peroxide oxidation.

The limiting current was evaluated by calculating the current due to the double layer capacitance in the hydrogen peroxide oxidation region of the cycle. As the surface area is large for the mesoporous Rh microelectrode, the capacitance is also large; therefore the capacitance needs to be considered to measure the limiting current. When a scan rate υ is applied, the expression for the current i at steady state is when the capacitance C is constant:

$$i = C\upsilon \quad (20)$$

The current due to the double layer capacitance, in absence of Faradaic processes, was measured for the potential at which the current attains the lowest value on the anodic scan; here, the chosen potential was 0.35 V since the anodic current seems constant over a short range of potentials. At this potential, the limiting current was assessed as the central current between the anodic and cathodic scans as the anodic and cathodic currents for the double layer capacitance are approximately similar.

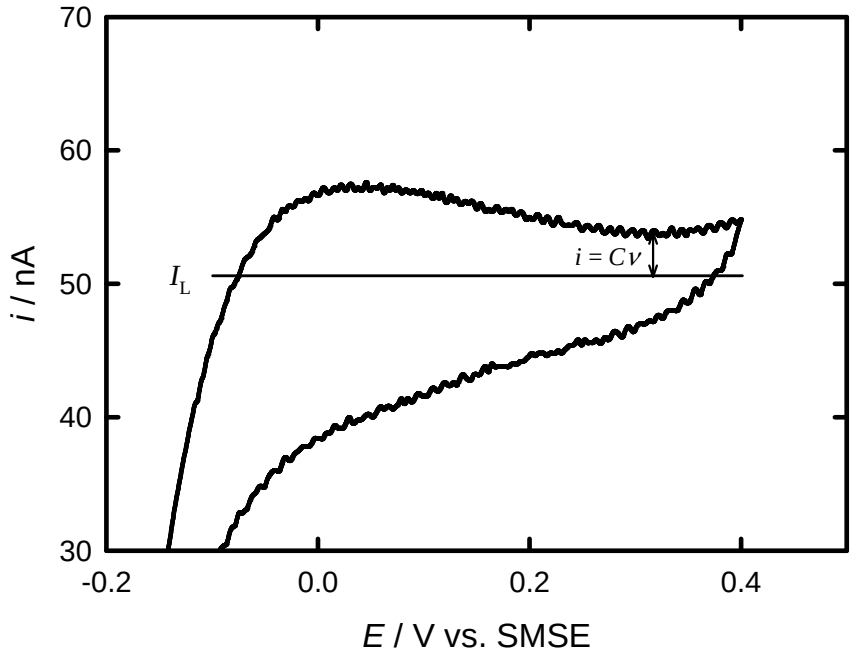

Figure 5-10. Magnification of the oxidation part of the cyclic voltammogram shown in Figure 5-9.

Once the current for the capacitance was obtained, the limiting current can be estimated by subtraction of the current due to the double layer capacitance from the current recorded on the oxidation wave. The technique was repeated for the cyclic voltammogram recorded in hydrogen peroxide for each size of the microelectrode. The diameter of the microelectrode was verified by SEM before and after deposition in case of an overgrowth of the film. With the applied deposition charge for each microelectrode, the size remains identical. The limiting current was then plotted as a function of the radius of the disc as shown in Figure 5-11. The error bars correspond to the limiting current measured on three different voltammograms recorded in 5 mM H_2O_2 in 0.1 M phosphate buffer.

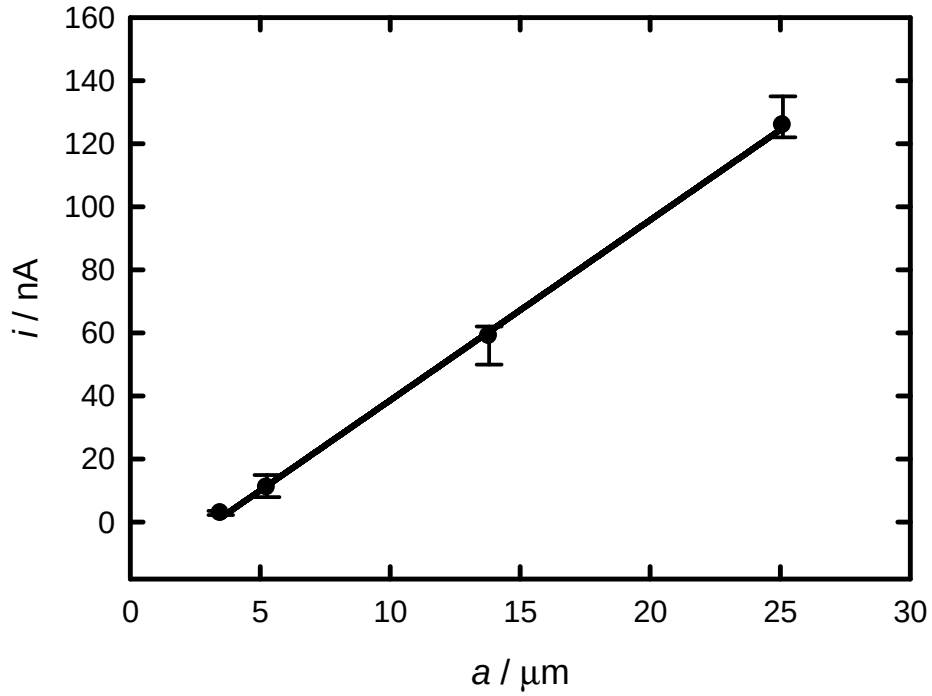

Figure 5-11. Limiting currents of hydrogen peroxide oxidation recorded for different radii of disc microelectrodes in 5 mM H_2O_2 in 0.1 M sodium phosphate buffer (pH = 7). The solid line represents a linear fit of the data points.

By linear regression, the diffusion coefficient was found to be $1.48\times10^{-9}\pm 0.08$ m s^{-1} ($r^2 = 0.9995$). The value estimated by this technique is within the range of values found by different workers using different methods of investigation at different temperatures as depicted in Table 5-1.

Table 5-1. Diffusion coefficients for the oxidation of hydrogen peroxide estimated at different temperatures using different techniques.

Authors	$D_{H_2O_2} \times 10^{-9}$ / $m^2\ s^{-1}$	T / °C	Method	Electrolytes
van Stroe-Biezen *et al.*[33]	1.43	25	Koutecky-Levich	0.1 M sodium phosphate buffer (pH=6.7)
van Stroe-Biezen *et al.*[33]	1.83	37	Koutecky-Levich	0.1 M sodium phosphate buffer (pH=6.7)
Brestovisky *et al.*[34]	1.2	not stated	Reverse pulse polarography	0.1 M $NaClO_4$
Prabhu *et al.*[8]	1.21 – 1.61 (pH=12.3-6.3)	25	Chronoamperometry	0.1 M HNO_3 + 0.05 M universal buffer
Prabhu *et al.*[8]	1.07 – 1.56 (pH=12.3-6.3)	25	Chronopotentiometry	0.1 M HNO_3 + 0.05 M universal buffer
Borggaard[35]	0.88	10	Polarography	N/A
Borggaard[35]	1.35	20	Polarography	N/A
Borggaard[35]	1.75	30	Polarography	N/A
Borggaard[35]	2.2	40	Polarography	N/A
Hall *et al.*[18]	0.66	20	Michaelis-Menten kinetics	0.1 M phosphate buffer (pH=7.26)
Evans *et al.*[1]	1.46	25	Microelectrodes	0.1 M sodium phosphate buffer (pH=7)
This study	1.48	25	Microelectrodes	0.1 M sodium phosphate buffer (pH=7)

5.3.8 Amperometric responses for hydrogen peroxide oxidation

Calibration plots were obtained by adding aliquots of hydrogen peroxide in 0.1 M phosphate buffer. Figure 5.12 compares the calibration curve obtained for a polished Pt microelectrode with a calibration curve recorded for a mesoporous Rh microelectrode of the same geometric surface area.

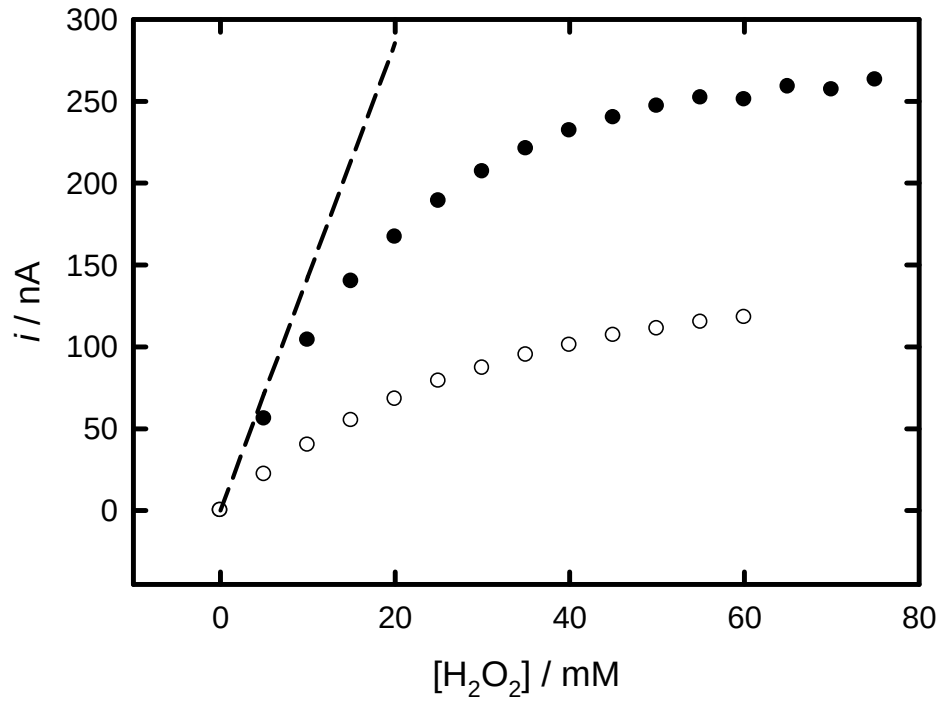

Figure 5-12. Calibration curves for hydrogen peroxide oxidation obtained from chronoamperometry of a polished Pt microelectrode (○) and a mesoporous rhodium film (●) electrodeposited on a platinum microelectrode in 0.1 M phosphate buffer (pH = 7, T = 25 °C). The deposition charge was 5.52 µC. The diameter of the microelectrodes was 25 µm. The electrode was held at 0 V vs. SMSE throughout the whole experiment. The electrode was held at 0 V vs. SMSE for 20 min before the addition of aliquots of hydrogen peroxide. (dashed line) Theoretical data obtained from the diffusion control current $i_L = 4nFDca$ using $D = 1.48\times10^{-9}$ m s^{-1}.

The two curves are significantly different. The current for the polished microelectrode is much lower than for the mesoporous Rh microelectrode and the shape of the curve is also different. The current response for the conventional platinum microelectrode is not proportional to the concentration of the hydrogen peroxide comparing the theoretical diffusion control response with the experimental data. When the concentration of hydrogen peroxide increases, the current response reaches a plateau since it is limited by the number of available platinum sites. One way to overcome this shortfall is to increase

the surface area by modifying the surface of the microelectrode while preserving the properties of microelectrodes. A mesoporous Rh film was electrodeposited on a Pt microelectrode exhibiting a high surface area. The current response for the mesoporous Rh microelectrode was linear for low concentrations of hydrogen peroxide up to 15 mM and shows a good agreement with the theoretical diffusion control current represented by the dashed line. Above this concentration, the current starts to deviate and reaches a plateau likely due to a saturation of the binding sites or a limited diffusion of hydrogen peroxide down the pores.

A quantitative analysis of the limiting current was undertaken to monitor hydrogen peroxide amperometrically. H_1 mesoporous Rh microelectrodes with different film thicknesses were characterised by cyclic voltammetry in 1 M sulphuric acid to estimate the surface area. All the cyclic voltammograms of the H_1 mesoporous Rh microelectrodes with different thicknesses look alike and resemble that shown in Figure 5-1. The film thicknesses can be controlled by the deposition charge. The surface areas were determined by the charge involved under the hydrogen desorption peak in sulphuric acid.

Figure 5-13 shows the calibration data for eight different thicknesses over the range of 0 and 75 mM of hydrogen peroxide.

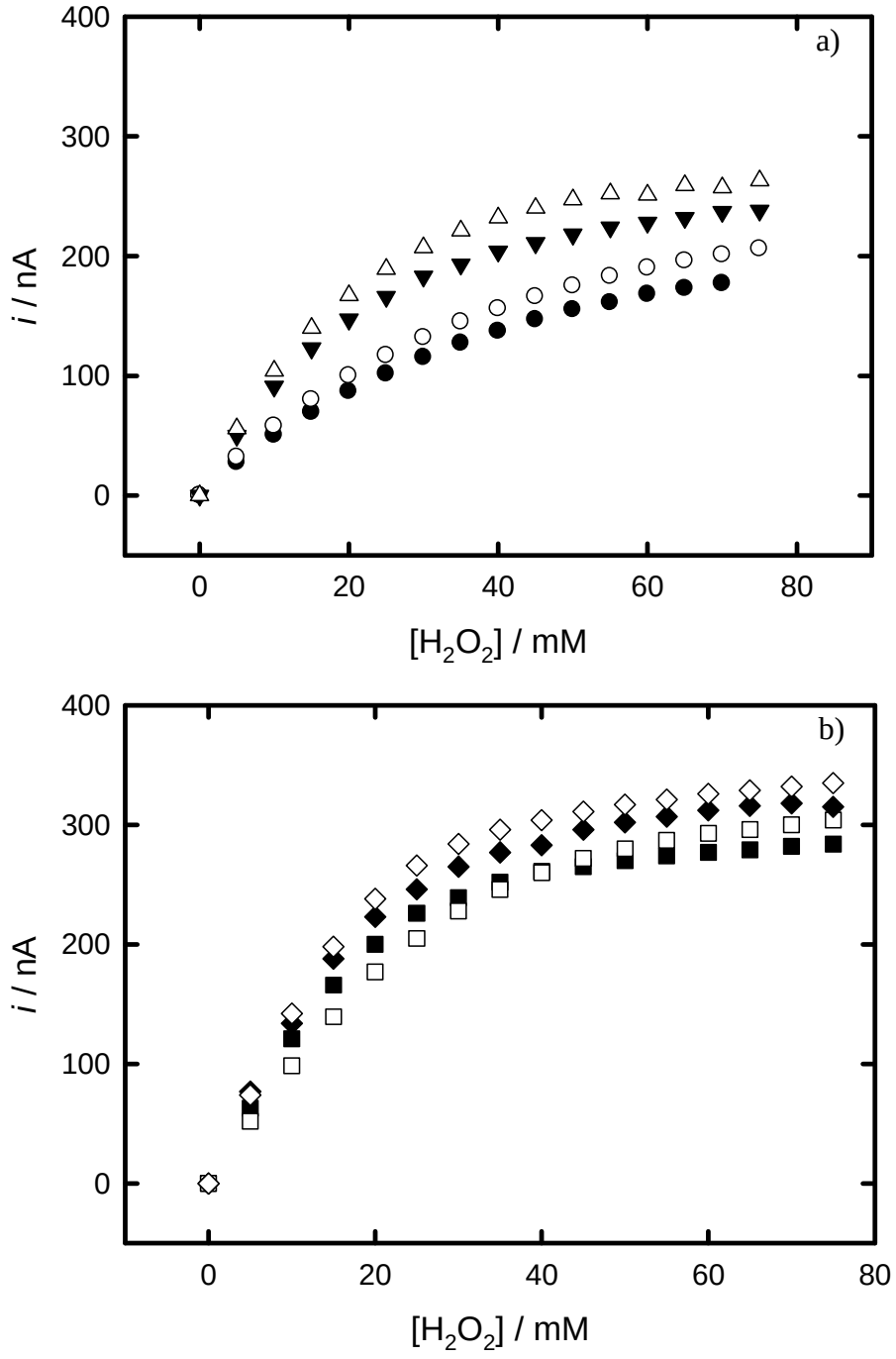

Figure 5-13. (a) Calibration curves for hydrogen peroxide oxidation obtained from chronoamperometry of mesoporous rhodium films electrodeposited on platinum microelectrodes for different thicknesses in 0.1 M phosphate buffer(pH = 7, *T* = 25 °C). The different thicknesses are obtained with different deposition charges: (●) 0.434 µC, (○) 0.868 µC, (▼) 1.74 µC, (Δ) 5.52 µC and (b) (■) 8.68 µC, (□) 17.36 µC, (♦) 26.04 µC, (◊) 34.72 µC. The electrode was held at 0 V vs. SMSE throughout the whole experiment. The electrode was held at 0 V vs. SMSE for 20 min before the addition of aliquots of hydrogen peroxide.

The effect of the film thickness was investigated by depositing H_1 mesoporous Rh films onto the polished Pt microelectrodes. The trend of the current response is linear over a low concentration range below 20 mM hydrogen peroxide. Indeed, thicker films increase the surface areas but have no beneficial effect on the current response. The current for a H_1 mesoporous Rh microelectrode tends to a constant value at high concentrations of hydrogen peroxide. Although the mesoporous film becomes thicker, the value for the current response remains similar. The mechanism of the oxidation of hydrogen peroxide was investigated by looking at the effect of film thickness using microelectrodes.

5.4 Kinetic Model

Our experimental results lead to the conclusion that a valid kinetic model could be attributed to the oxidation of hydrogen peroxide occurring throughout the mesoporous film. According to the data for the microelectrodes with different film thicknesses, the reaction is mass transport limited for low concentrations of hydrogen peroxide. The kinetic model described next has been suggested to take into account all the factors. The model was originally developed to the oxidation of NADH at poly(aniline)-coated electrodes[13].

A kinetic model was proposed from Albery's papers[36-38] to account for the reaction of H_2O_2 occurring through the mesoporous film. It is assumed that H_2O_2 diffuses into the film and it is adsorbed at sites within the pores.

$$H_2O_{2(bulk)} \underset{k'_{D,S}}{\overset{k'_{D,S}}{\rightleftharpoons}} H_2O_{2(0)}$$ **Mass transport to the electrode surface**

Where $H_2O_{2(bulk)}$ and $H_2O_{2(0)}$ represent H_2O_2 in the bulk of the solution and H_2O_2 at the electrode surface respectively and $k'_{D,S}$ is the mass transport rate for H_2O_2 at the microelectrode.

In the model for the oxidation of NADH at poly(aniline)-coated electrodes, a partition into the film was considered (the partition coefficient for NADH into the film was denoted K_S). In the present case, the pores are accessible to the solution. Hydrogen peroxide is uncharged, so there is not a Donnan exclusion effect and $K_S = 1$.

$$H_2O_2 + Rh(OH) \underset{}{\overset{K_M}{\rightleftharpoons}} Rh(OH).H_2O_2$$ **Complex formation at the surface of the pore walls**

$$Rh(OH).H_2O_2 \xrightarrow{k_{cat}} Rh + \frac{3}{2}H_2O + \frac{3}{4}O_2$$ **Chemical reaction within the film**

$$Rh + 3H_2O \longrightarrow Rh(OH)_3 + 3H^+ + 3e^-$$

where K_M is the equilibrium constant for H_2O_2 adsorption and k_{cat} the rate constant for the oxidation of the adsorbed H_2O_2.

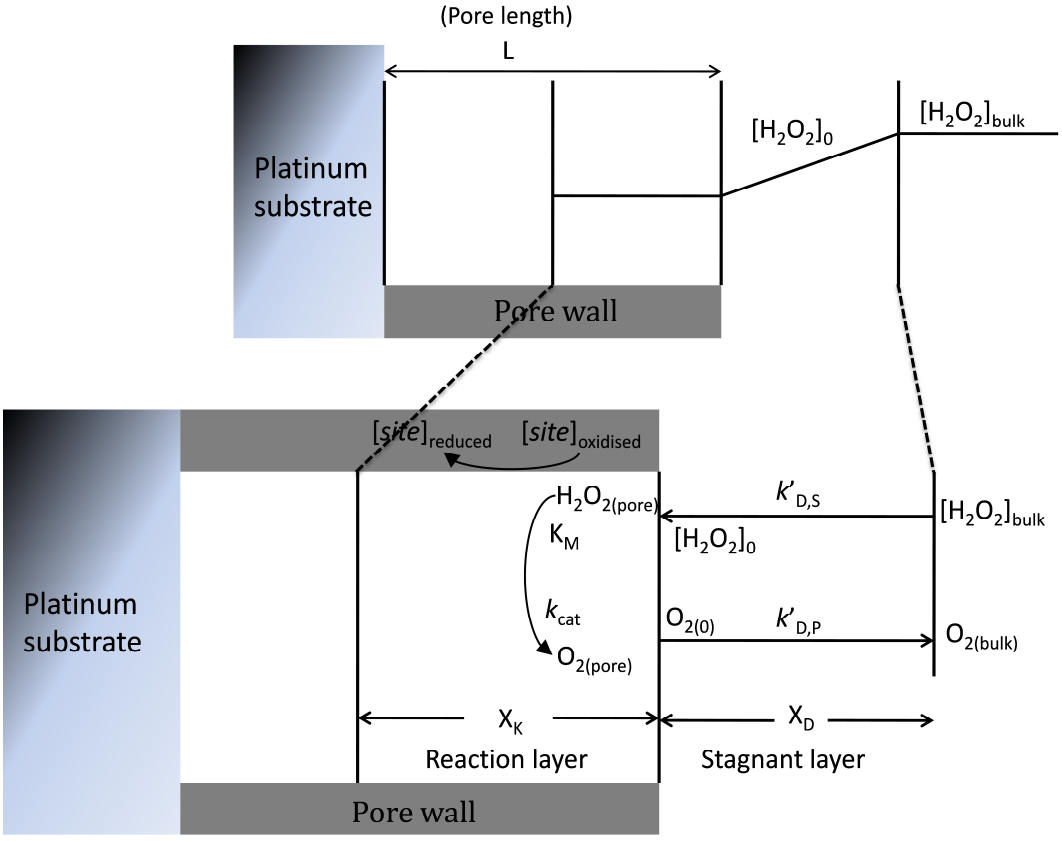

Figure 5-14. Schematic of the suggested reaction for the oxidation of hydrogen peroxide in the pores. (top) Concentration profile of hydrogen peroxide in the bulk and in the pore and (bottom) description of the different steps of the reaction in the pore.

This type of reaction mechanism was presented by Albery *et al.*[36-38] assuming that a steady state was established and its applications to amperometric chemical sensors presented by Lyons *et al.*[39]. In order to apply this model, it is important to know the

concentration of the reactant species at the electrode surface. The concentration of the reactant species at the electrode surface for a microelectrode was calculated by[40]

$$[H_2O_2]_0 = [H_2O_2]_{bulk} - i/nFAk'_{D,S} \quad (21)$$

This equation is valid only if $[H_2O_2]_{bulk} - i/nFAk'_{D,S} \geq 0$

In the case of a disc microelectrode, $k'_{D,S} = 4D/\pi a$. The diffusion coefficient was calculated previously in Section 5.3.8. Thus it is possible to evaluate the concentration of hydrogen peroxide at the electrode surface. Figure 5-15 shows the calibration curves of limiting currents measured at 0 V vs. SMSE as a function of the calculated H_2O_2 concentration at the electrode surface.

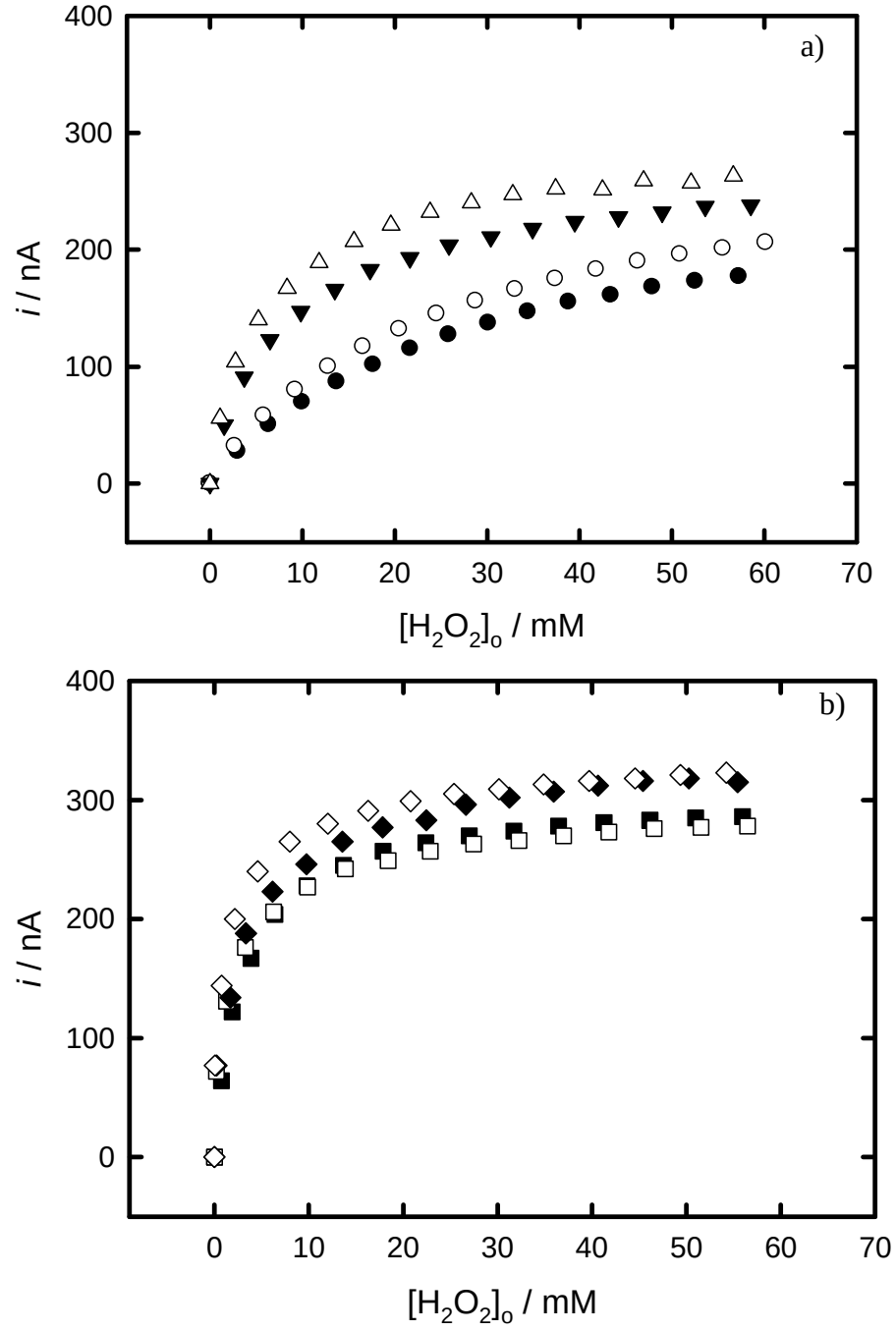

Figure 5-15. Calibration curves for the oxidation of hydrogen peroxide obtained from chronoamperometry of mesoporous rhodium film electrodeposited on platinum microelectrodes for different thicknesses in 0.1 M phosphate buffer, pH = 7, *T* = 25 °C. The different thicknesses are obtained with different deposition charges:(a) (●) 0.434 µC, (○) 0.868 µC, (▼) 1.74 µC, (Δ) 5.52 µC and (b) (■) 8.68 µC, (□) 17.36 µC, (♦) 26.04 µC, (◊) 34.72 µC. The data were modified for the concentration of hydrogen peroxide at the electrode surface. The electrode was held at 0 V vs. SMSE throughout the whole experiment. The electrode was held at 0 V vs. SMSE for 20 min before the addition of aliquots of hydrogen peroxide.

The semi-analytical model from Albery can then be used[36]. No inhibition will be considered and a fast desorption of O_2 was assumed; an expression for the current can be formulated from equation (6) and (23) of the paper by Albery[36] and the current is substituted by the flux to obtain:

$$i = nFAK_{\mathrm{M}}D_{\mathrm{S}}y / L \tag{22}$$

with A, the geometric area of the electrode (cm^2)
and,

$$y = \left\{2\varepsilon\left[\alpha - \ln\left(1+\alpha\right)\right]\right\}^{1/2} \tanh\left[\frac{\varepsilon^{1/2}\alpha}{\left(1+\alpha\right)\left\{2\left[\alpha - \ln\left(1+\alpha\right)\right]\right\}^{1/2}}\right] \tag{23}$$

Where L is the thickness of the film, D_S is the diffusion coefficient of H_2O_2 in the film (in this study, the diffusion coefficient of H_2O_2 into the pores will be assumed to be equal to the diffusion coefficient of H_2O_2 in the bulk in order to simplify the analysis) and the notation will be

$$\varepsilon = \frac{L^2\Gamma_{\mathrm{site}}k_{\mathrm{cat}}}{D_{\mathrm{S}}K_{\mathrm{M}}} \tag{24}$$

where Γ_{site} represents the coverage of the rhodium active sites (mol cm^{-2})
and

$$\alpha = \left[\mathrm{H_2O_2}\right]_0 / K_{\mathrm{M}} \tag{25}$$

The film thickness is determined by calculating the charge under the hydrogen desorption peaks, Q, on the cyclic voltammogram recorded in 1 M sulphuric acid after deposition:

$$L = \sigma Q \tag{26}$$

where σ is constant.

Equations (24) to (27) define four different limiting cases for the behaviour of the system. Before proceeding it is necessary to define the 'reaction layer thickness':

$$X_{\mathrm{k}} = \left(\frac{D_{\mathrm{S}}}{k'_{\mathrm{cat}}} \right)^{1/2} \tag{27}$$

This parameter corresponds to the distance over which hydrogen peroxide diffuses into the pore before it reacts on the Rh pore wall as shown on Figure 5-14.

Four cases are represented for this model[13].

No concentration polarisation in the pore (Case I)

In this case,oxygen diffused out of the pore and the concentration of H_2O_2 is equal through the pore. This is possible when the film is thin ($\varepsilon > 1$) and the concentration of H_2O_2 is insufficient in order to saturate the reaction sites ($\alpha < 1$). In case I, the current is given by:

$$i_{\mathrm{I}} = nFAk_{\mathrm{cat}}\Gamma_{\mathrm{site}}L\left[H_2O_2\right]_0 / K_{\mathrm{M}} \tag{28}$$

Overall the reaction is first order in H_2O_2 and occurs throughout the film.

Low substrate concentration : unsaturated kinetics (CaseII)

In this case, the concentration of H_2O_2 is insufficient to saturate the reaction sites ($\alpha < 1$) but here the film is thick ($\varepsilon > 1$) so all the H_2O_2 is consumed in a first order reaction layer at the outside of the film and the current is given by:

$$i_{\mathrm{II}} = nFA\left[\mathrm{H_2O_2}\right]_0 \left(k_{\mathrm{cat}}\Gamma_{\mathrm{site}}D_{\mathrm{S}} / K_{\mathrm{M}}\right)^{1/2} \tag{29}$$

In this case, the flux will be independent of the pore length and the chemical reaction will be far greater than the rate of diffusion of H_2O_2 in the film.

High substrate concentration : saturated kinetics (Case III)

The concentration of H_2O_2 is sufficient to saturate the sites ($\alpha > 1$) and the film is sufficiently thin ($\varepsilon < 2\alpha$) so that the reaction of H_2O_2 occurs with zero order kinetics throughtout the whole film. The current is given by:

$$i_{\mathrm{III}} = nFAk_{\mathrm{cat}}\Gamma_{\mathrm{site}}L \qquad (30)$$

The current depends on the pore length and the concentration of sites within the pore but is independent of H_2O_2 concentration.

Intermediate substrate concentration : partially saturated kinetics (Case IV)

The concentration of $H_2O_2$is sufficient to saturate the sites at the upper part of the pore ($\alpha > 1$) but falls as it is consumed within the film ($\varepsilon < 2\alpha$) so that the kinetics become unsaturated further into the film. The current is given by:

$$i_{\mathrm{IV}} = nFA\left(2k_{\mathrm{cat}}\Gamma_{\mathrm{site}}D_{\mathrm{S}}\left[\mathrm{H_2O_2}\right]_0\right)^{1/2} \qquad (31)$$

The current is independent of film thickness and has a half order with respect to the concentration of sites within the film and the concentration of H_2O_2. The current expressions for each Case with the reaction order of each parameter are summarised in Table 5-2.

Table 5-2. Summary of the current expressions for each case with the respective reaction orders of the different reaction variables.

Case	Current expression	Reaction order wrt.			Eq No
		$[H_2O_2]_o$	Γ_{site}	L	
I	$i_I = nFAk_{cat}\Gamma_{site}L[H_2O_2]_o / K_M$	1	1	1	28
II	$i_{II} = nFA[H_2O_2]_o \left(k_{cat}\Gamma_{site}D_S / K_M\right)^{1/2}$	1	½	0	29
III	$i_{III} = nFAk_{cat}\Gamma_{site}L$	0	1	1	30
IV	$i_{IV} = nFA\left(2k_{cat}\Gamma_{site}D_S[H_2O_2]_o\right)^{1/2}$	½	½	0	31

The different Cases with their respective concentration profiles are shown in Figure 5-16.

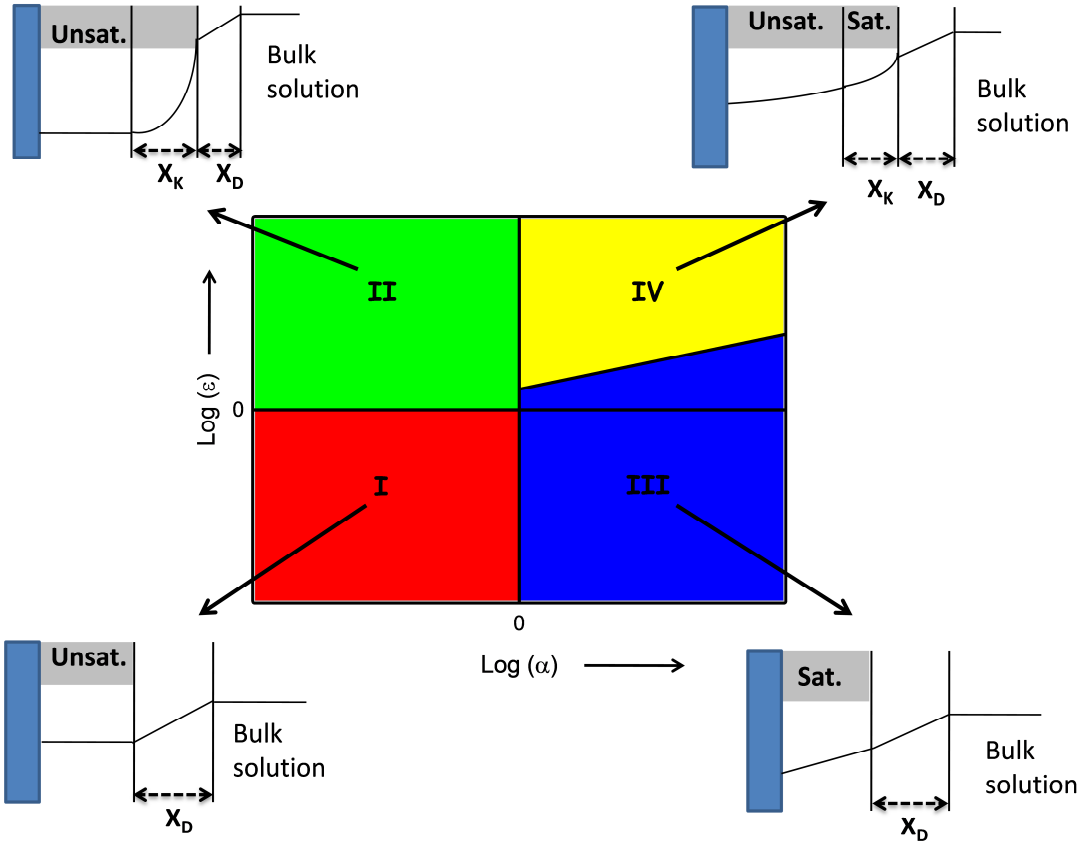

Figure 5-16. Case diagram representing the four different Cases and the respective concentration profiles. The grey areas represent the edge of the mesoporous film.

The expressions for the current across the case boundaries are shown in Table 5-3.

Table 5-3. Approximate analytical expressions for the currents across the different case boundaries.

Case Boundary	Approximate analytical expressions for the currents	Eq No
I / II	$nFAD_S\sqrt{\frac{k_{cat}\Gamma_{site}}{K_M D_S}}[H_2O_2]_o \tanh\left(\sqrt{\frac{k_{cat}\Gamma_{site}}{K_M D_S}L^2}\right)$	32
II / IV	$nFA\sqrt{2k_{cat}\Gamma_{site}K_M D_S\left\{\left(\frac{[H_2O_2]_o}{K_M}\right)-\ln\left(1+\frac{[H_2O_2]_o}{K_M}\right)\right\}}$	33
IV / III	$nFA\sqrt{2k_{cat}\Gamma_{site}D_S[H_2O_2]_o}\tanh\sqrt{\frac{k_{cat}\Gamma_{site}L^2}{2D_S[H_2O_2]_o}}$	34
I / III	$nFAk_{cat}\Gamma_{site}L\left(\frac{[H_2O_2]_o}{[H_2O_2]_o+K_M}\right)$	35

5.4.1 Application of the model

The experimental data from the calibration curves was used to test the kinetic model described above. Two steps are necessary to fit experiments to theory. Firstly, the equations do not include the concentration polarisation in the solution; therefore the equations are used to determine the concentrations of H_2O_2 at the solution/film interface. Secondly, the data was viewed to estimate which case it belongs to. From the reaction orders, it can be suggested which case the data corresponds to. Thus, from the case proposed, the equation with the parameters is written in the form in which the data should fit. The parameters have been calculated from the program where the best curve fit is obtained.

ε corresponds to the film thickness (or deposition charge). At a fixed value of ε, increasing $[H_2O_2]_o$ corresponds to increase in α; therefore the case boundaries have to be either I/III or II/IV unless ε = 1. In this situation (ε = 1), the case boundary approximations would not work since they are derived from making assumptions about relative magnitude of the terms of the full equation and hence would not be valid.

For example: Figure 5-17 shows a calibration curve of limiting currents measured at 0 V vs. SMSE as a function of the hydrogen peroxide concentration at the electrode surface for a H_1 mesoporous Rh film with a deposition charge of 8.68 µC.

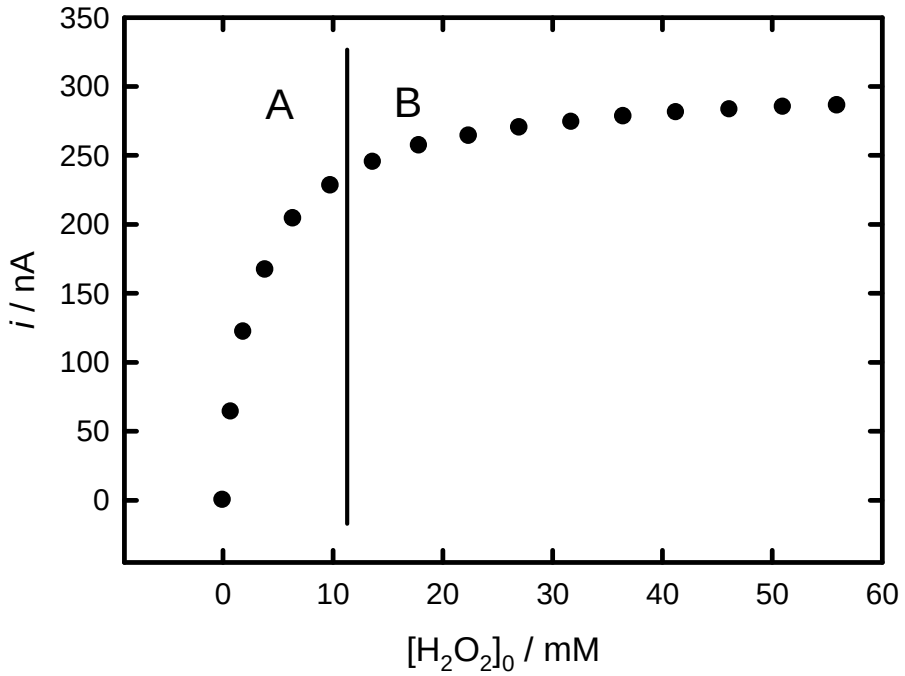

Figure 5-17. Calibration curve for the oxidation of hydrogen peroxide obtained from chronoamperometry of mesoporous rhodium film electrodeposited (deposition charge = 8.68 µC, diameter = 25 µm) on platinum microelectrodes for in 0.1 M phosphate buffer, pH = 7, *T* = 25 °C. The data are plotted as a function of the calculated concentration of hydrogen peroxide at the electrode surface. The electrode was held at 0 V vs. SMSE throughout the whole experiment. The electrode was held at 0 V vs. SMSE for 20 min before the addition of aliquots of hydrogen peroxide. 'A' represents the section in which the concentration of hydrogen peroxide has an effect on the current and 'B' represents the section in which the concentration of hydrogen peroxide does not influence the current.

The plot in Figure 5-17 was split in two sections (A) and (B). In section (A), the concentration has an effect so the data correspond to case I. In section (B), the concentration effect is vanishing; but the film thickness has an effect up to some extent, which could refer to case III. To analyse the data altogether, case boundaries expressions need to be determined as shown in Table 5-3.

The film thickness is incorporated in the expression for the case boundary I/III which could be used to fit the data[13]. Therefore, all the data plotted in Figure 5-15 can be analysed with the following equation.

$$i_{\mathrm{I/III}} = nFAk_{\mathrm{cat}}\Gamma_{\mathrm{site}}L\left(\frac{[\mathrm{H_2O_2}]_{\mathrm{o}}}{[\mathrm{H_2O_2}]_{\mathrm{o}} + K_{\mathrm{M}}}\right) \quad (35)$$

This equation was changed into a two parameter equation for the curve fit:

$$i = a\left(\frac{[\mathrm{H_2O_2}]_{\mathrm{o}}}{[\mathrm{H_2O_2}]_{\mathrm{o}} + b}\right) \quad (36)$$

where

$a = nFAk_{\mathrm{cat}}\Gamma_{\mathrm{site}}L$ (37) and $b = K_{\mathrm{M}}$ (39)

The software SigmaPlot 11.0 was used to fit data to this equation. The program varies the value of the two parameters until the theoretical current is as close to the experimental current as possible using non-linear least squares fitting.

The equation (36) needs to be modified as follows in order to check the accuracy of the data.

The equation was arranged by plotting the inverse of intensity versus the inverse of the concentration as shown in Figure 18, which is called the Lineweaver-Burk plot:

$$\frac{1}{i_{I/III}} = \frac{b}{a} \times \frac{1}{[H_2O_2]_0} + \frac{1}{a} \quad (40)$$

The calibration curve was plotted by considering the hydrogen peroxide concentration at the surface of the film $[H_2O_2]_0$.

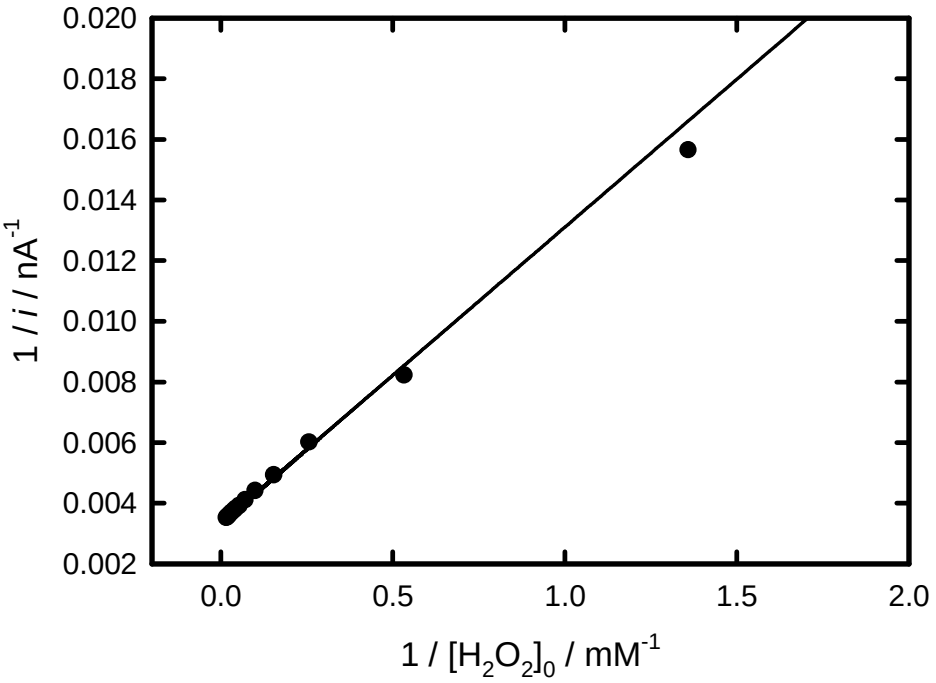

Figure 5-18. Data from the calibration curve in Figure 5-17 rearranged to be plotted as the inverse of the current as a function of the inverse of the concentration of hydrogen peroxide at the surface of the H_1 mesoporous Rh film. (solid line) fit of the data arranged in a Lineweaver-Burk plot (the fit was obtained from equation (36) and the data were arranged for the Lineweaver-Burk plot).

The fit (r^2 = 0.998) deviates slightly at low concentrations. This can indicate that the data of the calibration curve are of good quality but not perfect. The model can be applied.

5.5 Results

All the data were treated using this method to fit the parameters. After the inspection of the data, the curves are fit using two parameters with the appropriate equations. Once the parameters are obtained, they are compared to check the validity of the fit. The parameters are cast as $k_{cat}\Gamma_{site}\sigma$ and K_M. Figure 5-19 shows the values of $k_{cat}\Gamma_{site}\sigma$ and K_M as a function of the charge calculated from the hydrogen desorption region in 1 M sulphuric acid (the charge under the hydrogen desorption peak is related to the thickness of the mesoporous Rh film).

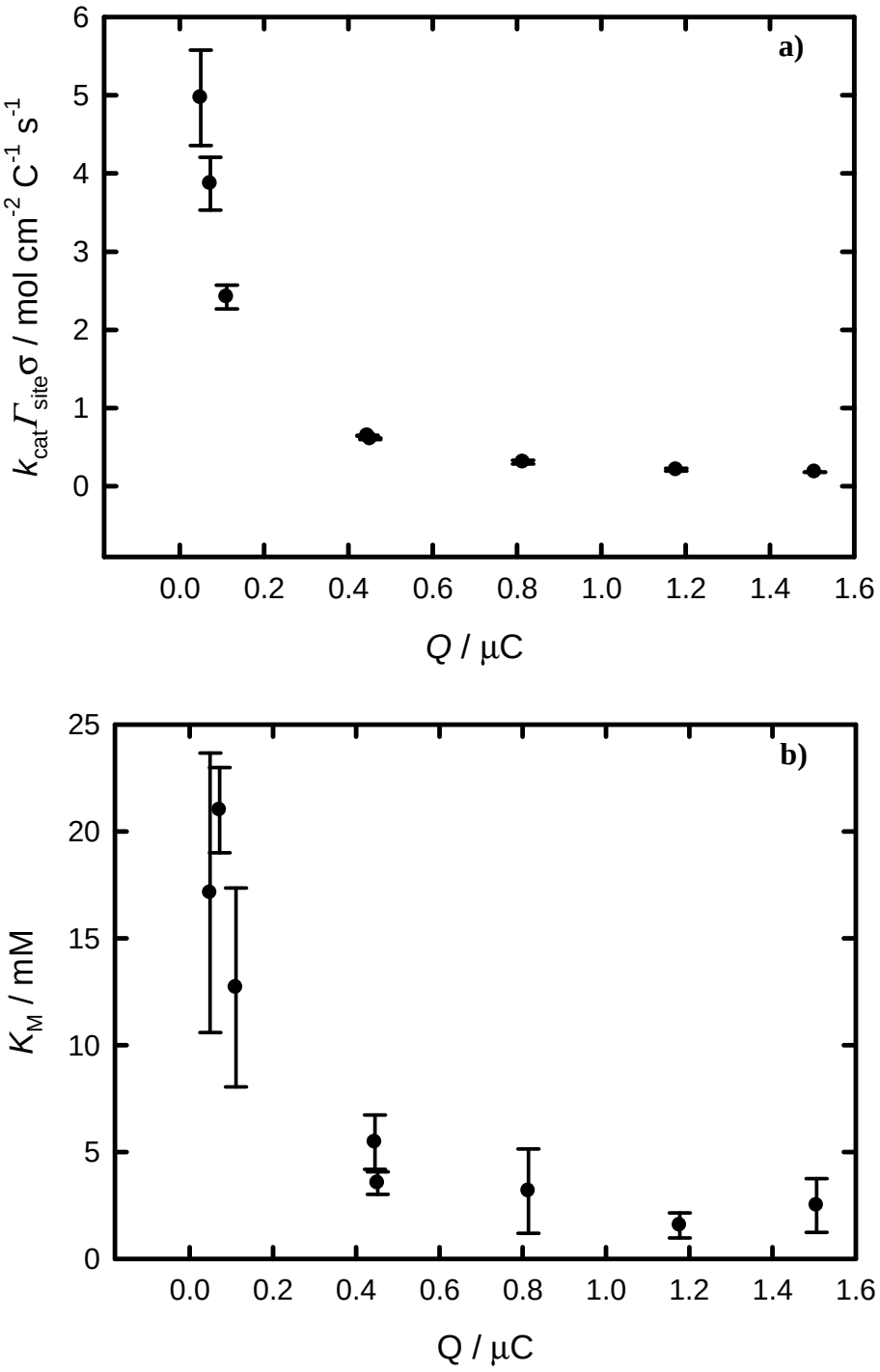

Figure 5-19. Plots of the fitted parameters (a) $k_{cat}\Gamma_{site}\sigma$ and (b) K_M as a function of the charge calculated under the hydrogen desorption peak from cyclic voltammograms recorded in 1 M sulphuric acid for different depositions of mesoporous Rh films on Pt microelectrodes (diameter = 25 µm). The values correspond to the mean of the measurements and the error bars stem from the standard error.

The values for $k_{cat}\Gamma_{site}\sigma$ decrease down to one order of magnitude when the charge calculated in sulphuric acid, related proportionally to the film thickness, increases as shown in Figure 5-19a; this suggests that $k_{cat}\Gamma_{site}\sigma$ is dependent of the film thickness. As the same surfactant was used, the $k_{cat}\Gamma_{site}\sigma$ value should be the same even when growing thicker films. The values for K_M also decrease when the charge calculated in acid increases but to a lesser extent as shown in Figure 5-19b.

The analysis of $k_{cat}\Gamma_{site}\sigma$ and K_M leads to a change of values with thicker films whereas these values should be independent of the film thickness. As the film thickness increases, the values for the current response at high concentrations of hydrogen peroxide seem similar though a slight increase can be observed. For example, by growing a film twice as thick, we would expect, based on our kinetic model, that the current response would be more significant for the thicker film but the values for the current response remain close for both films. Hence, this behaviour does not reflect the proposed kinetic model. A possible explanation for this could be a product inhibition. While the oxidation of hydrogen peroxide occurs within the pores, the produced oxygen could then adsorb onto the pore walls or oxygen bubbles could occupy the space within the pores and thus prevent hydrogen peroxide from diffusing down the pores. The current response would be then limited by the availability of sites.

5.5.1 Product inhibition: oxygen

Figure 5-20 shows Levich plots for the oxidation of hydrogen peroxide on a H_1 mesoporous Rh film electrodeposited on a Pt RDE. The data were recorded with the solution purged with argon gas and in presence of oxygen. The experiment was conducted for the recording of the current in three steps: the solution was first purged with argon gas, then the solution was bubbled with oxygen and finally the solution was purged with argon gas to ascertain that the current is recovered after bubbling the solution with oxygen.

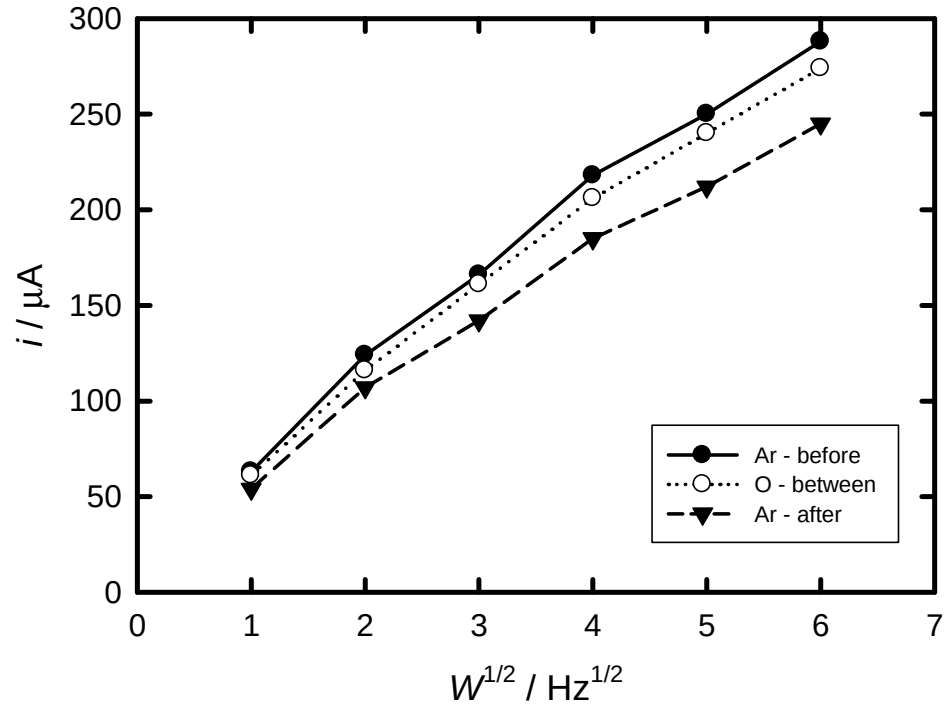

Figure 5-20. Current response for a mesoporous Rh film electrode (deposition charge 0.347 C, geometric area 0.196 cm^2) held at 0 V vs. SMSE in 0.1 M phosphate buffer at pH 7 as a function of the square root of the rotation rate. Results shown for a 1 mM H_2O_2 in 0.1 M phosphate buffer at different rotation rates. ●+line) the solution was purged with argon gas. ○+dot) the solution was purged with oxygen gas. ▼+dash) the solution was purged with argon gas after purging the solution with oxygen.

The aim of this experiment was to look for any changes when the solution was purged with argon gas or contained oxygen in order to indicate any effect of inhibition by oxygen. As the data in Figure 5-20 show, there is no evidence for significant inhibition by oxygen.

Another possibility is that electrogenerated oxygen may form bubbles that are trapped in the pores. Electrochemical impedance spectroscopy was used to monitor to check if gas bubbles form and block the pores during H_2O_2 oxidation. A mesoporous Rh film was electrodeposited onto a Pt rotating disc electrode. The impedance was recorded over a large range of frequencies (0.1 Hz and 100 kHz) in the absence and in the presence of hydrogen peroxide in the phosphate buffer. Figure 5-21 shows a Nyquist plot of a H_1 mesoporous Rh film for different concentrations of hydrogen peroxide where the potential was held 0 V vs. SMSE.

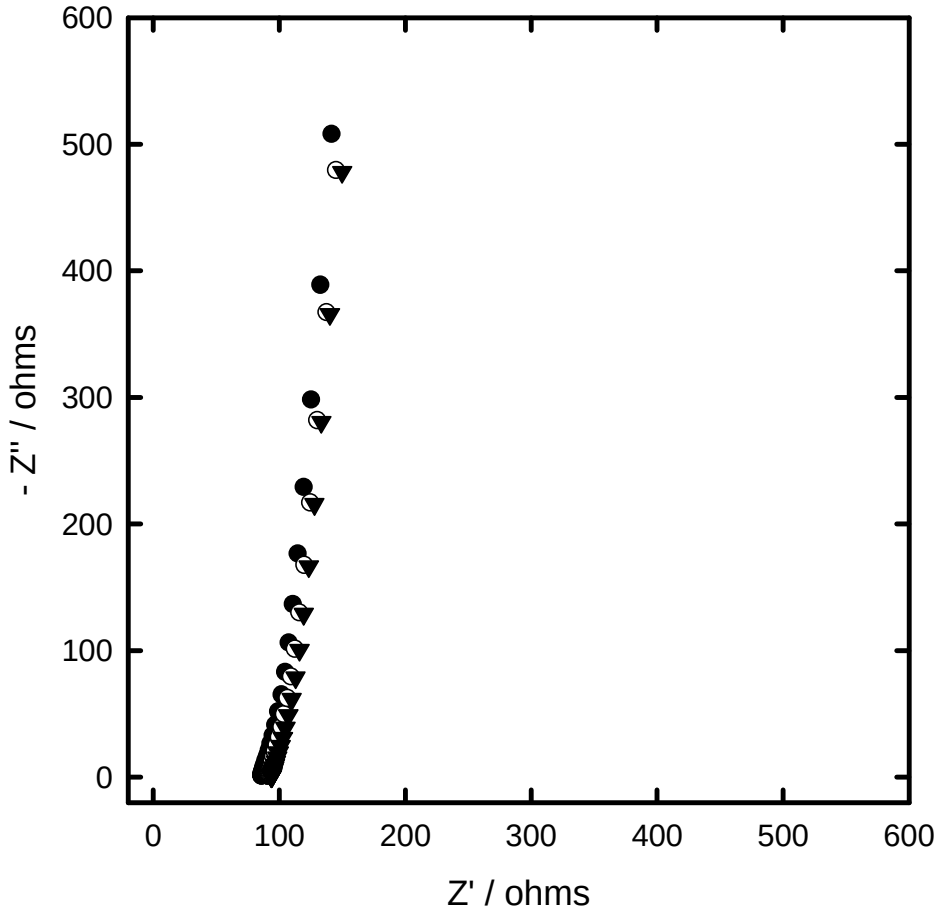

Figure 5-21. Nyquist plot for a mesoporous Rh film electrodeposited on a Pt RDE (deposition charge 0.347 C, geometric area 0.196 cm^2) held at 0 V vs. SMSE in 0.1 M phosphate buffer (pH = 7) with different concentrations of H_2O_2. ●) in 0.1 M phosphate buffer (pH = 7). ○) 1 mM [H_2O_2] in 0.1 M phosphate buffer (pH = 7). ▼) 3 mM [H_2O_2] in 0.1 M phosphate buffer (pH = 7). The solution was purged with argon gas. The frequency range was between 828 and 0.1 Hz.

The impedance remains similar in all cases. If oxygen was trapped into the pores, the presence of oxygen would have been reflected in the impedance showing a dramatic change in the capacitance caused by the reduction in electrochemical surface area. In consequence, the effect is not due to oxygen gas bubble formation.

According to the results of these experiments, oxygen does not act as a product inhibition which can affect the kinetic model.

5.5.2 Effect of the phosphate buffer concentration

Other possibilities could result in the limitation of the reaction down the pores such as a deficiency of the buffer capacity as observed by Kicela *et al.*[40]. In our study, a phosphate buffer was used and therefore modifying the concentration of the phosphate buffer would entail a change not only in the buffer capacity but also in the ionic strength. As there is no Donnan exclusion, the ionic strength should not cause any effect but will be investigated by state of mind. The effect of the ionic strength was first tested by adding K_2SO_4 while maintaining the concentration of the phosphate buffer. A 'thick' mesoporous Rh film (deposition charge = 34.72 µC) electrodeposited on a Pt microelectrode was used for the experiment to notice any effect. The current response was monitored for the hydrogen peroxide oxidation at 0 V vs. SMSE in different concentrations of hydrogen peroxide. Figure 5-22 shows calibration curves over a large range of hydrogen peroxide concentrations at a potential at which oxidation occurs for various K_2SO_4 concentrations.

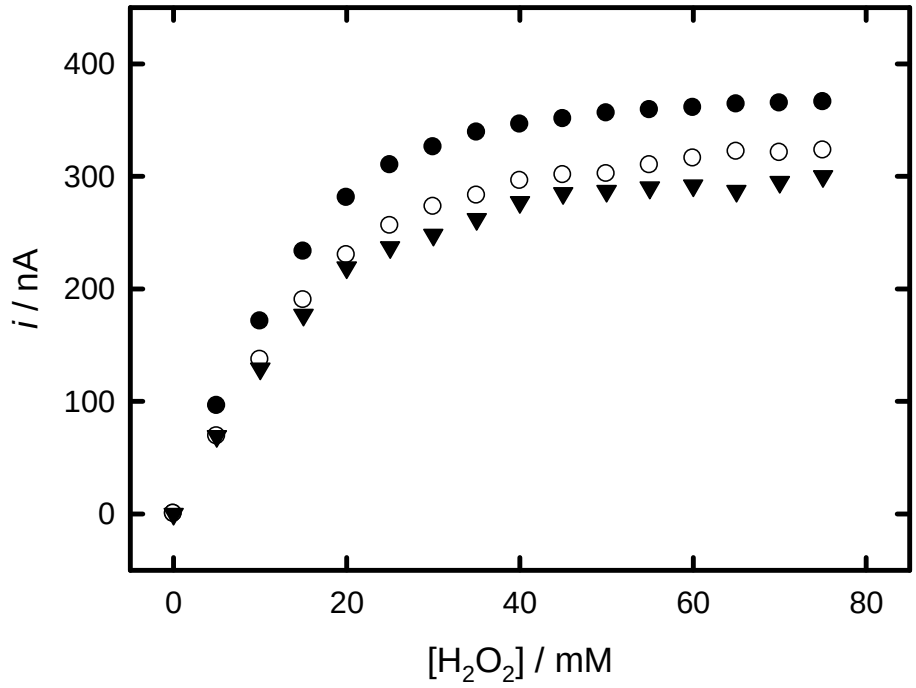

Figure 5-22. Calibration curves for the oxidation of hydrogen peroxide obtained from chronoamperometry of a mesoporous rhodium film electrodeposited on a platinum microelectrode (diameter = 25 µm, deposition charge = 34.72 µC) in 0.1 Mphosphate buffer(pH = 7, *T* = 25 °C) in presence of K_2SO_4. ●) in 0.1 M phosphate buffer (pH = 7). ○) in 0.1 M phosphate buffer + 0.1 M K_2SO_4 (pH = 6.86). ▼) in 0.1 M phosphate buffer + 0.2 M K_2SO_4 (pH = 6.83). The electrode was held at 0 V vs. SMSE throughout the whole experiment. The electrode was held at 0 V vs. SMSE for 20 min before the addition of aliquots of hydrogen peroxide.

Increasing the electrolyte concentration K_2SO_4 does not improve the current response; on the contrary, a slight decrease can be observed (10-15 % from the value without K_2SO_4). It was also noticed that the pH of the solution was approximately 0.15 pH unit less with the addition of K_2SO_4 which could account for the drop in the current response. The effect of the ionic strength can be discarded from our hypothesis to play a role to affect the current response due to the hydrogen peroxide oxidation.

The effect of buffer capacity was tested by changing the concentration of the phosphate buffer. Figure 5-23 shows calibration curves over a large range of hydrogen peroxide concentrations at a potential at which oxidation occurs for various concentrations of phosphate buffer.

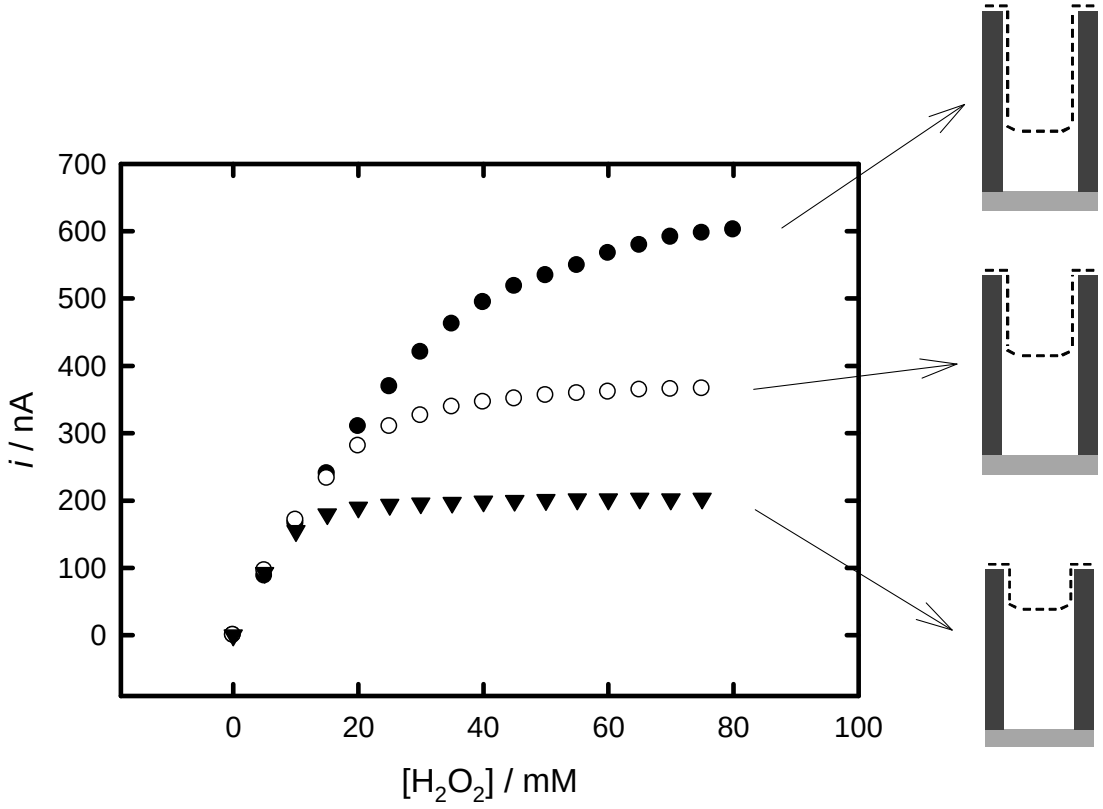

Figure 5-23. Calibration curves for the oxidation of hydrogen peroxide obtained from chronoamperometry of a mesoporous rhodium film electrodeposited on a platinum microelectrode (diameter = 25 µm, deposition charge = 34.72 µC) for different concentrations of the phosphate buffer, pH = 7, *T* = 25 °C. ●) in 0.2 M phosphate buffer (pH = 7). ○) in 0.1 M phosphate buffer (pH = 7). ▼) in 0.05 M phosphate buffer (pH = 7). The electrode was held at 0 V vs. SMSE throughout the whole experiment. The electrode was held at 0 V vs. SMSE for 20 min before the addition of aliquots of hydrogen peroxide. On the right, the drawings correspond to an approximate depth in which hydrogen peroxide penetrates into the pore.

The current response deviates rapidly from the mass transport behaviour in 0.05 M phosphate buffer. The release of the protons upon oxidation is accompanied by the uptake of the base electrolyte, which is responsible for a loss of the buffer capacity. The local buffer capacity is then reduced and then the local pH inside the pores decreases. The presence of protons in large quantities can lead to a more acidic medium within the pores. The decrease of the local pH can then entail a shift of the oxidation towards more anodic potentials and the Rh sites are in reduced state. As the potential remains constant upon our experimental conditions, the reaction will not occur down the pore. The hydrogen peroxide oxidation then occurs on the upper part of the pore. Figure 5-24 shows a schematic representation of a pore filled up with the phosphate buffer (pH=7) and a more acidic solution in the case the phosphate buffer concentration is low.

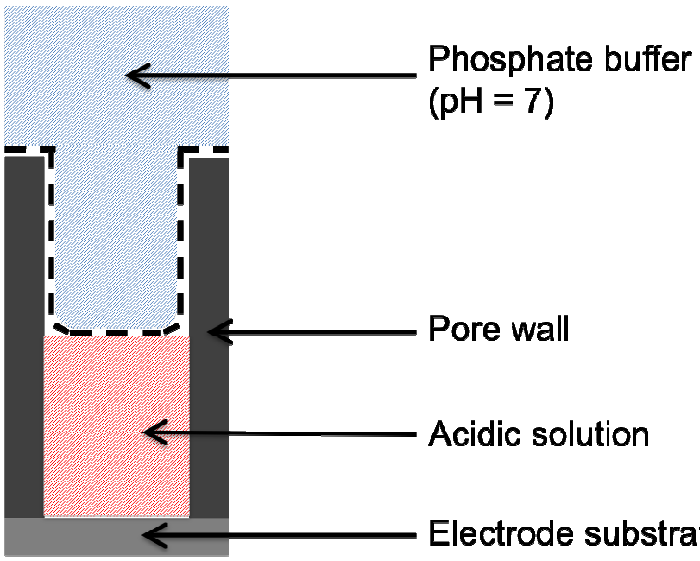

Figure 5-24. Schematic representation of a pore filled up with a phosphate buffer solution. The dashed line represents the demarcation between the phosphate buffer (pH = 7) (blue) and a more acidic solution down the pore (red).

At high concentrations of hydrogen peroxide (>10 mM), the production of protons is significant enough to lower the buffer capacity and the plateau appears more rapidly with a low concentration of phosphate buffer. As the pH becomes more acidic down the pore, the hydrogen peroxide oxidation will not occur. The current response is directly affected by the local change of pH.

When the concentration of the phosphate buffer is increased, the linear region (low concentrations of hydrogen peroxide) was extended over a larger hydrogen peroxide

concentration range. At high concentrations of hydrogen peroxide, the current response still becomes a plateau but exhibiting higher current values. This increase is attributed to the reaction of hydrogen peroxide oxidation further into the pore, which is consistent with an increase of the buffer capacity. Increasing the concentration of the phosphate buffer maintains the pH. Therefore, a sufficient phosphate buffer concentration is required to avoid any shift of pH within the pores.

5.5.3 Effect of the potential of oxidation

Figure 5-25 shows calibration curves recorded at different potentials for the hydrogen peroxide oxidation.

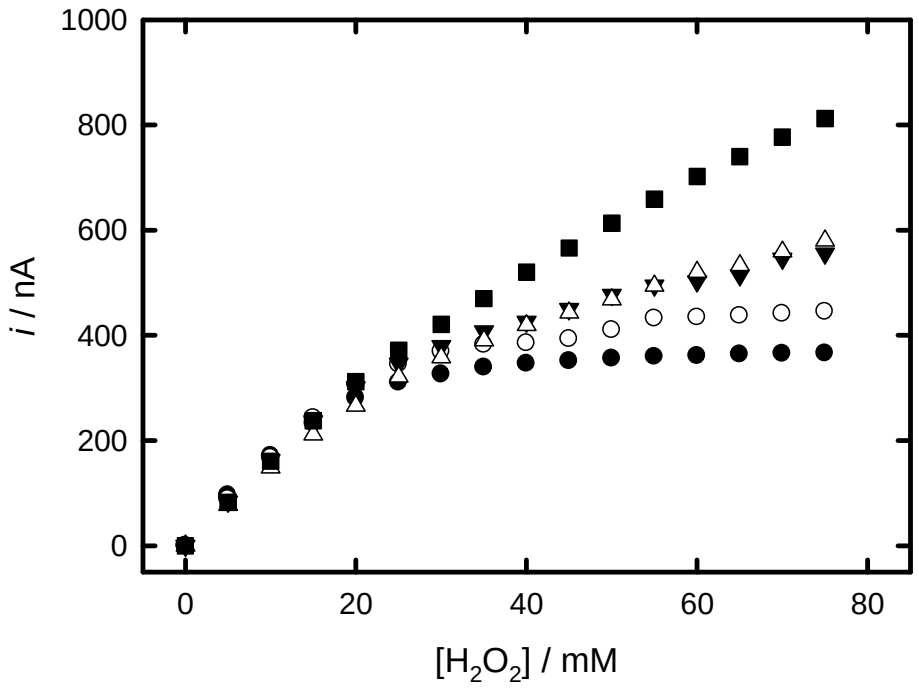

Figure 5-25. Calibration curves for the oxidation of hydrogen peroxide obtained from chronoamperometry of a mesoporous rhodium film electrodeposited on a platinum microelectrode (diameter = 25 µm, deposition charge = 34.72 µC) in 0.1 M phosphate buffer (pH = 7, *T* = 25 °C) recorded at different potentials. Potentials for hydrogen peroxide oxidation: ●) 0 V vs. SMSE, ○) 0.05 V vs. SMSE, ▼) 0.1 V vs. SMSE, ∆) 0.15 V vs. SMSE and ■) 0.2 V vs. SMSE. The electrode was held at the appropriate potential of the experiment for 20 min before the addition of aliquots of hydrogen peroxide.

At low concentrations of hydrogen peroxide (up to 25 mM), the current responses for the different potentials of oxidation are linear and have similar values. However, when the potential for the oxidation increases, the current responses are improved. When the potential is increased, more rhodium sites are under an oxidised state. Therefore, the reaction can occur over a larger coverage of oxidised rhodium sites on the catalyst surface. When concentrations of H_2O_2 are high, the current response is thus increased with the applied potential. According to the results of the experiments, the coverage of oxidised rhodium sites is strongly dependent of the pH of the solution and the applied potential.

The calibration curve obtained at 0.2 V vs. SMSE is consistent with that Evans *et al.*[1] obtained at + 0.6 V vs. Ag/AgCl though they used a mesoporous Pt microelectrode in their study. The values and the trend of the calibration curve in their study are similar to our present work.

5.5.4 Simulation of calibration curves

In this work, the effect of the film thickness was investigated in 0.1 M phosphate buffer but the current responses with 'thick' mesoporous Rh films were relatively similar due to a lack of buffer capacity. In this part, calibration curves are illustrated to observe the effect of the film thickness in 0.2 M phosphate buffer. Computational calibration curves are only an illustration and do not necessarily reflect the reality. It gives an idea to the reader how the calibration curves should appear for different thicknesses.

Based on the calibration curve obtained for the mesoporous Rh film (deposition charge = 34.72 μC) in a 0.2 M phosphate buffer, the current response for the 'thick' films was generated from the expression for the case boundary I/III (eq. 37) by choosing appropriate values of $k_{cat}\Gamma_{site}\sigma$ and K_M. Assuming that the values for K_M are correct for the 'thin' films, they can be used for a good starting approximation to the 'thick' films (see Table 5.4 where K_M varies). The values for $k_{cat}\Gamma_{site}\sigma$ depend on the film thickness so these latter for the 'thick' films were chosen from the trend of values for the 'thin' films. Figure 5-26 shows the calibration curves and the best fits for the 'thin' films and the computational curves for the 'thick' films.

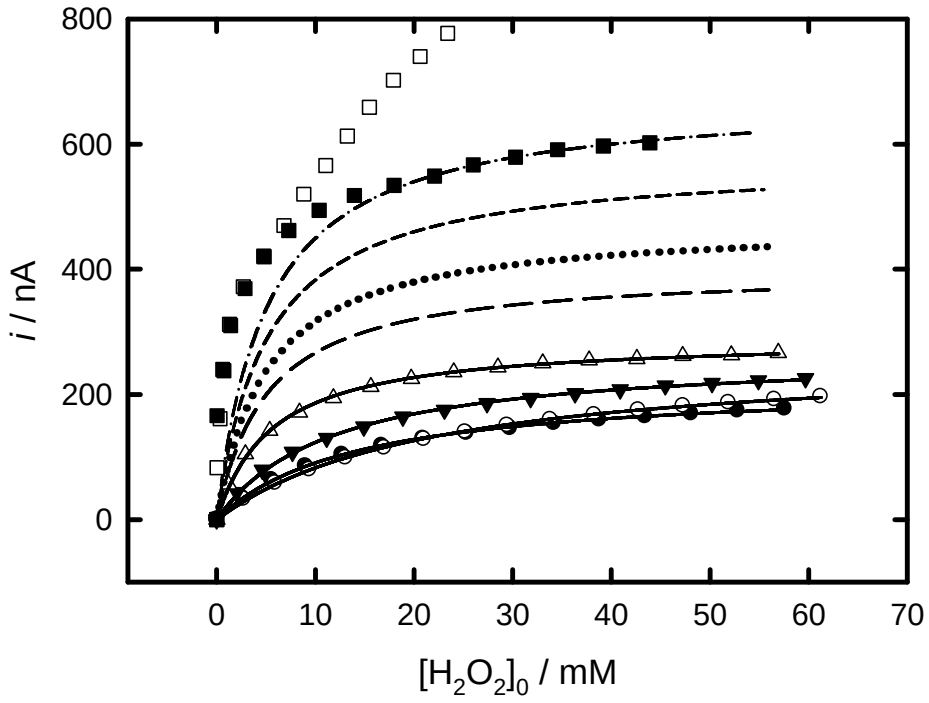

Figure 5-26. Real and expected calibrations curves for the oxidation of hydrogen peroxide obtained from chronoamperometry of a mesoporous rhodium films electrodeposited on a platinum microelectrode (diameter = 25 µm) in phosphate buffer, pH = 7, *T* = 25 °C. The real calibration curves were obtained in 0.1 M phosphate buffer for different deposition charges (●) 0.434 µC,(○) 0.868 µC, (▼) 1.74 µC and (Δ) 5.52 µC. The solid lines correspond to the best fits of the experimental curves to the expression for the case I-III. The long-dashed, dotted, short-dashed and dot-dashed lines represent the best fits of the expected curves to the expression for the case I-III for 'thick' mesoporous Rh films with the respective deposition charges of 8.68, 17.36, 26.04 and 34.72 µC. The data for the fits are presented in Table 5.4. The curves are generated for the electrodes held at 0 V vs. SMSE. Reproduction of the calibration curves for the oxidation of hydrogen peroxide obtained from chronoamperometry of a mesoporous rhodium film electrodeposited on a platinum microelectrode (diameter = 25 µm, deposition charge = 34.72 µC) recorded (■) in 0.2 M phosphate buffer(pH = 7, *T* = 25 °C) and(□) in 0.1 M phosphate buffer (pH = 7, *T* = 25 °C) at 0.2 V vs. SMSE.

Table 5.4 shows the values for the parameters from the best fits of the curves for the 'thin' films (deposition charges between: 0.434 and 5.52 µC) and the values chosen to generate the calibration curves for the 'thick' films (deposition charges between: 8.68 and 34.72 µC).

Table 5-4. Values for the parameters for the best fits of the expression for the case I-III.

Deposition charge / μC	$k_{cat}\Gamma_{site}\sigma$/ mol cm^{-2} C^{-1} s^{-1}	K_M / mM
0.434	4.675±0.607	14±6.5
0.868	3.882±0.337	22±2.0
1.74	2.382±0.153	11±4.7
5.52	0.627±0.006	5.5±1.3
8.68	0.802±0.011	5
17.36	0.492±0.024	5
26.04	0.383±0.017	5
34.72	0.377±0.002	5

In the light of the results from the buffer capacity experiment, the current responses of the thick films were simulated in a 0.2 M phosphate buffer. The simulated calibration curve fits the experimental calibration curve recorded in 0.2 M phosphate buffer for a deposition charge of 34.72 μC, though K_M might slightly less to match the data for low concentration of hydrogen peroxides. Interestingly, it can be observed that the calibration curve recorded at 0.2 V vs. SMSE in 0.1 M phosphate buffer fits with that of recorded in 0.2 M phosphate buffer at 0 V vs. SMSE at low concentration of hydrogen peroxide.

The results are consistent with the findings from Kicela *et al.* using platinum black high surface area electrode[40]. The reaction at the electrode surface is strongly affected by the local change of pH at high concentrations of H_2O_2. A concentration of phosphate buffer is thus recommended to avoid the inactivation of the surface sites.

In this work, the diffusion coefficient was considered the same in the bulk solution and into the pores for simplicity in the calculations. As reported by Amatore[39], diffusion within nanopores consisting of long cylinders with a radius of close to the size of ions is slower than in the bulk solution. Therefore, the diffusion coefficient in the nanopores may be smaller than those seen for species in the bulk solution. The species may attain the active bottom parts of the pores with difficulty. Amatore offers a theoretical model describing the interrelationship between diffusion and reaction within nanopores[39]. The

physico-mathematical modeling presents the trends of nanopores in contact with a solution of dilute species. The analysis led to distinct kinetic behaviours where diffusion plays a key role supplying the species from the bulk solution to the active sites on the pore walls[39].

5.6 Conclusion

Mesoporous Rh films were successfully electrodeposited onto platinum microelectrodes from lyotropic liquid crystalline templates used in the hexagonal phase. The properties of mass transport of microelectrodes were combined with the high surface area of macroelectrodes. Kinetically limited electrode reactions can thus be quantitatively analysed thanks to the high surface area provided by the internal surface of the pores. The voltammetry of hydrogen peroxide on conventional platinum microelectrodes was proved to be poor and unstable due to a rapid saturation of binding sites. The voltammogram of hydrogen peroxide on platinum microdiscs does not exhibit the usual sigmoidal shape of steady state voltammograms. In contrast, the electrodeposition of a mesoporous Rh film improved greatly the voltammetry exhibiting two well-defined plateaux for the oxidation and the reduction of hydrogen peroxide. We chose rhodium over platinum because the oxidation of hydrogen peroxide can occur at lower over-potentials resulting in avoiding interferences with other species such as uric acid or ascorbic acid. The potentials where hydrogen peroxide oxidizes and reduces depend on the surface state of the metal.

Calibration curves were obtained by adding aliquots of hydrogen peroxide into a 0.1 M phosphate buffer stepwise. The calibration curve for the polished platinum microelectrode deviates greatly from the theoretical values calculated from the diffusion equation. It has been reported that the linearity of the current response was not observed beyond 1 mM. However, the current in this work was measured for concentrations of hydrogen peroxide above 1 mM up to 70 mM. The electrodeposition of the mesoporous Rh microelectrode improved the current response dramatically of low concentrations of hydrogen peroxide (range between 0 mM and 20 mM) exhibiting a linear behaviour ensuring the mass transport control of the reaction using microelectrodes. Above 20 mM, the current response tends to a plateau probably due to a limitation of the hydrogen peroxide oxidation down the pores or due to a saturation of the binding sites. The

linearity of the current response was improved by increasing the concentration of the phosphate buffer resulting in a higher buffer capacity according to Figures 5-22 and 5-23. A higher concentration of the phosphate buffer maintains the pH down the pores and allows the reaction to occur. If the pH drops, the Rh binding sites are under a reduced state and the hydrogen peroxide oxidation stops as depicted in Figure 5-24.

A model to predict the current response of mesoporous Rh microdisc electrodes for the oxidation of hydrogen peroxide as a function of the film thickness and the concentration of the hydrogen peroxide has been described. The validity of the model was demonstrated for the 'thin' films but was not for the 'thick' films since a low concentration of phosphate buffer was used for the experiments. It was shown that a higher concentration of phosphate buffer was then necessary so that the effect of the film thickness could become pertinent. A change in the local pH may dramatically affect the electrode process, which in turn affects the current response. The electrode potential was chosen low enough to avoid the oxidation of other species but the current response depends on the potential of hydrogen peroxide oxidation. Thus the current response was increased by stepping the potential towards more positive potentials to 0 V vs. SMSE (potential initially chosen). The potential of oxidation and the concentration of the phosphate buffer need to be appropriate to support a reasonable analysis of the kinetic model for the hydrogen peroxide oxidation in a mesoporous Rh film.

5.7 References

[1] S. A. G. Evans, J. M. Elliott, L. M. Andrews, P. N. Bartlett, P. J. Doyle, G. Denuault *Anal. Chem.* **2002**, 74, 1322-1326.
[2] C. M. Welch, C. E. Banks, A. O. Simm, R. G. Compton *Anal. Bioanal. Chem.* **2005**, 382, 12-21.
[3] M. I. Prodromidis, M. I. Karayannis *Electroanalysis*. **2002**, 14, 241-261.
[4] X. Z. Li, H. S. Liu *Environ. Sci. Technol.* **2005**, 39, 4614-4620.
[5] F. A. Armstrong, G. S. Wilson *Electrochim. Acta*. **2000**, 45, 2623-2645.
[6] W. B. Nowall, W. G. Kuhr *Electroanalysis*. **1997**, 9, 102-109.
[7] K. Aoki, M. Ishida, K. Tokuda, K. Hasebe *J. Electroanal. Chem.* **1988**, 251, 63-71.
[8] V. G. Prabhu, L. R. Zarapkar, R. G. Dhaneshwar *Electrochim. Acta*. **1981**, 26, 725-729.
[9] H. Y. Liu, T. L. Ying, K. Sun, H. H. Li, D. Y. Qi *Anal. Chim. Acta*. **1997**, 344, 187-199.
[10] B. R. Horrocks, D. Schmidtke, A. Heller, A. J. Bard *Anal. Chem.***1993**, 65, 3605-3614.
[11] T. Ruzgas, E. Csoregi, J. Emneus, L. Gorton, G. MarkoVarga *Anal. Chim. Acta*. **1996**, 330, 123-138.
[12] A. A. Karyakin *Electroanalysis*. **2001**, 13, 813-819.
[13] E. E. Ferapontova, V. G. Grigorenko, A. M. Egorov, T. Borchers, T. Ruzgas, L. Gorton *Biosens. Bioelectron.* **2001**, 16, 147-157.
[14] R. Garjonyte, A. Malinauskas *Sens. Actuator B-Chem.* **1999**, 56, 93-97.
[15] Y. Zhang, G. S. Wilson *J. Electroanal. Chem.* **1993**, 345, 253-271.
[16] L. Gorton *Anal. Chim. Acta*. **1985**, 178, 247-253.
[17] D. A. Johnston, M. F. Cardosi, D. H. Vaughan *Electroanalysis*. **1995**, 7, 520-526.
[18] S. B. Hall, E. A. Khudaish, A. L. Hart *Electrochim. Acta*. **1998**, 43, 579-588.
[19] S. B. Hall, E. A. Khudaish, A. L. Hart *Electrochim. Acta*. **1998**, 43, 2015-2024.
[20] S. B. Hall, E. A. Khudaish, A. L. Hart *Electrochim. Acta*. **1999**, 44, 2455-2462.
[21] S. B. Hall, E. A. Khudaish, A. L. Hart *Electrochim. Acta*. **1999**, 44, 4573-4582.
[22] S. B. Hall, E. A. Khudaish, A. L. Hart *Electrochim. Acta*. **2000**, 45, 3573-3579.
[23] J. M. Elliott, P. R. Birkin, P. N. Bartlett, G. S. Attard *Langmuir*. **1999**, 15, 7411-7415.
[24] J. H. Han, H. Boo, S. Park, T. D. Chung *Electrochim. Acta*. **2006**, 52, 1788-1791.
[25] P. N. Bartlett, J. Marwan *Microporous Mesoporous Mat.* **2003**, 62, 73-79.
[26] P. N. Bartlett, E. Simon *PCCP Phys. Chem. Chem. Phys.* **2000**, 2, 2599-2606.
[27] T. Biegler, D. A. J. Rand, R. Woods *J. Electroanal. Chem.* **1971**, 29, 269-&.
[28] G. Jerkiewicz, J. J. Borodzinski *Langmuir*. **1993**, 9, 2202-2209.
[29] G. Jerkiewicz, J. J. Borodzinski *J. Chem. Soc.-Faraday Trans.* **1994**, 90, 3669-3675.
[30] M. Peuckert *Surf. Sci.* **1984**, 141, 500-514.
[31] M. I. Florit, A. E. Bolzan, A. J. Arvia *J. Electroanal. Chem.* **1995**, 394, 253-262.
[32] C. Amatore, A. Oleinick, O. V. Klymenko, C. Delacote, A. Walcarius, I. Svir *Anal. Chem.* **2008**, 80, 3229-3243.
[33] S. A. M. Vanstroebiezen, F. M. Everaerts, L. J. J. Janssen, R. A. Tacken *Anal. Chim. Acta*. **1993**, 273, 553-560.

[34] A. Brestovisky, E. Kirowaeisner, J. Osteryoung *Anal. Chem.* **1983**, 55, 2063-2066.
[35] Borggaar.Ok *Acta Chem. Scand.* **1972**, 26, 3393-3394.
[36] W. J. Albery, A. E. G. Cass, Z. X. Shu *Biosens. Bioelectron.* **1990**, 5, 367-378.
[37] W. J. Albery, A. E. G. Cass, Z. X. Shu *Biosens. Bioelectron.* **1990**, 5, 379-395.
[38] W. J. Albery, A. E. G. Cass, B. P. Mangold, Z. X. Shu *Biosens. Bioelectron.* **1990**, 5, 397-413.
[39] C. Amatore *Chem.-Eur. J.* **2008**, 14, 5449-5464.
[40] A. Kicela, S. Daniele *Talanta*. **2006**, 68, 1632-1639.

Chapter 6: Electrochemical impedance characterisation of nanostructured mesoporous platinum films in ionic liquid electrolyte

In Chapter 5, the diffusion of hydrogen peroxide within the nanochannels of the mesoporous film was investigated. Hydrogen peroxide is a small molecule which is able to get into a nanopore of a few nanometer diameter. Aqueous electrolytes are fluid, which facilitates the liquid to penetrate easily through the mesoporous films. In contrast, ionic liquids possess larger molecules than in aqueous electrolytes and are more viscous stemming from their electrostatic interactions, which is a limiting factor to penetrate in these confined spaces. In this Chapter, the accessibility of the ionic liquids in the H_1 mesoporous Pt is investigated as to look at the properties of this type of nanostructure in ionic liquids.

6.1 Overview

Due to their high boiling point, negligible vapour pressure, these compounds provide an alternative option as solvents in chemical processes[1, 2]. Their use in electrochemistry is of prime interest attributed to their inherent ionic conductivity without the need of using a supporting electrolyte[3]. A key advantage over aqueous electrolytes is the wide electrochemical window spanning up to 6 V, indicating a high resistance for the cation and anion to reduce and oxidise[4]. Room Temperature Ionic Liquids (RTILs) are very attractive, thanks to their physical and chemical properties, for a wide range of applications such as batteries[5], fuel cells[6, 7], solar cells[8], electrodeposition[4, 9-11]. The wide potential stability with low vapour pressures and high ionic conductivity that ionic liquids possess make them preferable for new electroplating routes[3, 9]. Also oxygen-free ionic liquids are highlighted as a safety advantage over non-aqueous electrolytes for lithium battery applications[12].

Supercapacitors are energy storage devices with a high energy density and high power. Currently, supercapacitors operate in aqueous and organic electrolytes leading to low values of cell voltage (1.23 V for aqueous electrolytes, 2~3 V for organic electrolytes). The maximum energy and power of a supercapacitor is proportional to the square of the

cell voltage. Therefore the performance of the supercapacitor is thus limited by the electrochemical window. The wide electrochemical window (up to ~ 6 V) of RTILs could improve significantly their performances. The motivation to use ionic liquids for supercapacitors has generated many studies on the double layer capacitance at the interface between the electrolyte and the electrode material[13]. The capacitance behaviour depends on the applied potential, electrode material, the nature of the different ions and the surface structure at the electrode/ionic liquid interface[13]. Experimental[13-15] and theoretical[16, 17] studies on these systems have suggested a "bell"-shape for the plots of the capacitance as a function of the potential or "camel"-shape. The complicated shape of the curves depends on the double layer at the electrolyte/electrode interface. The distinction between these two shapes was related to the combination of different processes including the ionic polarizability, the relative permittivity, the void density and the specific adsorption of both cations and anions[13].

These studies have considered the capacitance on planar electrodes where the curvature of the surface is small compared to the size of the ions. However, a recent study established that the ion size and the electrode curvature have an impact on the electrical double layer capacitance. Many applications require high specific area electrodes which are a result of the exposed area offered by the nanostructures such as mesoporous carbon black[18]. The capacitance on the mesoporous structure is not well known. Recent studies have demonstrated an anomalous large capacitance when the pore size is comparable to the size of the ions[19]. In contrast, it is expected that charging rates become slower due to an impeded ionic mobility and a higher resistance along the small pores within the structure[20]. These effects are important to understand the influence of the structure properties in ionic liquids.

This Chapter deals with the study of the interface between an ionic liquid and a nanostructured Pt electrode with high specific surface area. Nanostructured Pt films were grown by electrodeposition through the hexagonal phase of the lyotropic liquid crystalline phase as described as in Chapter 3. The nanostructure exhibits an hexagonal array of pores with radii close to the size of the ions or small ionic clusters. In a previous study, the impedance analysis of sulphuric acid contained in a mesoporous Pt film showed a large capacitance of 110 mF cm^{-3} and short access time with frequencies

up to 1 kHz[21]. The same method was applied in the present work to assess the accessibility of the ionic liquid 1-n-butyl-3-3methylimidazolium hexafluorophosphate (BMIM-PF_6) within the H_1 mesoporous Pt film and to evaluate the performance of BMIM-PF_6 in H_1 mesoporous films as a supercapacitor electrode.

6.2 Preparation and characterisation of the electrodes

Platinum disc electrodes (0.00196 cm^2) were fabricated by sealing 500 μm diameter platinum wire in glass. The platinum disc electrodes were polished using silicon carbide paper (CC 1200, English abrasive) and water/alumina slurries (Buehler) with particle sizes of 1 μm and 0.3 μm. The microdiscs were then electrochemically characterised in 1 M sulphuric acid. Around 30 scans between –0.65 and 0.85 V vs. SMSE were necessary to remove the impurities at the surface of the electrode by oxidizing and reducing the species and thus obtain a stable cyclic voltammogram.

The H_1 mesoporous Pt film was deposited onto a polished Pt disc electrode from different plating mixtures. The plating solutions were a ternary system of surfactant ($C_{12}EO_8$) (42 % wt), water (29 % wt) and H_2PtCl_6 (29 % wt) and a quaternary system of surfactant ($C_{16}EO_8$) (41 % wt), water (28.5 % wt) and H_2PtCl_6 (28.5 % wt) and heptane (2 % wt). These proportions were chosen to form the hexagonal lyotropic liquid crystalline phase. This phase was confirmed by using polarized light microscope. The use of different surfactants varies the pore size; in this case, the use of $C_{12}EO_8$ yields a pore size of ~1.8 nm and a pore size of ~3.5 nm is obtained with the use of $C_{16}EO_8$ + heptane[22].

The potential was held - 0.1 V vs. SCE until the desired deposition charge had been passed (6.27 mC for each deposition). The film obtained was first cleaned in isopropanol and then soaked in water for several hours to remove the surfactant.

Cyclic voltammetry in 1 M sulphuric acid was performed to characterise each electrode and to estimate the surface area. The cyclic voltammograms for the polished platinum electrode and for the two mesoporous platinum electrodes are similar to those in Figure 3-2. The charges under the peaks for hydrogen desorption were evaluated by integration of the anodic current between - 0.65 and - 0.2 V vs. SMSE with subtraction of the

double layer capacitance. The electroactive surface areas were calculated using the conversion factor 210 μC cm^{-2}[23]. The double layer capacitance was measured in each case by dividing the central minimum current by the scan rate. These values are given in Table 6-1.

6.3 Capacitance in the ionic liquid

6.3.1 Voltammetry of a polished and mesoporous Pt in ionic liquid

Figure 6-1 shows cyclic voltammograms obtained for a polished platinum electrode and for each H_1 mesoporous Pt film of the same geometric surface area in [BMIM]-[PF_6].

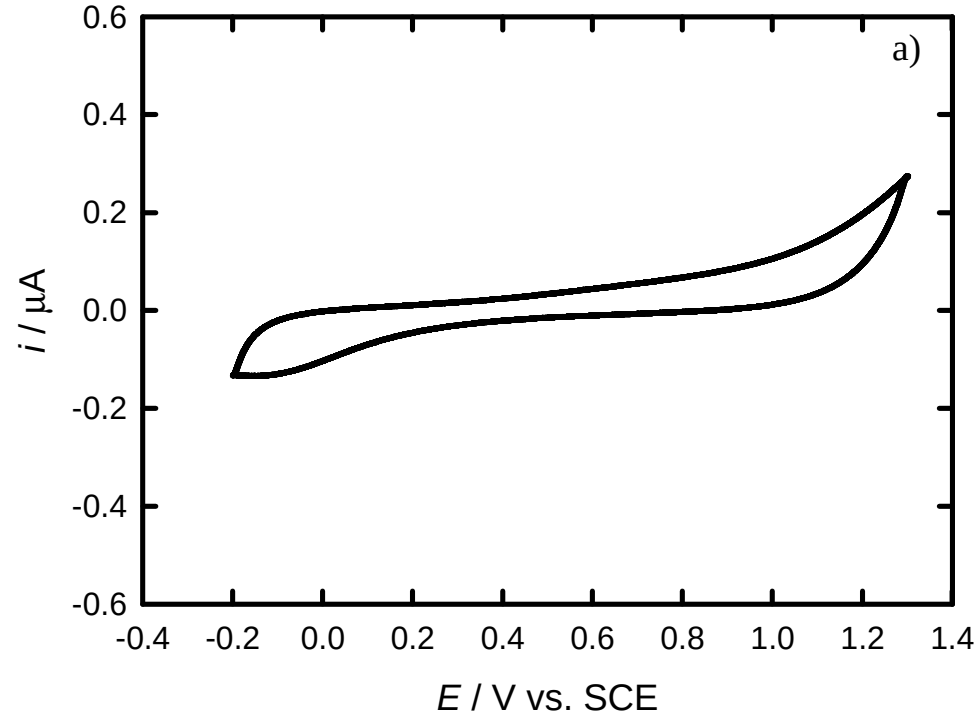
a)
0.6
0.4
0.2
0.0
-0.2
-0.4
-0.6
i / µA
-0.4 -0.2 0.0 0.2 0.4 0.6 0.8 1.0 1.2 1.4
E / V vs. SCE

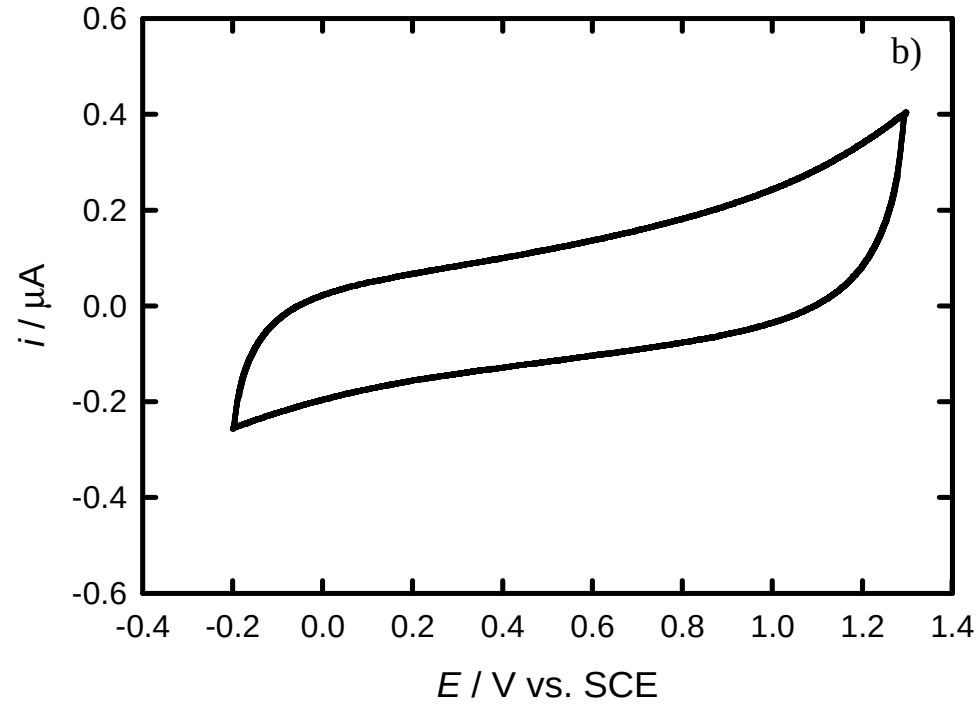
b)
0.6
0.4
0.2
0.0
-0.2
-0.4
-0.6
i / µA
-0.4 -0.2 0.0 0.2 0.4 0.6 0.8 1.0 1.2 1.4
E / V vs. SCE

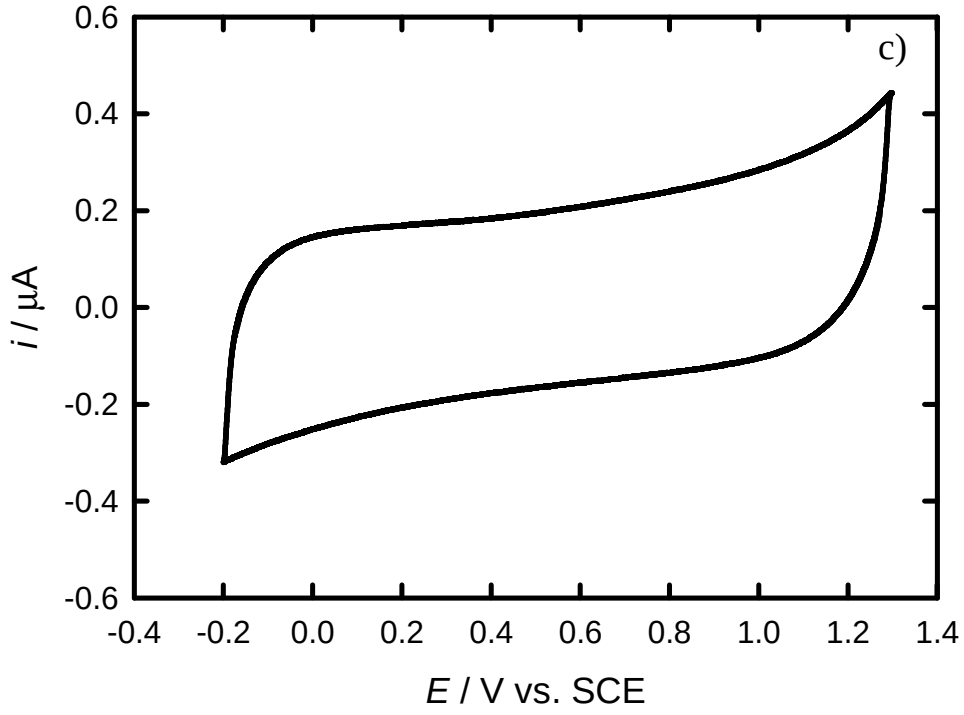

Figure 6-1. Cyclic voltammograms for the platinum disc electrode (500 µm in diameter) and for the H_1 mesoporous Pt films electrodeposited onto a Pt disc electrode (500 µm in diameter, deposition charge = 6.27 mC) in a BMIM-PF_6 solution recorded at 100 mV s^{-1}. The three types of electrodes were: (a) polished polycrystalline platinum, (b) H_1 mesoporous Pt electrodeposited from a $C_{12}EO_8$ and (c) H_1 mesoporous Pt electrodeposited from a $C_{16}EO_8$+heptane template.

The electrochemical potential window was restricted to the double layer region and the potential limits were selected to avoid the oxidation and the reduction of the respective anion and cation. The stable potential window of [BMIM]-[PF_6] on a similar Pt disc electrode of the same diameter was over 3.1 V as reported by Hultgren *et al.*[3]. However, the presence of impurities reduces dramatically the potential window. Water was observed as a common impurity in ionic liquids. Schroder *et al.* reported that only a small content of water decreased the potential window; for example, the presence of water in BMIM-BF_4 (such as 3 % in mass) decreased the potential window from 4.1 V under dry conditions to 1.9 V[9]. The cyclic voltammograms recorded in this work are consistent with those reported in the literature[1, 15, 24]. From the cyclic voltammograms, capacitances were estimated by dividing the charging current by the scan rate. The charging currents were assessed in the potential range of 0.3 and 0.5 V vs. SCE in which the current of both anodic and catholic scans is minimal. The values are shown in Table 6-1.

Table 6-1. Charge under the hydrogen peaks, double layer capacitances in 1 M sulphuric acid and in BMIM-PF_6 calculated from the cyclic voltammograms for the polycrystalline platinum disc electrode, the $C_{12}EO_8$ mesoporous Pt film electrodeposited onto a platinum disc electrode and the $C_{16}EO_8$+heptane mesoporous platinum film electrodeposited onto a platinum disc electrode. The electrodes are of the same geometric surface area (500 μm in diameter).

Measured data	Polished Pt	$C_{12}EO_8$ mesoporous Pt	$C_{16}EO_8$+heptane mesoporous Pt
H desorption charge / μC	1.03 ± 0.01	38.0 ± 0.2	66.1 ± 0.5
Capacitance measured at 100 mV s^{-1} in H_2SO_4 / μF	0.48 ± 0.01	18 ± 1	32 ± 1
Capacitance measured at 100 mV s^{-1} in [BMIM]-[PF_6] / μF	0.197 ± 0.007	1.03 ± 0.03	1.72 ± 0.05

It is clear that the charges under the hydrogen desorption peaks and the double layer capacitance are higher for the H_1 mesoporous Pt films than for the polished platinum electrode. This is expected from the internal surface area provided by the porous channels of the films and shows that [BMIM]-[PF_6] penetrates in pores at least to some extent (the capacitance is between 5 and 10 times that of the polished Pt electrode of the same geometric surface area). The data were shown as plots in Figure 6-2 to be more explicit. Figure 6-2a shows the capacitance measured in 1 M sulphuric acid as a function of the hydrogen desorption charge for each type of electrode. Figure 6-2b shows the capacitance measured in [BMIM]-[PF_6] as a function of the capacitance measured in 1 M sulphuric acid for each electrode.

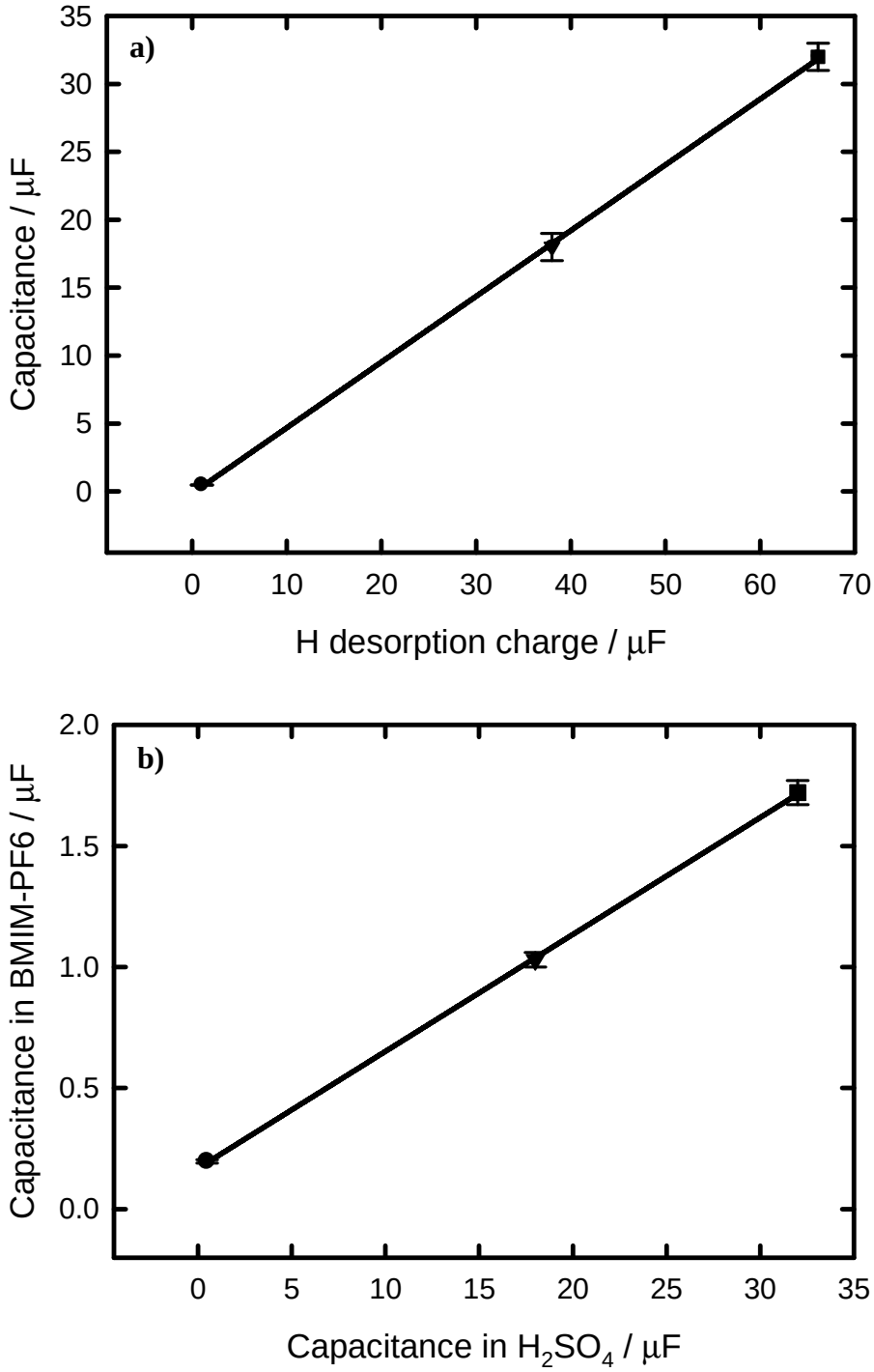

Figure 6-2. a) Capacitance as a function of the hydrogen desorption charge for each electrode, both calculated from the cyclic voltammogram recorded 1 M sulphuric acid. b) Capacitance measured in [BMIM]-[PF_6] as a function of the capacitance measured in 1 M sulphuric acid for each electrode. (●) polished Pt electrode, (▼) $C_{12}EO_8$ mesoporous Pt and (■) $C_{16}EO_8$+heptane mesoporous Pt. The solid lines in each graph represent a linear fit.

A linear trend was observed for the capacitance measured in 1 M sulphuric acid and the hydrogen desorption charge calculated for each type of electrode. It was also noticed that a linear trend exists between the capacitance measured in [BMIM]-[PF_6] and in 1 M sulphuric acid.

Further analysis of the Table 6-1 leads to the calculations of different parameters as shown in Table 6-2. One of the important parameter is the specific capacitance (F cm^{-2}) which corresponds to the capacitance normalised by the total surface area obtained from the hydrogen desorption.

Table 6-2. Electrochemical surface area, ratio of the hydrogen charge and the capacitance in 1 M sulphuric acid, the ratio of the capacitances in BMIM-PF_6 and in 1 M sulphuric acid and specific capacitance in BMIM-PF_6 per total surface area. Those were calculated for each electrode aforementioned.

Derived data	Polished Pt	$C_{12}EO_8$ mesoporous Pt	$C_{16}EO_8$+heptane mesoporous Pt
Electrochemical surface area / cm^2	0.0049	0.1808	0.3147
(H charge/capacitance in acid) / V	2.146	2.111	2.066
Capacitance ratio ([BMIM]-[PF_6]/H_2SO_4)	0.4104	0.0572	0.0538
Specific capacitance in [BMIM]-[PF_6] / μF cm^{-2}	40.2	5.691	5.465

Observations from Table 6-2 are:

- The ratio of hydrogen desorption charge to the double layer capacitance in 1 M sulphuric acid is about 2.1 V for each electrode, which can be expected. This result reflects the interfacial capacitance of platinum in sulphuric acid in respect to the charge measured from hydrogen desorption.
- The area specific capacitance for both mesoporous films is reduced by a factor of ~ 7 in [BMIM]-[PF_6] compared with that on a polished platinum electrode.
- The capacitance decrease is much less significant than in 1 M sulphuric acid.

The capacitance decrease appears to reflect the significance of the size of the ions compared to the pore diameters as suggested in Figure 6-3. Figure 6-3 shows a cross-section of a single Pt pore with a diameter of ~1.8 nm. It is obvious that [BMIM]-[PF_6] adsorbed on the pore wall takes more space than the protons and thus prevents the neighbouring platinum sites from adsorbing as opposed to protons H_3O^+ which occupy most of the platinum sites available. Hence, the ratio between the capacitances measured in [BMIM]-[PF_6] and H_2SO_4 for the H_1 mesoporous Pt is much less than for the polished Pt electrode. The decrease in the capacitance could also be explained by some ionic liquid molecules not responding within the pores due to a confinement effect. Based from the observations from Chmiola *et al.*[19], another possibility would be that the ionic liquid does not penetrate within the pores due to the very small size of the pores compared to the molecules of the ionic liquid. Supplementary experiments using electrochemical impedance spectroscopy are needed to examine the behaviour of the nanostructured films in the ionic liquid.

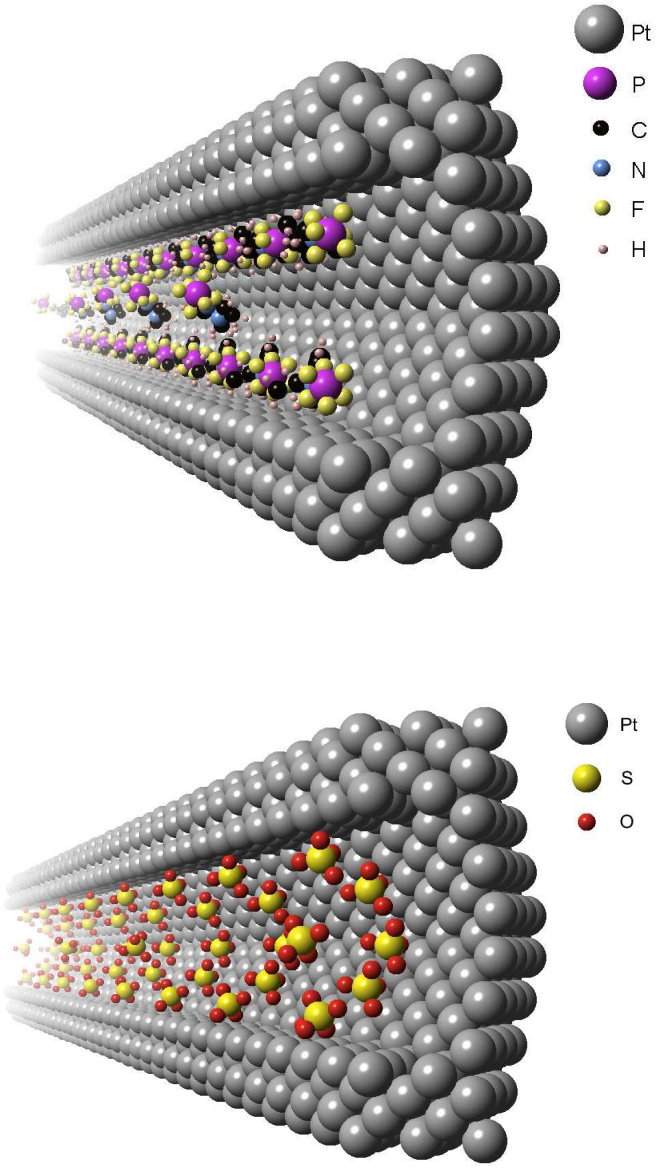

Figure 6-3. Drawing of cross-sections of a single Pt pore, diameter 1.8 nm. Schematic representations showing (top) [BMIM]-[PF_6] and (bottom) sulphate ions compared with the Pt atoms on the pore walls (H_3O^+ are assumed to be present but are not in the picture for clarity). The Pt atoms were created along the [111] facet.

The measurements of the capacitance by cyclic voltammetry have some limitations. First, it is difficult to deconvolute the voltage dependence of the charge from the time dependence. Hence, the capacitance-potential measurements do not have the same profiles at different scan rates and thus difficult to compare. Secondly, cyclic voltammetry involves large perturbations on the capacitances that may be far from

equilibrium. Thirdly, cyclic voltammetry results in a loss of information on resistances due to energy losses while charging the interface.

Electrochemical Impedance Spectroscopy could thus be more suitable to measure the capacitance at a fixed potential with a small perturbation. The advantage of this technique is the distinction between energy storage (capacitance) and energy losses (resistance) as a function of frequency.

6.4 Electrochemical Impedance Spectroscopy

6.4.1 Nyquist plot for a polished platinum disc electrode

Figure 6-4 shows a Nyquist plot for a polycrystalline polished platinum electrode in [BMIM]-[PF_6]. *Z*' and *Z*'' represent respectively the real and the imaginary parts of the impedance.

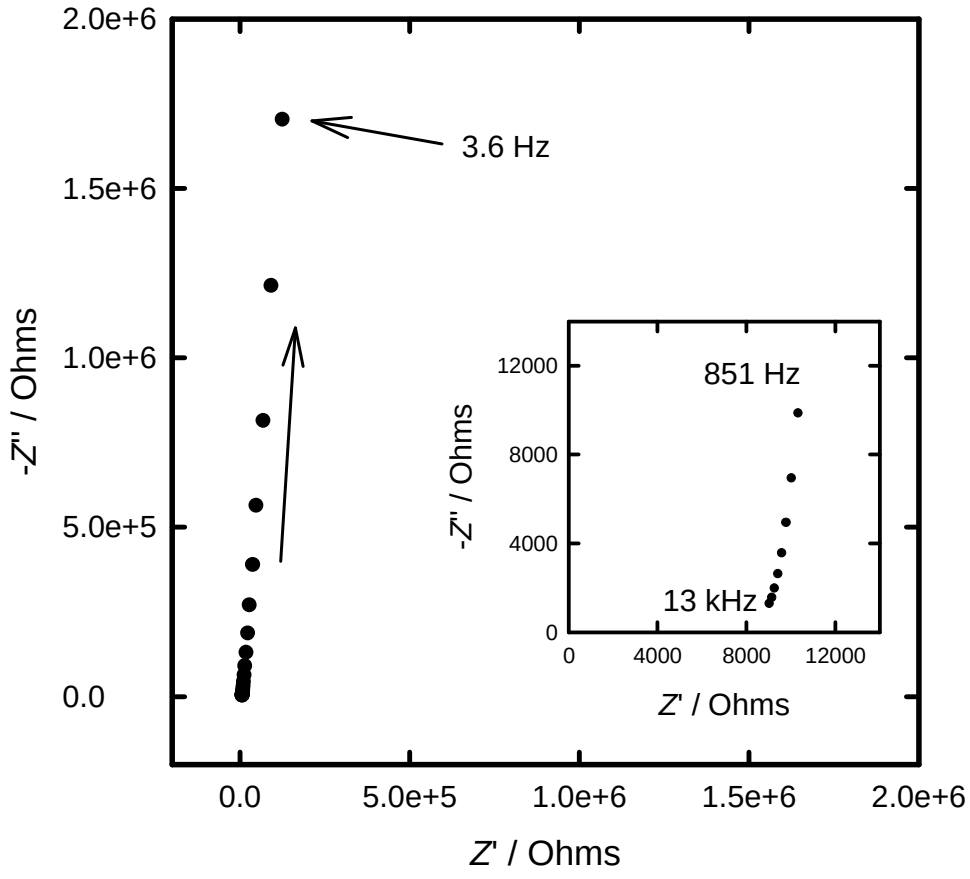

Figure 6-4. Nyquist plot for the polycrystalline platinum disc electrode (500 µm in diameter) in [BMIM]-[PF_6] at OCP. Inset: zoom at high frequencies.

Almost an ideal capacitive behaviour can be observed since the complex impedance function displays a near-vertical slope, which makes an angle of Φ = 85.8 ° to the real axis. The deviation from the vertical line expected for ideal behaviour is usually observed and attributed to the surface roughness or some slow molecular reorientations during double layer charge/discharge. This behaviour is modelled by a constant phase element (CPE) in equation (1), which also incorporates a series resistance due to the uncompensated electrolyte resistance path R_u between the working and reference electrodes.

$$Z = R_u + k\left(j\omega\right)^{-\alpha} \qquad (1)$$

where Z is the complex impedance, k is a constant, $j=\sqrt{(-1)}$, ω is the angular frequency and α is the phase.

Figure 6-5 shows the frequency dependence of the capacitance C for the polished platinum electrode in BMIM-PF_6, which is a consequence of a non-unity value of α.

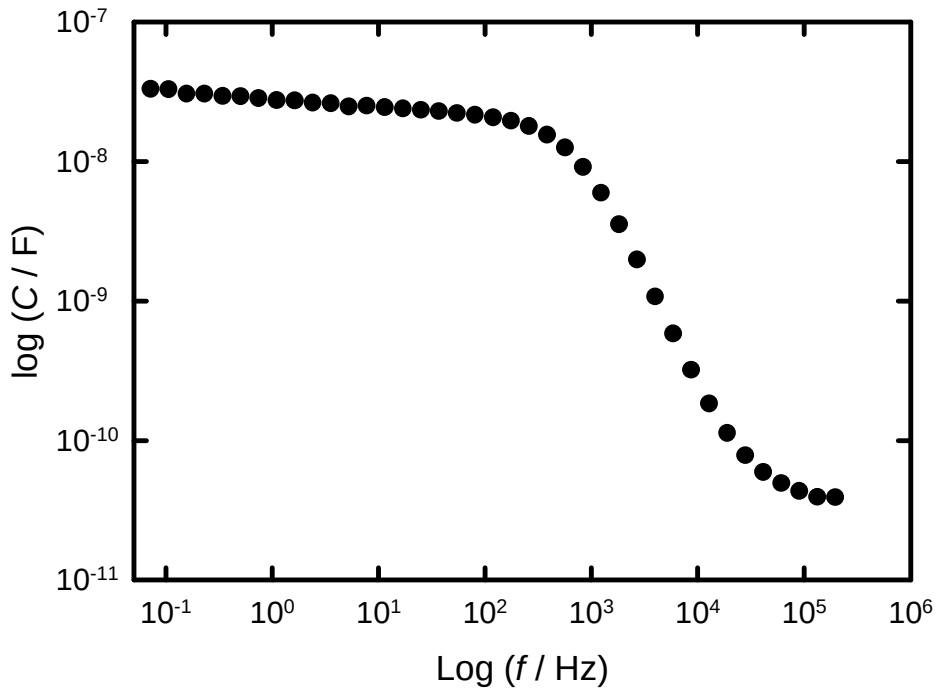

Figure 6-5. Capacitance as a function of the frequency for the polished polycrystalline platinum disc electrode (500 µm in diameter) in BMIM-PF_6 at OCP.

The capacitance measured at 0.1 Hz is a 7-fold decrease from the value obtained by cyclic voltammetry (see Table 6-1). Though surprising, such a variation with the test conditions was already noticed by Lockett *et al.* who reported similar variations with potential, starting potential and temperature[13]. This suggests that the observed capacitance is not purely thermodynamically controlled and that slow kinetics may be involved due to difficulties in structure reorganisation on plane surfaces as observed spectroscopically[24]. The reorganisation is presumed to be smaller in the impedance experiment than in cyclic voltammetry because of a much smaller applied overpotential.

6.4.2 Nyquist plot for mesoporous platinum electrode

Figure 6-6 shows the Nyquist plots for both H_1 mesoporous Pt films in [BMIM]-[PF_6] at open circuit potential (OCP).

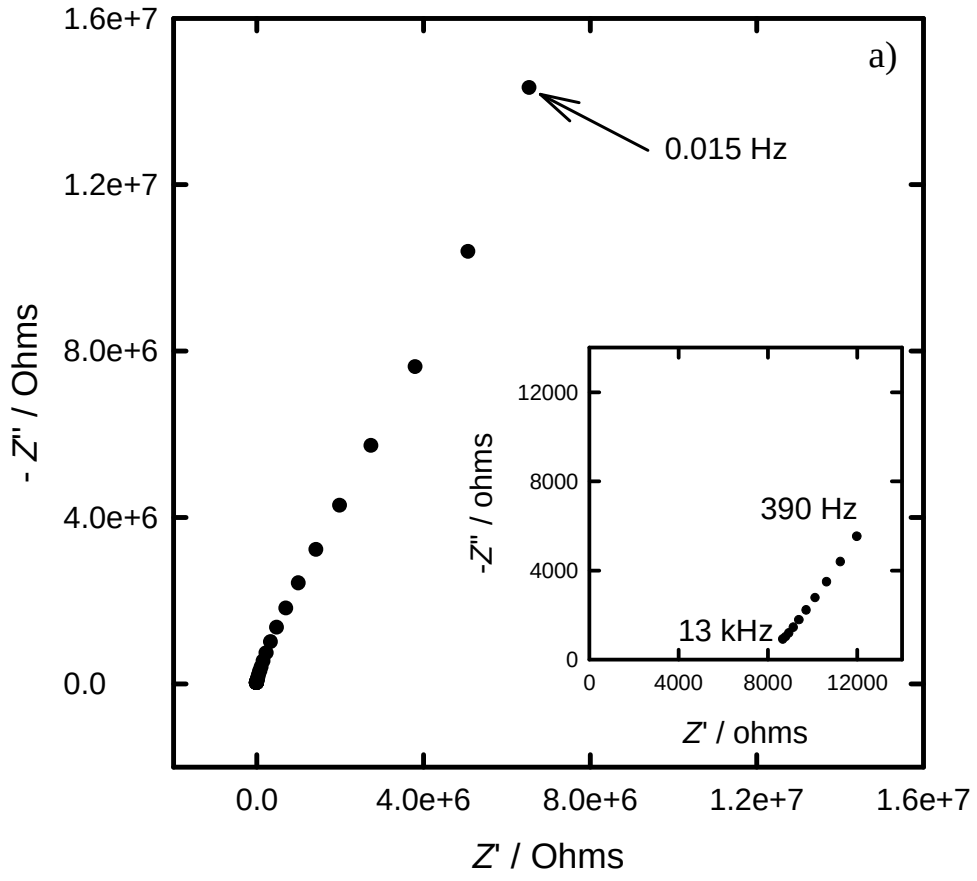

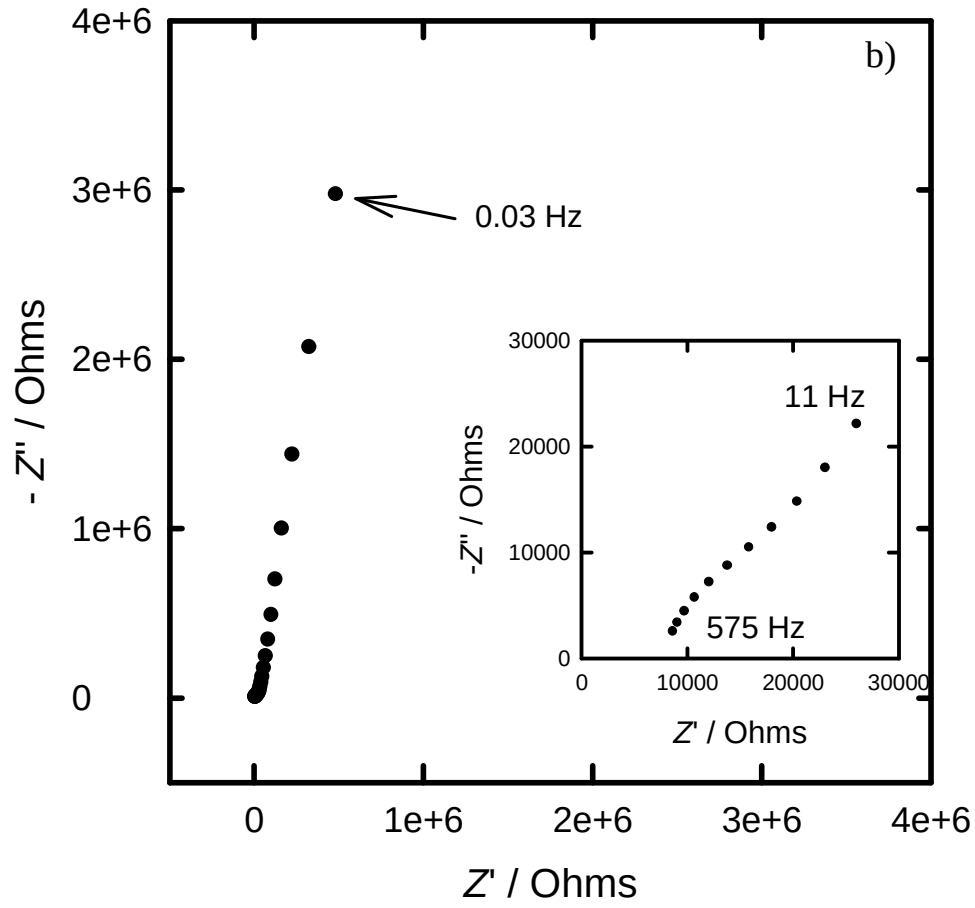

Figure 6-6. Nyquist plots in [BMIM]-[PF_6] at OCP for the H_1 mesoporous platinum films electrodeposited onto a platinum disc electrode (500 µm in diameter, 6.27 mC for the deposition charge) (a) from a $C_{12}EO_8$ template and (b) from a $C_{16}EO_8$ + heptane template. Insets: Zoom at high frequencies.

Both films have low impedances compared with the values obtained on the polished platinum electrode, consistent with larger surface areas provided by the nanostructure. For the H_1 mesoporous Pt templated with $C_{12}EO_8$ a slope of 54° can be observed at low frequencies indicating a resistive behaviour associated with a capacitive behaviour. The resistance at high frequencies may stem from impurities in the ionic liquid. With a closer inspection of the graph at high frequencies, the data show a diffusive slope of 63°. For the H_1 mesoporous Pt deposited from a template mixture containing $C_{16}EO_8$+heptane, a slope of around 80° confirms the non-ideal capacitive behaviour in the low frequency. The data in the inset show a slope of approximately 45° indicating a diffusive behaviour at high frequencies which will be investigated later.

Figure 6-7 shows the capacitances as a function of the frequency for the H_1 mesoporous Pt films.

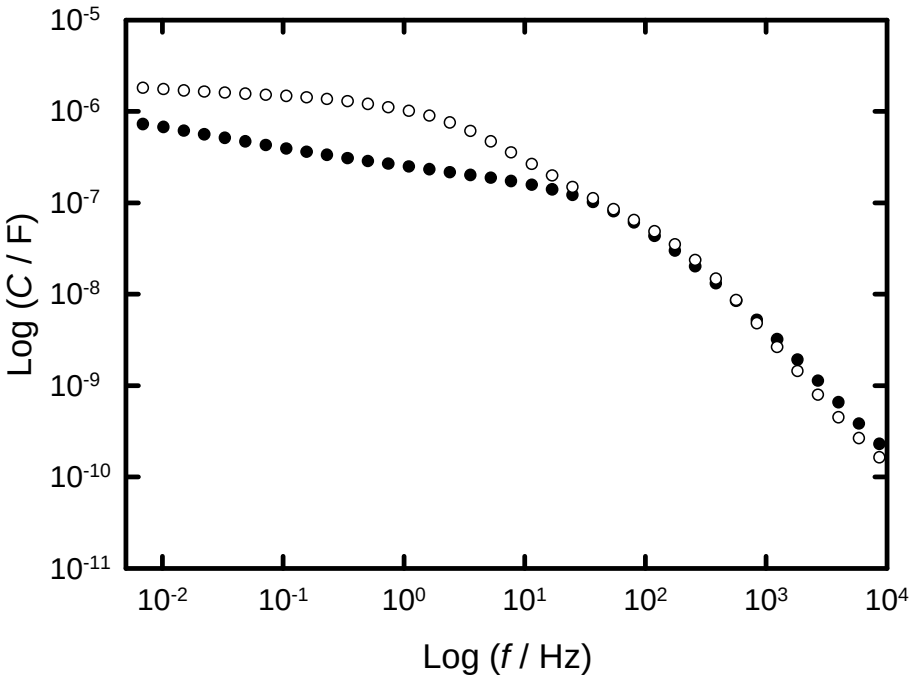

Figure 6-7. Capacitances as a function of the frequency for the H_1 mesoporous Pt films electrodeposited onto a Pt disc electrode (500 µm in diameter, deposition charge = 6.27 mC) in BMIM-PF_6 at OCP (●) from a mixture containing $C_{12}EO_8$ and (○) from a mixture containing $C_{16}EO_8$+heptane.

The value of the capacitance is larger for the $C_{16}EO_8$+heptane mesoporous Pt film than for the $C_{12}EO_8$ mesoporous Pt film which is due to a higher surface area of the $C_{16}EO_8$+heptane templated film (0.181 as opposed to 0.315 cm^2). The capacitance for the $C_{16}EO_8$+heptane mesoporous Pt film decreases significantly below 100 Hz. The capacitance data decrease more gradually for the $C_{12}EO_8$ mesoporous Pt film than the $C_{16}EO_8$+heptane mesoporous Pt film. The capacitance for the $C_{12}EO_8$ mesoporous Pt film starts to decrease just around 1 Hz suggesting a severe kinetic limitation to the molecular reorganisation mechanism.

The results are summarised in Table 6-3. The area specific capacitance at low frequency for the $C_{16}EO_8$+heptane mesoporous Pt film is similar to that for a polished platinum electrode. The values for the $C_{12}EO_8$ mesoporous Pt film are much reduced, especially at high frequency.

Table 6-3. Capacitance at 0.1 Hz, specific capacitances per total surface area at 0.1, 10 and 1000 Hz for the polished platinum electrode and each H_1 mesoporous Pt film electrodeposited onto a Pt disc electrode from $C_{12}EO_8$ and $C_{16}EO_8$ + heptane templates.

Impedance data	Polished Pt	$C_{12}EO_8$ mesoporous Pt	$C_{16}EO_8$+heptane mesoporous Pt
Capacitance at 0.1 Hz / μF	0.03	0.5	1.59
Specific capacitance at 0.1 Hz / μF cm^{-2}	6.12	2.77	5.05
Specific capacitance at 10 Hz / μF cm^{-2}	5.09	1.11	2.22
Specific capacitance at 1000 Hz / μF cm^{-2}	4.08	0.28	0.32

6.4.3 Bode plot for a polished platinum disc electrodes

The uncompensated series resistance was estimated from the Nyquist plot at high frequencies by extrapolation of the data to the x-axis as shown in Figure 6-8. The subtraction of the uncompensated series resistance simplifies the analysis in the Bode plot and the estimation of the parameters from the CPE model is now possible. Figure 6-9 shows the Bode plots for the polished platinum electrode recorded in [BMIM]-[PF_6] at OCP without and with the uncompensated series resistance subtracted off.

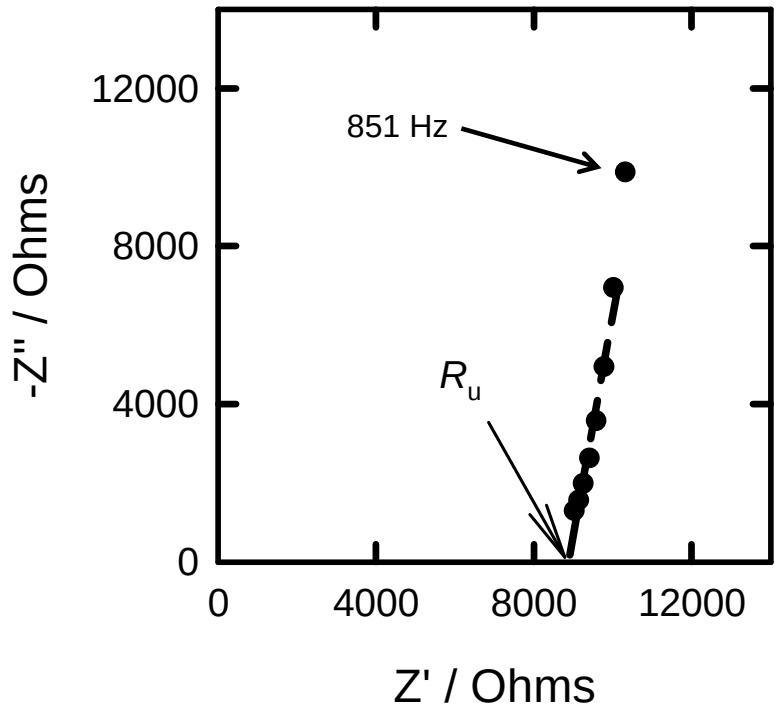

Figure 6-8. Nyquist plot for the polycrystalline platinum disc electrode (500 µm in diameter) in BMIM-PF_6 at OCP at high frequencies.

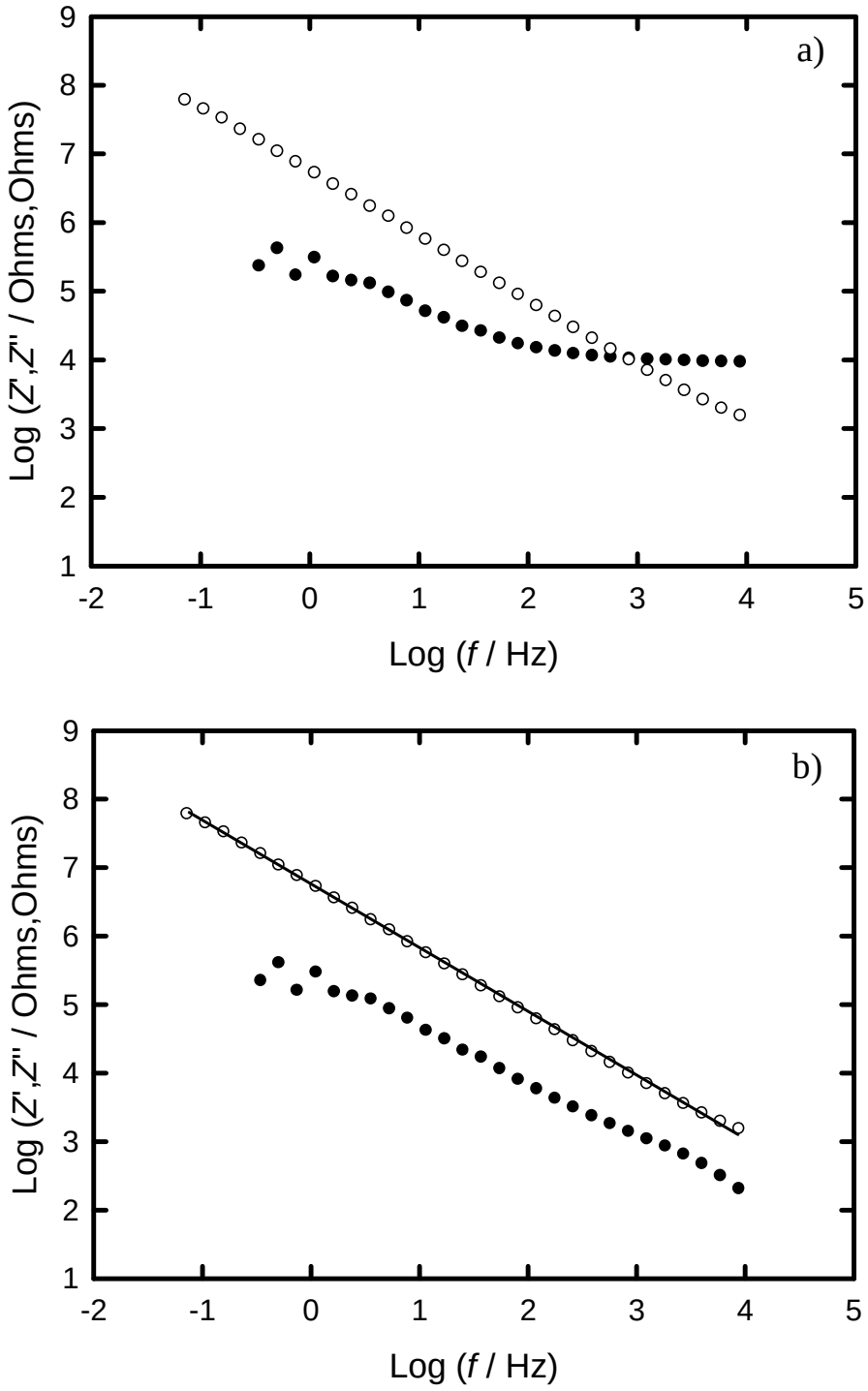

Figure 6-9. (a) Bode plot for the polished polycrystalline platinum disc electrode (500 µm in diameter) in BMIM-PF_6 at OCP. (b) Bode plot for the same electrode with the data modified by the subtraction of R_u = 8980 Ω and (solid line) linear fitting of the data for Z''. (●) Data for Z' and (○) data for Z''.

The imaginary part of the impedance shows a slope of α = 0.90 or Φ = 81° over 5 decades of frequency. From Figure 6-9a, the real part of the impedance contains two different slopes due to the uncompensated electrolyte resistance R_u. After subtraction of R_u from the raw data, the real and imaginary parts do not cross anymore as shown in Figure 6-9b. This is consistent with a CPE with the theoretical displacement given in (2)[21]:

$$\log(-Z'') - \log(Z') = \log\left(\tan\left(\frac{\alpha\pi}{2}\right)\right) \qquad (2)$$

Although the real part seems less accurate because of a greater phase error, the central section shows a displacement of ~ 1 decade from the imaginary part in the Bode plot (Figure 6-9b) corresponding to a value of α = 0.90 according to equation (2). The value of the phase angle measured in the Bode plot is consistent with the value found from the corresponding Nyquist plot. Therefore, it can be seen that the phase angle in the Nyquist plot is dependent of the frequency, which proves that the data are recorded from a real physical phenomenon and not from some artefacts of the instrument.

A model for the impedance of a porous electrode was proposed by De Levie[25]. Following De Levie, a porous electrode can be modelled on a transmission line to give the open circuit terminated Warburg impedance expression, corresponding to diffusion into a finite length end-blocked pore. Figure 6-10a shows the transmission line with a series and parallel elements associated with the equation (3):

$$Z = \sqrt{\frac{z}{y}}\coth\left(l\sqrt{zy}\right) \qquad (3)$$

Where z is the series element impedance per unit length, y is the parallel element admittance per unit length and l is the transmission line length.

Figure 6-10b shows the application of the transmission line impedance to a mesoporous electrode filled with an electrolyte. The expression of equation (3) substitutes its series and parallel elements into resistive and capacitive components, $z = r$ and $y = j\omega c$ as shown in equation (4):

$$Z = \sqrt{\frac{r}{j\omega c}} \coth\left(L\sqrt{j\omega rc}\right) \qquad (4)$$

where r is the electrolyte resistance per unit pore length, c is the capacitance per unit pore length and l is the pore length.

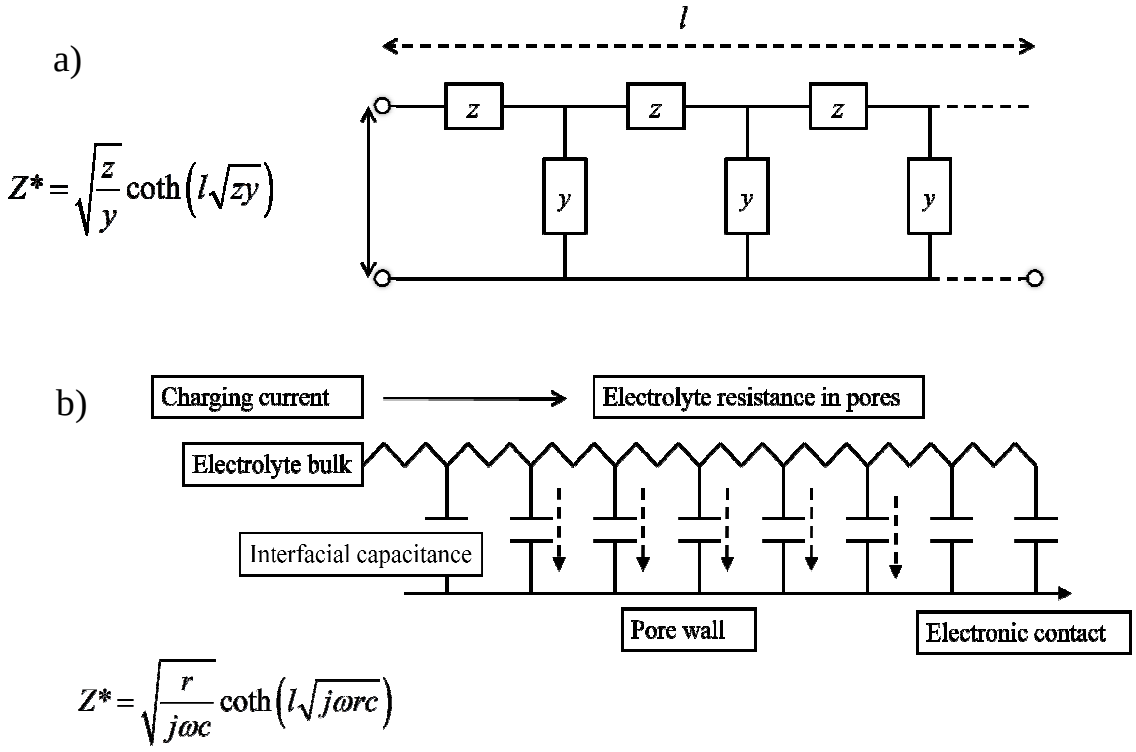

Figure 6-10. a) Transmission line impedance and (b) its representation for a mesoporous electrode filled with an electrolyte.

Substituting a CPE for the capacitance gives an equation similar to (4) which can be expressed as equation (5) in terms of different parameters:

$$Z = \frac{R\coth\left(j\omega T\right)^P}{\left(j\omega T\right)^P} \qquad (5)$$

where R is the total pore resistance ($R = lr$), T is the charge relaxation time constant corresponding to l^2/D for a diffusion process or l^2rc for the transmission line model and $P = \alpha/2$ with α representing the CPE exponent. For an ideal capacitance, $P = 0.5$. Alternatively, using the total resistance, R, and capacitance, C, T = RC.

To show the frequency dependence as well as the interrelation between the real and imaginary parts shown in equation (2), the data are presented as Bode plots of log(*Z*',*Z*'') vs. log(frequency). An example of this frequency dependence is simulated in Figure 6-11. The real and imaginary branches show two identifiable regions A and B. In the region A corresponding to low frequencies, e.g. for $\omega T << 1$, the function coth can be simplified as in equation (6):

$$\coth\left(j\omega T\right)^{P} \approx \left(j\omega T\right)^{-P} + \tfrac{1}{3}\left(j\omega T\right)^{P} \qquad (6)$$

In this case, equation (5) results in equation (7):

$$Z = R\left(j\omega T\right)^{-2P} + \tfrac{1}{3}R = R\left(j\omega T\right)^{-\alpha} = \tfrac{1}{3}R + R\left(j\omega T\right)^{-\alpha} \qquad (7)$$

The above formula indicates a dissociation of the effective electrolyte resistance $R/3$ from the CPE, $R(j\omega T)^{-\alpha}$, in the finite length diffusion approximation, i.e. uniform state of charge along the pore length. At high frequencies (region B), e.g. for $\omega T >> 1$, the function coth can be simplified as in equation (8):

$$\coth\left(j\omega T\right)^{P} \sim 1 \qquad (8)$$

In this case, equation (5) results in equation (9):

$$Z = R\left(j\omega T\right)^{-P} = R\left(j\omega T\right)^{-\alpha/2}$$

$$= R\left(\omega T\right)^{-\alpha/2}\cos\left(\frac{\alpha\pi}{4}\right) - jR\left(\omega T\right)^{-\alpha/2}\sin\left(\frac{\alpha\pi}{4}\right) \qquad (9)$$

Both real and imaginary parts have the same slope $\alpha/2$ in the log plot, corresponding to incomplete charging according to the semi-infinite boundary condition. At the cross-over frequency, real and imaginary parts are equal, representing the transition from A to B.

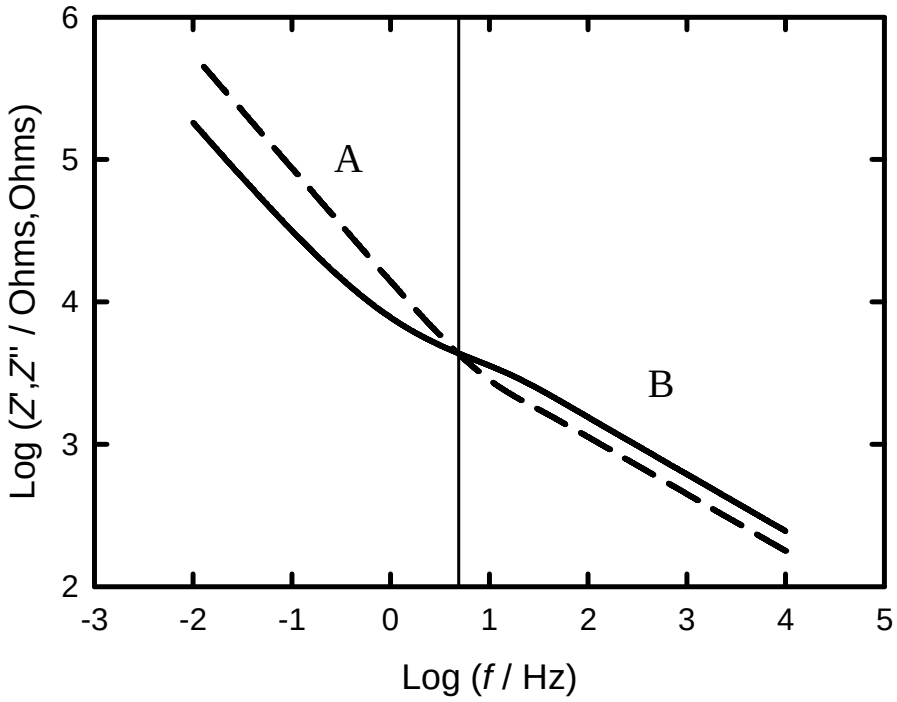

Figure 6-11. Theoretical data from the Warburg equation $Z = R\coth(j\omega T)^P/(j\omega T)^P$ with $R = 10000$, $T = 0.1$ and $P = 0.4$. (solid line) data for Z' and (dotted line) data for Z''.

6.4.4 Nyquist plot for mesoporous platinum electrodes

The corresponding Bode plot for a $C_{12}EO_8$ mesoporous Pt film is shown in Figure 6-12.

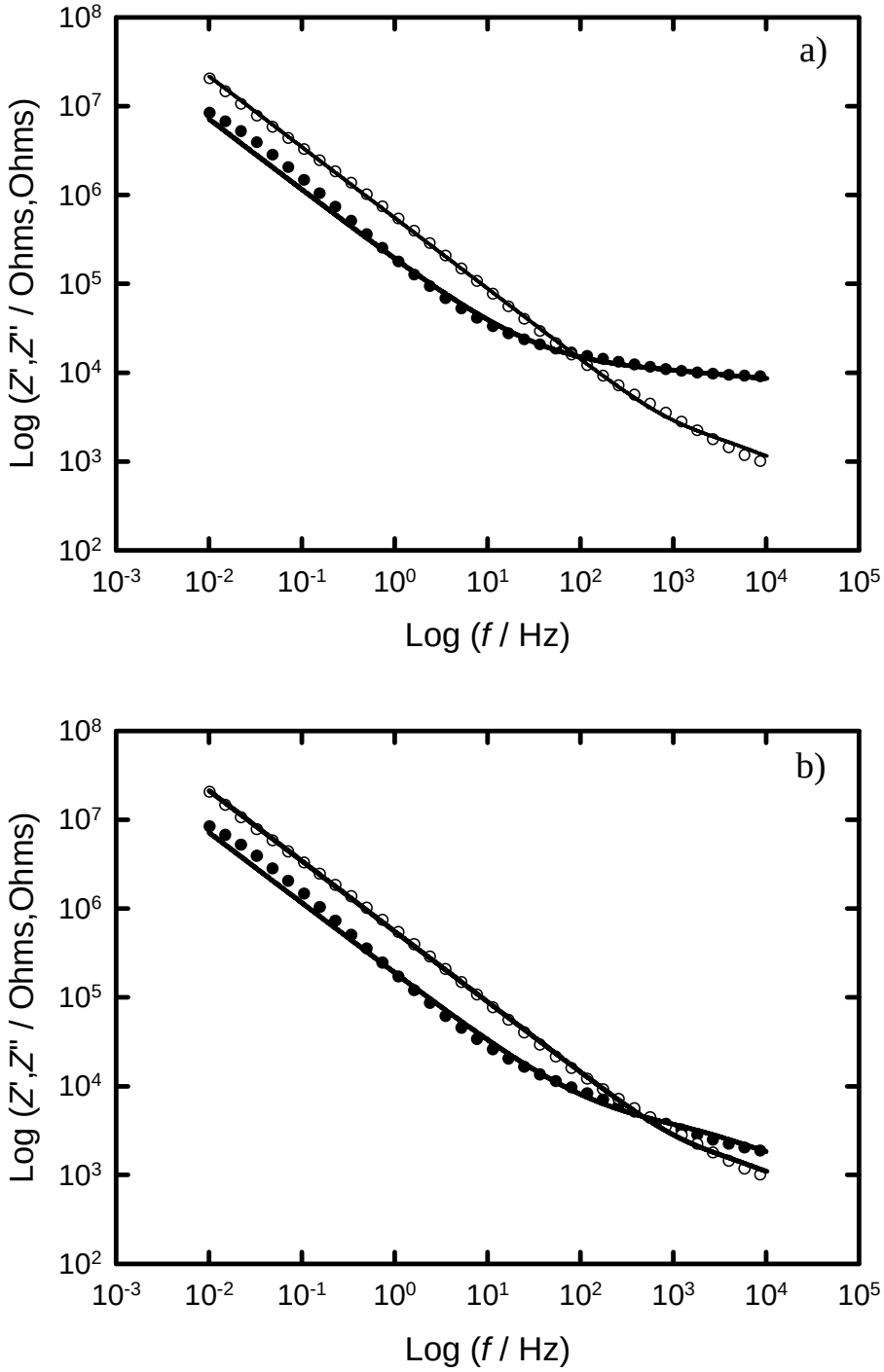

Figure 6-12. Bode plots for a $C_{12}EO_8$ mesoporous platinum film electrodeposited onto a platinum disc electrode (500 µm in diameter, 6.27 mC for the deposition charge) in BMIM-PF_6 at OCP (a) without and (b) with the data modified by the subtraction of R_u = 7000 Ω. (solid line) fitting of the data generated by the equation. (●) Data for *Z'* and (○) data for *Z''*.

The imaginary part displays a straight line over 5 orders of magnitude in the frequency range. After the subtraction of the value of R_u, the data get close to the model in the high frequency range as in Figure 6-11. However, the slope is about 0.9; this value is less than 1 due to the non-ideality of the capacitance. The importance of this non-ideality of the capacitance is that it contributes significantly to the real part, which can obscure the effect of the pore resistance.

The corresponding Bode plot for a $C_{16}EO_8$+heptane mesoporous Pt film is shown on the Figure 6-13.

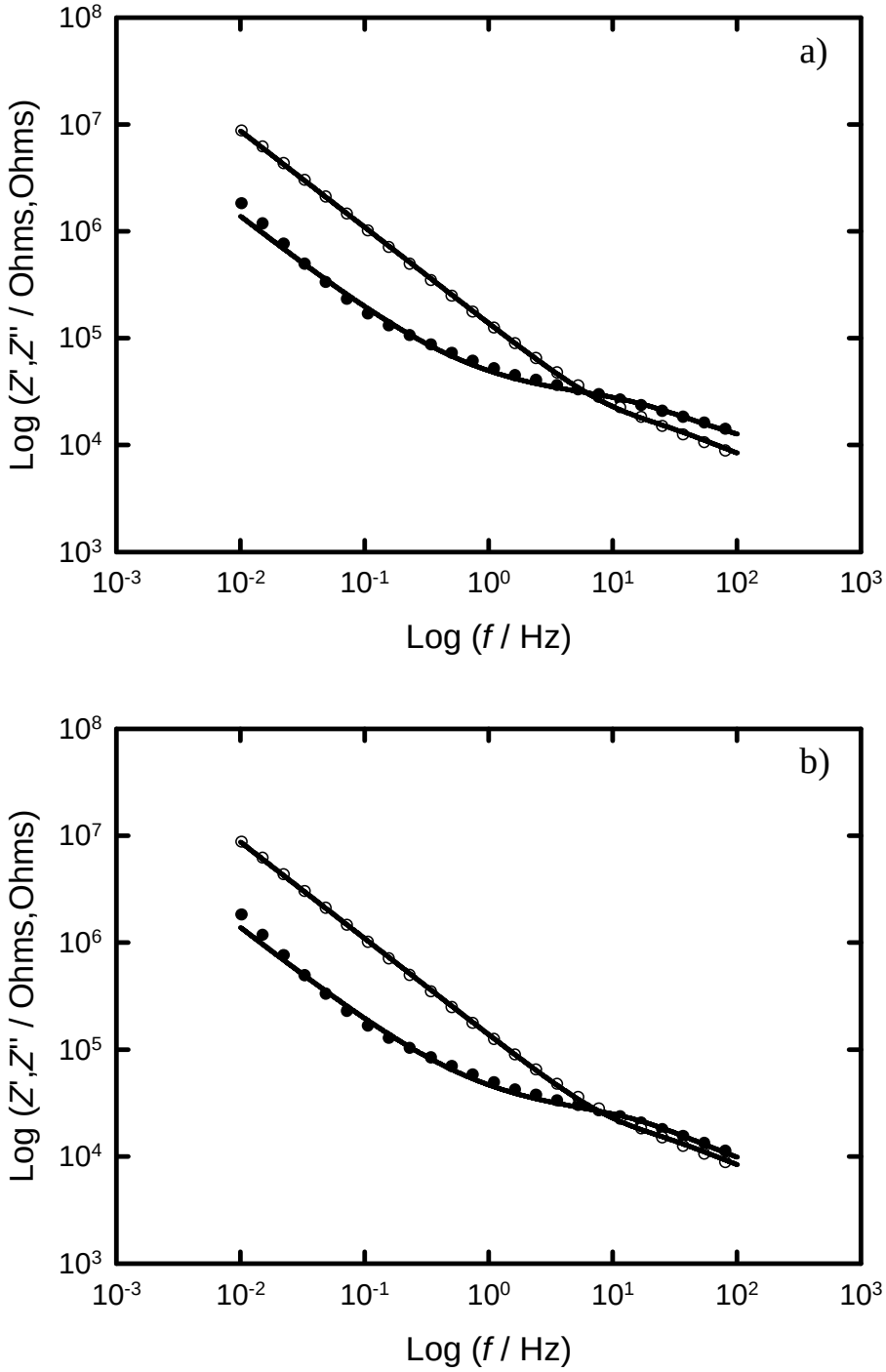

Figure 6-13. Bode plots for a $C_{16}EO_8$ + heptane mesoporous platinum film electrodeposited onto a platinum disc electrode (500 µm in diameter, 6.27 mC for the deposition charge) in BMIM-PF_6 at OCP (a) without and (b) withthe data modified by the subtraction of R_u = 2800 Ω. (solid line) fitting of the data generated by the equation. (●) Data for Z' and (○) data for Z''.

The impedance data fit the simulations quite well for both electrodes, showing the transition between finite and semi-infinite conditions.

From the analysis, some parameters are extracted for both H_1 mesoporous Pt electrodes as shown in Table 6-4. An important output of this analysis is the pore resistance, which can be identified as the value of *R* in the above equations. This allows an estimation of an effective conductivity of the ionic liquid in the H_1 mesoporous Pt film:

$$R = \frac{L}{\sigma_{eff} A} \tag{10}$$

where *R* is the resistance, *A* the area of the electrode, *L* the thickness of the film and σ_{eff} the effective ionic conductivity of the filled porous structure as if it were a homogeneous medium. The effective conductivity of the ionic liquid in the H_1 mesoporous Pt was calculated to be 8.3×10^{-7} S cm^{-1}. The bulk conductivity of the ionic liquid was calculated using the formula for hemispherical current flow to a flat disc electrode using (10):

$$R = \frac{1}{4\sigma a} \tag{11}$$

where *R* is the resistance, *A* the radius of the electrode and $\sigma$the conductivity. The conductivity of the ionic liquid on the polished platinum electrode was calculated to be 1×10^{-3} S cm^{-1}. The effective conductivity is about 3 orders of magnitude less. For the actual conductivity in the pores we should take account of the cross-sectional area and the current path along the pores. Such a decrease in the conductivity may be explained by a reduced mobility of the ionic liquid molecules within the pores, hence, a lower conductivity than the free electrolyte. This observation compares well with the reduced diffusivity due the pore size and the relative dynamic viscosity as described by Amatore[26].

Table 6-4. Values of the parameters from the equations fitted to the Bode plots for the $C_{12}EO_8$ mesoporous Pt film electrodeposited onto a platinum disc electrode and the $C_{16}EO_8$+heptane mesoporous Pt film electrodeposited onto a platinum disc electrode in BMIM-PF6.

	Polished Pt	**$C_{12}EO_8$ mesoporous Pt**	**$C_{16}EO_8$+heptane mesoporous Pt**
Pore resistance *R* / kΩ		9 ± 0.6	76 ± 2
Pore time constant, τ / s		0.00082 ± 0.00008	0.08 ± 0.003
Phase, α	0.90	0.39 ± 0.002	0.45 ± 0.001
Capacitance / μF = $10^3\tau$ /*R*	0.03	0.09	1
Electrochemical surface area / cm^2	0.0049	0.18	0.31
Area capacitance / μF cm^{-2}	40.163	0.5	3.2

6.5 Discussion

Cyclic voltammetry in sulphuric acid has shown high surface areas and high capacitances for each H_1 mesoporous Pt electrode by comparison to a polished Pt electrode of the same geometric area. The values for the high capacitances and the high surface areas arise from the internal area provided by the nanostructure. Cyclic voltammetry in [BMIM]-[PF_6] has also shown a higher capacitance for each H_1 mesoporous Pt electrode compared to a polished Pt electrode but to a lesser extent than in sulphuric acid. However, further analysis showed that the capacitance per surface area for each H_1 mesoporous Pt electrode is reduced greatly compared to the polished Pt surface, probably due to the size of the ions for [BMIM]-[PF_6] within the pores occupying more space than H_2SO_4. This effect could be also explained by the ionic liquid which does go down the pores but undergoes some restriction on mobility of the ionic liquid due to the difficulty of the place exchange of ions in the pore. The large size of the ions compared to the small size of the pores (1.8 – 3.5 nm) might prevent the ionic liquid from accessing the pores and from going at the bottom of the pores. Another explanation could also be the non-responsive behaviour of the ionic liquid in

the pores due to a confinement effect within the pores. Feng *et al.* reported that the electrode curvature has an effect on the capacitance of the electrical double layer in ionic liquids[27]. Feng *et al.* studied the structure and the capacitance of the electrical double layer on cylindrical electrodes[27]. However, our study focused on an electrode made up of porous channels in the range of 1.8 and 3.5 nm in diameter. The ionic liquid is confined within the pores conferring a specific relationship between the electrode and the ionic liquid affecting the structural properties of the electrical double layer. Although it will be fundamental to understand the structure of the electrical double layer in ionic liquids with H_1 mesoporous electrodes, this is not the goal of our study. The shape of the internal pore wall could play an important role in understanding the feature of the electrical double layer. The confined spaces in the pores might affect the molecule arrangement and probably have an impact on the capacitance. To be realistic, only 2 or 3 molecules of the ionic liquid can occupy the space in the diameter dimension of the pores (~ 2-3 nm in diameter) compared to tens of H_2SO_4 molecules. Although the mesoporous Pt electrodes in sulphuric acid exhibit high surface areas, the capacitance per surface area measured in BMIM-PF_6 is much more reduced for H_1 mesoporous electrode that for a flat surface. The pore size is not only important for the access of the electrolyte but also for the efficiency of the capacitance.

It was noticed that the capacitance measured by electrochemical impedance spectroscopy significantly decreased compared to the measure in cyclic voltammetry. This difference could be accounted for by the reorientation of the ions electrodes by sweeping the potential over a wide potential window as seen for flat electrodes[24]. However, Rivera-Rubero and Baldelli reported to observe reorientation of the ions on the surface by applying high overpotentials[24]. In the present case, the potential does not vary much from the equilibrium. Nevertheless, the capacitances for the H_1 mesoporous Pt electrodes measured at different frequencies are higher than the capacitance for the polished electrode. In contrast, the area specific capacitances for different frequencies show the opposite, larger for the polished Pt electrode than the H_1 mesoporous Pt which can be explained by the confinement effect mentioned earlier.

Elliott and Owen have shown that a transmission line model could be applied for the H_1 mesoporous Pt electrodes to analyse the data of electrochemical impedance

spectroscopy in sulphuric acid[21]. In this work, an identical method was used to characterise the H_1 mesoporous Pt films in ionic liquid. The simulations of the equations from the transmission line model fit quite well with the impedance data recorded in [BMIM]-[PF_6]. From the analysis of fittings, we found a higher pore resistance for the $C_{16}EO_8$+heptance than for the $C_{12}EO_8$ templated H_1 mesoporous Pt electrodes. This result seems surprising but it is worth mentioning the sequence of the experiments. First of all, the experiments were carried out in the same solution of [BMIM]-[PF_6] under "wet" conditions. The experiments (cyclic voltammetry + electrochemical impedance spectroscopy) with the $C_{16}EO_8$+heptane H_1 mesoporous Pt were performed first and the next day with the $C_{12}EO_8$ H_1 mesoporous Pt electrode. The water content in the ionic liquid could have been higher when the experiments were carried out for the $C_{12}EO_8$ H_1 mesoporous Pt electrode. The water content has dramatic effects in the properties of the ionic liquid. In presence of water, the electrostatic attractions are reduced between the ions, decreasing the energy of the system and as a result the viscosity of the ionic liquid[28]. As the electrical resistance is dependent of the viscosity, the measures for the pore resistance can be affected. As the water content increases the resistance of the ionic liquid decreases. Therefore, the pore resistance for $C_{12}EO_8$ H_1 mesoporous Pt electrode might be higher than measured in this experiment. The access time for the capacitance was found to be 100 times higher for the $C_{16}EO_8$+heptane H_1 mesoporous Pt electrode than for the $C_{12}EO_8$ H_1 mesoporous Pt electrode. Such a difference in the access time could also be explained by the conditions in which the experiments were performed as mentioned previously.

6.6 Conclusion

H_1 mesoporous Pt electrodes are characterised by high surface area highlighted by cyclic voltammetry in sulphuric acid. Hence, double layer capacitances were revealed to be much higher for these electrodes than for the polished platinum electrode. The capacitances measured in [BMIM]-[PF_6] were also larger for the H_1 mesoporous Pt electrodes than for the polished Pt electrode. However the capacitance surface areas for the H_1 mesoporous Pt electrodes were lower than for the polished Pt electrode, probably due to the confined spaces within the pores. However, the capacitances measured by EIS are different from those calculated by cyclic voltammetry by a factor of 7 due to a possible molecular rearrangement at the surface when sweeping the potential. The

results have also revealed that the capacitance is frequency dependent. The impedance data is consistent with a transmission line model for the H_1 mesoporous Pt electrode. The electrochemical impedance spectroscopy method employed in aqueous electrolytes is also valid to characterise the mesoporous films in the ionic liquids. From the analysis of the fittings, the pore resistance was found higher for the $C_{16}EO_8$+heptane H_1 mesoporous Pt electrode than for the $C_{12}EO_8$ H_1 mesoporous Pt electrode. Although this seems to be incoherent at first, the effect of the water content in the ionic liquid should not be excluded in our results. Indeed, the water in the ionic liquid may change its physicochemical properties affecting the measurements.

Despite the small size of the pores of the electrode, the results confirm the accessibility of the ionic liquid within the mesoporous electrodes. Therefore the mesoporous structure obtained from the hexagonal lyotropic liquid crystalline phase can be considered for the structure of supercapacitor materials.

6.7 References

[1] J. Zhang, A. M. Bond *Analyst*. **2005**, 130, 1132-1147.
[2] A. E. Visser, R. P. Swatloski, R. D. Rogers *Green Chem.* **2000**, 2, 1-4.
[3] V. M. Hultgren, A. W. A. Mariotti, A. M. Bond, A. G. Wedd *Anal. Chem.* **2002**, 74, 3151-3156.
[4] M. Armand, F. Endres, D. R. MacFarlane, H. Ohno, B. Scrosati *Nat. Mater.* **2009**, 8, 621-629.
[5] J. Fuller, R. T. Carlin, R. A. Osteryoung *J. Electrochem. Soc.* **1997**, 144, 3881-3886.
[6] M. Doyle, S. K. Choi, G. Proulx *J. Electrochem. Soc.* **2000**, 147, 34-37.
[7] R. Hagiwara, T. Hirashige, T. Tsuda, Y. Ito *J. Electrochem. Soc.* **2002**, 149, D1-D6.
[8] N. Papageorgiou, Y. Athanassov, M. Armand, P. Bonhote, H. Pettersson, A. Azam, M. Gratzel *J. Electrochem. Soc.* **1996**, 143, 3099-3108.
[9] U. Schroder, J. D. Wadhawan, R. G. Compton, F. Marken, P. A. Z. Suarez, C. S. Consorti, R. F. de Souza, J. Dupont *New J. Chem.* **2000**, 24, 1009-1015.
[10] F. Endres, S. Z. El Abedin *Chem. Commun.* **2002**, 892-893.
[11] F. Endres, M. Bukowski, R. Hempelmann, H. Natter *Angew. Chem.-Int. Edit.* **2003**, 42, 3428-3430.
[12] P. A. Johns, M. R. Roberts, Y. Wakizaka, J. H. Sanders, J. R. Owen *Electrochem. Commun.* **2009**, 11, 2089-2092.
[13] V. Lockett, M. Horne, R. Sedev, T. Rodopoulos, J. Ralston *Phys. Chem. Chem. Phys.* **2010**, 12, 12499-12512.
[14] R. Costa, C. M. Pereira, F. Silva *Phys. Chem. Chem. Phys.* **2010**, 12, 11125-11132.
[15] F. Silva, C. Gornes, M. Figueiredo, R. Costa, A. Martins, C. M. Pereira *J. Electroanal. Chem.* **2008**, 622, 153-160.
[16] A. A. Kornyshev *J. Phys. Chem. B.* **2007**, 111, 5545-5557.
[17] M. V. Fedorov, N. Georgi, A. A. Kornyshev *Electrochem. Commun.* **2010**, 12, 749-749.
[18] R. Lin, P. Huang, J. Segalini, C. Largeot, P. L. Taberna, J. Chmiola, Y. Gogotsi, P. Simon *Electrochim. Acta*. **2009**, 54, 7025-7032.
[19] J. Chmiola, G. Yushin, Y. Gogotsi, C. Portet, P. Simon, P. L. Taberna *Science*. **2006**, 313, 1760-1763.
[20] C. Largeot, C. Portet, J. Chmiola, P. L. Taberna, Y. Gogotsi, P. Simon *J. Am. Chem. Soc.* **2008**, 130, 2730-+.
[21] J. M. Elliott, J. R. Owen *Phys. Chem. Chem. Phys.* **2000**, 2, 5653-5659.
[22] G. S. Attard, P. N. Bartlett, N. R. B. Coleman, J. M. Elliott, J. R. Owen, J. H. Wang *Science*. **1997**, 278, 838-840.
[23] D. A. J. Rand, R. Woods *J. Electroanal. Chem.* **1972**, 35, 209-&.
[24] S. Rivera-Rubero, S. Baldelli *J. Phys. Chem. B.* **2004**, 108, 15133-15140.
[25] R. de Levie *Electrochim. Acta*. **1963**, 8, 751-780.
[26] C. Amatore *Chem.-Eur. J.* **2008**, 14, 5449-5464.
[27] G. Feng, R. Qiao, J. Huang, S. Dai, B. G. Sumpter, V. Meunier *Phys. Chem. Chem. Phys.* **2011**, 13, 1152-1161.
[28] R. Fortunato, C. A. M. Afonso, M. A. M. Reis, J. G. Crespo *J. Membr. Sci.* **2004**, 242, 197-209.

Chapter 7: Conclusions

The objective of the work presented in this thesis was to investigate the properties of nanostructured metal films electrodeposited from the lyotropic liquid crystalline template. Lyotropic liquid crystalline phases are formed by the combination of surfactant and an aqueous solution in which the appropriate metal salt is dissolved. The hexagonal lyotropic liquid crystalline phase is obtained with the appropriate proportions of surfactant and the aqueous solution. The metal film electrodeposited from the hexagonal phase consists of cylindrical porous channels arranged into an hexagonal array. The pore diameter can be changed by choice of the surfactant and/or the addition of heptane. The metal film was characterised by cyclic voltammetry in sulphuric acid and has been shown to have high surface area provided by the internal surface of the pores.

Cyclic voltammetry in sulphuric acid for the H_1 mesoporous Pt electrode displays the features of a polycrystalline platinum electrode made up of low index facets. CO stripping voltammetry was carried out on H_1 mesoporous Pt electrode and on polished Pt electrode. The voltammetric responses were compared between these two platinum electrodes. Although these two types of platinum electrode are both polycrystalline, CO stripping voltammetry has revealed differences resulting from the concave structure of the H_1 mesoporous Pt electrodes. The CO stripping voltammogram for a H_1 mesoporous Pt electrode exhibits a pre-wave, a main peak and a shoulder whereas that for a polished Pt electrode exhibits a single peak. It is suggested that the different features observed on the CO stripping voltammogram resulted from the morphology of the electrode surface. For the electrodeposition of H_1 mesoporous platinum using the surfactant $C_{12}EO_8$, the pore size was estimated to ~ 1.8 nm. A schematic model of a single pore suggests that the pore walls form an hexagonal shape constituted of 4-5 atoms. The charge calculated under the pre-wave represents 15 % of the total CO stripping charge consistent with this model. Based on studies on stepped surfaces, the pre-wave could be attributed to the existence of the trough sites within the pores, corresponding to the Pt sites in the intersection of two pore walls. CO is sterically hindered from adsorbing on the trough

sites as CO is adsorbed on the pore walls. The results seem to indicate that oxygenated species, more likely OH, are adsorbed on the trough sites accounting for the pre-wave and promoting CO oxidation occurring at lower overpotentials.

The cyclic voltammogram in sulphuric acid of a H_1 mesoporous Pt electrode shows different peaks in the hydrogen region that correspond to the adsorption of hydrogen on the diverse Pt facets. However, the peaks corresponding to the electrochemical response for different Pt facets are so close to each other that deconvolution of each of them becomes difficult. The nature of these facets was investigated by the adsorption of foreign atoms. Foreign atoms can adsorb on specific surface sites of the platinum surface. The adsorption of bismuth and germanium on the platinum surface is used to determine the proportion of Pt(111) and Pt(100) sites respectively. Cyclic voltammetry of H_1 mesoporous platinum electrodes modified with bismuth adatoms does not show any evidence for the existence of large Pt(111) domains which can be explained by the small width of the pore walls. The adsorption of Ge atoms on the Pt sites of the H_1 mesoporous films provided evidence for the existence of Pt(100) sites. It was found that 6 % of the total Pt sites of the H_1 mesoporous Pt electrode corresponds to Pt(100) sites.

The co-adsorption of CO and foreign atoms has shown interesting features on the CO stripping voltammetry. The CO stripping voltammogram for the H_1 mesoporous Pt electrode modified with Bi adatoms exhibited two separated peaks. One of the pair is related to the oxidation of adsorbed CO and the other is associated with the contribution of the oxidation for both species, Bi and CO. Numerous studies in the literature have shown that; the incorporation of Bi atoms on the platinum surface promoted CO oxidation. However, in the case of Bi adsorption on H_1 mesoporous Pt, CO oxidation was not encouraged. The CO stripping voltammogram for an unmodified H_1 mesoporous Pt exhibited a pre-wave whereas the pre-wave feature did not appear for the H_1 mesoporous Pt modified with Bi adatoms. As previously stated, the existence of the pre-wave was associated with the adsorption of oxygenated species on the trough sites. As the pre-wave is absent on the CO stripping voltammogram, we can suppose that the adsorption of Bi atoms occurs on the trough sites within the pores preventing oxygenated species from adsorbing. This results in Bi atoms adsorbing on the trough sites and CO adsorbing in the middle of the pore walls. In contrast, CO stripping

voltammetry for the H_1 mesoporous Pt modified with Ge adatoms shows a massive pre-wave and the CO oxidation peak. The pre-wave occurred at lower potentials than for an unmodified H_1 mesoporous Pt electrode. Ge atoms on the H_1 mesoporous Pt electrode facilitate CO oxidation. The catalytic properties for the Pt-Ge combination greatly facilitated CO oxidation in comparison to Pt-Bi on H_1 mesoporous Pt.

A particular interest for the H_1 mesoporous materials is to investigate the coupling of diffusion and surface reaction within the pores. Hydrogen peroxide oxidation can give some insight into both diffusion and surface reaction within the pores of nanoscale dimensions. The hydrogen peroxide oxidation was investigated at H_1 mesoporous rhodium films electrodeposited onto platinum microelectrodes and platinum rotating disc electrodes. Cyclic voltammetry in sulphuric acid indicates that the H_1 mesoporous rhodium films are polycrystalline and possess high surface areas. TEM observation revealed that the structure of these films consists of 4 nm diameter pores arranged into an hexagonal lattice. Furthermore, XRD also confirms TEM observation.

The oxidation of hydrogen peroxide was the subject of many studies showing notably the lack of quality for the voltammetry on bare platinum electrodes. The electrodeposition of a mesoporous platinum or rhodium film greatly enhances the stability and reproducibility of the voltammetry. The cyclic voltammogram displays plateaux for the oxidation and reduction of hydrogen peroxide unlike the polished platinum microelectrodes. This is due to the combined effect of high electrode surface area with efficient mass transport to the microelectrode. In this work, the kinetic study of hydrogen peroxide was carried out with H_1 mesoporous rhodium films. According to the cyclic volatmmograms in sulphuric acid, the oxide formation of rhodium starts at lower overpotentials than platinum. The early oxide formation could avoid the interference between the oxidation of hydrogen peroxide and other species such as ascorbic acid or uric acid in biological samples. Rhodium seems to be a more suitable catalyst than platinum in regards to this study.

A kinetic model originally developed by Albery was adapted to predict the current response due to the oxidation of hydrogen peroxide for H_1 mesoporous rhodium films. The data were obtained for different film thicknesses over a wide range of hydrogen

peroxide concentrations. The model describes the diffusion of hydrogen peroxide from the bulk solution to the electrode surface, hydrogen peroxide then diffuses into the pores and reacts on the internal surface of the pores. For thicker mesoporous film, the experimental data becomes inconsistent with the model at first; this was due to the lack of buffer capacity. The concentration of the phosphate buffer was not high enough to preserve the pH down the pores. The pH down the pores becomes more acidic and therefore, the rhodium sites are reduced bringing the reaction to a stop. A high concentration of buffer is needed to maintain the pH of the solution within the pores so that the reaction can then continue throughout the porous film. The potential of oxidation was also investigated. When the potential is increased towards more anodic potentials, the current response is improved for a thick mesoporous film. It is assumed that oxidised rhodium sites occupy a larger coverage of the catalyst surface when increasing the potential of oxidation overcoming the pH shift within the pores.

A part of this thesis dealt with determining the performance of the ionic liquid BMIM-PF_6 in the H_1 mesoporous film. Ionic liquids are more viscous than aqueous electrolytes and their molecules are quite large in comparison to hydrogen or CO molecules studied previously. For this study, H_1 mesoporous platinum were electrodeposited from plating mixtures of a ternary system containing $C_{12}EO_8$ and of quarternary system containing $C_{16}EO_8$ plus heptane. The nature of the surfactant and the addition of a swelling agent vary the pore size. The use of $C_{16}EO_8$ with heptane yields a pore size of 3.5 nm. The performance of the ionic liquid in H_1 mesoporous Pt films was investigated by the double layer capacitance for the H_1 mesoporous platinum electrodes of different pore size and the polished platinum electrode. The results indicate that the double layer capacitance for a H_1 mesoporous platinum electrode was larger than for a polished platinum electrode of the same geometric area and even larger for a larger pore size. The behaviour of the ionic liquid within the pores was investigated by electrochemical impedance spectroscopy. Previous work has shown that a De Levie model for porous electrodes could be applied for the H_1 mesoporous platinum electrode in sulphuric acid. The same model was used for identical H_1 mesoporous platinum electrodes in BMIM-PF_6. The simulations of the experimental data fit quite well with the model but the parameters taken from the fittings did not concur with the properties of the films.

Further work

The characterisation of the surface structure of the H_1 mesoporous Pt could be achieved by cyclic voltammetry in sulphuric acid. Another possible way would be to discriminate the different peaks in the hydrogen peaks associated with the low index Pt facets. This method could be developed using the characterisation in sulphuric acid of Pt single-crystals to identify the peaks for each crystal surface symmetry. Deconvoluting the peaks in the hydrogen region of the voltammogram in acid for a H_1 Pt mesoporous electrode would probably give information on the surface structure. This work could be accompanied with electron microscopy observation of the surface.

Further work could be undertaken with the combination of the high surface area electrode and high rate of mass transport thanks to the electrodeposition of mesoporous films. It would be possible to obtain kinetic information for various molecules. Investigations on hydrogen peroxide, oxygen and carbon monoxide with the H_1 mesoporous films have been undertaken. Another topic of interest could be related to the detection of enzyme product (e.g. H_2O_2) when the enzyme is in the solution above the nanoporous structure. Varying the pore size is an important factor to give access to large molecules.

The experiments performed with the ionic liquid were under “wet” conditions. The reference electrode could be replaced by a metal wire or bridge junction made with the ionic liquid to avoid any contamination. As the time of the experiments, the water content in the ionic liquid was not known which could be a good indication of the purity of the ionic liquid.

The penetration of the ionic liquid into the nanopores could also be investigated under different atmospheres such as under argon, nitrogen or under vacuum. When the pores are filled with ionic liquid, it could be possible that gas bubbles are trapped into the pores and the interface between the ionic liquid and the electrode surface is not complete.

In this work, the experiments for the electrochemical impedance spectroscopy in the ionic liquid were performed at unique potential (OCP) and simple scan rate for cyclic voltammetry. The capacitance depends strongly on the applied potential and presumably on the scan rate in cyclic voltammetry; therefore, changes in the structure of the double layer at the ionic liquid/electrode interface can be assessed. This could be useful in understanding the double layer in ionic liquids by comparing with existing experimental and theoretical studies.